

Parton Propagation and Fragmentation in QCD Matter

ALBERTO ACCARDI⁽¹⁾, FRANÇOIS ARLEO⁽²⁾, WILLIAM K. BROOKS⁽³⁾,
DAVID D'ENTERRIA⁽⁴⁾, and VALERIA MUCCIFORA⁽⁵⁾(*)

⁽¹⁾ *Hampton University, Hampton, VA, 23668, USA, and Jefferson Lab, Newport News, VA 23606, USA*

⁽²⁾ *LAPTH(**), Université de Savoie, CNRS, BP 110, 74941 Annecy-le-Vieux cedex, France*

⁽³⁾ *Departamento de Física y Centro de Estudios Subatómicos, Universidad Técnica Federico Santa María, Casilla 110-V, Valparaíso, Chile*

⁽⁴⁾ *CERN, PH-EP, CH-1211 Geneva 23, Switzerland, and LNS, MIT, Cambridge, MA 02139-4307, USA*

⁽⁵⁾ *INFN-Laboratori Nazionali di Frascati, via E.Fermi 40, 00044 Frascati (Rome), Italy*

(ricevuto ?)

Summary. — We review recent progress in the study of parton propagation, interaction and fragmentation in both cold and hot strongly interacting matter. Experimental highlights on high-energy hadron production in deep inelastic lepton-nucleus scattering, proton-nucleus and heavy-ion collisions, as well as Drell-Yan processes in hadron-nucleus collisions are presented. The existing theoretical frameworks for describing the in-medium interaction of energetic partons and the space-time evolution of their fragmentation into hadrons are discussed and confronted to experimental data. We conclude with a list of theoretical and experimental open issues, and a brief description of future relevant experiments and facilities.

PACS 24.85.+p – Quarks, gluons, and QCD in nuclear reactions.

PACS 13.87.Fh – Fragmentation into hadrons.

PACS 25.30.-c – Lepton-induced reactions.

PACS 13.85.-t – Hadron-induced high- and super-high-energy interactions.

PACS 25.75.-q – Relativistic heavy-ion collisions.

PACS 12.38.Mh – Quark-gluon plasma.

(*) valeria.muccifora@lnf.infn.it

(**) Laboratoire d'Annecy-le-Vieux de Physique Théorique, UMR5108

3	1.	Introduction
4	1'1.	Parton fragmentation in elementary collisions
6	1'2.	Parton propagation and fragmentation in cold and hot QCD matter
7	1'3.	Hadronisation and colour confinement
8	1'4.	Hadronisation and neutrino oscillations
8	2.	Kinematics, observables, and hadronisation time estimates
8	2'1.	Kinematic variables
8	2'1.1.	<i>Deep inelastic collisions</i>
9	2'1.2.	<i>Hadron-hadron collisions</i>
13	2'1.3.	<i>Drell-Yan processes</i>
13	2'2.	Comparison of hadron-hadron and DIS kinematics
18	2'3.	Nuclear modification observables
20	2'4.	Hadronisation time estimates
24	3.	Experimental results in lepton-nucleus deep inelastic scattering
24	3'1.	Hadron production in ν -nucleus DIS
26	3'2.	Hadron production in e -nucleus (SLAC) and μ -nucleus (CERN) DIS
29	3'3.	Hadron production in e -nucleus DIS at the HERMES experiment
33	3'4.	Hadron production in e -nucleus DIS at CLAS/JLab
36	3'5.	Di-hadron correlations in nuclear DIS
37	4.	Experimental results in hadron-nucleus collisions
37	4'1.	Drell-Yan production
39	4'2.	High- p_T hadron production: "Cronin effect"
41	5.	Experimental results in nucleus-nucleus collisions
41	5'1.	High- p_T hadron production
43	5'1.1.	<i>Magnitude of the suppression and medium properties</i>
43	5'1.2.	<i>Universality of (light) hadron suppression</i>
44	5'1.3.	<i>Centre-of-mass energy dependence</i>
44	5'1.4.	<i>Transverse momentum dependence</i>
45	5'1.5.	<i>Centrality (system-size) dependence</i>
46	5'1.6.	<i>Path-length dependence</i>
46	5'1.7.	<i>Non-Abelian (colour factor) dependence</i>
47	5'2.	Heavy flavour production
49	5'3.	High- p_T di-hadron correlations
51	5'4.	High- p_T photon production
52	6.	Parton propagation and energy loss
52	6'1.	In-medium parton propagation and the Cronin effect
52	6'1.1.	<i>Parton multiple scatterings</i>
55	6'1.2.	<i>Final state parton recombination</i>
56	6'1.3.	<i>Origin of the Cronin effect</i>
57	6'2.	Energy loss in hot QCD matter
57	6'2.1.	<i>Formalisms</i>
59	6'2.2.	<i>Quenching weights</i>
60	6'2.3.	<i>Phenomenology</i>
60	6'2.4.	<i>Modified DGLAP evolution</i>
62	6'3.	Energy loss in cold QCD matter
64	6'3.1.	<i>Nuclear DIS in the BDMPS formalism</i>
66	6'3.2.	<i>Nuclear DIS in the higher-twist formalism</i>
68	6'3.3.	<i>Drell-Yan processes</i>
70	6'3.4.	<i>Hadron-nucleus and nucleus-nucleus collisions</i>
72	6'4.	Jet quenching from AdS/CFT duality
73	7.	Hadron formation, propagation and interaction
74	7'1.	Early string-based absorption models
77	7'2.	Modern string-based absorption models
78	7'3.	The colour dipole model

80	7.4.	The GiBUU transport Monte Carlo
83	7.5.	Q^2 evolution and time-dependence of the prehadron cross section
86	7.6.	Prehadron absorption in hot QCD matter
87	8.	Challenges and outlook
88	8.1.	Partonic versus (pre)hadronic energy loss in nuclear DIS
88	8.1.1.	<i>Mass number dependence</i>
88	8.1.2.	<i>Production time scaling in nDIS</i>
89	8.1.3.	<i>p_T-broadening and prehadron formation time</i>
92	8.1.4.	<i>A path forward</i>
92	8.2.	π^0 vs. η attenuation
93	8.3.	Baryon formation
93	8.4.	High- p_T hadrons at fixed-target energies
93	8.5.	The heavy flavour puzzle
93	8.6.	Dihadron and photon-hadron correlations
95	8.7.	Future perspectives
95	8.7.1.	<i>The 12-GeV Jefferson lab upgrade</i>
96	8.7.2.	<i>Other fixed target experiments: DIS and DY</i>
97	8.7.3.	<i>Other fixed target experiments: high-p_T hadron spectra</i>
97	8.7.4.	<i>Electron-ion colliders</i>
99	8.7.5.	<i>RHIC II</i>
99	8.7.6.	<i>LHC</i>
101	9.	Conclusions
104		References

1. – Introduction

The transition from coloured partons (quarks and gluons) to colourless hadrons – the so-called hadronisation process – is an exemplary process of the fundamental theory of the strong interaction, Quantum Chromo-Dynamics (QCD), which still lacks a quantitative understanding from first principle calculations. The process by which a highly virtual parton radiates gluons or splits into a quark-antiquark pair can be theoretically described by QCD evolution equations such as the DGLAP (Dokshitzer-Gribov-Lipatov-Altarelli-Parisi) equations [1-3]. However, the final “bleaching” of partons into hadrons takes place at a low virtualities ($Q \approx \Lambda_{\text{QCD}} \approx 0.2$ GeV) and so is dominated by nonperturbative QCD effects which cannot be theoretically addressed with the existing perturbative techniques. Modeling and phenomenology – e.g. as implemented in the Lund string [4] or cluster fragmentation [5] approaches – are often used to describe hadronisation processes.

One way to study fragmentation and hadronisation is to perturb the environment surrounding the hard-scattered parton by introducing a nuclear medium [6]. The nuclear medium provides a sensitive probe of parton evolution through the influence of initial-state (IS) and/or final-state (FS) interactions. Such IS and FS may result on modifications of the final hadron yield distributions compared to “vacuum” production and can help us understand for example the time-scale of the hadronisation process [7].

Nuclear modifications of hadron production have been indeed observed in Deep Inelastic lepton-nucleus Scattering nDIS ($\ell^\pm + A$), in hadron-nucleus ($h + A$) and in heavy-ion ($A + A$) collisions, compared to “elementary” DIS on a proton target or proton-proton collisions. In nDIS and $h + A$ collisions, the medium is the nuclear target itself, also called “cold QCD matter”. In $A + A$ reactions, the produced parton must in addition traverse the created hot and dense medium (“hot QCD matter”), be it a hadron gas at low temperature, or a Quark-Gluon Plasma (QGP) at high temperatures. In all cases, at high enough p_T where hadrons mostly come from parton

fragmentation, one typically observes two different phenomena: (i) a suppression of hadron multiplicities, called hadron or jet quenching, and (ii) a broadening of hadron transverse momentum spectra, which induces a local enhancement of the hadron p_T spectrum known as “Cronin effect” [8, 9]. Such nuclear effects are due to elastic and inelastic interactions of the incoming or outgoing partons and/or of the produced hadrons while traversing the surrounding medium.

In nDIS, the target nucleus allows one to test the hadronisation mechanism and colour confinement dynamics in a clean environment. Knowledge of partonic in-medium propagation gained from nDIS can be used in Drell-Yan (DY) lepton pair production in $h + A$ collisions to factor out FS effects (such as medium-induced gluon radiation) from IS effects (such as nuclear modifications of parton distributions). A precise knowledge of parton propagation and hadronisation mechanisms obtained from nuclear DIS and DY studies can be very useful for e.g. testing and calibrating theoretical tools used to determine the properties of the QGP produced in high-energy heavy-ion collisions, as well as to reduce the systematic uncertainties in neutrino experiments with nuclear targets.

This review is structured as follows. For a non technical overview of motivations, lessons learned, and an outlook, the remainder of this introduction (where we discuss hadronisation in elementary collisions, cold and hot QCD matter) can be followed by a reading of the concluding Section 9. The intervening sections detail the experimental and theoretical status, and discuss open issues and future experimental possibilities. In Section 2, we define the relevant observables and kinematic variables for nDIS and hadronic collisions, comparing the phase-spaces for hadron production in these two cases; and we discuss the space-time development of hadronisation, introducing various estimates of the hadron formation time. In Sections 3, 4, and 5, we review the most relevant experimental results. Specifically, in Section 3 hadron production in ν -nucleus, μ -nucleus, and e -nucleus DIS with emphasis on recent HERMES and CLAS data are discussed. Sections 4 and 5 are devoted to high- p_T hadron production in $h + h$, $h + A$ and $A + A$ collisions, focusing on recent results from the Relativistic Heavy Ion Collider (RHIC). The existing theoretical frameworks for interpreting the experimental data based on partonic or hadronic degrees of freedom, are discussed respectively in Sections 6 and 7. Specifically, parton propagation and energy loss in both *cold* and *hot* QCD matter is addressed in Section 6, where data from DIS, DY, $h + A$ and $A + A$ collisions are confronted to different theoretical models. In Section 7, the interaction of the prehadronic system and of the formed hadron with the nuclear medium is discussed. Finally, in Section 8, we discuss observables sensitive to the time scales and different mechanisms involved in parton propagation and hadronisation, along with experimental measurements at future facilities that would help to clarify the whole picture.

1.1. Parton fragmentation in elementary collisions . –

In perturbative Quantum Chromodynamics (pQCD), collinear factorisation theorems [10] allow one to explicitly separate the short and long distance QCD dynamics involved in the mechanism of hadron production from parton fragmentation. In a general $H_1 + H_2$ inelastic collision, one writes the inclusive hadronic cross sections for production of a hadron h at large momentum transfer or “hard” scale Q^2 , as

$$(1) \quad \sigma_{\text{hard}}(H_1 + H_2 \rightarrow h + X) = \sum_{f_i, j=\{q, g\}} \left[\prod_{i=0, N} \phi_{f_i|H_i}(x_i, M^2) \right] \otimes \hat{H}_{\text{hard}}^{\{f_i\} \rightarrow j+X}(\{x_i\}, z_j, \mu^2) \otimes D_{j \rightarrow h}(z; M_F^2),$$

where \otimes denotes a convolution over the kinematical internal variables of the process and N is

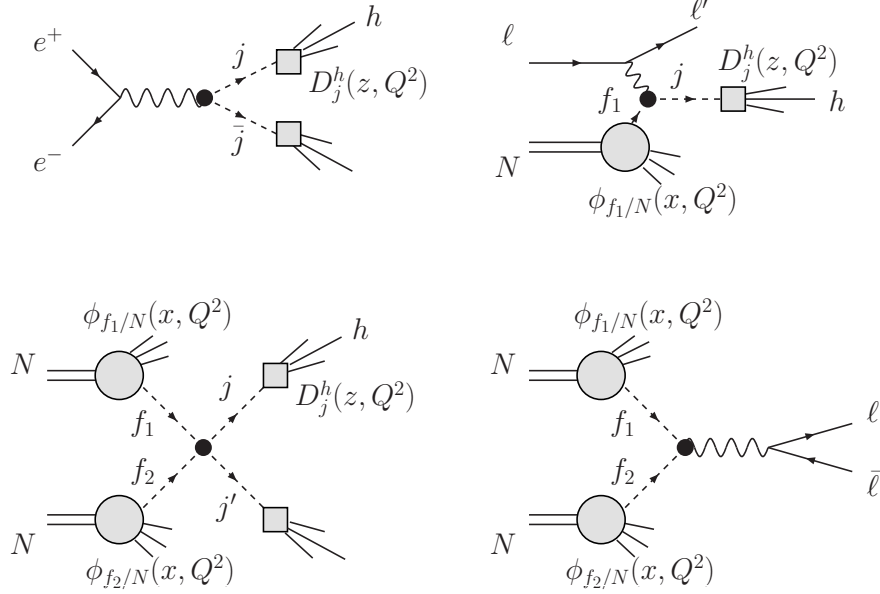


Fig. 1. – Illustration of universality of PDFs ($\phi_{f/N}$) and FFs ($D_{j \rightarrow h}$) in leading order processes. Clockwise from top left: $e^+ + e^-$ annihilation, Deep Inelastic Scattering (DIS), lepton pair (Drell-Yan) emission, and hadron production in hadronic collisions. Solid lines indicate leptons, dashed lines quarks. The small black disc represents the perturbatively calculable hard interaction coefficient \hat{H}_{hard} .

the number of hadrons in the initial state. In Eq. (1), Q^2 is the typical hard scale of the process and \hat{H}_{hard} is the short-distance and perturbatively calculable hard coefficient function for the $\{f_i\} \rightarrow j + X$ partonic process. The long-distance dynamics is factorised into (a) the Parton Distribution Functions (PDF) $\phi_{f_i|H_i}(x_i)$, which can be interpreted as the probability of finding a parton of flavour f_i and momentum fraction x_i inside the projectile (H_1) and/or target (H_2) hadron, and (b) the Fragmentation Function (FF) $D_{j \rightarrow h}$, which gives the equivalent “probability” that the parton j fragments into the observed hadron h with fractional momentum z . These functions are non-perturbative and need to be extracted from experimental data. Typically, PDFs are extracted from “global QCD fits” of inclusive hadron production in lepton-nucleon DIS [$N = 1$ and $D_{j \rightarrow h}(z; Q^2) = 1$ in Eq. (1)] At large hadron fractional momenta⁽¹⁾ $z = p_{\text{hadron}}/p_{\text{parton}} \gtrsim 0.1$, the FFs obey DGLAP evolution equations and are obtained from electron-positron annihilation into hadrons [$N = 0$ in Eq. (1)]. The obtained PDFs and FFs are provided by various authors, e.g., CTEQ6.6, MRST/MSTW [12-14], and HKNS, DSS, AKK08 [15-19] respectively, to mention the most recent sets. Once they are known at a given scale Q_0^2 their value at any other scale can be perturbatively computed by means of the DGLAP evolution equations [1-3]. The factorisation scales M^2 and M_F^2 entering PDFs and FFs, as well as the renormalisation scale μ^2 in the perturbative cross section, should be $\mathcal{O}(Q^2)$ in order to avoid large logarithmic corrections.

An important consequence of factorisation theorems is that PDFs and FFs are universal i.e.

⁽¹⁾ At small z , successful QCD resummation techniques (e.g. the Modified Leading Logarithmic Approximation, MLLA [11]) have been also developed to describe the evolution of a highly-virtual time-like partons into final hadrons.

process-independent. The measured FFs in $e^+ + e^- \rightarrow h + X$ and the PDFs in $e^\pm + p \rightarrow h + X$ can then be used to compute observables in any other process, e.g., hadron spectra in proton-proton collisions [$N = 2$ in Eq. (1)], or Drell-Yan production of lepton pairs [$N = 2$ and $j = \ell\bar{\ell}$ in Eq. (1)], see Fig. 1. When dealing with hadron production with nuclear systems, universality is however experimentally observed to breakdown: the details of the hadron production cross sections depend on the collision process that yields the final particles, as we discuss next.

1'2. Parton propagation and fragmentation in cold and hot QCD matter. –

The basic assumption behind the factorised form of Eq. (1) is that the characteristic time of the parton-parton interaction is much shorter than any long-distance interaction occurring before (among partons belonging to the same PDF) or after (during the evolution of the struck partons into their hadronic final-state) the hard collision itself. In that case, one can treat each nucleus as a collection of free partons, i.e., in the absence of initial-state effects the parton density in a nucleus with mass number A is expected to be simply equivalent to that of a superposition of A independent nucleons⁽²⁾: $\phi_{a/A}(x, Q^2) = A \cdot \phi_{a/N}(x, Q^2)$. In addition, in the absence of final-state effects the parton fragments with universal FFs and, therefore, the pQCD factorisation theorem for collisions involving nuclei A predicts that minimum-bias inclusive hard cross sections scale respectively as

$$(2) \quad \begin{aligned} d\sigma_{hard}(l, h + A \rightarrow h + X) &= A d\sigma_{hard}(l, h + p \rightarrow h + X) , \\ d\sigma_{hard}(A + A \rightarrow h + X) &= A^2 d\sigma_{hard}(p + p \rightarrow h + X) . \end{aligned}$$

The cleanest environment to test the validity of Eqs. (2) and study possible nuclear modifications of hadron production (i.e. “violations” of the expectations given by Eqs. (2)) is nuclear Deep Inelastic Scattering (nDIS). In nDIS processes one experimentally controls many kinematic variables; the nuclear medium (i.e., the nucleus itself) is well known; and the particle multiplicity in the final state is low, leading to precise measurements. The nucleons act as femtometer-scale detectors of the scattered hadronising quark, allowing one to study its space-time evolution into the observed hadrons (Fig. 2, left). The relevant observable in semi-inclusive nDIS processes is the ratio of the single hadron multiplicity on a target of mass number A normalised to the multiplicity on a deuteron target. At leading order, this multiplicity ratio corresponds to good approximation to the ratio of fragmentation functions (FF) in cold nuclear matter (the nucleus A) over that in the “vacuum” (deuteron). Recent HERMES measurements show that this ratio is significantly below 1 clearly showing a breakdown of universality for fragmentation functions, see Section 3 and Refs. [21-24].

A complementary means to study parton propagation in cold QCD matter is by measuring the Drell-Yan (DY) process in hadron-nucleus collisions: $h + A \rightarrow \ell^+ \ell^- + X$, where hadronisation does not play a role (Fig. 2, centre). If the invariant mass of the lepton pair is large, the process can be described perturbatively as a parton-parton scattering producing a virtual photon which subsequently decays into the lepton pair. Any modification of this process will come from initial-state nuclear interactions of the projectile parton inside the target (as well as from nuclear modifications of the PDF, which can be isolated by other means).

Tests of pQCD factorisation in hot-dense QCD matter can be carried out studying high- p_T hadron production in head-on nucleus-nucleus reactions (Fig. 2, right). The suppression of large

⁽²⁾ In reality, nuclear PDFs are modified compared to proton PDFs by initial-state “(anti)shadowing” effects (see [20] for a recent review).

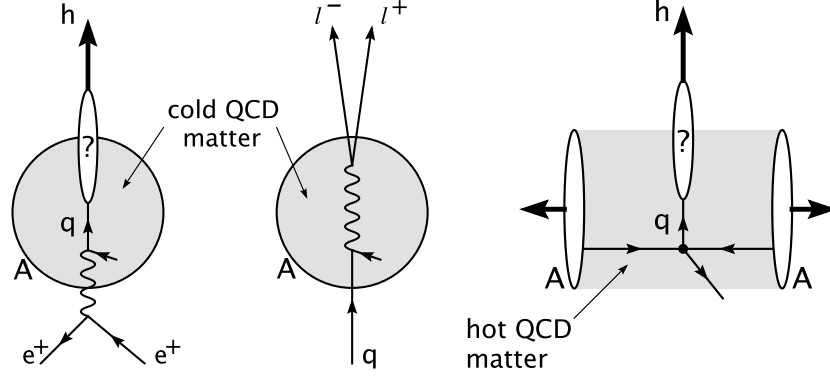


Fig. 2. – Quark propagation inside a target nucleus (“cold QCD matter”) in lepton-nucleus (*left*) and hadron-nucleus $h + A$ collisions \rightarrow Drell-Yan (*centre*) collisions. *Right*: Hard scattered parton traveling through the “hot QCD matter” produced in a nucleus-nucleus collision.

transverse momentum hadron production in $A + A$ compared to proton-proton ($p + p$) and hadron-nucleus $h + A$ collisions at RHIC [25-28] (see Sect. 5), is also indicative of a breakdown of the universality of the fragmentation process. The standard explanation is that the observed suppression is due to parton energy loss in the strongly interacting matter. This assumes of course that the quenched light-quarks and gluons are long-lived enough to traverse the medium before hadronising, which can be expected at large enough p_T because of the Lorentz boost of the hadronisation time scales. However, dynamical effects may alter this argument (see, e.g., Ref. [29]), with hadronisation starting at the nuclear radius scale or before. In this case, in-medium hadron interactions should also be accounted for, possibly leading to a different suppression pattern. Such mechanisms may be especially important in the case of heavy (charm, bottom) quarks which – being slower than light-quarks or gluons – can fragment into D or B mesons still inside the plasma [30].

In summary, a precise knowledge of parton propagation and hadronisation mechanisms can be obtained from nDIS and DY data, allowing one to test the hadronisation mechanism and colour confinement dynamics. In addition, such cold QCD matter data are essential for testing and calibrating our theoretical tools, and to determine the (thermo)dynamical properties of the QGP produced in high-energy nuclear interactions.

1.3. Hadronisation and colour confinement. –

While not having a direct bearing on the traditional topics of confinement such as the hadron spectrum, the hadronisation process nonetheless contains elements that are central to the heart of colour confinement, as already emphasised 30 years ago by Bjorken [6]. For instance, in the DIS process, a quark is briefly liberated from being associated with any specific hadron while traveling as a “free” particle, and it is the mechanisms involved in hadron formation that enforces the colour charge neutrality and confinement into the final state hadron. The dynamic mechanism leading to colour neutralisation, which is only implicitly assumed in the traditional treatments of confinement based on potential models [31] or lattice QCD [32], can be studied quantitatively using the theoretical and experimental techniques discussed in this review. As an example, the lifetime of the freely propagating quark may be inferred experimentally from the nuclear modification of hadron production on cold nuclei, which act as “detectors” of the hadro-

nisation process. Finally, as already discussed, the behaviour of partons propagating through the medium created in high energy heavy-ion collisions can give tomographically insight into the properties of large-scale deconfined QCD matter (i.e., of the Quark-Gluon Plasma). While still at an early stage, the understanding of such elements will ultimately provide deeper insights into the confinement-related properties of QCD.

1'4. Hadronisation and neutrino oscillations. –

Neutrino oscillation experiments use nuclear targets to enhance the neutrino detection rate. Nuclear effects change the topology and total energy of the experimentally measured hadronic final-state and are known to be one of the largest sources of systematic errors in current analyses. For the lower energy oscillation experiments that use the quasi-elastic channel, several problems arise among which the distortion of the knock-out nucleon due to final state interactions, the contamination from hadron resonances, e.g. the $\pi + N \rightarrow \Delta$ process by which a final-state pion is absorbed in the nucleus, and the unexplained depletion of low-virtuality events, much stronger than Pauli blocking can account for [33]. Experiments such as MINOS measure the neutrino energy adding up the muon and hadronic energies, $E_\nu = E_\mu + E_{\text{had}}$. Experiments such as OPERA [34] need to estimate the background to τ -neutrino appearance events due to charmed mesons production and decay. It is thus crucial to have a good understanding of hadron modifications in the nuclear medium and of the space-time evolution of the hadronisation process [35,36]. However, at the low hadronic invariant mass involved in these experiments, the theoretical methods discussed in this review should be supplemented by those described in Refs. [37-40].

2. – Kinematics, observables, and hadronisation time estimates

In this Section, we cover background material which will be used throughout the review. We define the kinematic variables and relevant observables for nDIS and hadronic collisions, and compare the phase-space for hadron production in both types of collisions. Finally, the space-time development of the hadronisation process is discussed.

2'1. Kinematic variables. –

We discuss the kinematics for hadron production in nDIS, hadron-hadron ($h + h$), hadron-nucleus ($h + A$) and nucleus-nucleus ($A + A$) collisions, and for the Drell-Yan (DY) process. We will explicitly make reference to the leading order (LO) processes in perturbative QCD, but most of the definitions are of general nature.

Throughout this discussion we use light-cone coordinates $p^\mu = (p^+, p^-, \vec{p}_T)$, where $p^\pm = (p^0 \pm p^3)/\sqrt{2}$ and $\vec{p}_T = (p^1, p^2)$. Our reference frame is such that the z axis is aligned with the beam, and a particle moving in the positive z direction has large light-cone plus-momentum. The transverse plane is the plane transverse to the beam and $p^+ p^- = m^2 + p_T^2 \equiv m_T^2$, where $m^2 = p^2$ is the invariant mass squared of the particle, and m_T its transverse mass.

2'1.1. Deep inelastic collisions. – Deep inelastic scattering at LO in pQCD proceeds by exchange of a virtual photon in the \hat{t} -channel (Fig. 3 left). The DIS Lorentz invariants are defined in Table I. Note that the variable x_B , Q^2 and ν are not independent but related through $x_B = Q^2/(2M\nu)$ in any reference frame. Analysis of inclusive DIS is usually carried out using x_B and Q^2 , because of the x_B -scaling of the total cross section in the Bjorken limit: $Q^2 \rightarrow \infty$, x_B fixed. Note that in DIS one can experimentally measure all the listed variables, especially ν , Q^2 and z_h , because the initial and final state electron is observable. This is markedly different

<i>Variable</i>	<i>Definition</i>	<i>Target rest frame form</i>	
M^2	$=$	P^2	Target mass
x_B	$=$	$\frac{-q^2}{2P \cdot q}$	Bjorken scaling variable
Q^2	$=$	$-q^2$	Negative four-momentum squared of the exchanged virtual photon
ν	$=$	$\frac{q \cdot P}{\sqrt{P^2}}$	Energy of the virtual photon in the target rest frame
y	$=$	$\frac{q \cdot P}{k \cdot P}$	Fractional energy loss of the incident lepton (inelasticity)
W^2	$=$	$(P + q)^2$	Invariant mass squared of the hadronic final state
z_h	$=$	$\frac{p_h \cdot P}{q \cdot P}$	Fraction of the virtual photon energy carried by the hadron
p_T	$=$	$ \vec{p}_T $	Hadron transverse momentum (relative to the virtual photon momentum)

TABLE I. – *Definitions of the kinematic variables for semi-inclusive DIS. The Lorentz invariant definition and its form in the target rest frame are provided. Particle 4-momenta are defined in Fig. 3 and 4. All variables are experimentally measurable, hence typeset in boldface. Note that $x_B = Q^2/(2M\nu)$ independently of the chosen reference frame.*

from the situation in hadronic collisions, where only final state hadrons can be observed and not the partons themselves. The hadron transverse momentum in DIS is defined with respect to the virtual photon direction, see Fig. 4. Its analog in hadronic collisions would be the transverse momentum of a hadron with respect to the beam axis.

Nuclear DIS experiments have been performed in fixed-target (*ft*) conditions in facilities like Stanford Linear Accelerator Center – SLAC (E665), Super Proton Synchrotron – SPS (EMC), Deutsches Elektronen Synchrotron – DESY (HERMES), Jefferson Lab – JLab (CLAS); and are planned in collider mode (*cl*) e.g. at the proposed Electron-Ion Collider – EIC or Large Hadron-electron Collider – LHeC. The colliding nucleon and lepton momenta are

$$(3) \quad \begin{aligned} P_{ft} &= \left(\frac{M}{\sqrt{2}}, \frac{M}{\sqrt{2}}, \vec{0}_T \right), \quad k_{ft} = (\sqrt{2}E, 0, \vec{0}_T) \\ P_{cl} &= \left(\frac{M^2}{2\sqrt{2}E_N}, \sqrt{2}E_N, \vec{0}_T \right), \quad k_{cl} = (\sqrt{2}E, 0, \vec{0}_T) \end{aligned}$$

where E and E_N are the lepton and nucleon energies measured in the laboratory frame. To discuss both modes at the same time, it is convenient to introduce the target rest frame energy of the lepton, E_{trf} :

$$(4) \quad E_{trf} = \begin{cases} E & \text{fixed-target} \\ \frac{2E_N E}{M} & \text{collider mode} \end{cases}$$

Then the invariant inelasticity y for both modes can be written as $y = \nu/E_{trf}$.

2.1.2. Hadron-hadron collisions. – Parton production in hadronic collisions at leading order in the coupling constant α_s proceeds through $2 \rightarrow 2$ partonic collisions (see Fig. 3 right and

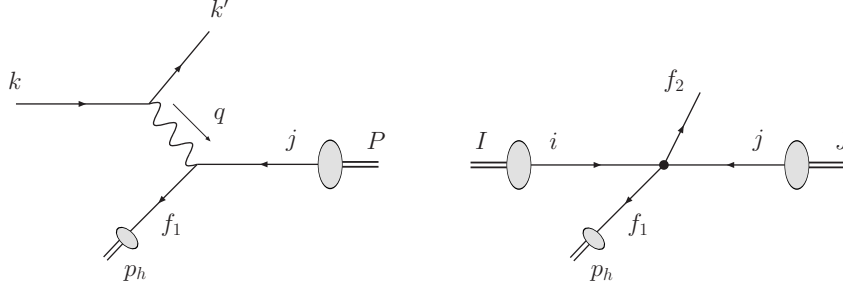


Fig. 3. – LO kinematics for parton production in DIS collisions (*left*) and in hadron-hadron collisions (*right*). Double lines indicate hadrons or nuclei, thin single lines are partons or leptons. The labels define the particles 4-momenta.

Table II). Several LO processes can contribute to a given $ij \rightarrow f_1 f_2$ collision, represented by a black dot in the cartoon, see Ref. [41] for details. The momenta of the two nucleons colliding in the centre-of-mass-frame (c.m.f.) with energy $\sqrt{s}/2$ each are

$$(5) \quad I = \left(\sqrt{\frac{\tilde{s}}{2}}, \frac{M^2}{\sqrt{2\tilde{s}}}, \vec{0}_T \right) \quad J = \left(\frac{M^2}{\sqrt{2\tilde{s}}}, \sqrt{\frac{\tilde{s}}{2}}, \vec{0}_T \right)$$

where M is the nucleon mass and

$$(6) \quad \tilde{s} = s \frac{1 + \sqrt{1 + M^4/s^2}}{2}.$$

We will neglect terms of order $\mathcal{O}(M^2/s)$ compared to terms of $\mathcal{O}(1)$, and will use $\tilde{s} \approx s$. In Eq. (5), we explicitly retain the nucleon mass to be able to perform boosts to the rest frame of either nucleon. If we assume the partons to be massless and collinear to their parent nucleons, their 4-momenta in terms of the parton fractional momenta x_i read $i = (x_1 \sqrt{s}/2, 0, \vec{0}_T)$ and $j = (0, x_2 \sqrt{s}/2, \vec{0}_T)$.

Particle production (partons or hadrons) is described in terms of the particle rapidity and transverse momentum. The rapidity of a particle of 4-momentum p and mass squared $m^2 = p^2$ is defined as

$$(7) \quad y = \frac{1}{2} \log \left(\frac{p^+}{p^-} \right) = \log \left(\frac{p^+}{m_T} \right).$$

Positive rapidity describes a particle moving in the positive z direction, and likewise for negative rapidity. In the non-relativistic limit the rapidity coincides with the particle longitudinal velocity β_L in units of the speed of light, $y \rightarrow \beta_L$. Given the rapidity, one can compute $p^0 = m_T \cosh y$ and $p^3 = m_T \sinh y$. Note that under a longitudinal boost of velocity β , the rapidity transforms additively: $y' = y - y_\beta$, where $y_\beta = 0.5 \log[(1 + \beta)/(1 - \beta)]$ is the rapidity of the particle rest frame. As an example, let us boost the target hadron momentum P from the target rest frame, $P = (M/\sqrt{2}, M/\sqrt{2}, \vec{0}_T)$, to a frame in which $P' = (\sqrt{s}/2, M^2/\sqrt{2s}, \vec{0}_T)$. This boost is accomplished by $\alpha = \sqrt{s}/M$. Likewise, boosting a nucleon from energy $\sqrt{s}/2$ to $\sqrt{s'}/2$ requires $\alpha = \sqrt{s'}/s$.

Measuring the rapidity of a particle requires measuring two independent variables, say, its energy and longitudinal momentum. Not in all experiments this is possible, while just measuring

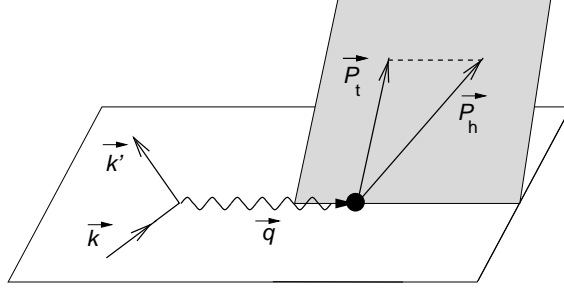


Fig. 4. – Kinematic planes for hadron production in semi-inclusive deep-inelastic scattering and definitions of the relevant lepton and hadron variables. The quantities k (k') and E (E') are the 4-momentum and the energy of the incident (scattered) lepton; p_h is the 4-momentum of the produced hadron, and its transverse component relative to the lepton plane is denoted by \vec{p}_T .

the polar angle θ^* between the particle trajectory and the beam axis in the centre-of-mass frame is easier. This justifies the definition of the particle pseudorapidity,

$$(8) \quad \eta = -\log \tan(\theta^*/2) ,$$

such that $|\vec{p}| = p_T \cosh \eta$ and $p^3 = p_T \sinh \eta$. For massless particles it coincides with the rapidity: $\eta = y$; for massive particles, they are approximately equal if $|\vec{p}| \gg m$ (and θ not too small). Differential particle distributions in y and η are related by

$$(9) \quad \frac{dN}{dy dp_T^2} = \frac{dN}{d\eta dp_T^2} \sqrt{1 - \frac{m^2}{m_T^2 \cosh^2 y}} = \frac{dN}{d\eta dp_T^2} \frac{E}{m_T} .$$

In order to compare collider and fixed-target experiments, and different beam energies, it is useful to consider the rapidity in the c.m.f.:

$$(10) \quad y_{c.m.f.} = y - y_{cm} .$$

The backward rapidity region (target hemisphere) corresponds to $y_{c.m.f.} < 0$, and the forward rapidity region (projectile hemisphere) to $y_{c.m.f.} > 0$.

At LO, the 4-momenta of the two produced partons can be expressed in terms of their final state rapidities y_i and transverse momentum p_T (see Table II for definitions)

$$(11) \quad f_1 = \left(\frac{p_T}{\sqrt{2}} e^{y_1}, \frac{p_T}{\sqrt{2}} e^{-y_1}, -\vec{p}_T \right) \quad f_2 = \left(\frac{p_T}{\sqrt{2}} e^{y_2}, \frac{p_T}{\sqrt{2}} e^{-y_2}, \vec{p}_T \right) ,$$

and their fractional momenta are

$$(12) \quad x_1 = \frac{p_T}{\sqrt{s}} (e^{y_1} + e^{y_2}) \quad x_2 = \frac{p_T}{\sqrt{s}} (e^{-y_1} + e^{-y_2}) .$$

Variable	Definition	
s		Nucleon-nucleon centre-of-mass energy squared
x_1	$= i^+ / I^+$	Initial-state projectile parton fractional momentum
x_2	$= j^- / J^-$	Initial-state target parton fractional momentum
p_{iT}	$= \vec{f}_{iT} $	Final state partons transverse momentum (relative to beam)
y_i	$= 0.5 \log(f_i^+ / f_i^-)$	Final state partons rapidity
y_{cm}	$= 0.5 \log(\frac{I^+ + J^+}{I^- + J^-})$	Rapidity of the centre-of-mass
z	$= p_h^+ / f_1^+$	Hadron fractional momentum relative to parent parton f_1
p_{hT}	$= \vec{p}_{hT} $	Hadron transverse momentum (relative to beam)
y_h	$= 0.5 \log(p_h^+ / p_h^-)$	Hadron rapidity
η	$= -\log \tan(\theta^* / 2)$	Hadron pseudorapidity (θ^* is the polar angle between the parton and the beam in the centre-of-mass reference frame)

TABLE II. – Relevant kinematic variables for semi-inclusive parton (top) and hadron (bottom) production. Particle 4-momenta are defined in Fig. 3, right. Boldface variables are experimentally measurable; the others are theoretically defined in perturbative QCD.

Finally, the Mandelstam invariants are defined as follows,

$$\begin{aligned}
 \hat{s} &= (i + j)^2 \\
 \hat{t} &= (i - f_1)^2 = (f_2 - j)^2 \\
 \hat{u} &= (i - f_2)^2 = (f_1 - j)^2 .
 \end{aligned}
 \tag{13}$$

and $\hat{s} + \hat{t} + \hat{u} = 0$ by momentum conservation. In terms of rapidities and transverse momentum, the Mandelstam invariants read

$$\begin{aligned}
 \hat{s} &= x_1 x_2 s \\
 \hat{t} &= -p_T^2 (1 + e^{y_2 - y_1}) \\
 \hat{u} &= -p_T^2 (1 + e^{y_1 - y_2}) .
 \end{aligned}
 \tag{14}$$

Hadronisation in the collinear factorisation framework proceeds through independent parton fragmentation into a hadron. It is universal, i.e., independent of the process which produced the fragmenting hadron, e.g., hadronic or DIS collisions [42]. The hadron fractional momentum z is defined by

$$p_h^+ = z f_1^+ \quad \vec{p}_{hT} = z \vec{f}_{1T} .
 \tag{15}$$

Therefore the on-shell hadron momentum p_h reads

$$p_h = \left(z f_1^+, \frac{m_h^2 + z^2 f_{1T}^2}{2z f_1^+}, z \vec{f}_{1T} \right) .
 \tag{16}$$

The parton and hadron rapidities are related by $y_1 = y_h + \log(m_{hT} / p_{hT})$.

The partonic variables p_T , y_i , x_i and the fractional hadron momentum z are not experimentally measurable, but are needed in the theoretical computation of the cross section. The experimentally measurable variables are typed in boldface in Table II. Note that the hadron transverse

<i>Variable</i>	<i>Definition</i>	LO in α_s	
\mathbf{x}_F	$= 2p_z^*/\sqrt{s}$	$= x_1 - x_2$	Feynman x
\mathbf{M}	$= \sqrt{p_{\ell^+}^2 + p_{\ell^-}^2}$	$= x_1 x_2 s$	Dilepton invariant mass
\mathbf{p}_T	$= \vec{p}_T $		Dilepton transverse momentum

TABLE III. – Kinematic variables for Drell-Yan dilepton production. The dilepton momentum is $p = p_{\ell^+} + p_{\ell^-}$, where p_{ℓ^\pm} are the lepton and anti-lepton momenta. A star indicates momenta measured in the centre-of-mass frame. The three DY variables are experimentally measurable, hence typeset in boldface. See Table II for the definition of $x_{1,2}$ and s .

momentum p_T in hadron-hadron collisions is defined with respect to the beam axis, so that at midrapidity it is the analog of the hadron energy E_h in DIS.

2'1.3. Drell-Yan processes. – Drell-Yan production of a lepton pair in hadronic collisions occurs, at zero-th order in α_s via the quark-antiquark annihilation channel

$$q + \bar{q} \rightarrow \gamma^* \rightarrow \ell^+ + \ell^-,$$

as shown in the lower-right panel of Fig. 1. As before, the initial partons carry a momentum fraction x_1 and x_2 of the projectile and target hadron, respectively. At this order, the dilepton is produced with zero transverse momentum, with invariant mass $M_{\ell^+\ell^-}$ and with longitudinal momentum fraction $x_F = 2p_z^*/\sqrt{s}$, also called Feynman- x , where p^* is the dilepton momentum in the centre-of-mass frame. These variables are summarised in Table III. By energy-momentum conservation and assuming $M^2 \ll s$, we have

$$(17) \quad \begin{aligned} M^2 &= \hat{s} = x_1 x_2 s \\ x_F &= x_1 - x_2, \end{aligned}$$

from which it follows immediately that

$$(18) \quad x_{1,2} = \frac{1}{2} \left(\sqrt{x_F^2 + 4 M^2/s} \pm x_F \right).$$

Usually, Drell-Yan production is measured between the charmonium and bottomonium masses ($4 \leq M \leq 8 \text{ GeV}/c^2$) or above the Υ . At higher orders in α_s , new channels open up, such as Compton scattering, $q g \rightarrow \gamma q$. The virtual photon acquires a finite transverse momentum, and it is no longer possible to relate x_F and M to the momentum fractions of the partons probed in the projectile and target hadron.

2'2. Comparison of hadron-hadron and DIS kinematics . –

If we consider parton and hadron production at LO in hadronic and DIS collisions, it is easy to relate the relevant variables in both processes, that allows one to compare their corresponding phase spaces. The discussion closely follows Ref. [43], to which we refer for details. To connect the DIS and hadron-hadron kinematics (Fig. 3) we can boost the DIS collision to a frame in which the target has energy $\sqrt{s}/2$ per nucleon, and imagine the lepton to be a parton of a collinear

	SPS	FNAL	RHIC	RHIC	LHC
\sqrt{s} [GeV]	17.5	27.4	63	200	5500
Δy_1	2.4	2.0	1.2	0	-3.3

TABLE IV. – Rapidity shifts Δy_1 of the RHIC-equivalent DIS phase space, tabulated for some energies of interest.

phantom nucleon of energy $\sqrt{s}/2$ and with 4-momentum $P'^{\pm} = P^{\mp}$. Comparing the left and right parts of Fig. 3 we can identify

$$(19) \quad P \equiv J, \quad P' \equiv I, \quad k \equiv i, \quad k' \equiv f_2.$$

The virtual photon momentum q , the fractional momentum x_e of the initial-state lepton and the rapidity y_e of the final state lepton are identified as follows

$$q = k - k' \equiv i - f_2, \quad x_e = k^+ / P'^+ \equiv x_1, \quad y_e \equiv y_2.$$

In this way, we can relate the DIS to the hadron-hadron kinematics discussed in Sect. 2'1. As an example, it is immediate to see that, in terms of hadron-hadron variables, $Q^2 = -\hat{t}$. The full translation “dictionary” from DIS to hadron-hadron variables can be obtained in a straightforward way by combining the results of Sect. 2'1 and the definitions of Tables I–II.

First, we can express the DIS invariants in terms of parton rapidities and transverse momenta. Neglecting target-mass corrections, i.e. up to terms of $\mathcal{O}(M^2/s)$, we obtain

$$(20) \quad \begin{aligned} x_B &= \frac{p_T}{\sqrt{s}} (e^{-y_2} + e^{-y_1}) \\ Q^2 &= p_T^2 (1 + e^{y_1 - y_2}) \\ \nu &= \frac{p_T \sqrt{s}}{2M} e^{y_1} \\ y &= \frac{1}{1 + e^{y_2 - y_1}} \\ z_h &= z. \end{aligned}$$

Note that the first three variables are not independent because $Q^2 = 2Mx_B\nu$, and that $x_B = x_2$ is interpreted as the struck parton fractional momentum, as expected in DIS at LO. Note also that ν increases with increasing p_T and increasing y_1 . This is because a parton of positive and large y_1 in the c.m. frame travels in the opposite direction as the left-moving nucleus, considered as the “target nucleus” (see Fig. 3). Hence in that nucleus rest frame it is very fast. Conversely, a parton of negative and large y_1 travels in the same direction as the target nucleus, which means quite slow in the target rest frame. It is also interesting to note that up to terms of order $\mathcal{O}(M^2/s)$, the parton and hadron energy in the target rest frame are $E = \nu$ and $E_h = z_h\nu$ respectively. Finally,

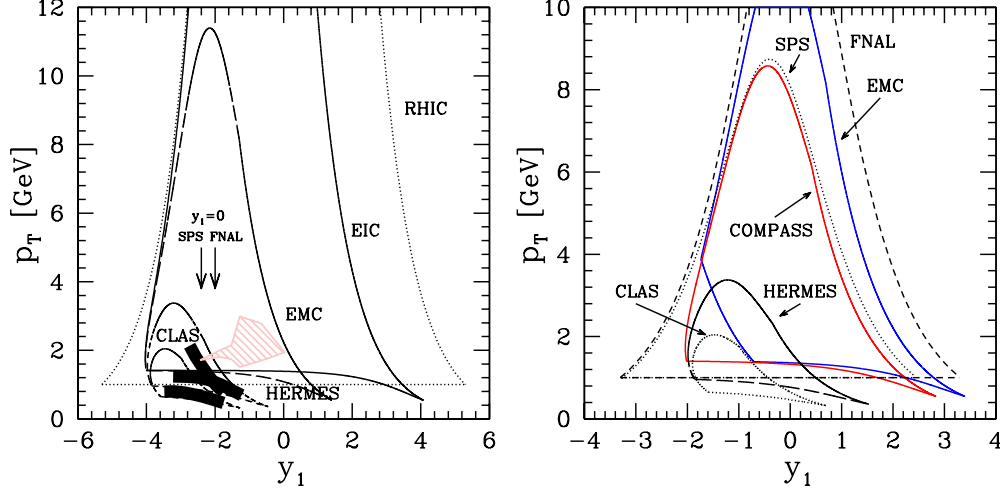


Fig. 5. – *Left*: RHIC-equivalent phase space of nuclear DIS experiments at $E_e = 27.6$ GeV (HERMES, solid line), at $E_e = 12$ GeV (HERMES and JLab, dashed line), and at $E_e = 280$ GeV (EMC, dot-dashed line). The dotted line shows the borders of the LO pQCD phase space in $p, A + A$ at top RHIC energy, $\sqrt{s_{NN}} = 200$ GeV. The two arrows show the location of the midrapidity region at SPS and FNAL ($p, A + A$) fixed-target experiments. The shaded regions show the region of phase-space experimentally explored at HERMES [23, 44] and EMC [45]. *Right*: Hadron-hadron-equivalent EMC and COMPASS ($\ell + A$) phase space at $\sqrt{s_{NN}} = 27.4$ GeV, compared to the SPS and FNAL ($p, A + A$) phase spaces.

we can invert Eq. (20) to obtain the hadron-hadron variables in terms of DIS invariants:

$$\begin{aligned}
 p_T^2 &= (1-y)Q^2 \\
 y_1 &= -\log\left(\frac{Q\sqrt{s}}{2ME_{trf}} \frac{(1-y)^{1/2}}{y}\right) \\
 y_2 &= y_1 + \log\left(\frac{1-y}{y}\right) \\
 z &= z_h
 \end{aligned}
 \tag{21}$$

with $y = \nu/E_{trf}$. Note that in DIS, the electron energy E_{trf} , hence the electron x_e , is fixed by the experimental conditions; this is different from hadronic collisions where the parton j has an unconstrained fractional momentum. Changing the c.m.f. energy to $\sqrt{s'}$ simply results in a shift of the parton rapidity,

$$y_1 \xrightarrow{s \rightarrow s'} y_1 + \Delta y_1
 \tag{22}$$

where $\Delta y_1 = \log(\sqrt{s}/\sqrt{s'})$. The value of Δy_1 compared to RHIC top energy $\sqrt{s_{NN}} = 200$ GeV is listed in Table IV for the experiments of interest in this paper.

Given a DIS phase space (say a given experiment acceptance region in the (ν, Q^2) plane), we define its hadron-hadron-equivalent phase-space as its image in the (p_T, y_1) under Eqs. (21). The reason for this definition is that for both hadronic and DIS collisions we can identify the parton f_1 of Fig. 3 with the “observed” parton in hadronic and DIS collisions, i.e., the parton which

fragments into the observed hadron. Then the variables p_T and y_1 fully characterise the observed parton. An analogous definition holds when using x_B instead of ν as independent variable. As an example, the HERMES DIS phase space in the (ν, Q^2) plane is determined by the values of W_{min}^2 , Q_{min}^2 and y_{max} :

$$(23) \quad \begin{aligned} \frac{Q_{min}^2 + W_{min}^2 - M^2}{2M} &\leq \nu \leq y_{max} E_{trf} \\ Q_{min}^2 \leq Q^2 &\leq M^2 + 2M\nu - W_{min}^2. \end{aligned}$$

Additionally, one may impose stronger cuts on ν , e.g., $\nu \geq \nu_{min}$, as at the EMC experiment, and in some HERMES analysis.

Using Eqs. (21) the *hadron-hadron equivalent* DIS phase space in the (y_1, p_T) plane can be determined. As an example, in Fig. 5 left, we consider the RHIC-equivalent phase space of the fixed target $e + A$ experiments and the planned Electron-Ion Collider (EIC), using $\sqrt{s_{NN}} = 200$ GeV. Note that according to Eq. (22), the hadron-hadron-equivalent phase space at other centre-of-mass energies can be obtained by a shift $y_1 \rightarrow y_1 + \Delta y_1$, see Table IV and Fig. 5 right where the Fermilab-equivalent phase space is shown. We assume the pQCD formulae used to define the hadron-hadron-equivalent phase space to be valid for $p > p_0 = \mathcal{O}(1 \text{ GeV}/c)$, see Eq. (25) below for details. We can see that the HERMES and CLAS experiments, with $E_{trf} = 27.6$ and 12 GeV, cover less than one third of the available RHIC p_T range at $y_1 \approx -3$, with shrinking p_T coverage at larger rapidity. In the SPS/FNAL midrapidity region it reaches $p_T = 2.5 \text{ GeV}/c$ at most. Since

$$(24) \quad y_1 \leq \log \left(\frac{\sqrt{s}}{2ME_{trf}} \frac{p_T}{y_{max}} \right),$$

the only way to effectively reach larger values of y_1 is to increase the electron beam energy E_{trf} . Indeed, the EMC experiment, with $E_{trf} = 100 - 280 \text{ GeV}$, covers a larger span in rapidity and extends to $y_1 \gtrsim 0$ (as would a $\mu + A$ programme at COMPASS). Moreover, the increased energy allows one in principle to reach much higher p_T than at HERMES and CLAS. However, only the $p_T \lesssim 3 \text{ GeV}/c$ region has been explored in actual measurements. The proposed Electron-Ion Collider (EIC) [46, 47] will be able to effectively study the $y_1 > 0$ region and cover most of the RHIC phase space, but only the $y_1 < 0$ part of the LHC phase space.

The *direct* use of HERMES and CLAS data to understand nuclear effects in high- p_T hadron production in heavy-ions collisions is therefore not possible. Instead, one needs to use those data to understand in detail the hadronisation dynamics and to constrain the various models in the context of heavy-ion collisions, by extrapolating them to unmeasured regions of phase space.

The *DIS-equivalent hadron-hadron phase space* is defined as the image of Eqs. (25) in the (ν, Q^2, y, z_h) space under Eqs. (20). Then, the hadron-hadron phase space at a given y_1 is defined

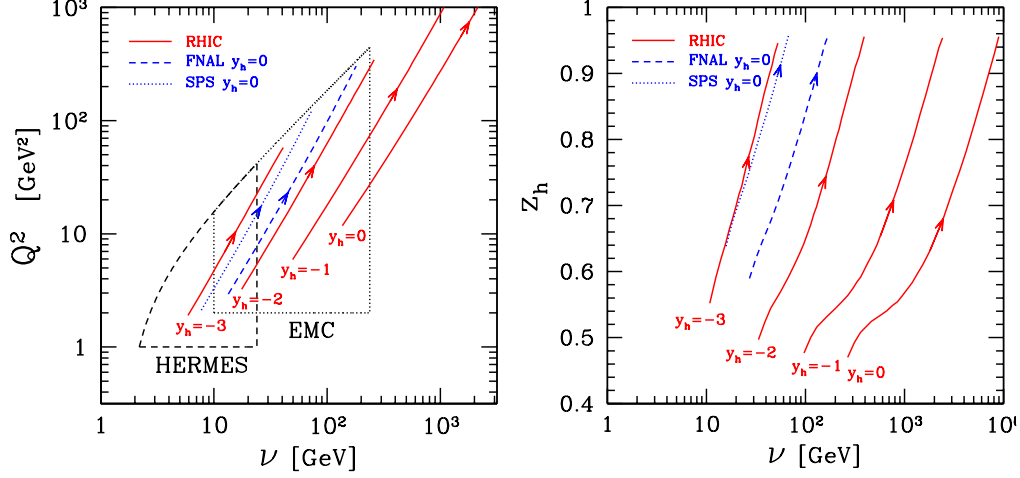


Fig. 6. – *left*: Fixed- y_1 hadron-hadron trajectories plotted in the DIS-equivalent (ν, Q^2) phase space for RHIC at $\sqrt{s_{NN}} = 200$ GeV and various rapidities, for FNAL and SPS at midrapidity. The dashed line encloses the HERMES phase space; the dotted line encloses the EMC phase space. The arrow indicates the direction of increasing $\langle p_T \rangle$ and $\langle z_h \rangle$. *Right*: Trajectories in the (ν, z_h) plane. The arrows indicate increasing p_T and Q^2 .

by the kinematic bounds on $2 \rightarrow 2$ parton scatterings [48]:

$$\begin{aligned}
 |y_1| &\leq \cosh^{-1} \left(\frac{\sqrt{s}}{2p_0} \right) \\
 p_0 &\leq p_T \leq \frac{\sqrt{s}}{2 \cosh(y_1)} \\
 -\log \left(\frac{\sqrt{s}}{p_T} - e^{-y_1} \right) &\leq y_2 \leq \log \left(\frac{\sqrt{s}}{p_T} - e^{y_1} \right) \\
 \frac{m_{hT}}{\sqrt{s}} e^{y_h} \left(1 + \frac{p_{hT}^2}{m_{hT}^2 e^{y_h}} \right) &\leq z \leq 1
 \end{aligned}
 \tag{25}$$

where hard scatterings satisfy $p_T \geq p_0$, with $p_0 \gtrsim 1$ GeV/c a lower cutoff [48, 49].

Introduction of next-to-leading order kinematics [50], would relax somewhat these bounds. At large rapidity, where the phase space for $2 \rightarrow 2$ parton processes is becoming more and more restricted, $2 \rightarrow 1$ parton fusion may become the dominant mechanism because it is sensitive to much lower fractional momenta x_i [51]. Hence, at the boundary of the hadron-hadron phase space, the presented analysis becomes unreliable.

This phase-space is 4-dimensional and difficult to directly visualise. A way around this problem is to define suitable trajectories in hadron-hadron phase space averaged over y_2 , and to project them into the DIS-equivalent (ν, Q^2) and (ν, z_h) phase spaces. We can define a p_{hT} - and

	SPS $\sqrt{s_{NN}} = 17.5$ GeV	FNAL $\sqrt{s_{NN}} = 27.4$ GeV		RHIC $\sqrt{s_{NN}} = 200$ GeV		
y_h	0	0	0	-1	-2	-3
p_{hT}	1–8	1–12	1–90	1–60	1–25	1–9

TABLE V. – Range of hadron transverse momentum (p_{hT} , in GeV/c) spanned along trajectories at fixed rapidity y_1 at RHIC top energy $\sqrt{s_{NN}} = 200$ GeV and at fixed-target energies $\sqrt{s_{NN}} = 17 - 28$ GeV.

y_h -dependent average observable as follows

$$(26) \quad \langle \mathcal{O} \rangle_{p_{hT}, y_h} = \frac{\int dz dy_1 dy_2 \mathcal{O}(p_T, y_1, y_2, z) \frac{d\hat{\sigma}_{AB \rightarrow hX}}{dp_T^2 dy_1 dy_2 dz}}{\int dz dy_1 dy_2 \frac{d\hat{\sigma}_{AB \rightarrow hX}}{dp_T^2 dy_1 dy_2 dz}},$$

where

$$(27) \quad \frac{d\hat{\sigma}_{AB \rightarrow hX}}{dp_T^2 dy_1 dy_2 dz} = \sum_{f_1} \frac{1}{z^2} D_{f_1}^h(z) \frac{d\hat{\sigma}_{AB \rightarrow f_1 X}}{dp_T^2 dy_1 dy_2},$$

$d\hat{\sigma}_{AB \rightarrow f_1 X}$ is the LO pQCD differential cross-section for production of a f_1 parton in a collision of hadrons A and B (nucleons or nuclei), and $D_{f_1}^h$ is its fragmentation function into the observed hadron. Then we can define fixed- y_h trajectories $\{(\langle \nu \rangle_{p_T, \bar{y}}, \langle Q^2 \rangle_{p_T, \bar{y}}); p_T \geq p_0\}$ and $\{(\langle \nu \rangle_{p_T, \bar{y}}, \langle z_h \rangle_{p_T, \bar{y}}); p_T \geq p_0\}$ in the DIS-equivalent phase space.

As an example, in Fig. 6 we considered hadronic collisions at RHIC top energy $\sqrt{s_{NN}} = 200$ GeV and at fixed-target energies $\sqrt{s_{NN}} = 17 - 27$ GeV, and plotted the fixed- y_h trajectories in the DIS-equivalent phase space. The range of p_T spanned along each trajectory is tabulated in Table V. The spanned range in Q^2 is limited by the maximum p_T at each rapidity, according to Eq. (25). As expected, the smaller the rapidity $y_h \approx y_1$ the smaller the spanned ν . RHIC trajectories with $y_h \lesssim -2$ span relatively low values of $\nu \lesssim 60$ GeV and large values of $z_h \gtrsim 0.5$, where the EMC and HERMES experiments have shown non negligible cold QCD matter suppression of hadron production. At higher rapidity, the larger spanned values of ν will make cold QCD matter effects less prominent. The consequences of these remarks for the interpretation of hadron production in $h + A$ and $A + A$ collisions will be further discussed in Section 6.3.4.

2.3. Nuclear modification observables. –

In lepton-nucleus DIS, the experimental results for hadron production are usually presented in terms of the *hadron multiplicity ratio* R_M^h , which represents the ratio of the number of hadrons of type h produced per deep-inelastic scattering event on a nuclear target of mass A to that from a deuterium target (D). The multiplicity ratio R_M^h depends on the leptonic variables ν and Q^2 , and on the hadronic variables $z = E_h/\nu$ and p_T^2 defined in Section 2.1. It is defined as the super-ratio

$$(28) \quad R_M^h(z, \nu, Q^2, p_T^2) = \left(\frac{N_h(z, \nu, Q^2, p_T^2)}{N_e(\nu, Q^2)} \right)_A \bigg/ \left(\frac{N_h(z, \nu, Q^2, p_T^2)}{N_e(\nu, Q^2)} \right)_D,$$

where N_h is the yield of semi-inclusive hadrons in a given (z, ν, Q^2, p_T^2) -bin, and N_e the yield of inclusive deep-inelastic scattering leptons in the same (ν, Q^2) -bin. Normalising the hadron yield

to the DIS yield allows one to cancel, to a large extent, initial-state nuclear effects such as nuclear modifications of PDFs and to isolate final-state nuclear modifications of hadron production as a deviation of R_M from unity. A suppression of R_M is experimentally observed to increase with z , and to decrease with ν , and more mildly with Q^2 (see discussion in Section 3). When plotting R_M as a function of p_T , one observes a suppression at small p_T and an enhancement above $p_T \approx 1.5$ GeV/c. This behaviour is also known as “Cronin effect” (Sections 3.2 and 4.2). The amount of transverse momentum broadening (defined with respect to the direction of the virtual photon, see Fig. 4) is quantified via

$$(29) \quad \Delta \langle p_T^2 \rangle^h = \langle p_T^2 \rangle_A^h - \langle p_T^2 \rangle_D^h.$$

Here, $\langle p_T^2 \rangle_A^h$ is the average transverse momentum squared of a hadron of type h produced on a nuclear target A

$$(30) \quad \langle p_T^2 \rangle^h = \frac{\sum_{p_T, z, \nu, Q^2} p_T^2 N_h(z, \nu, Q^2, p_T^2)|_A}{\sum_{p_T, z, \nu, Q^2} N_h(z, \nu, Q^2, p_T^2)|_A},$$

and $\langle p_T^2 \rangle_D^h$ is the same quantity for a deuterium target.

In high-energy proton-nucleus and nucleus-nucleus collisions what is usually presented is the *nuclear modification ratio* or ratio of the hadron transverse momentum spectrum measured in $A + B$ at a given rapidity y and impact parameter b (or centrality class) normalised by the nuclear overlap function $T_{AB}(b)$ – related to the “parton luminosity” at b – over the $p + p$ spectrum:

$$(31) \quad R_{AB}^h(p_T, y; b) = \frac{1}{T_{AB}(b)} \frac{d^2 N_h^{A+B}(b)}{dp_T^2 dy} \bigg/ \frac{d^2 \sigma_{p+p}^h}{dp_T^2 dy}.$$

$T_{AB}(b)$ is computed with a geometrical Glauber eikonal model of the nucleus-nucleus collision (see e.g. [52]). In the absence of nuclear effects, one would expect $R_{AB} = 1$. The behaviour of $R_{AB}^h(p_T, y; b)$ as a function of p_T will be discussed in Sections 4 and 5.

For Drell-Yan processes, one defines an analogous nuclear ratio:

$$(32) \quad R_{DY} = \frac{1}{A} \frac{d\sigma_{h+A}^{DY}}{dM dx_F dp_T^2} \bigg/ \frac{1}{B} \frac{d\sigma_{h+B}^{DY}}{dM dx_F dp_T^2}.$$

The dilepton p_T -broadening is defined analogously to Eq. (29), with $h \equiv \ell^+ \ell^-$. Results for R_{DY} will be presented in Section 4.1.

Medium modifications of hadron production in nDIS and heavy-ion collisions can also be revealed by means of multi-particle azimuthal correlations, which are sensitive to the underlying parton-medium interaction and to the properties of the medium. For example, two-hadron correlations measured at RHIC revealed significant broadening and softening of associated hadrons on the away side of a triggered high- p_T particle, which is consistent with the observation of the hadron suppression in the single inclusive measurements. In nDIS processes, the distribution of associated sub-leading hadrons to the leading hadron challenges various models of single inclusive hadron suppression.

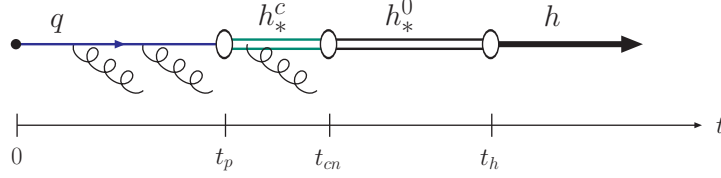


Fig. 7. – Sketch of the time evolution of the hadronisation process with definition of various time scales. A quark q created at time 0 in a hard collision turns into a coloured prehadron h_*^c , which subsequently neutralises its colour, h_*^0 , and collapses on the wave function of the observed hadron h . Gluon radiation lasts until colour neutralisation.

2.4. Hadronisation time estimates . –

Even though hadronisation is a non perturbative process, a few features can be extracted from general grounds. A parton created in a high-energy collision can travel in the vacuum as a free particle only for a limited time because of colour confinement: it has to dress-up in a colour-field of loosely bound partons, which eventually will evolve into the observed hadron. The same dressing process can be expected for partons traveling in QCD matter, yet it will be modified by interactions with the surrounding medium. In a deconfined nuclear medium such as the QGP, the dressing process might furthermore be delayed until the medium cools down and comes closer to the confinement transition.

The bare parton-medium cross section is dominated by the elastic $a + b \rightarrow a + b$ parton-parton scattering and gluon bremsstrahlung. The gluon-gluon cross-section is of order $\sigma_{gg} = 9/2 \pi \alpha_s^2 / \mu^2 \approx 2$ mb (for $\alpha_s = 0.5$ at a p_T -cutoff of order $\mu = 1$ GeV), but the dressed parton is likely to develop an inelastic cross section of the order of the hadronic one, $\mathcal{O}(40$ mb), becoming subject to nuclear absorption similarly to the final state hadron. Hence, it can be viewed as a “prehadron” (denoted here by h_*). The prehadron may still be for a short time in a coloured state and radiate gluons neutralising its colour before its wave function collapses onto the observed hadron wave function. We can therefore identify three relevant time scales, see Fig. 7: (1) the “prehadron production time” or “quark lifetime” t_{preh} , at which the dressed quark develops an inelastic cross section, (2) the “colour neutralisation time” t_{cn} , at which gluon bremsstrahlung stops, and (3) the “hadron formation time” t_h , at which the final hadron is formed. Typically, model applications further simplify the process and merge steps (2) and (3) assuming $t_{preh} = t_{cn}$. Note that the prehadron and the formation times are introduced as a phenomenological tool, rather than a well defined quantity, in order to distinguish between the stage in which the parton can be described as an asymptotically free particle and treated in pQCD from the stage in which colour confinement and non-perturbative interactions kick in and warrant a treatment in terms of different degrees of freedom. Such a phenomenology is well suited to the present status of the theoretical and experimental investigation, but will need to be substantiated or replaced by a more fundamental QCD description. Finally, note that strictly speaking the very question “is the prehadron formed within or without the medium?” is ill-posed: in quantum mechanics it can happen one way in the amplitude and the other in its complex conjugate, and the interference between the two may be non-negligible [53].

A simple estimate of the hadron formation time $\langle t_h \rangle$ can be obtained by defining it as the time for the struck partons to build up its colour field and to develop the hadronic wave function [11]. In the hadron rest frame this time is related to the hadron radius R_h , and in the laboratory frame

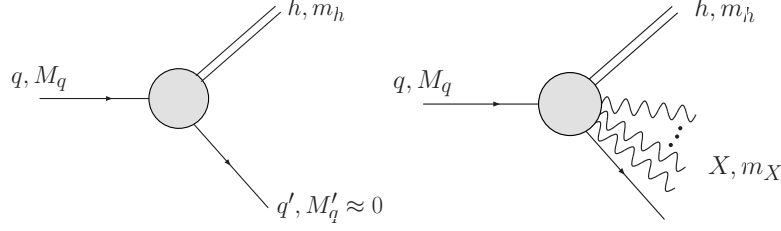


Fig. 8. – Quark hadronisation by emission of one parton (*left*) and emission of one parton accompanied by many soft gluons (*right*).

it is boosted by $\gamma = E_h/m_h$:

$$(33) \quad \langle t_h \rangle \propto R_h \frac{E_h}{m_h}$$

In Table VI we show the hadron formation time estimated with Eq. (33) for a typical 7 GeV pion ($R_h \approx 0.7$ fm [54]) at the kinematics conditions found in HERMES ($z \approx z_h \approx 0.5$, $E_h \approx z_h v \approx 7$ GeV) and at RHIC mid-rapidity ($z \approx 0.7$, $E_h \approx p_T^h \approx 7$ GeV/c). We find $\langle t_\pi \rangle \approx 35$ fm $\gg R_A$, which points towards a long quark lifetime with hadron formation outside the medium. However, for the heavier kaons, η , and protons (with radii $R_K \approx 0.6$ fm [55], $R_\eta \approx R_\pi$, $R_p \approx 0.9$ fm [56] resp.) we obtain much shorter formations times $\langle t_K \rangle \approx 8$ fm, $\langle t_\eta \rangle \approx 9$ fm and $\langle t_p \rangle \approx 6$ fm, which are comparable to the size of the medium. Heavy D and B mesons, with average radii $R_D = 0.57$ fm and $R_B = 0.5$ fm respectively [57], clearly fragment in-medium ($\langle t_{D,B} \rangle \lesssim 2$ fm).

An estimate of the prehadron production time can be obtained by looking at hadronisation in light-cone coordinates [30]. Consider a relativistic on-shell quark of mass m_q and plus-momentum p^+ , hadronising into a hadron of mass m_h and 4 momentum $p_h^+ = zp^+$. Minimally prehadron formation, i.e., the formation of a colorless partonic object, proceeds by emission of an additional, (typically light) parton to carry away the initial state colour, see Fig. 8 left. The process in momentum space is

$$(34) \quad \left[p^+, \frac{m_q^2}{2p^+}, \vec{0}_T \right] \longrightarrow \left[zp^+, \frac{m_h^2 + \vec{k}^2}{2zp^+}, \vec{k} \right] + \left[(1-z)p^+, \frac{\vec{k}^2}{2(1-z)p^+}, -\vec{k} \right]$$

where we imposed 4-momentum conservation. In time-ordered perturbation theory, the light-cone separation Δx^+ between the initial and final state can be estimated by the uncertainty principle:

$$(35) \quad \Delta x^+ \approx 1/\Delta p^- = \frac{2z(1-z)p^+}{\vec{k}^2 + (1-z)m_h^2 - z(1-z)m_q^2},$$

where $\Delta p^- = p_q^- + p_h^- - p_q^-$. Since $\Delta x^+ = (\Delta t_h + \Delta z_h)/\sqrt{2}$, and $\Delta z_h = (p_q/E_q)\Delta t_h$ with $p_q(E_q)$ the momentum (energy) of the quark, the prehadron formation time is

$$(36) \quad \langle t_{preh} \rangle = \frac{\sqrt{2}}{1 + p_q/E_q} \Delta x^+.$$

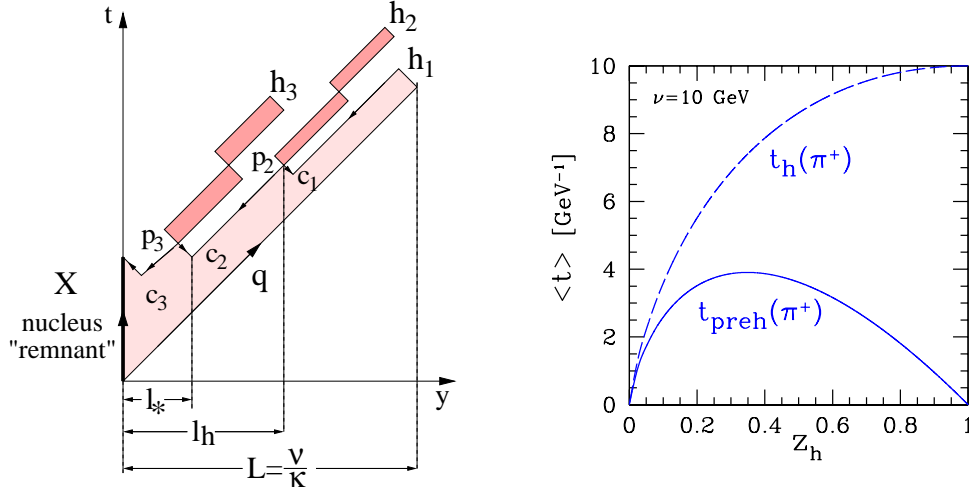


Fig. 9. – *Left*: Hadronisation in the Lund string model in the target rest frame. *Right*: Prehadron production time $\langle t_{preh} \rangle$, and hadron formation times $\langle t_h \rangle$, for $\nu = 10$ GeV quarks fragmenting into pions with fractional momentum z_h , as computed within the Lund string model in Ref. [61].

This estimate should be used with care since actually prehadron formation is likely to be accompanied by the emission of many soft gluons, see Fig. 8, and the system of emitted partons has an invariant mass m_X^2 . Taking this into account, we should add an additional zm_X^2 term at the denominator of Eq. (35), which would reduce the estimated formation time. In Table VI we show the hadron formation time from Eq. (36) for typical hadrons at HERMES and RHIC, where we assumed $k^2 \approx \Lambda_{QCD}^2$. High energy pre-pions are formed outside the medium ($\langle t_{pre-\pi} \rangle \approx 25$ fm), while pre-kaons and pre- η ($\langle t_{pre-K} \rangle \approx 6 - 9$ fm) and pre-protons ($\langle t_{pre-p} \rangle \approx 4$ fm) have formation times comparable to the medium size, and heavy pre-mesons are produced rapidly inside the medium.

At least for light mesons, these estimates can be used to justify the computation of hadron quenching in terms of parton-medium interactions alone, as done in radiative energy loss models [58-60], see Section 6.

A successful non-perturbative model of hadronisation is the Lund string model [62], see Fig. 9 left. The confined colour field stretching from the struck quark to the rest of the nucleus is modeled as a string of tension $\kappa_{str} \approx 1$ GeV/fm, and spans the lightly shaded area in space-time. The prehadron formation point is identified with the $q\bar{q}$ pair production point C_i which breaks the string in smaller pieces [63]. Hadrons are formed at points P_i when a quark and an antiquark at the endpoint of a string fragment meet. The subscript i indicates the so-called rank of the produced (pre)hadron, counted from the right of the figure. Average prehadron production times can be analytically computed [61, 63, 64] and have the following general structure:

$$(37) \quad \langle t_{preh} \rangle = f(z_h) (1 - z_h) \frac{z_h \nu}{\kappa_{str}} \quad , \quad \langle t_h \rangle = \langle t_{preh} \rangle + \frac{z_h \nu}{\kappa_{str}} \quad ,$$

$\langle t_h \rangle$	kinematics	π	K	η	p	D	B
Eq. (33)	HERMES	34 fm	8 fm	9 fm	6 fm	1.9 fm	0.6 fm
Eq. (33)	RHIC	34 fm	8 fm	9 fm	6 fm	1.9 fm	0.6 fm
Eq. (37)	HERMES	11 fm	9 fm		18 fm		
Eq. (37)	RHIC	9 fm	8 fm		13 fm		
$\langle t_{preh} \rangle$							
Eq. (36)	HERMES	28 fm	9 fm	7 fm	3 fm	0.8 fm	0.1 fm
Eq. (36)	RHIC	18 fm	7 fm	6 fm	3 fm	0.8 fm	0.1 fm
Eq. (37)	HERMES	4 fm	4 fm		6 fm		
Eq. (37)	RHIC	2 fm	3 fm		1 fm		

TABLE VI. – Estimates of typical hadron formation times $\langle t_h \rangle$ and prehadron production times $\langle t_{preh} \rangle$ for pions, kaons, η , protons, and D and B mesons at HERMES ($z_h \approx 0.5$, $\nu \approx 14$ GeV) and at RHIC at mid-rapidity ($p_T^h \approx 7$ GeV/c, $z \approx 0.7$) obtained with Eqs. (33), (36), and (37).

where ν is the struck quark energy, the function $f(z_h)$ is a small correction of $\langle t_{preh} \rangle$, which can be computed analytically in the standard Lund model [61, 63], and $\kappa_{str} = (1 \text{ GeV/fm}) R_\pi^2/R_h^2$ with R_h the hadron radius is taken from Ref. [61]. The factor $z_h \nu$ can be understood as a Lorentz boost factor; the $(1 - z_h)$ factor is due to energy conservation: a high- z_h hadron carries away an energy $z_h \nu$; the string remainder has a small energy $\epsilon = (1 - z_h) \nu$ and cannot stretch farther than $L = \epsilon/\kappa_{str}$. Thus the string breaking occurs on a time-scale proportional to $1 - z_h$. The resulting pion formation time scaled by a factor ν/κ_{str} is plotted in Fig. 9 left. A typical pion produced at HERMES energies (i.e. with fractional energy $z_h \approx 0.5$ from a parent quark with energy $\nu \approx 14$ GeV) has $\langle t_{preh} \rangle \approx 6 \text{ fm} \lesssim R_A$ and $\langle t_h \rangle \approx 13 \text{ fm} \gtrsim R_A$, with similar values at RHIC at mid-rapidity. Therefore, the final hadron is typically formed at the periphery or outside the nucleus so that its interaction with the medium is negligible (see Table VI). However, the prehadron is formed inside and can start interacting with the nucleus. A detailed space-time analysis of hadronisation in the PYTHIA/JETSET Monte Carlo implementation of the Lund string model has been performed in [65], with similar conclusions regarding the magnitude of the pion prehadron production time.

In Ref. [66-68] the formation of a leading hadron ($z_h \gtrsim 0.5$) is described in a pQCD model, see Fig. 10. The struck quark radiates a gluon. The gluon then splits into a $q\bar{q}$ pair, and the \bar{q} recombines with the struck q to form the leading prehadron, which later on collapses on the hadron wave function. The cross-section can be computed from the modulus squared of the sum of the two gauge-invariant amplitudes shown in the figure. At $z_h \approx 1$, higher twist effects spoil this simple mechanism for hadronisation. The dipole model of Ref. [29] approximates the described cross-section as a convolution of a Gunion-Bertsch radiation cross section [69] with the gluon splitting plus quark recombination process, see Fig. 10 right. The prehadron is identified with the $q\bar{q}$ pair which includes the struck quark, and its production time is identified with the time at which the gluon becomes decoherent from the struck quark. Note that, strictly speaking, the resolved quark-gluon system may be in an octet state from the production time until gluon splitting occurs. However, in this model, gluon radiation is neglected during the octet stage. The model can compute the probability distribution in the prehadron production time, see Fig. 11,

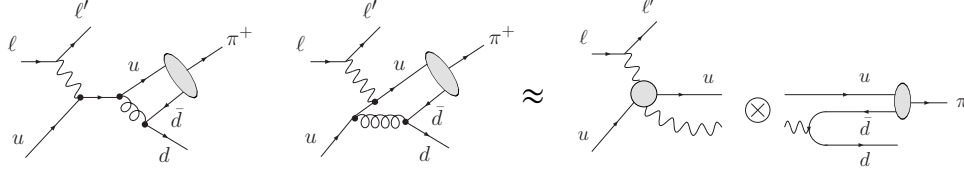


Fig. 10. – Diagrams for leading hadron formation in $\ell + A$ collisions: Gauge-invariant set [66] (left), and dipole-model approximation [29] (right).

and the average $\langle t_{preh} \rangle$ is

$$(38) \quad \langle t_{preh} \rangle \propto (1 - z_h) \frac{z_h \nu}{Q^2}.$$

The interpretation of the $1 - z_h$ factor is in terms of energy conservation: the longer the struck quark propagates, the larger its energy loss; hence to leave most of its energy to a $z_h \rightarrow 1$ hadron, the quark must be short lived. The scale is set by $\kappa_{dip} = Q^2$. At HERMES, with $Q^2 \approx 10 \text{ GeV}^2$, this model obtains for pion production $\langle t_{preh} \rangle \lesssim 5 \text{ fm}$ at $z_h > 0.5$: pre-pions are formed inside the medium. At RHIC, where $Q^2 \propto p_T^2$, and $z_h \nu \approx p_T$ for mid-rapidity hadrons, one obtains the counter-intuitive result that $\langle t_{preh} \rangle \propto 1/p_T$: prehadrons are formed the quicker the higher their transverse momentum [29, 70], typically inside the medium.

In summary, given the model dependences of the theoretical estimates of the hadron formation time – and hence of the length of the partonic phase of the hadronisation process – it is important to study the kinematic- and flavour-dependences of various hadron production processes through a careful analysis of experimental data and tests of phenomenological models, see the discussion Section 8.

3. – Experimental results in lepton-nucleus deep inelastic scattering

Deep inelastic lepton-nucleus scattering offers a direct way to study the hadronisation process which follows the hard scattering. In contrast to hadronic collisions, in nuclear DIS no deconvolution of the parton distributions of the projectile and target particle is needed, so that the experimental observables can be more directly related to the nuclear effects on the quark propagation and fragmentation. Moreover, in electron and muon experiments the incoming and outgoing leptons are detected and they provide an extra handle to determine the kinematical variables of the produced partons/hadrons.

In the past, semi-inclusive lepton production of undifferentiated hadrons from nuclei has been studied with neutrinos at FNAL, CERN and Serpukhov; with electrons at SLAC [71], and at CERN and FNAL with high-energy muons by EMC [72] and by E665 [73] respectively. Recently, HERMES has reported more precise data [21-23] on the production of charged hadrons as well as, for the first time, various identified hadrons (π^+ , π^- , π^0 , K^+ , K^- , p and \bar{p}) in deep-inelastic positron scattering off nuclei. Finally, high-statistics data have been collected at JLab [74] with a 5.0 GeV electron beam on targets of carbon, aluminum, iron, tin, and lead at large luminosities ($2 \cdot 10^{34} \text{ cm}^{-2} \text{ s}^{-1}$), with detection of several identified hadrons, particularly π^+ , π^0 , π^- , K^0 , and Λ . In the next Sections the most significant experimental results for DIS of neutrino, muon, electron and positron beams on nuclei are presented.

3.1. Hadron production in ν -nucleus DIS. – Neutrinos can interact via the exchange of Z^0 (neutral current), or can turn into charged leptons via W^\pm exchange, while at the energies of

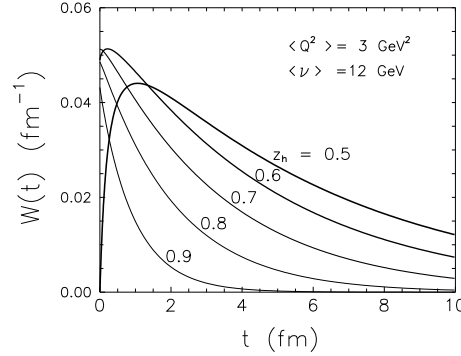


Fig. 11. – Probability distribution of the prehadron production time $t_{preh} \equiv t$ obtained in the colour-dipole model of [29].

interest here electrons scatter primarily through the exchange of photons. One thus has at hand various methods to extract information on the parton production and propagation combining results from experiments encompassing all four (neutral and charged) exchanged bosons. In contrast to hadron-induced collisions, which preferentially scatter from the front hemisphere of a nucleus due to their strong interaction probability, neutrinos and electrons directly scatter with partons or nucleons inside the nuclear target because of their weak interaction probability. This means that the fragments of the struck parton in neutrino and electron scattering experiments should suffer the same final-state interactions. In general, the laboratory energy E_ν of the incoming (anti)neutrino cannot be determined directly since there is substantial energy that goes to undetected neutral particles. Corrections on the estimation of the neutrino energy reflect on most of the kinematic quantities and significantly increase the systematic uncertainties for neutrino experiments.

Neutrino-induced hadron production was first studied in the bubble chamber at FNAL [76]

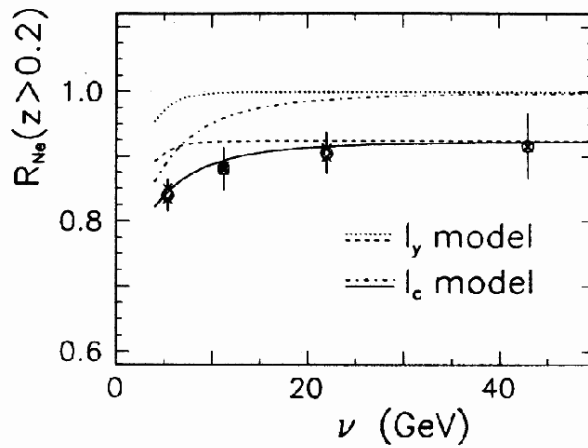


Fig. 12. – Ratio of the differential hadron multiplicity distribution in (anti)neutrino- Ne over $-He$ collisions as function of the transferred quark energy ν for fast ($z_h > 0.2$) charged hadrons [75] compared to model predictions for “constituent” (l_c) and “yo-yo” (l_y) lengths (see text for details).

and later in the bubble chamber BEBC at CERN [77]. The main objective of these experiments was the study of global properties of hadron production in nuclei. Fast hadron production on nuclei was found to be attenuated as compared to that in hydrogen target and to depend both on the variables z and ν [76].

The production of hadrons in charged-current (anti)neutrino interaction was studied with higher accuracy by the BEBC WA21/WA59 Collaborations [75]. While in the previous experiments the analysis was limited to negative hadrons in order to exclude systematic uncertainties due to 'knock-on' protons, charged hadron production was studied in this experiment in terms of z_h -distribution normalised to the number of events. A small but significant reduction of fast hadron ($z_h > 0.2$) production was found in a neon target as compared to that in a hydrogen target. This is shown in Fig. 12 where the ratio of the normalised distribution is presented as function of the transferred energy $\nu = E_\nu - E_\mu$, where E_μ is the laboratory energy of the muon beam. The data indicates a significant (10% – 20%) attenuation ($R_{Ne} < 1$) of fast charged hadron yields over the whole ν -range with a stronger attenuation at low ν and high z_h . The experimental results are compared to theoretical predictions of Ref. [63] in which two hadron formation lengths are considered: the constituent (l_c) and the "yo-yo" (l_y) lengths. Specifically, the constituent length corresponds to the time after which the first constituent of the hadrons is formed, the yo-yo length corresponds to the time after which the quark and antiquark meet to form the color singlet [78]. The l_y -model overshoots the value of R_{Ne} , while a l_c -model give a fair description of the data thus pointing out that significant interactions of the hadronising system start as early as at the constituent point.

The role of the formation length for the description of hadroproduction in DIS of neutrino on nuclei has been investigated by the NOMAD experiment at CERN [79, 80]. The backward-going protons and π^- produced in charged current neutrino interaction have been compared with intra-nuclear cascade (INC) models. In these models the production of particles in kinematically forbidden regions can be seen as the result of multiple scattering and of interactions of secondary hadrons with the other nucleons while they propagate through the nucleus. Experimentally it has been observed that the cascade is restricted to slow particles only, while the fast ones do not re-interact inside the nucleus. A proposed explanation for this effect is that, since the formation time is proportional to the hadron energy (via the Lorentz time-dilation factor $\gamma = E/m$), the INC process is restricted to slow hadrons which have formation lengths smaller than the nuclear radius [79].

The inclusive spectra of hadrons have been also measured with the aid of the SKAT propane-freon bubble chamber irradiated with a beam of 3 to 30 GeV neutrinos from the Serpukhov accelerator [81]. The ratio of the yields of charged hadrons in the subsamples of nuclear interactions B_A and of deuteron interactions B_D is shown in Fig. 13 as a function of z_h (left) and ν (right) respectively. The left part of Fig. 13 displays the ratio measured at $\langle A \rangle = 28$ and energies in the range $2 < \nu < 15$ GeV, compared with the multiplicity ratio obtained from deep inelastic scattering of positron on nitrogen nuclei ($A = 14$) at higher transfer energies of $7 < \nu < 24$ GeV [21].

The suppression of the hadron yield appears more pronounced for the most energetic hadrons ($z_h > 0.6$). The ν dependence of the ratio for leading charged hadrons with $z_h > 0.5$ is shown in the right part of Fig. 13, which shows the SKAT data at $\langle \nu \rangle = 3.3$ and 7.7 GeV, along with data from e^\pm - ^{14}N interactions in the region $\nu > 8$ GeV. The reduction of the yields occurs for hadrons produced in processes where the parent quark has the lowest energies. The neutrino data, within their larger uncertainties, show the same trend as observed with electron beams.

3'2. Hadron production in e -nucleus (SLAC) and μ -nucleus (CERN) DIS. – In contrast to the neutrino scattering experiments, in electron- and muon-induced DIS the incoming and scattering leptons are detected and provide a well defined reference system for the measurements of the

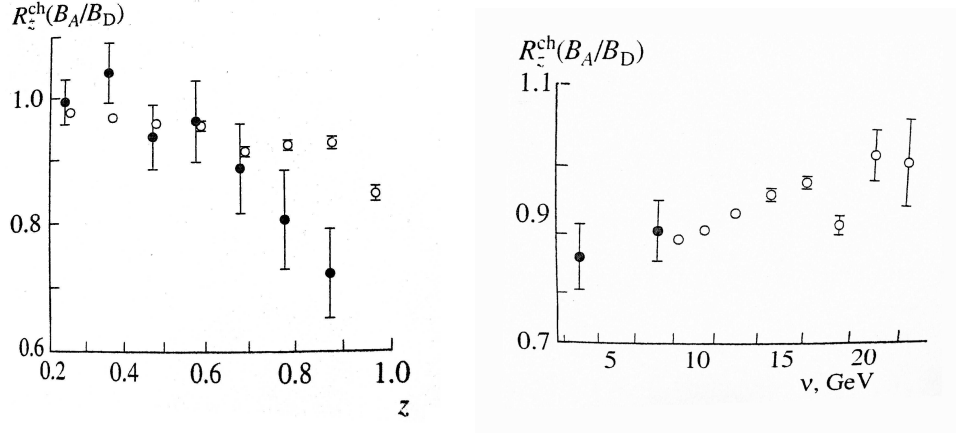


Fig. 13. – Ratio of the yields of charged hadrons in neutrino DIS on nuclei A over deuteron D targets (closed circles) [81] and in e^+ DIS on nitrogen and deuteron nuclei (open circles) [21]. *Left:* z_h -distribution for hadrons produced in processes with transferred energy $2 < \nu < 15$ GeV. *Right:* ν -distribution for hadrons with $z_h > 0.5$.

kinematics of the outgoing parton/hadrons.

Electroproduction of hadrons from nuclei was studied for the first time at the SLAC using a 20.5 GeV/c electron beam incident on different targets (H , D , Be , C , Cu , Sn) in the late seventies [71]. A single arm spectrometer was used to measure the scattered electrons and the produced hadrons. The ratio between the number of single inclusive hadrons detected per gram per square centimeter per incident electron for nucleus to the analogous number for deuterium was measured. The results were presented in the original paper [71] as a function of the trans-

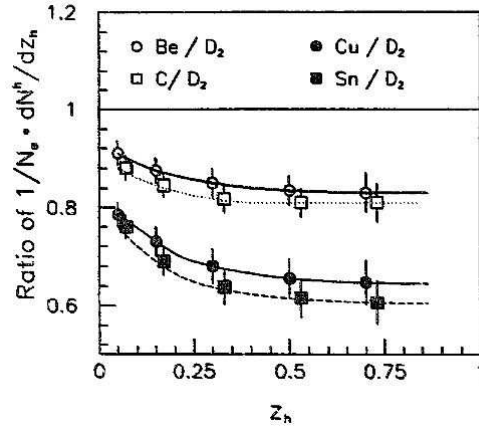


Fig. 14. – Ratio of differential charged hadron multiplicities as function of z_h measured in $e + A$ interactions at SLAC [71] and derived in Ref. [82]. The curves represent a fit to the data in the functional form $(A/2)^{\alpha(z)}$.

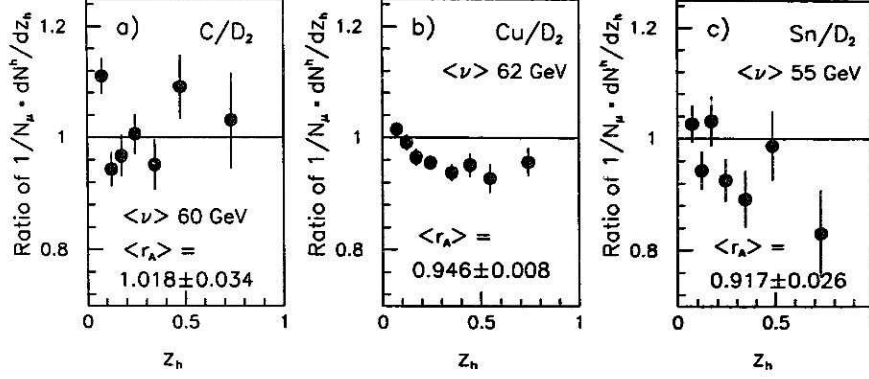


Fig. 15. – Ratio of the differential hadron multiplicity distribution as function of z_h measured in μ -A interactions by EMC [45].

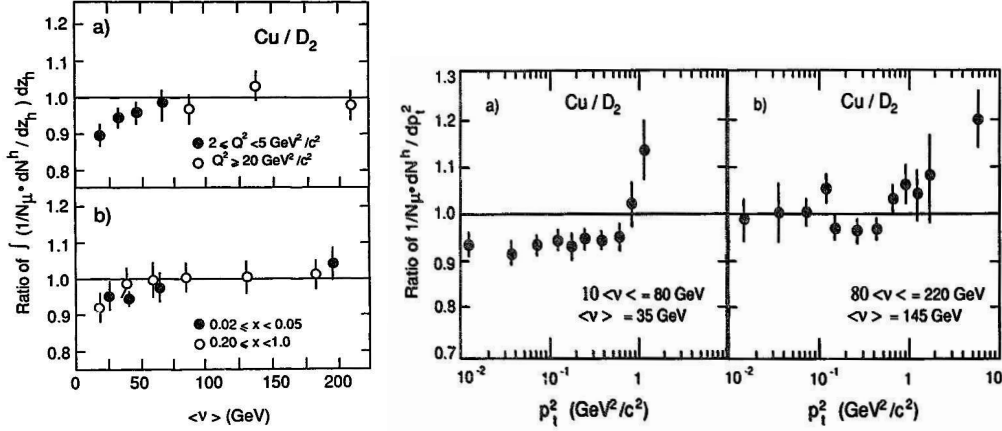


Fig. 16. – Ratio of the differential hadron multiplicity distribution as function of ν (left) and p_T^2 (right) measured in μ -A collisions at EMC [45].

verse momentum p_T of the hadron in the photon-nucleon system and $z_{c.m.} = p_l/p_{max}$, where p_l is the longitudinal hadron momentum and $p_{max} = \sqrt{s}/2$. The ratio of differential charged hadron multiplicities as a function of z_h , derived in Ref. [82] from the values published in the original paper, is shown in Fig. 14. This experiment shows an attenuation of the electroproduced hadrons which clearly increases with the size of the target nucleus. In addition the nuclear attenuation increases for increasing hadronic momenta. This measurement performed prior to the discovery of the EMC effect, does not account for modifications of the nuclear PDFs and, thus, needs correction because a semi-inclusive cross section ratio was measured instead of the multiplicity ratio as defined in Eq. (28). An estimate of the correction for this effect based on Ref. [21] results in a 4% increase of the original ratio.

After the pioneering measurements with muon beams performed at FNAL [83,84], hadron production in DIS of muons was studied by the EMC-collaboration first in the ν range 50-140 GeV [72] and later on in the ν range 20-220 GeV [45]. Their large single-arm spectrometer

allowed this experiment to carry out a precise determination of the muon momentum with a good acceptance for forward produced hadrons. In addition, due to the simultaneous measurements of nuclear targets and deuterium, most of the systematics uncertainties cancel in this measurement.

The ratio of the hadron multiplicity distribution as function of z_h is shown in Fig. 15 for different targets. The corresponding mean value of the multiplicity ratios and of the ν variable are noted on the figure. For large nuclei (Cu, Sn) a small but distinct reduction of the fast hadron production compared to that of deuterium is observed, whereas for carbon the ratio is compatible with unity over the whole range in z_h . The left part of Fig. 16 shows the hadron multiplicity ratio as a function of ν in two Q^2 bins. The same variation with ν is seen in all intervals, thus no trend in Q^2 is observed. The ratios show a gradual decrease with decreasing ν below 60 GeV, whereas they slowly approach unity for higher ν . The depletion of the fast hadron multiplicity in muon interaction with heavy targets is only $\sim 10\%$ even in the low- ν bin. The p_T dependence was measured as shown in the right part of Fig. 16 for two ν intervals. At high p_T the ratio rises above unity in both ν intervals. The observed trend is consistent with the Cronin enhancement reported in hadron-nucleus collisions [8, 9] (see Section 4). Since in lepton-nucleus, at variance with hadron-nucleus, collisions neither multiple scattering of the incident particle nor interaction of its constituents can contribute to the Cronin effect, the observed enhancement can be ascribed to rescattering effects in the *final-state* only.

In conclusion, the results from the experiments performed at SLAC with electrons and at CERN with muons have shown that the multiplicity ratios mainly depend on the energy of the virtual photon ν , and on the fraction z_h of this energy carried out by the final hadron. These experiments demonstrate that the nuclear effects on the ratios decrease with increasing ν . This has been confirmed by the Fermilab experiment E665 [73] in DIS of 490 GeV muons off xenon and deuterium targets. No nuclear dependence in the z_h -distributions of the forward-produced hadrons was found in the ν -range from 50 GeV to 500 GeV. Thus we can conclude from the performed measurements that the transfer energies ν where nuclear effects are the largest are in the range from a few GeV to few tens of GeV. Such an energy dependence is easily understood within parton energy loss models: since the energy lost by quarks propagating through QCD media, ϵ , is independent of their energy (i.e. ν in this context) in the high-energy limit, the *relative* energy-loss ϵ/ν – which controls the amount of hadron suppression in nuclear DIS – vanish at high energy making the ratio R_m^h tend to 1. In the hadron-oriented picture, the larger ν (parton energy) the longer the formation time, which therefore decreases the amount of nuclear absorption.

3.3. Hadron production in e -nucleus DIS at the HERMES experiment. – The influence of the nuclear medium on lepto-production of hadrons has been recently extensively studied by the HERMES experiment at DESY in semi-inclusive deep-inelastic scattering of 27.6 GeV positrons off deuterium, nitrogen, neon, krypton and xenon targets. The data were collected in the ν -range 3-23 GeV using high density gas targets internal to the positron storage ring. During these high-density runs HERA operated in a dedicated mode for the HERMES experiment.

For the first time the ν -dependence of the multiplicity ratio has been measured for various identified hadrons (π^+ , π^- , π^0 , K^+ , K^- , p and \bar{p}) and neutral pions [22], as shown for a krypton target in Fig. 17. The identification of charged pions, kaons, protons and antiprotons was accomplished using the information from the RICH detector [85], which replaced a threshold Čerenkov counter used in the previously reported measurements for the charged hadrons multiplicity on ^{14}N [21]. The corresponding z_h -dependences of R_M^h with $\nu > 7$ GeV are shown in the right part of Fig. 17. In the bottom panels the average values for Q^2 and z_h or ν are displayed for all the presented data.

The results presented in Fig. 17 and the average R_M^h values reported in Table VII for $z_h > 0.2$,

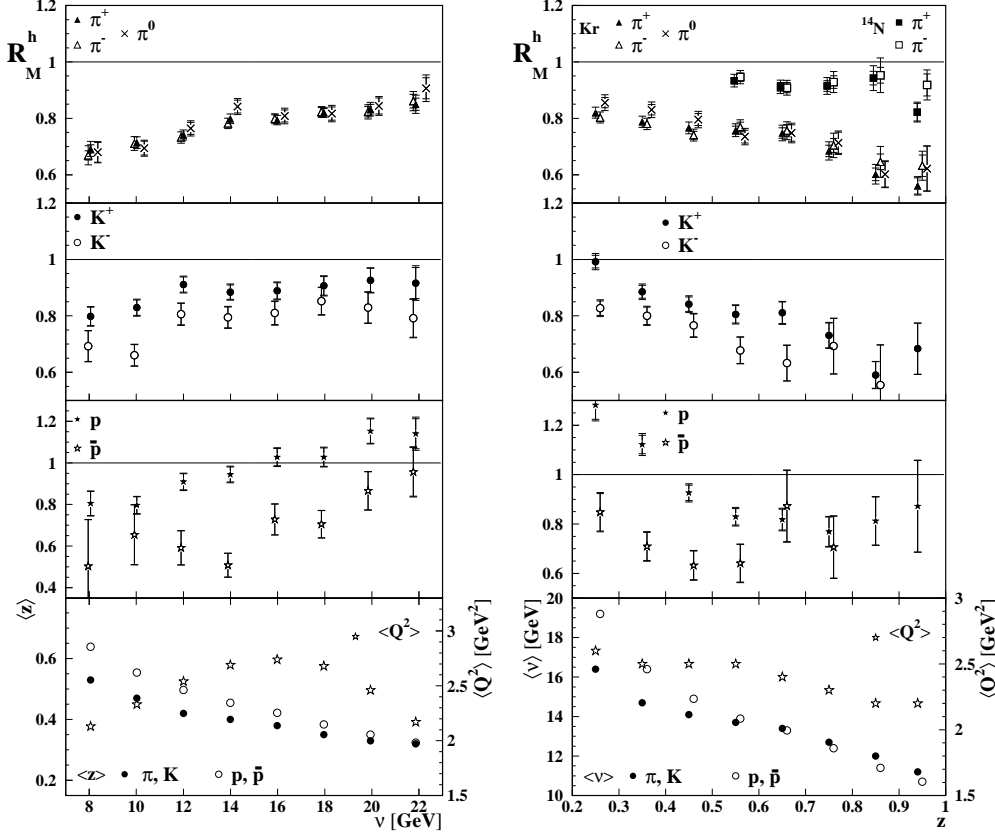


Fig. 17. – Multiplicity ratios for identified pions, kaons, protons and antiprotons from a Kr target as a function of ν for $z_h > 0.2$ (left), and as a function of z_h for $\nu > 7$ GeV (right). In the upper right panel the multiplicity ratio for identified pions from a ^{14}N target are also shown. The closed (open) symbols represent the positive (negative) charge states, and the crosses represent π^0 mesons. In the bottom panels the average z_h and ν values are displayed: pions and kaons (protons and antiprotons) are shown as closed (open) circles; the average Q^2 values are indicated by the open stars referring to the right-hand scales. The inner (outer) error bars represent the statistical (total) uncertainties. Multiplicity ratios for negative kaons and antiprotons at the highest z_h -bins are not displayed due to their poor statistical significance.

show that the multiplicity ratios for positive, negative and neutral pions as well as for negative kaons are similar. However, R_M^h for positive kaons is significantly larger. An even larger difference is observed between protons and their antiparticles compared to the meson case. These differences in R_M^h of positive and negative kaons, as well as those between protons and antiprotons, are still present at $z_h > 0.5$. This is shown in the last column of Table VII, where the average R_M^h values are reported for $z_h > 0.5$, i.e. when emphasising leading hadrons. In addition the $z_h > 0.5$ range is most suitable to compare R_M^h of mesons and baryons as this comparison is performed at the same average ν as shown in the bottom right panel of Fig. 17. The difference observed in mesons and baryons multiplicity ratios resembles the anomalous baryon enhancement reported at intermediate p_T 's ($p_T \approx 1.5 - 8$ GeV/c) in proton-nucleus and heavy-ion collisions [86, 87]

hadron	$\langle R_M^h \rangle (z_h > 0.2)$	$\langle R_M^h \rangle (z_h > 0.5)$
π^+	0.775 ± 0.019	0.712 ± 0.023
π^-	0.770 ± 0.021	0.731 ± 0.031
π^0	0.807 ± 0.022	0.728 ± 0.024
K^+	0.880 ± 0.019	0.766 ± 0.024
K^-	0.783 ± 0.021	0.668 ± 0.036
p	0.977 ± 0.027	0.816 ± 0.029
\bar{p}	0.717 ± 0.038	0.705 ± 0.067

TABLE VII. – HERMES multiplicity ratios for various hadron species produced in $e + Kr$ over e -deuterium collisions integrated over fractional hadron energies $z_h > 0.2$ and 0.5 for struck quark energies $\nu > 7$ GeV [22]. Total experimental uncertainties are quoted.

(see Sections 4 and 5).

Recently, new data on neon and xenon and more krypton data have been collected at HERMES [23]. This allows for a multidimensional analysis of the multiplicity ratio thus reducing the correlation between i.e. the ν and z_h variables shown in the bottom panels of Fig. 17. In addition, the dependence of the R_M^h of the other variables like Q^2 , p_T^2 as well the mass number dependence can be studied.

The p_T dependence of the multiplicity ratio for identified charged hadrons is shown in Fig. 18 for different nuclei. A nuclear enhancement is observed at $p_T^2 \geq 0.7$ (GeV/c)² similar to the Cronin effect observed in hadron-nucleus collisions (see Section 4'2). The conventional explanation of the Cronin effect in $p + A$ collisions ascribes this effect to the multiple scattering of projectile partons within the target nucleus (see Section 6'1). HERMES data highlight the role of partonic *final-state* multiple scattering (whereas Drell-Yan data are sensitive to initial-state parton multiple scattering, see Section 4'1) although explanations of the HERMES p_T^2 broadening in terms of *prehadronic* final-state interactions also exist, see Section 7'4. The larger Cronin enhancement for protons compared to mesons and antiprotons (note also the already discussed difference in the multiplicity ratio of p and \bar{p}) is also seen in $h + A$ and $A + A$ collisions, where both baryons and antibaryons are enhanced compared to mesons, see Section 4.

The two-dimensional analysis of the charged pion multiplicity ratio is presented in Fig. 19, where the multiplicity ratio is shown in three z_h -ranges as a function of ν , Q^2 and p_T^2 . The leftmost panels indicate that the dependence on ν hardly depends on z_h . The Q^2 -dependence is similar for the various z_h -bins therefore, the dependence on z_h is not affected when integrating over Q^2 . The data in the rightmost plots indicate that the increase of R_A^h for Kr and Xe at large p_T^2 is smaller for larger z_h . Such a dependence was predicted in Ref. [29] and is consistent with the idea that the rise of R_A^h at large p_T^2 is of partonic origin.

An analysis of the hadron p_T -broadening has been recently performed at HERMES [88], which measured the observable $\Delta\langle p_T^2 \rangle = \langle p_T^2 \rangle_A^h - \langle p_T^2 \rangle_D^h$, introduced in Section 2'3, for different hadron species and nuclear targets. The p_T -broadening measurement is expected to provide new insights on the space-time evolution of the propagating quark [29], and on the multiparton correlation function inside the nucleus [89] (see Section 8'1.3).

The HERMES results for p_T -broadening are shown in Fig. 20 for π^\pm and K^+ produced on He , Ne , Kr , and Xe targets. The panels presented in Fig. 20 show $\langle p_T^2 \rangle$ for deuterium (top row) and the p_T -broadening (remaining rows) as a function of ν , Q^2 , x and z_h . The data do not reveal a significant dependence on ν in the kinematic range covered. An increase of the broadening

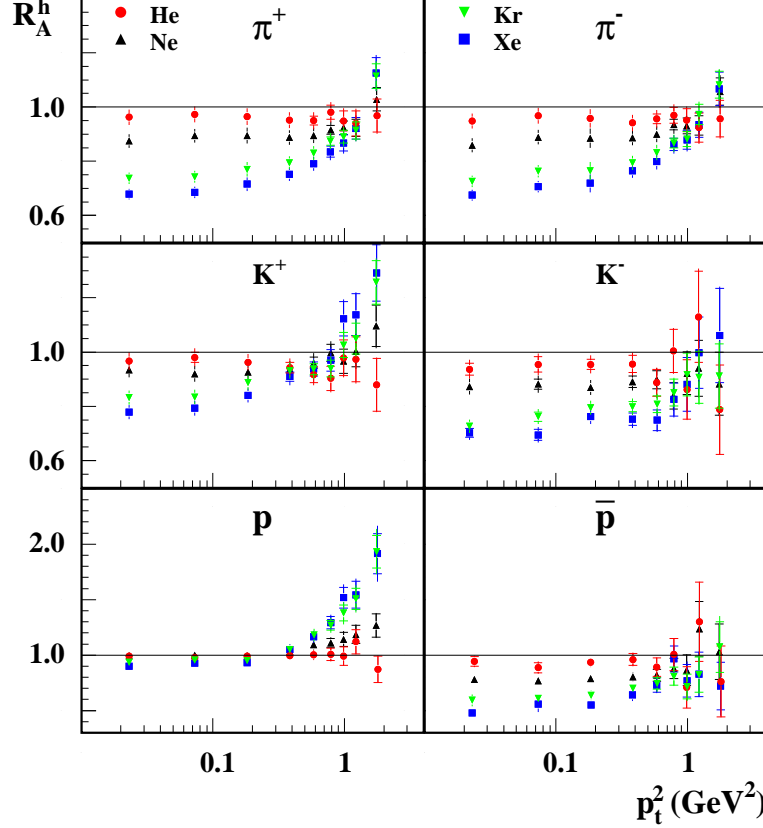


Fig. 18. – HERMES multiplicity ratio versus p_T^2 for identified charged hadrons on krypton, neon and helium.

with Q^2 is observed, the behavior as function of x is very similar to the Q^2 behaviour, due to the strong correlation between x and Q^2 in the HERMES kinematics; hence it can not be excluded that the Q^2 dependence is actually an underlying x dependence or both a Q^2 and x dependence. The p_T -broadening is seen to vanish as z approaches unity while the $\langle p_T^2 \rangle$ for deuterium is 0.2 or higher in the highest energy bin. The results on the mass number (A) dependence of the p_T -broadening are shown in the left part of Fig. 21. The broadening is similar for π^\pm while is systematically higher for K^\pm ; it increases with A , however the uncertainties of the data do not allow to firmly establish the mass number dependence. In addition, the preliminary results for the HERMES ratio $\langle p_T^2 \rangle_A^h / \langle p_T^2 \rangle_D^h$ are displayed in the left part of Fig. 22 as a function of Bjorken x_B for charged hadrons, thus showing a non-negligible x -dependence of the broadening in the x -range explored. In particular the p_T -broadening appears to increase from low to high x_B , with a tendency to flatten out at $x_B \gtrsim 0.2$.

As discussed in detail in Section 7, the new HERMES data allow one to definitely rule out nuclear absorption models based on one-step hadronisation process in which the struck quark propagates in the nucleus, interacts with the surrounding nucleons with perturbative cross section σ_q , and fragments into a leading hadron in the vacuum. Instead, they support a more complex picture where the space-time evolution of the fragmentation process – as encoded e.g. in the Lund string fragmentation model – is largely modified by the surrounding matter. However, in spite of

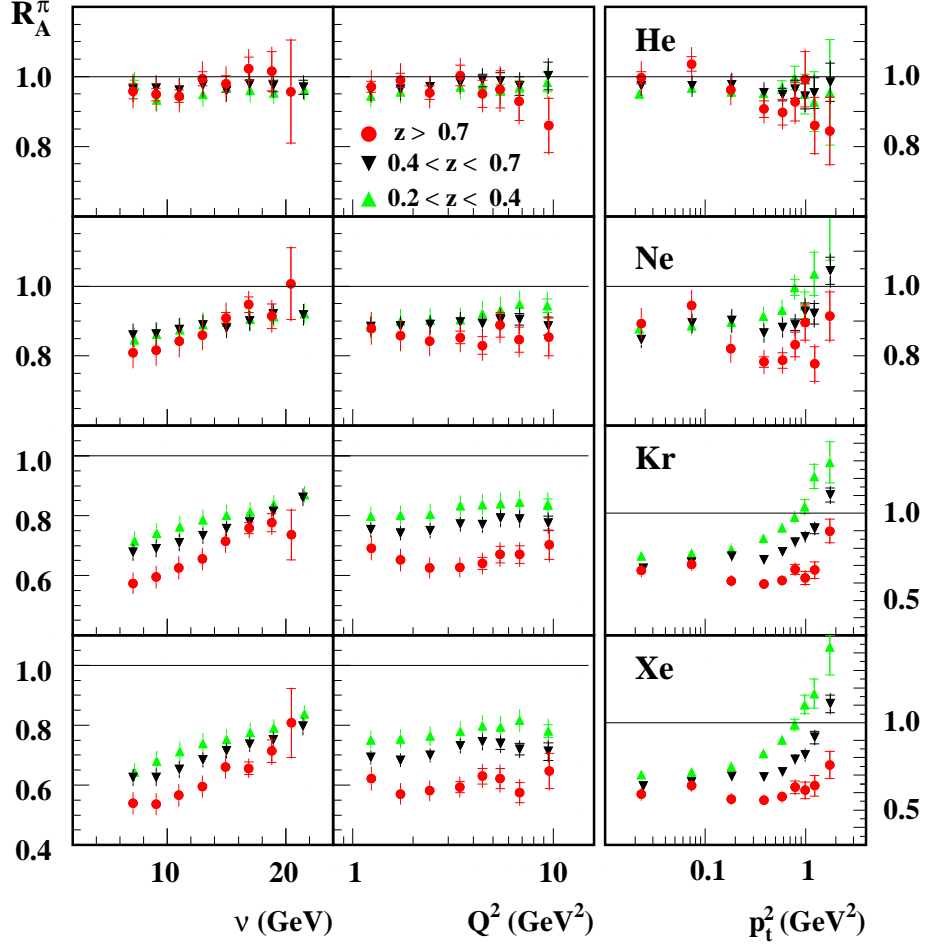


Fig. 19. – HERMES multiplicity ratio versus ν , Q^2 and p_T^2 for charged pions in different z_h -bins.

the theoretical effort in developing new calculations for describing the wide range of data shown in this section, the observed (μ, z, p_T^2) kinematical dependences can be described both in term of interaction of the intermediate prehadronic stage in absorption models (see Section 7), as well as in terms of parton energy loss calculations as discussed in Section 6. It is therefore important to extend the nDIS kinematical region with new measurements and to analyse other observables in order to disentangle the relative role of perturbative parton energy loss and prehadron absorption.

3.4. Hadron production in e -nucleus DIS at CLAS/JLab. – Hadron production has been measured with a 5.0 GeV electron beam with the CLAS detector at Jefferson Lab. Approximately 25 fb^{-1} of integrated luminosity was taken among the three primary solid targets, carbon, iron, and lead. In each case a 2-cm long liquid deuterium cryo-target was located in the beam simultaneously, providing a normalisation for the nuclear ratios. A small amount of data was also taken on aluminum and isotopically enriched tin. The small spacing of 4-cm between the deuterium and solid targets limited the acceptance differences between the two targets for the large CLAS detector.

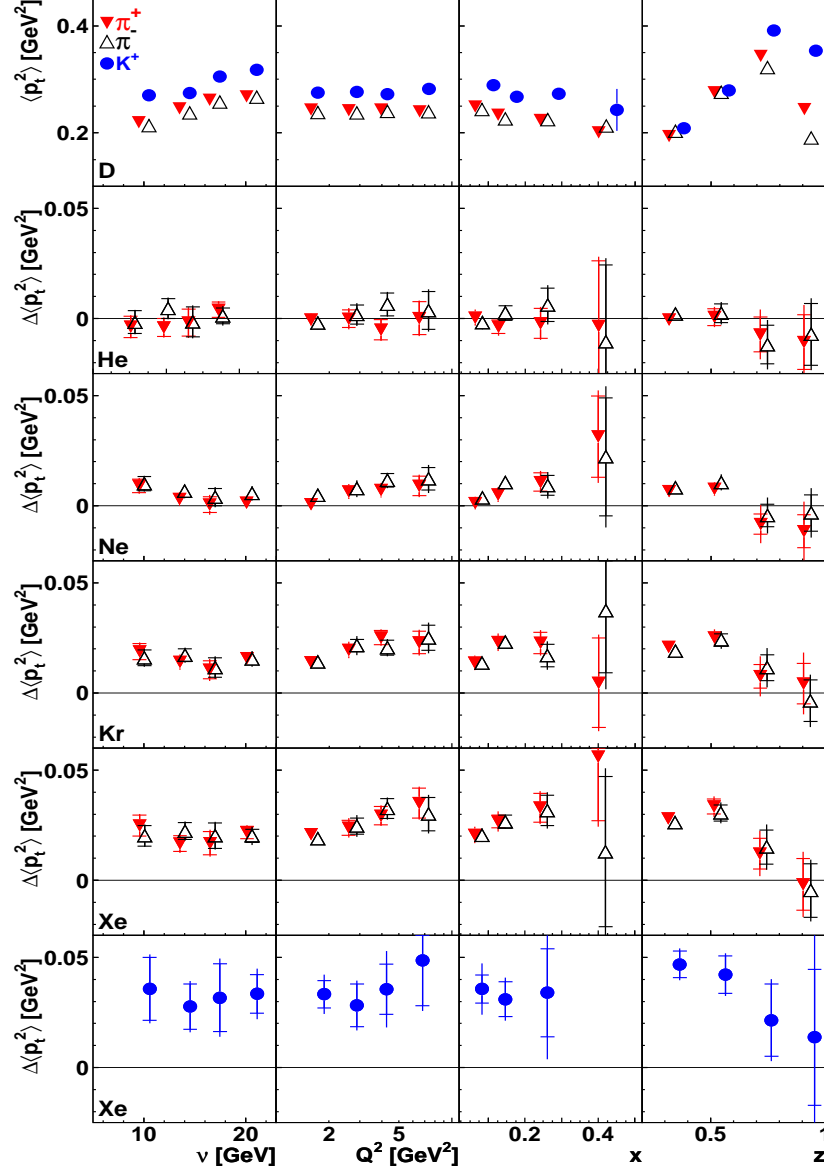


Fig. 20. – From left to right, the ν , Q^2 , x and z_h dependence of $\langle p_T^2 \rangle$ for deuterium (top row) and p_T -broadening (remaining rows) for π^\pm produced on *He*, *Ne*, *Kr* targets and for K^+ produced on *Xe* target (bottom row) at HERMES.

Particle identification for hadrons consisted of the standard CLAS instrumentation, which uses tracking and time-of-flight (TOF) systems, an electromagnetic shower calorimeter (EC) and a gas Čerenkov counter (CC). Identification of positive pions and protons was possible through the full momentum range using a combination of TOF and CC with the EC to reject positrons, while a somewhat more limited range of momentum was available for negative pions. Neutral pions and η mesons were measured in their two-photon decay mode in the EC, while neutral

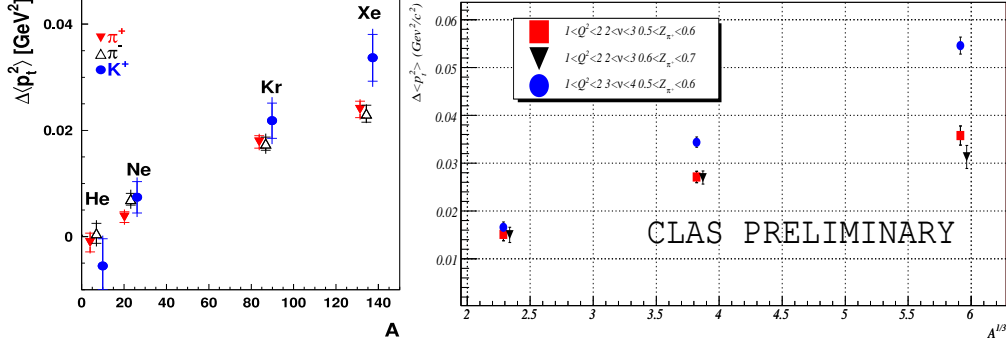


Fig. 21. – Mass number dependence of hadron p_T -broadening in nuclear DIS. *Left*: HERMES data for π^+ and K^+ production with Ne , Kr and Xe targets. The inner error bars represent the statistical uncertainties, the total bars represent the statistical and systematic uncertainties. *Right*: CLAS preliminary data for π^+ for C , Fe and Pb targets threefold differential in Q^2 , ν , and z_h as shown in the legend. The errors shown are statistical only.

kaons were also measured in the $\pi^+\pi^-$ channel, all over the full momentum range, but requiring a background subtraction. This very large data set is currently under analysis, and preliminary results are only available for positive pions, and for neutral kaons at the present. The kinematical range of the data was for $\nu = 2 - 4$ GeV, $Q^2 = 1 - 4$ GeV²; the full range of z_h and p_T^2 was available for analysis. Analysis cuts include $y = \nu/\nu_{max} < 0.85$, $W^2 > 4.0$ GeV², and target vertex cuts. While the CLAS/JLab data have a much more limited range in ν , they offer two orders of magnitude more integrated luminosity than the HERMES data. This feature provides access to three-fold dimensional binning for at least positive pions, and should provide a first look at hadron formation in some previously unmeasured hadrons, such as η , Λ , and K^0 . Because of the limited range in $W^2 \approx 4 - 10$ GeV², the initial analysis is being focused on the region $z_h = 0.4 - 0.7$. All the (preliminary) data shown hereafter have not been corrected for acceptance

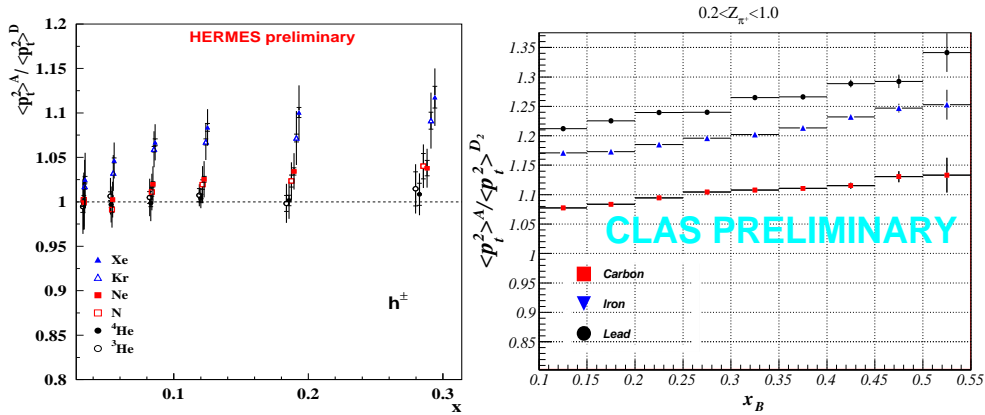


Fig. 22. – Preliminary x_B -dependence of the A/D average $\langle p_T^2 \rangle$ ratio at HERMES (*left*) and CLAS (*right*). For the HERMES data the inner error bars represent the statistical uncertainties, the total bars represent the statistical and systematic uncertainties. For the CLAS data the errors shown are statistical only and the data have not been corrected for acceptance or radiative effects.

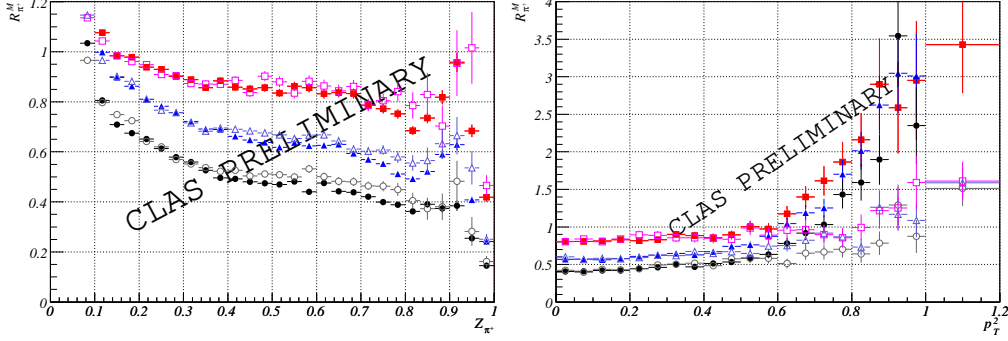


Fig. 23. – *Left*: CLAS preliminary data for the $z \equiv z_h$ dependence (left) and $p_T^2 \equiv p_{Th}^2$ of the hadronic multiplicity ratio for π^+ for carbon, iron, and lead targets. The data with solid (hollow) symbols correspond to the range $\nu = 2.2 - 3.2$ ($3.2 - 3.7$) GeV and $Q^2 = 1.0 - 1.3$ GeV². The errors shown are statistical only.

or radiative effects; however, these corrections are known to be rather small.

Figure 23 shows preliminary data for the CLAS hadronic multiplicity ratio [90]. The data are shown in just two plots for compactness, but the statistical accuracy is adequate to divide the data further into multidimensional bins in Q^2 , ν , and p_T^2 . In qualitative terms, these data are remarkably consistent with the HERMES results. The drop in multiplicity ratio with increasing z_h (and slow rise with increasing ν) as well as the rise with increasing p_T^2 are observed in the JLab data as they are with the HERMES data (Figs. 17, 18, 19). The dependence on Q^2 , although visible, is also small in these data, as inferred from the HERMES studies. Thus, it is hoped that the two datasets can be inter-compared quantitatively in detailed model studies.

In Fig. 21 right, are shown preliminary CLAS data for transverse momentum broadening (defined in Eq. (29)). Three sets of data are shown; each data point is binned in a multidimensional bin in Q^2 , ν , z_{π^+} as well as $A^{1/3}$. The available statistical sample is adequate to make more than two dozen sets of points with good statistical precision. The naive expectation that Δp_T^2 is linear with the nuclear radius i.e. with $A^{1/3}$, is seen to approximately hold, although the data for the heaviest nucleus (lead) appear to undershoot the linear behavior. This flattening behaviour suggests the possibility that the partonic-level multiple scattering presumed to cause the broadening does not continue uniformly through the largest nucleus. If this picture is correct, then the production length can be estimated from the data in a rather direct fashion, using the well-known nuclear densities and sizes.

In the right part of the Fig. 22 the preliminary x_B -dependence of the p_T broadening at CLAS is shown for positive pions. Note that the x_B range is different from HERMES. As can be seen, the x_B dependence is reasonably consistent for these two datasets, which are integrated over all other variables. The errors shown are statistical only; the CLAS data shown are not corrected for small effects due to acceptance or radiative processes.

3.5. Di-hadron correlations in nuclear DIS. –

In nuclear DIS, double-hadron leptonproduction on N , Kr and Xe relative to deuterium have been studied [24] via the ratio

$$(39) \quad R_{2h}(z_2) = \left(\frac{dN^{z_1>0.5}(z_2)/dz_2}{N^{z_1>0.5}} \right)_A \bigg/ \left(\frac{dN^{z_1>0.5}(z_2)/dz_2}{N^{z_1>0.5}} \right)_D ,$$

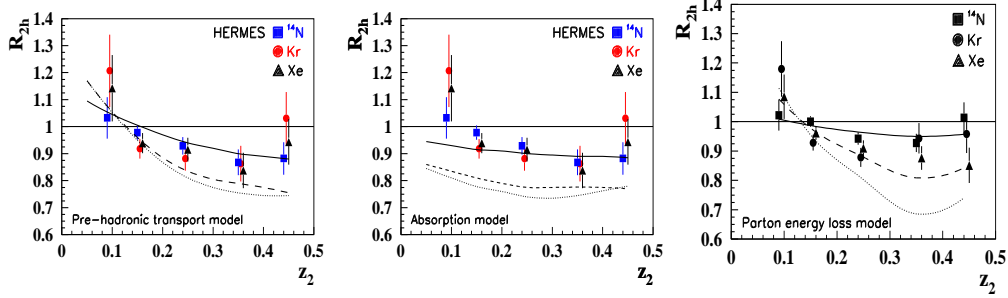


Fig. 24. – Double-ratio R_{2h} as a function of z_2 for ^{14}N (squares), Kr (circles) and Xe (triangles) with $z_1 > 0.5$, compared to various theoretical predictions (solid for ^{14}N , dashed for Kr and dotted for Xe): BUU prehadronic transport model [91] (left), hadron absorption model [91] (centre), parton energy loss calculations [92] (right).

where z_1 and z_2 correspond to the leading (largest z) and sub-leading (second largest z) hadrons, respectively. The quantity $dN^{z_1 > 0.5}$ is the number of events with at least two detected hadrons in a bin of width dz_2 at z_2 with $z_1 > 0.5$. The quantity $N^{z_1 > 0.5}$ is the number of events with at least one detected hadron with $z_1 > 0.5$. The label $A(D)$ indicates that the term is calculated for a nuclear (deuterium) target.

If partonic energy loss of the struck quark were the only mechanism involved, it would be naively expected that the attenuation effect does not depend strongly on the number of hadrons involved, and the double-hadron to single-hadron ratio for a nuclear target should be only slightly dependent on the mass number A . On the contrary, if final hadron absorption is the dominant process, the requirement of an additional slower sub-leading hadron that is more strongly absorbed would suppress the two-hadron yield from heavier nuclei [29], so that this ratio should decrease with A .

Results from HERMES are presented in Fig. 24, and show that the double-hadron ratio R_{2h} is generally below unity with no significant difference between the ^{14}N , Kr and Xe . The nuclear effect is much smaller than for the single-hadron attenuation measured under the same kinematic conditions. The displayed model computations, based on prehadron absorption [91] or parton energy loss [92, 93], can reproduce the general trend in z_2 of the data, but predict a significant A -dependence which is not seen in the data⁽³⁾.

The small nuclear effect and its relative independence on A may simply point toward a strong surface bias of the photon-hadron interaction point. Such a bias is very natural in NLO dihadron production, in which the virtual photon's hard scattering produces two partons with energy $\nu_{1,2} \leq \nu$, which independently hadronise with fractional momentum $\tilde{z}_{1,2} = z_{1,2}\nu_{1,2}/\nu$.

4. – Experimental results in hadron-nucleus collisions

4.1. Drell-Yan production. –

The production of dileptons with high invariant mass through the $q\bar{q} \rightarrow l^+l^-$ Drell-Yan (DY) process has been measured extensively in hadronic collisions, typically focusing on dilepton invariant masses between the charmonia and bottomonia masses ($4 \lesssim M_{l^+l^-} \lesssim 9 \text{ GeV}/c^2$) or

⁽³⁾ Alternative string model approaches to two-particle correlations are discussed in [94, 95].

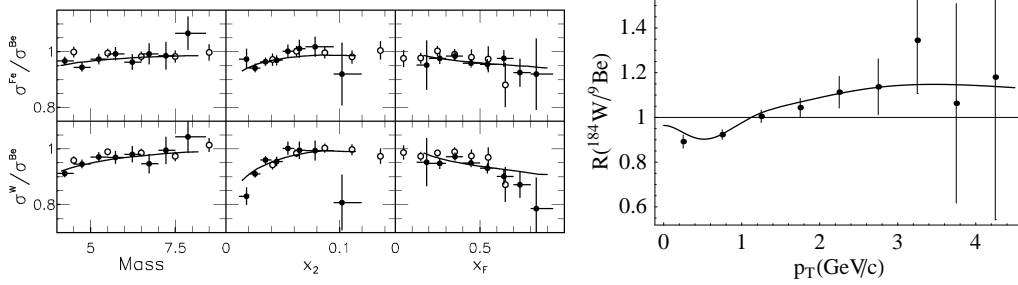


Fig. 25. – *Left*: Invariant mass, x_2 and x_F dilepton distributions in $p + Fe$ and $p + W$ scaled by that in $p + Be$ measured by E866/NuSea [100]. Solid curves are computations using the EKS98 shadowing parametrisation [101]. *Right*: p_T distribution in $p + ^{184}W$ normalised by $p + ^9Be$ measured by E772/E866 [100, 102] compared to the calculations of [103].

above ($M_{l+l-} \gtrsim 11 \text{ GeV}^2$) – see Refs. [96-98] for a review. NLO pQCD calculations describe well the experimental mass and transverse momentum distributions in hadronic collisions [99]. In hadron-nucleus collisions several nuclear effects are expected to modify the pQCD expectation of a linear dependence of the cross section with the mass number A (Eq. (2)). First of all, the modifications of parton densities in nuclei (nPDF) – such as shadowing at small parton fractional momentum $x \lesssim 10^{-2}$, or the EMC effect at large $x \gtrsim 0.1$ (see [20] for a recent review) – affect DY production in $h + A$ with respect to that in $h + p$ collisions. On top of nPDF effects, the projectile (anti)quark propagating through the nucleus may experience multiple scattering and lose some energy before the hard process takes place. In that sense, DY production data in $h + A$ collisions is particularly appropriate to study parton propagation in cold nuclear matter (see theoretical discussion in Section 6.3.3).

Drell-Yan lepton pairs have been measured in $p + A$ and $\pi^- + A$ collisions in fixed target experiments at the CERN SPS (NA3 [104], NA10 [105], NA38 [106]) and at Fermilab (E772 [102, 107], E866/NuSea [100] and older experiments [108]). The first measurements of DY production in nuclei were performed by the NA3 and NA10 collaborations using 150 GeV, 200 GeV and 280 GeV pion beams on fixed-target nuclei ($\sqrt{s_{NN}} = 16.5\text{--}23 \text{ GeV}$). NA3 reported on the nuclear dependence of DY production as a function of the longitudinal momentum-fraction of the incoming parton, x_1 [104], while NA10 measured the p_T -broadening of lepton pairs [105]. These data cover a phase-space range ($0.2 \lesssim x_1 \lesssim 0.9$) ideal to probe energy loss effects, even though the experimental uncertainties are quite large at the edge of phase space. Later, the Fermilab E772 experiment measured similarly DY production on various nuclear targets (D, C, Ca, Fe, W) as a function of x_F using the 800 GeV proton beam (i.e. $\sqrt{s_{NN}} = 38.7 \text{ GeV}$) [102]. More recently, the E866/NuSea collaboration reported on very high-statistics data in the same kinematical region of E772 and using Be, Fe , and W nuclear targets [100].

Although the total cross section was found to approximately scale with A and therefore shows no nuclear effects within the experimental uncertainties, more differential measurements such as mean transverse momentum or longitudinal momentum (or x_F) distributions actually exhibit a small, yet significant, nuclear dependence. Moreover, the data show p_T -broadening, also reported in hadron production in semi-inclusive lepton-nucleus DIS and hadron-nucleus collisions. Figure 25 shows the DY distribution ratios as a function of M , x_2 , x_F and p_T from the E866 [105] and E772 [102] experiments. At $x_F \gtrsim 0.2$, more than 90% of the DY cross-section is due to the scattering of a quark from the hadron with an *antiquark* from the nucleus. Hence the DY process, unlike DIS, yields direct information on the nuclear modifications of the antiquark distribution.

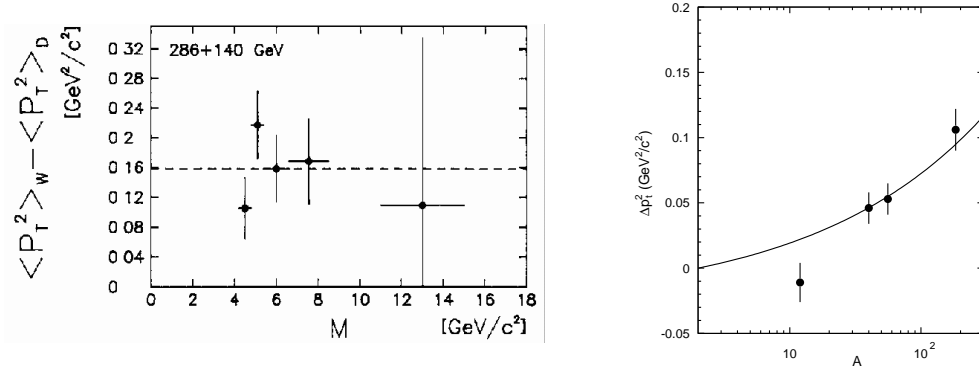


Fig. 26. – Transverse momentum broadening $\langle p_T^2 \rangle_W - \langle p_T^2 \rangle_D$ of Drell-Yan dileptons as a function of the invariant mass (NA10 dimuon data in $\pi + A$ collisions [105], *left*) and as a function of A (E772 $p + A$ data [96], *right*).

The experimental results show no nuclear enhancement of the \bar{q} distribution at moderate x_2 , contrary to the predictions of “pion cloud” models which explain the EMC effect in terms of nuclear enhancement of exchanged mesons [96, 109-111]. Unless a large quark energy loss compensates for the predicted antiquark enhancement, DY data put strong constraints on nuclear models describing the EMC effect [109-113]. At variance with the p_T -integrated ratios just discussed, the dilepton p_T -broadening is mostly sensitive to the parton rescattering dynamics in the target nucleus. Measurements from NA10 as a function of M and from E772 as a function of A are shown in Fig. 26. While no significant dependence on the DY mass is observed by NA10, the clear increase of the p_T -broadening with the atomic mass number in the E772 data is qualitatively consistent with initial-state parton scatterings.

4.2. High- p_T hadron production: “Cronin effect” . –

High-energy proton-nucleus collisions in fixed-target experiments at FNAL [8,9,114], SPS [115] and at HERA-B [116] have observed an enhancement of the single inclusive hadron production yield relative to proton-proton collisions for transverse momenta above $p_T \approx 1.5$ GeV/c (Fig. 27). Such a high- p_T enhancement, called “Cronin effect” [8,9], is evidenced by a nuclear modification factor that exceeds unity, and has also been observed in nDIS, see Figs. 16, 18 and 23 (right). The fact that $R_{pA} < 1$ below $p_T \approx 1$ GeV/c is simply because the incoherent binary scaling assumption behind Eq. (31), is not valid for soft particle production in hadronic collisions.

The HERA-B collaboration has recently studied the production of K_s^0 mesons and Λ^0 , $\bar{\Lambda}^0$ baryons in $p+C, Ti, W$ interactions at $\sqrt{s_{NN}} = 41.6$ GeV [116]. The Cronin effect is clearly observed for all three species for transverse momenta above $p_T \approx 1.5$ GeV/c (Fig. 28). The mass number dependence is parameterised as $\sigma_{pA} = \sigma_{pN} \cdot A^\alpha$ where σ_{pN} is the proton-nucleon cross section. The values of α are above one, in particular for the baryon species (Λ^0 , $\bar{\Lambda}^0$).

At RHIC, inclusive hadron production in minimum-bias deuteron-nucleus ($d + Au$) collisions at $\sqrt{s_{NN}} = 200$ GeV also features a small Cronin effect above $p_T = 1.5$ GeV/c at mid-rapidity (Fig. 29). The enhancement is smaller, or practically absent, in the case of mesons ($R_{dAu} \approx 1$) but is visible, of order $R_{dAu} \approx 1.4$, for baryons. The enhancement peaks in the range $p_T \approx 2.5$ –4 GeV/c, and then starts to decrease and disappears beyond 8 GeV/c, an observation also apparent

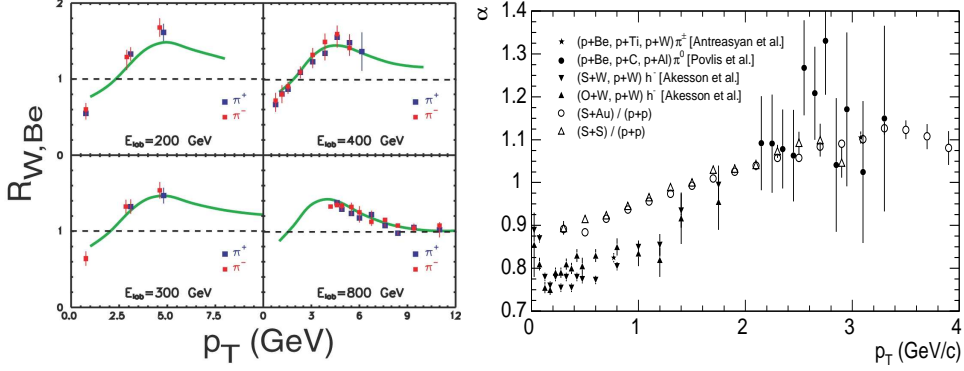


Fig. 27. – Cronin enhancement in high- p_T hadron production in proton-nucleus collisions at FNAL [8, 9, 114] (left) compared to the predictions of [117], and at FNAL and SPS [115] (right).

in the fixed-target data (Fig. 27). This peak structure is also progressively suppressed as the rapidity of the hadrons is increased [25, 118].

Such a transverse momentum broadening of high- p_T hadrons in hadron-nucleus collisions is usually interpreted (see Section 6.1) as due to either (i) multiple elastic scatterings of the incoming or outgoing parton inside the cold nuclear medium [117, 124], or (ii) recombination at the hadronisation stage of the scattered parton with other final state partons created in the collision [125, 126]. The larger Cronin effect for baryons than for mesons is naturally explained by the latter mechanism: the combination of three quark momenta boosts up the final baryon spectra more than the two-quark coalescence into mesons. The lower Cronin enhancement of all hadrons, in general, at RHIC centre-of-mass energies compared to fixed-target results can be explained by the steeper parton spectra at lower energies, which makes it easier to get a relatively larger boost for the same amount of k_T “kick”. The fast disappearance of the Cronin enhancement with increasing rapidities is well accounted for by models based on non-linear QCD evolution of the gluon densities in the nuclei [127-130]. The position of the maximum is thus connected to

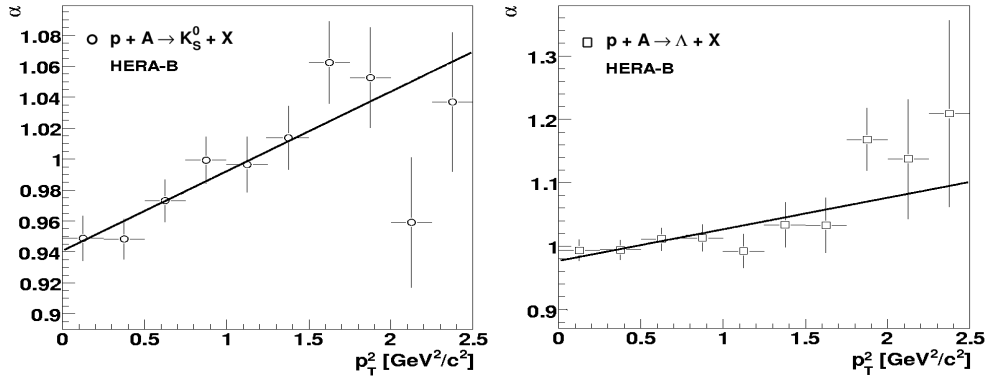


Fig. 28. – Cronin enhancement in high- p_T K_s^0 (left) and Λ (right) production in $p+A$ collisions measured by HERA-B at $\sqrt{s_{NN}} = 41.6$ GeV [116]. Note that $\alpha \approx 1.05$ corresponds to $R_{pA} = A^{\alpha-1} \approx 1.2$ for Ti or W (with $A = 22, 74$).

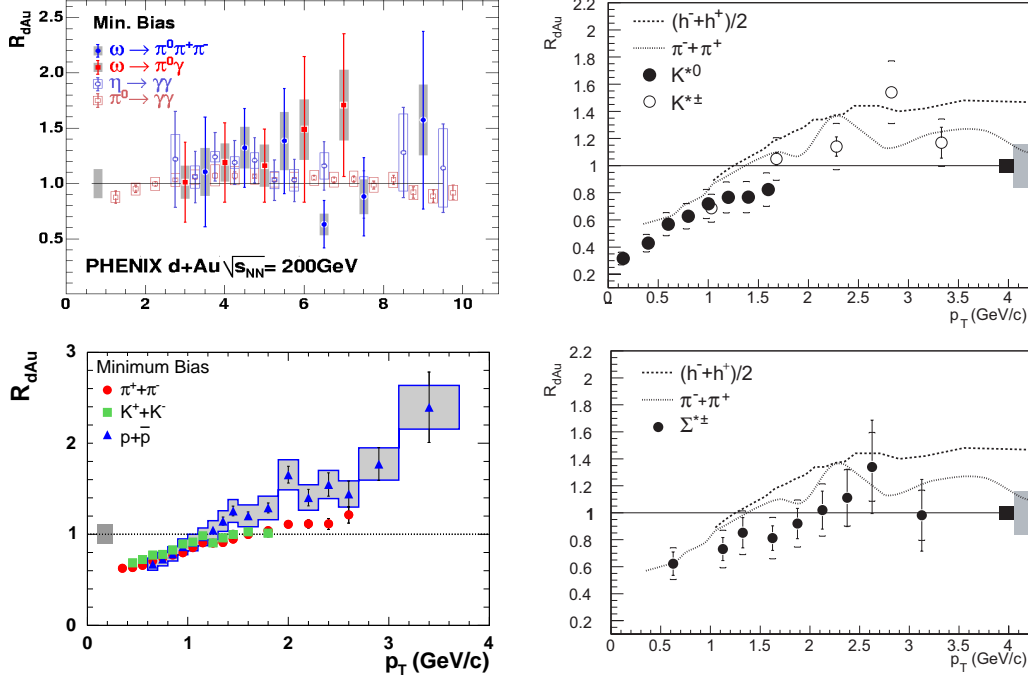


Fig. 29. – Nuclear modification factor $R_{dAu}(p_T)$ measured in $d + Au$ collisions at $\sqrt{s_{NN}} = 200$ GeV at RHIC. Mesons: π^0 , η and ω (PHENIX [119, 120], *top-left*), and charged pions and kaons (STAR [121], *top-right*). Hadrons: π^\pm , K^\pm and $p + \bar{p}$ (PHENIX [122, 123], *bottom-left*), and π^\pm , h^\pm , and Σ^\pm (STAR [121], *bottom-right*).

the rapidity-dependent value of the “saturation momentum” $Q_s(y)$ (see Section 6.1).

5. – Experimental results in nucleus-nucleus collisions

5.1. High- p_T hadron production . –

The production of hadrons at large transverse momentum has been since long proposed as a valuable “tomographic” probe of the hot and dense QCD matter produced in heavy-ion collisions [131]. If the final-state system is dense enough, the hard scattered partons will be attenuated while traversing it, resulting in a variety of “jet quenching” phenomena, e.g., suppression of leading hadron spectra [132], distortion of azimuthal correlations between back-to-back jets [133, 134], modifications of the energy-particle flow within the final jets [135, 136]. The study of these modifications provides valuable information on the (thermo)dynamical properties of the produced system such as the initial gluon density dN^g/dy , or the \hat{q} transport coefficient characterising the “scattering power” of the medium. A detailed recent review of jet quenching results and phenomenology can be found in [137]. Here we highlight the main findings.

The dominant contribution to the energy loss of partons is believed to be medium-induced gluon radiation as described in the Gyulassy–Lévai–Vitev (GLV) [138, 139] and Baier, Dokshitzer, Mueller, Peigné and Schiff (BDMPS) [140–142] (or LPCI [143]) formalisms (see Section 6.2). In the GLV approach, the initial gluon density dN^g/dy of the expanding plasma (with

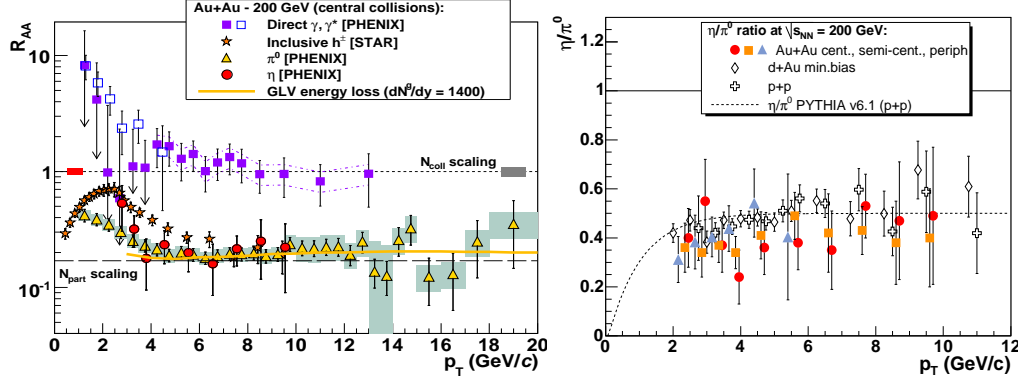


Fig. 30. – *Left*: $R_{AA}(p_T)$ in central $Au + Au$ collisions at $\sqrt{s_{NN}} = 200$ GeV for π^0 [120] and η [146] mesons, and for prompt γ, γ^* [147, 148], and h^\pm [149] compared to parton energy loss predictions in a medium with gluon densities $dN^s/dy = 1400$ (yellow curve) [150]. *Right*: η/π^0 ratios in $p + p$, $d + Au$ and $Au + Au$ collisions measured by PHENIX [147] compared to the PYTHIA prediction for $p + p$ (dashed line) [151].

original transverse area $A_\perp = \pi R_A^2 \approx 150 \text{ fm}^2$ and thickness L) can be estimated from the measured energy loss ΔE :

$$(40) \quad \Delta E \propto \alpha_s^3 C_R \frac{1}{A_\perp} \frac{dN^s}{dy} L,$$

where C_R is the Casimir colour factor of the parton ($4/3$ for quarks, 3 for gluons). In the BDMPS framework, the transport coefficient \hat{q} – characterising the squared average momentum transfer of the hard parton per unit path-length: $\hat{q} \equiv m_D^2/\lambda = m_D^2 \rho \sigma$, where m_D is the medium Debye mass, ρ its density, and σ the parton-matter interaction cross section – can be derived from the average energy loss via:

$$(41) \quad \langle \Delta E \rangle \propto \alpha_s C_R \langle \hat{q} \rangle L^2.$$

For example, for an equilibrated gluon plasma at $T = 0.4$ GeV with coupling $\alpha_s = 0.5$ – i.e. with density $\rho_g = 16/\pi^2 \zeta(3) \cdot T^3 \approx 15 \text{ fm}^{-3}$, Debye mass $m_D = (4\pi\alpha_s)^{1/2} T \approx 1 \text{ GeV}/c^2$, and LO perturbative cross section $\sigma_{gg} \approx 1.5 \text{ mb}$, one finds $\hat{q} \approx 2.2 \text{ GeV}^2/\text{fm}$ [144].

Experimentally, the standard method to quantify the medium effects on the yield of a large- p_T particle produced at rapidity y in a $A + A$ reaction is given by the nuclear modification factor $R_{AA}(p_T, y; b)$, see Eq. (31), which measures the deviation of hadron spectra in $A + A$ collisions at impact parameter b from an incoherent superposition of spectra in nucleon-nucleon collisions ($R_{AA} = 1$). If the $A + A$ and $p + p$ invariant spectra are both a power-law with exponent n , i.e. $1/p_T dN/dp_T \propto p_T^{-n}$, the fraction of energy lost $\epsilon_{loss} = \Delta p_T/p_T$, can be (grossly) estimated from R_{AA} via $\epsilon_{loss} \approx 1 - R_{AA}^{1/(n-2)}$ [145].

Among the RHIC highlights is the observation (Fig. 30, left) of a strong suppression of the products of parton fragmentation such as high- p_T neutral mesons (π^0 , η) [146, 152, 153] and charged hadrons [149, 154-156]. The $R_{AA} \approx 1$ perturbative expectation which holds above $p_T \approx 4 \text{ GeV}/c$ for other hard probes such as “colour blind” prompt photons [157, 158] (Fig. 30, left) or for mesons in $d + Au$ reactions (Fig. 29, top), is badly broken in central $Au + Au$ collisions where one measures $R_{AA} \approx 0.2$. The measured π^0 power-law spectral exponents of

$n \approx 8$ and the $R_{AA} \approx 0.2$ imply an average fractional energy loss of the high- p_T hadrons, of $\epsilon_{loss} \approx \Delta p_T / p_T \approx 0.2$ [145]. Such a significant suppression was not observed at SPS where – even after reevaluating the $p + p$ baseline spectrum [159, 160] – the central $Pb + Pb$ meson spectra show an R_{AA} around unity (Fig. 32). Yet, this does not exclude the possibility of energy loss at SPS, since the factor of the $\sim 50\%$ Cronin enhancement observed in $p + Pb$ at $\sqrt{s_{NN}} \approx 20$ GeV [161] likely compensates for the same amount of final-state suppression in the hot medium [159, 162] or in the cold nuclei [43].

As discussed next, most of the empirical properties of the suppression factor are in quantitative agreement with the results of the non-Abelian parton energy loss models presented in more detail in Section 6.2.

5.1.1. Magnitude of the suppression and medium properties. – The $Au + Au$ high- p_T suppression can be well reproduced by parton energy loss calculations in a very dense system with initial gluon rapidity densities $dN^g/dy \approx 1400$ (GLV curve in Fig. 30, left) [139], plasma temperatures $T \approx 0.4$ GeV (AMY model) [163], and time-averaged transport coefficients $\langle \hat{q} \rangle \approx 13$ GeV²/fm (PQM model in Fig. 31, left) [120, 164], or initial-time transport coefficients $\hat{q}_0 \approx 10 - 18$ GeV²/fm (ASW curve in Fig. 31, right).

The consistency between the extracted \hat{q} , dN^g/dy and T values in the various models has been studied e.g. in [137, 165, 166]. Whereas the agreement between the fitted thermodynamical variables dN^g/dy and T is good, the values of the transport parameter \hat{q} extracted from the data within the various models differ by factors of 2 – 3, and are much larger than the LO BDMPS estimate $\hat{q} \approx 2$ GeV²/fm at $T = 0.4$ GeV given before⁽⁴⁾. The discrepancy with the perturbative estimate is a factor $K = 3.6$ in the case of ASW [166] and an order of magnitude regarding the value extracted within PQM. At least part of the uncertainty is due to the relative insensitivity of the \hat{q} parameter to the irreducible presence of hadron from (unquenched) partons emitted from the surface of the plasma [167]. Although relating transport properties to thermodynamical quantities is model- (and medium-) dependent, an accord between the fitted \hat{q} and dN^g/dy values – via $\hat{q} = m_D^2 \rho \sigma$ with $\rho \propto dN^g/dy$ – can only be seemingly achieved for parton-medium cross-sections much larger than the $\sigma_{gg} = \mathcal{O}(1 \text{ mb})$ LO perturbative expectation. Such an observation lends support to the strongly-coupled nature of the QGP produced at RHIC [168]. It is however not satisfactory to obtain parameter values which are typically non-perturbative based on a purely perturbative framework, see e.g. the discussion in [144]. Additional constraints on \hat{q} can be placed by requiring also the model reproduction of the suppressed dihadron azimuthal correlations (see Section 5.3).

5.1.2. Universality of (light) hadron suppression. – Above $p_T \approx 5$ GeV/c, π^0 [153], η [147], and inclusive charged hadrons [149, 156] (dominated by π^\pm [156]) show all a common factor of ~ 5 suppression relative to the $R_{AA} = 1$ perturbative expectation which holds for hard probes, such as prompt photons, insensitive to final-state interactions [157] (Fig. 30, left). Such a “universal” hadron deficit is consistent with in-medium partonic energy loss of the parent quark or gluon prior to its fragmentation in the vacuum. The high- p_T π^0/η ratio is indeed found to be independent of the collision system (or centrality in $Au + Au$ collisions) within uncertainties (Fig. 30, right). Since both hadrons have similar valence quark content but very different masses (the η is four times heavier than the π^0), and different meson-nucleus cross sections, a natural explanation for the observation is that quenching happens at the parton level: the medium induced energy

⁽⁴⁾ It is also interesting to note that the BDMPS transport coefficient for cold nuclear matter $\hat{q}^{\text{cold}} \approx 0.6$ GeV/fm², extracted via Eq. (58) from hadron quenching in nDIS is also a factor 10 larger than the perturbative estimate $\hat{q}^{\text{cold}} \sim 0.05$ GeV/fm² discussed in Eq. (54).

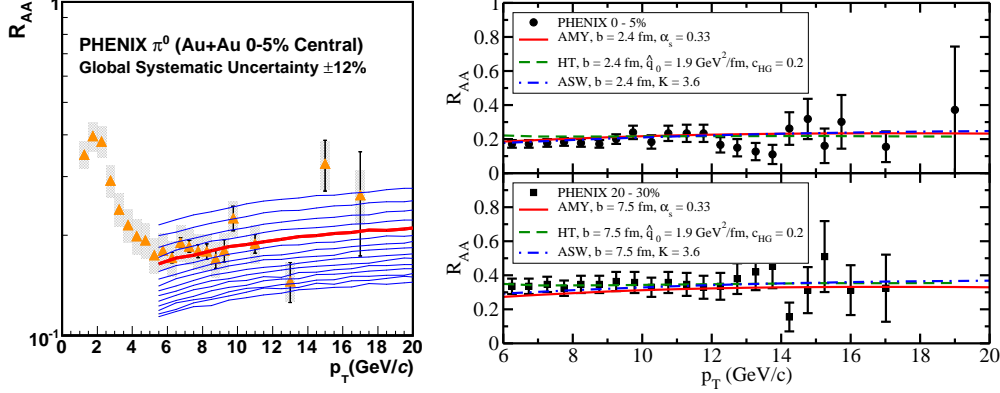


Fig. 31. – *Left*: $R_{AA}(p_T)$ for pions in central $Au + Au$ collisions (triangles) [120] compared to PQM predictions [164] for varying values of the \hat{q} coefficient (red curve, best fit for $\langle\hat{q}\rangle = 13 \text{ GeV}^2/\text{fm}$). *Right*: Central and semi-central pion suppression at PHENIX [120] compared to AMY, HT and ASW models within a common space-time evolution medium profile [166].

loss experienced by the parent parton is the same independently of the meson which is to be produced, and hadronisation occurs in vacuum, according to the same fragmentation functions extracted from e^+e^- and $p + p$ collisions.

5.1.3. Centre-of-mass energy dependence. – As one increases the collision energy in $A + A$ collisions, the produced medium reaches higher energy and particle densities, the system stays longer in the QGP phase, and correspondingly the traversing partons are more quenched. Figure 32 compiles the measured $R_{AA}(p_T)$ for high- p_T π^0 in central $A + A$ collisions at $\sqrt{s_{NN}} \approx 17.3$ and 200 GeV compared to parton energy loss calculations that assume the formation of a QGP with initial gluon densities $dN^g/dy \approx 400, 1400$ [139, 169] or, equivalently, averaged transport coefficients $\langle\hat{q}\rangle \approx 3.5, 13 \text{ GeV}^2/\text{fm}$ [164] respectively. Table VIII collects these results as well as those for central $Au + Au$ reactions at $\sqrt{s_{NN}} \approx 62$ and 130 GeV [152, 170]. For each collision energy the derived values for dN^g/dy are consistent with the final charged hadron density $dN_{ch}/d\eta$ measured in the reactions⁽⁵⁾. This is expected in an isentropic expansion process, where all the hadrons produced at midrapidity come directly from the original gluons released in the collision:

$$(42) \quad \frac{dN^g}{dy} \approx \frac{N_{tot}}{N_{ch}} \left| \frac{d\eta}{dy} \right| \frac{dN_{ch}}{d\eta} \approx 1.8 \cdot \frac{dN_{ch}}{d\eta} .$$

This relationship is relatively well fulfilled by the data as can be seen by comparing the fourth and fifth columns of Table VIII.

5.1.4. Transverse momentum dependence. – At RHIC top energies, the hadron quenching factor remains basically constant from 5 GeV/c up to the highest transverse momenta measured so far, $p_T \approx 20 \text{ GeV/c}$ (Fig. 30). As can be seen in Eq. (45), the suppression is roughly proportional to the z -slope of the fragmentation functions, $\partial D(z, Q^2)/\partial z$. Consequently, even though

⁽⁵⁾ The charged particle multiplicity itself follows a logarithmic dependence on the c.m. energy [171]: $dN_{ch}/d\eta \approx 0.75 \cdot (N_{part}/2) \cdot \ln(\sqrt{s_{NN}} [\text{GeV}]/1.5)$ (N_{part} is the number of participant nucleons in the collision).

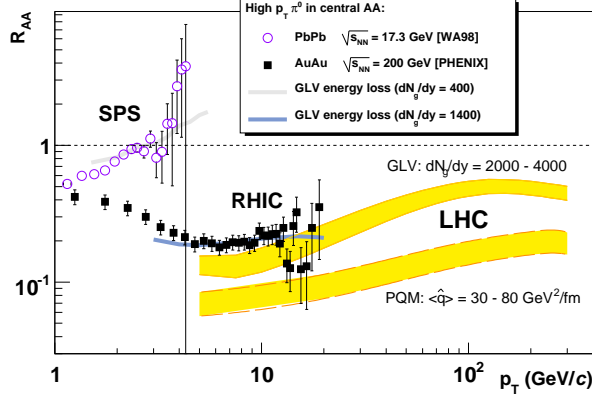


Fig. 32. – Nuclear modification factor, $R_{AA}(p_T)$, for high- p_T π^0 's at CERN-SPS [159, 160] and RHIC [120] compared to the predictions of the GLV parton energy loss model ($dN_g/dy = 400, 1400$) [139]. The bottom bands show the predicted R_{AA} for high- p_T charged hadrons in central $Pb + Pb$ collisions at $\sqrt{s_{NN}} = 5.5$ TeV as given by the GLV ($dN_g/dy = 2000-4000$) and the PQM ($\hat{q} \approx 30-80$ GeV²/fm) models [172].

the relative parton energy loss, ϵ/k_T , becomes smaller at higher p_T (leading naively to a smaller suppression and an increase of R_{AA} with p_T), the larger steepness of the partonic spectrum due to the restricted phase space to produce high- p_T partons at RHIC leads to a significant suppression even at large transverse momenta. Indeed, full calculations [139, 164, 167, 174] including the combined effect of (i) energy loss kinematics constraints, (ii) steeply falling p_T spectrum of the scattered partons, and (iii) $\mathcal{O}(20\%)$ p_T -dependent (anti)shadowing differences between the proton and nuclear parton distribution functions (PDFs), result in an effectively flat $R_{AA}(p_T)$ as found in the data. The much larger kinematical range opened at the LHC TeV-energies [172] will allow one to test the p_T -dependence of parton energy loss, and the associated radiation spectrum, over a much wider domain than at RHIC. As can be seen in Fig. 32 (yellow bands) the PQM model seemingly predicts a slower (and smaller) rise of $R_{AA}(p_T)$ than the GLV model.

5.1.5. Centrality (system-size) dependence. – The volume of the produced plasma in a heavy-ion collision can be “dialed” modifying the overlap area between the colliding nuclei either by selecting a given impact-parameter b – i.e. by choosing more central or peripheral reactions – or by colliding larger or smaller nuclei, e.g. Au ($A = 197$) versus Cu ($A = 63$). The relative energy

TABLE VIII. – Suppression factors measured in central $A + A$ collisions in the range $\sqrt{s_{NN}} \approx 20 - 200$ GeV, and initial gluon densities dN_g/dy [139, 169], and transport coefficients $\langle \hat{q} \rangle$ [164, 173] obtained from parton energy loss calculations reproducing the observed high- p_T π^0 suppression at each $\sqrt{s_{NN}}$. The measured charged particle densities at midrapidity, $dN_{ch}^{exp}/d\eta|_{\eta=0}$ [171], are also quoted.

	$\sqrt{s_{NN}}$ (GeV)	$R_{AA}(\pi^0, p_T \approx 4 \text{ GeV/c})$	$\langle \hat{q} \rangle$ (GeV ² /fm)	dN_g/dy	$dN_{ch}^{exp}/d\eta _{\eta=0}$
SPS	17.3	~ 1.0 [159, 160]	3.5	400	312 ± 21
RHIC	62.4	~ 0.4 [170]	7.	800	475 ± 33
RHIC	130.	~ 0.3 [152]	11	1000	602 ± 28
RHIC	200.	~ 0.2 [153]	13	1400	687 ± 37

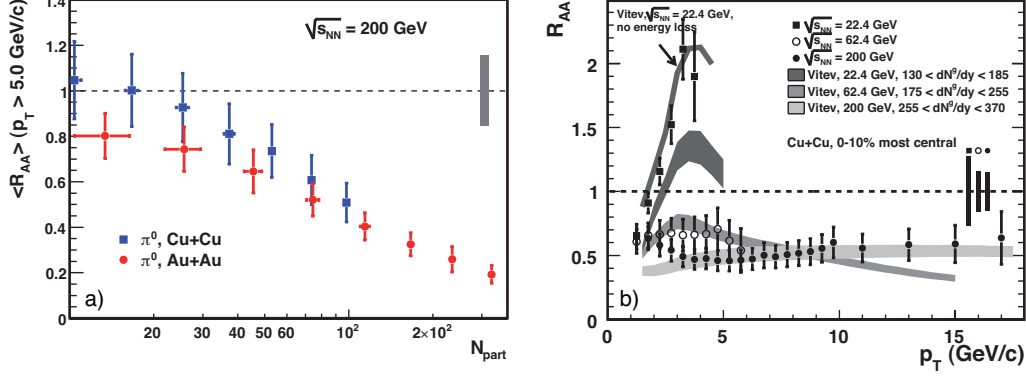


Fig. 33. – Left: Centrality (N_{part}) dependence of the high- p_T π^0 suppression in $Cu + Cu$ and $Au + Au$ at 200 GeV [175]. Right: $R_{AA}(p_T)$ for π^0 in central $Cu + Cu$ collisions at $\sqrt{s_{NN}} = 22.4, 62.4$ and 200 GeV compared to GLV calculations with initial gluon densities $dN^g/dy \approx 100 - 370$ [176].

loss depends on the effective mass number A_{eff} or, equivalently, on the number of participant nucleons in the collision N_{part} , as: $\Delta E/E \propto A_{eff}^{2/3} \propto N_{part}^{2/3}$ [164, 177]. The measured $R_{AA}(p_T)$ in central $Cu + Cu$ at 22.4, 62.4, and 200 GeV [176] is a factor of $(A_{Au}/A_{Cu})^{2/3} \approx 2$ lower than in central $Au + Au$ at the same energies (Fig. 33, right). Yet, for a comparable N_{part} value, the suppression in $Au + Au$ and $Cu + Cu$ is very similar (Fig. 33, left). Fitting the N_{part} dependence to $R_{AA} = (1 - \kappa N_{part}^\alpha)^{n-2}$ yields $\alpha = 0.56 \pm 0.10$ [120], consistent also with parton energy loss calculations [164, 177].

5.1.6. Path-length dependence. – The analytical quadratic dependence of the energy loss on the thickness of a *static* medium L , Eq. (41), becomes effectively a linear dependence on the *initial* value of L when one takes into account the expansion of the plasma, see Eq. (40). Experimentally, one can test the dependence of parton suppression on the plasma thickness (L) by exploiting the spatial asymmetry of the system produced in non-central nuclear collisions. Partons produced “in plane” (“out-of-plane”) i.e. along the short (long) direction of the ellipsoid matter with eccentricity ϵ will comparatively traverse a shorter (longer) thickness. PHENIX has measured the high- p_T neutral pion suppression as a function of the angle with respect to the reaction plane, $R_{AA}(p_T, \phi)$ [145, 178]. Each azimuthal angle ϕ can be associated with an average medium path-length L_ϕ via a Glauber model. The energy loss is found to satisfy the expected $\Delta E \propto L$ dependence, Eq. (40), above a “threshold” length of $L \approx 2$ fm, interpreted in [179] as due to a geometric “corona” effect.

5.1.7. Non-Abelian (colour factor) dependence. – The amount of energy lost by a parton in a medium is proportional to its colour Casimir factor: $C_A = 3$ for gluons, $C_F = 4/3$ for quarks. Asymptotically, the probability for a gluon to radiate another gluon is $C_A/C_F = 9/4$ times larger than for a quark and thus g -jets are expected to be more quenched than q -jets in a QGP. One can test such a genuine non-Abelian property of QCD energy loss by measuring hadron suppression at a fixed p_T for increasing c.m. energy [173, 180]. At large (small) x , the PDFs are dominated by valence-quarks (low- x gluons) and consequently hadroproduction will be dominated by quark (gluon) fragmentation. Figure 34 (left) shows the R_{AA} for 4-GeV/c pions measured at SPS and RHIC compared to two parton energy loss curves [180]. The lower (upper) curve shows the expected R_{AA} assuming a normal (arbitrary) behaviour with $\Delta E_g/\Delta E_q = 9/4$

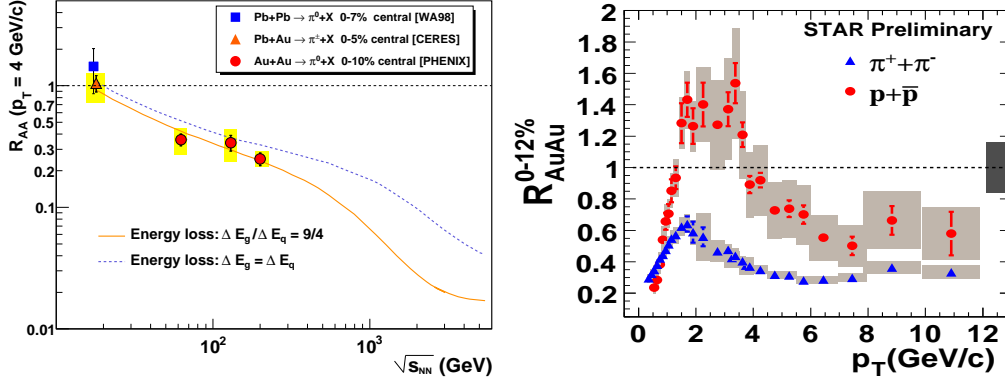


Fig. 34. – *Left*: Excitation function of the nuclear modification factor, $R_{AA}(\sqrt{s_{NN}})$, for π^0 in central AA reactions at a fixed $p_T = 4$ GeV/c [173], compared to non-Abelian (solid) and “non-QCD” (dotted) energy loss curves [180]. *Right*: $R_{AA}(p_T)$ for pions and (anti)protons in central Au + Au at $\sqrt{s_{NN}} = 200$ GeV [181].

($\Delta E_g = \Delta E_q$). The experimental high- p_T π^0 data supports the expected colour-factor dependence of $R_{AA}(\sqrt{s_{NN}})$ [173].

A second test of the colour charge dependence of hadron suppression has been proposed based on the fact that gluons fragment comparatively more into (anti)protons than quarks do. One would thus naively expect $R_{AA}^{p,\bar{p}} < R_{AA}^{\pi}$. The STAR results (Fig. 34, right) are however seemingly at variance with this expectation: pions appear more suppressed than protons at high- p_T [181]. Yet, the use of (anti)protons as a reference for perturbative particle production is questionable. First, it is worth reminding that the assumption of production from parton fragmentation in vacuum may well not hold for protons which have estimated formation time-scales a factor ~ 5 shorter than for pions (Table VI). Second, p, \bar{p} are already found to be Cronin-enhanced in $d + Au$ compared to $p + p$ collisions by a factor $\sim 50\% - 100\%$ (see Fig. 29 bottom-left) for p_T ’s as large as 7 GeV/c [182]. It is likely that there is an extra mechanism of baryon production, based e.g. on in-medium quark coalescence [183-185] (see Section 6.1), which compensates for the energy loss suffered by the parent partons. Finally, another explanation has recently been proposed in Ref. [186]: protons could be produced in a compact colour-singlet configuration (through higher-twist processes) and therefore, because of colour transparency, escape more easily the dense medium than pions do.

5.2. Heavy flavour production . –

As seen in the previous Section, most of the empirical properties of the quenching factor for light-flavour hadrons – magnitude, p_T -, centrality-, $\sqrt{s_{NN}}$ - dependences of the suppression – are in quantitative agreement with the predictions of non-Abelian parton energy loss models. A robust prediction of radiative energy loss models is the hierarchy $\Delta E_{\text{heavy-Q}} < \Delta E_{\text{light-q}} < \Delta E_g$: gluons, which fragment predominantly into light hadrons, are expected to lose more energy than quarks because of the larger color coupling to the radiated gluon; whereas massive c, b quarks are expected to lose less energy than light quarks due to a suppression of small-angle gluon radiation already in the vacuum (“dead-cone” effect) [187, 188]. Grossly, the in-medium radiative energy loss is suppressed by a factor $\mathcal{O}(m_D/M_Q)$ (where $m_D \sim 1$ GeV/c² is the medium Debye mass) [189], i.e. it is a factor about 25% (75%) less for a charm (bottom) quark than for a

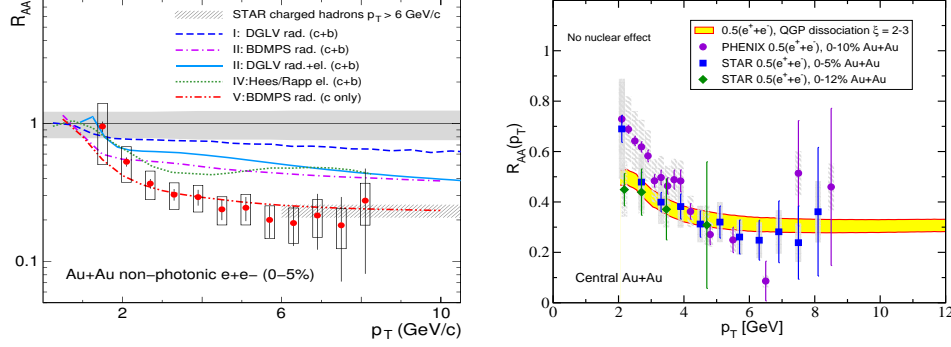


Fig. 35. – Nuclear modification factor R_{AA}^e of heavy-quark decay electrons in central $Au + Au$ collisions at $\sqrt{s_{NN}} = 200$ GeV [190, 191] compared to various radiative+elastic energy loss models for c and b quarks (left) and to a model of heavy-meson (D , B) dissociation in a plasma (right) [30].

light-quark.

Yet, RHIC measurements [190-192] of high- p_T electrons from the semi-leptonic decays of D - and B -mesons (Fig. 35) indicate the same suppression factor for light and heavy mesons: $R_{AA}(Q) \sim R_{AA}(q, g) \approx 0.2$. In order to reproduce the high- p_T open charm/bottom suppression, jet quenching models require either initial gluon rapidity densities $dN^g/dy \approx 3000$ [193] which are inconsistent with the total hadron multiplicities, see Eq. (42), as well as with the $dN^g/dy \approx 1400$ needed to describe the quenched light hadron spectra. Various explanations have been proposed to solve this ‘heavy flavor puzzle’ (see e.g. [194, 195]).

- First, precise comparisons between theory and data require a better determination of the relative contribution of the c and b quarks to the measured non-photon electron yields [193, 196]. If only c quarks (roughly three times more suppressed than the heavier b quarks) actually contributed to the measured high- p_T decay electron spectrum, then one would indeed expect $R_{AA}(c) \approx 0.2$ [197]. However, indirect measurements from PHENIX [198] and STAR [199] have confirmed the similar production yields of e^\pm from D and B decays above $p_T \approx 5$ GeV/c predicted by next-to-leading-log pQCD [196, 200];
- The second mechanism points to an additional contribution from elastic (i.e. non-radiative) energy loss for heavy-quarks [201, 202] which was considered negligible so far [132]. Recent works [203-206] have shown that a proper evaluation of the QCD running coupling substantially increases the amount of collisional energy loss suffered by the heavy-quarks. ΔE_{coll} can indeed be a significant contribution for heavy quarks (see ‘rad.+el.’ curves in Fig. 35, left);
- Two works [207, 208] have argued that in a plasma the large charm-quark coalescence into Λ_c baryons (with a small semileptonic decay branching ratio) would deplete the number of open-charm mesons, and correspondingly reduce the number of decay electrons, compared to $p + p$ collisions;
- The assumption of vacuum hadronisation (after in-medium radiation) implicit in all parton energy loss formalisms may well not hold in the case of a heavy quark. The discussed quark-hadronisation time estimates (see Section 2.4) are inversely proportional to the mass m_h of the final produced hadron: the heavier the hadron, the fastest it is formed. From Eq. (35), one can see that in the rest frame of the hot QCD medium of the fragmenting

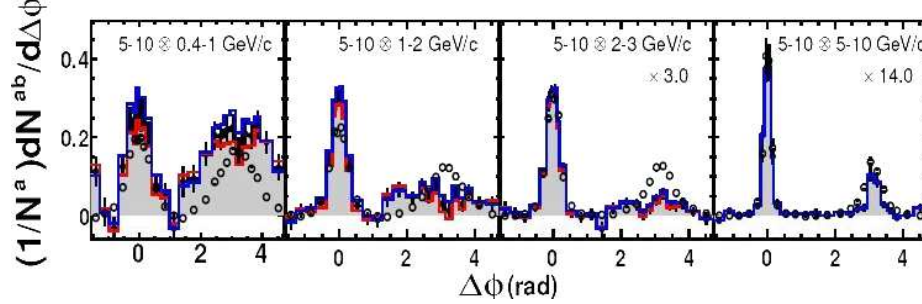


Fig. 36. – Comparison of the azimuthal di-hadron correlation $dN_{pair}/d\Delta\phi d\eta$ for $p + p$ (open symbols) and central $Au + Au$ (histograms) at $\sqrt{s_{NN}} = 200$ GeV for $p_T^{trig} = 5-10$ GeV/c and increasingly smaller (right to left) values of p_T^{assoc} [211].

heavy-Q, the formation time of D - and B -mesons [30] is of order⁽⁶⁾ $\langle t_h \rangle \approx 0.4 - 1$ fm, respectively. Thus, one may need to account for both the energy loss of the heavy-quark as well as the possible dissociation of the heavy-quark meson inside the QGP. The expected amount of suppression in that case is larger and consistent with the data (Fig. 35, right).

5.3. High- p_T di-hadron correlations . –

At leading order, the parton-parton $2 \rightarrow 2$ scatterings are balanced in p_T i.e. they are back-to-back in azimuthal angle, $\Delta\phi = \pi$, modulo some smearing due to the partons intrinsic transverse momentum. Such azimuthal correlation is smeared out if one or both partons suffer rescatterings inside the plasma. The dijet-acoplanarity arising from the interactions of a parton in an expanding QGP is $\langle k_T^2 \rangle_{med} \simeq (m_D^2/\lambda)L \ln(L/\tau_0) \propto \hat{q}L$ [209] and, thus, the final azimuthal correlations between the hadrons issuing from the fragmentation of quenched partons will show a dependence on the transport coefficient and thickness of the medium: $d^2N_{pair}/d\Delta\phi = f(\hat{q}, L)$. Jet-like correlations in heavy-ion collisions have been measured on a statistical basis by selecting a high- p_T trigger particle and measuring the azimuthal ($\Delta\phi = \phi - \phi_{trig}$) and pseudorapidity ($\Delta\eta = \eta - \eta_{trig}$) distributions of its associated hadrons ($p_T^{assoc} < p_T^{trig}$): $C(\Delta\phi, \Delta\eta) = \frac{1}{N_{trig}} \frac{d^2N_{pair}}{d\Delta\phi d\Delta\eta}$. In $p + p$ collisions, a dijet signal appears as two distinct back-to-back Gaussian-like peaks at $\Delta\phi \approx 0$, $\Delta\eta \approx 0$ (near-side) and at $\Delta\phi \approx \pi$ (away-side). At variance with such a topology, early STAR results [210] showed a monojet-like topology with a complete disappearance of the opposite-side peak for $p_T^{assoc} \approx 2 - 4$ GeV/c.

Fig. 36 shows the increasingly distorted back-to-back azimuthal correlations in high- p_T triggered central $Au + Au$ events as one decreases the p_T of the associated hadrons (right to left). Whereas, compared to $p + p$, the near-side peak remains unchanged for all p_T 's, the away-side peak is only present for the highest partner p_T 's but progressively disappears for less energetic partners [211,212]. The correlation strength over an azimuthal range $\Delta\phi$ between a trigger hadron h_t and a partner hadron h_a in the opposite azimuthal direction can be constructed as a function of

⁽⁶⁾ Note that in the laboratory system there is an extra Lorentz boost factor: $\tau_{lab} = \gamma_Q \cdot \tau_{form}$.

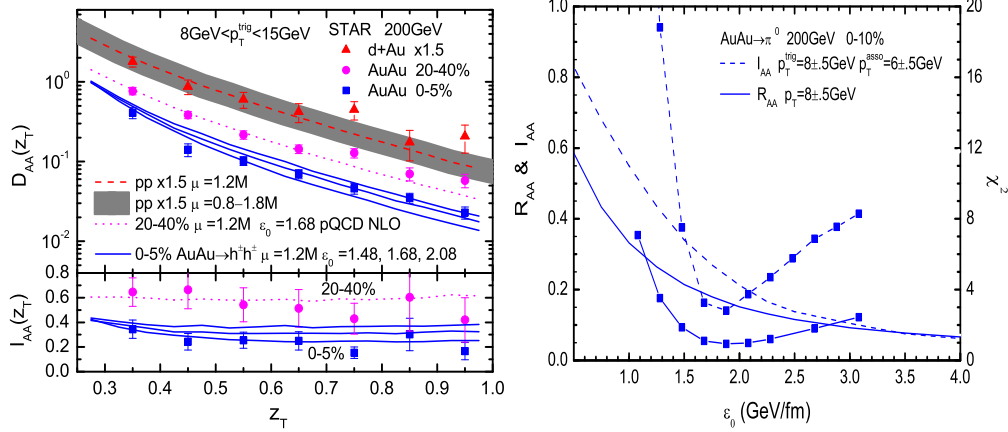


Fig. 37. – *Left*: $D_{AA}^{away}(z_T)$ distributions for $d + Au$ and $Au + Au$ and $I_{AA}(z_T)$ ratio for central $Au + Au$ at 200 GeV [214], compared to HT calculations for varying ϵ_0 energy losses [213]. *Right*: Data vs. theory χ^2 values for the fitted ϵ_0 parameter [213].

the momentum fraction $z_T = p_T^{assoc}/p_T^{trig}$ via a “pseudo-fragmentation function”:

$$(43) \quad D_{AA}^{away}(z_T) = \int dp_T^{trig} \int dp_T^{assoc} \int_{\Delta\phi > 130^\circ} d\Delta\phi \frac{d^3\sigma_{AA}^{h_i h_a}/dp_T^{trig} dp_T^{assoc} d\Delta\phi}{d\sigma_{AA}^{h_i}/dp_T^{trig}}.$$

shown in Fig. 37 (top-left) compared to various values of the ϵ_0 parameter characterising the amount of energy loss [213] (see the Higher-Twist model discussion in Section 6.2.1). Similarly to $R_{AA}(p_T)$, the magnitude of the suppression of back-to-back jet-like two-particle correlations can be quantified with the ratio $I_{AA}(z_T) = D_{AA}(z_T)/D_{pp}(z_T)$. I_{AA}^{away} is found to decrease with increasing centrality, down to about 0.2 – 0.3 for the most central events (Fig. 37, bottom-left) [210, 214].

The right plot of Fig. 37 shows the best $\epsilon_0 \approx 1.9$ GeV/fm energy loss value that fits the measured R_{AA} and I_{AA} factors. Due to the irreducible presence of (unquenched) partons emitted from the surface of the plasma, the single-hadron quenching factor $R_{AA}(p_T)$ is in general less sensitive to the value of ϵ_0 than the dihadron modification ratio $I_{AA}(z_T)$. The combination of $R_{AA}(p_T)$ and $I_{AA}(z_T)$ provides more robust quantitative information on the medium properties.

Since energy and momentum are conserved, the “missing” fragments of the away-side (quenched) parton at intermediate p_T ’s should be either shifted to lower energy ($p_T \lesssim 2$ GeV/c) and/or scattered into a broadened angular distribution. Both, softening and broadening, are seen in the data when the p_T of the away-side associated hadrons is lowered (see two leftmost panels of Fig. 36). As a matter of fact, the away-side hemisphere shows a very unconventional double-hump angular distribution with a “dip” at $\Delta\phi \approx \pi$ and two neighbouring local maxima at $\Delta\phi \approx \pi \pm 1.1 - 1.3$. Such a “volcano”-like profile has been interpreted as due to the preferential emission of energy from the quenched parton at a finite angle with respect to the jet axis. This could happen in a purely radiative energy loss scenario due to large-angle radiation [215], but more intriguing explanations have been put forward based on the dissipation of the lost energy into a collective mode of the medium in the form of a wake of lower energy gluons [216] with Mach- [217, 218] or Čerenkov-like [219, 220] angular emissions assuming that the hard parton velocity exceeds the speed of sound or speed of light, respectively, of the QCD medium. Theoretically, it is

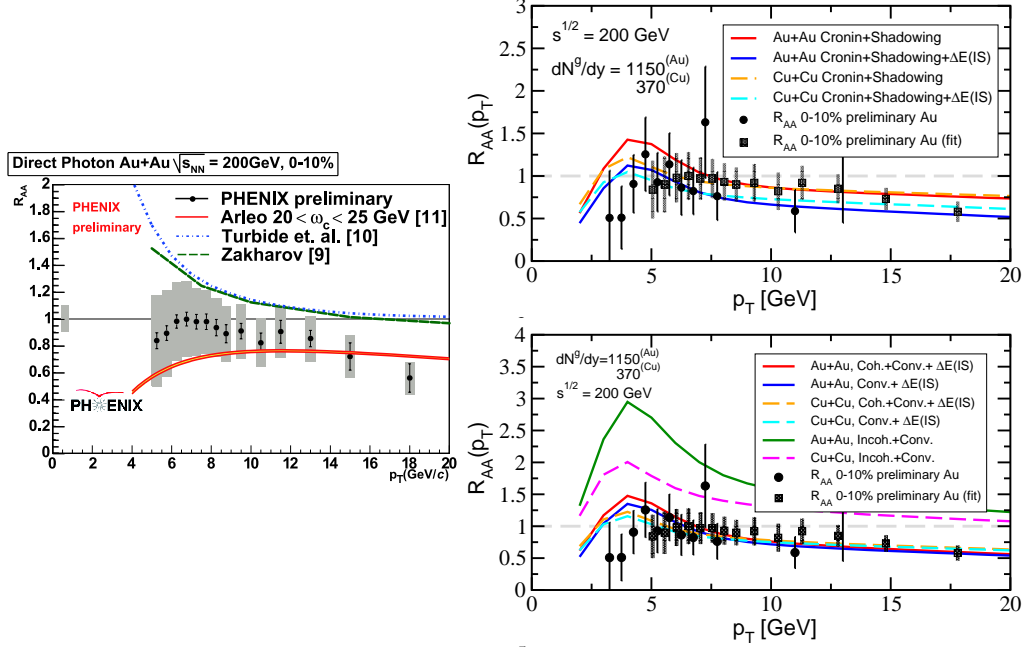


Fig. 38. – Prompt photon spectrum compared to preliminary PHENIX data. *Left*: Spectrum computed in Refs. [222–224]. Plot taken from Ref. [225]. *Right*: Spectrum computed in the GLV formalism including a variety of effects. Plots taken from Ref. [226].

unclear if such partonic collective wake(s) and cone survive both hadronisation and the final hadronic freeze-out [221]. More involved studies, e.g., accounting for the plasma expansion and the hadronic phase evolution, are needed before a final conclusion can be reached.

5.4. High- p_T photon production . –

Photon production in cold and hot QCD media is a particularly interesting probe because, unlike the gluon, photons can escape without final-state interactions, therefore carrying information about the medium at the location of its production. Moreover, it avoids the ambiguities related to the hadronisation process, so that it is in principle a cleaner probe of the underlying dynamics. However, several mechanisms proposed over the last few years showed that prompt photon production could actually be somehow affected by the quark-gluon plasma formation in heavy-ion collisions, and in principle by cold nuclear matter as well.

First, prompt photons are also produced from the collinear fragmentation of quarks and gluons produced in the hard process. Such fragmentation photons are thus sensitive to energy loss of their parent fragmenting parton. The formation time needed to produce such a photon-parton system with a small invariant mass exceeds by far the typical lifetime of the hot medium: the multiple scattering of the hard parton in the medium is followed on a much larger time-scale by the parton-to-photon fragmentation process in the vacuum. Consequently, one expects that those “fragmentation” photons should be as quenched, at least qualitatively, as the hadron yield [222, 227, 228].

Second, the multiple scattering incurred by the hard partons traversing the produced medium induces the emission of soft gluons – leading to the usual “jet quenching” – as well as soft

photons [163, 224, 229] (although with a probability in principle governed by the much smaller α_{em}). Within a path-integral picture for the parton energy loss mechanism [143, 230], Zakharov computed this medium-induced photon bremsstrahlung contribution at RHIC [231]. The enhancement of photon production is particularly noticeable in the moderate $p_{T\gamma}$ range, say below 20 GeV, raising hopes that it could be measured. It has also been proposed that large p_T partons may couple to the thermal quarks and gluons in the medium through Compton scattering or $q\bar{q}$ annihilation. This so-called jet-photon conversion mechanism, [232], would enhance the production of photons, leading to a nuclear production ratio, R_{AA} , larger than one. Each one of these individual mechanisms, with opposing (quenching and enhancement) effects, is unfortunately under poor theoretical control and the medium effects on (prompt) photon production still remain rather model-dependent.

Experimentally, the photon quenching factor has been measured at RHIC by the PHENIX collaboration, up to large $p_T \approx 20$ GeV/c [225]. Despite the still rather large error bars of those preliminary data, it seems that the prompt photon R_{AA} is consistent with unity in the range $p_T \approx 4\text{--}15$ GeV/c, while a suppression is reported, $R_{AA} \approx 0.6$, in the highest p_T bin. Therefore it appears that the photon enhancement predicted either due to parton multiple scattering [224] or jet-photon conversion [232] is not seen at RHIC. The BDMPS energy loss calculation, Ref. [228], supplemented by the proper treatment of protons and neutrons in the Au nuclei (leading to a suppression at large p_T due to smaller electric charge of d compared to u valence quarks), is on the contrary able to reproduce the shape and magnitude of the PHENIX data.

6. – Parton propagation and energy loss

6.1. *In-medium parton propagation and the Cronin effect* . –

The Cronin effect is the enhancement of single inclusive hadron production at intermediate p_T 's ($p_T \approx 1\text{--}8$ GeV/c) observed in hadroproduction in $e + A$ (Fig. 18) and $h + A$ (Fig. 27) collisions, as well as in Drell-Yan events (Fig. 25, right). Theoretically, such an effect has been usually explained in terms of initial- or final-state multiple scattering of the parton prior to its fragmentation leading to a broadening of the transverse momentum of the produced hadrons [124]. More recently, a modification of the hadronisation mechanism due to the recombination of the scattered parton with other partons produced in the collision has been proposed [125, 126] and accounts for the experimental data as well [233]. We review here both theoretical interpretations of the Cronin enhancement.

6.1.1. *Parton multiple scatterings.* – Parton multiple scatterings have been discussed in the pQCD factorisation formalism, in the colour dipole model and in the Colour Glass Condensate approach. We briefly review their main features, similarities and differences.

- Glauber-Eikonal models.

The Glauber-Eikonal (GE) approach [49, 234–237] to the Cronin effect treats multiple $2 \rightarrow 2$ partonic collisions in collinearly factorised pQCD. The cross-section for the production of a hadron with transverse momentum p_T and rapidity y in $h + A$ collisions at fixed impact

parameter b is written as [49]

$$(44) \quad \frac{d\sigma_h}{d^2p_T dy d^2b} = \sum_i \phi_{i|h} e^{-\sigma_{iN} T_A(b)} \otimes D_{i \rightarrow h} \otimes \sum_{n=1}^{\infty} \frac{1}{n!} \int d^2b d^2k_1 \cdots d^2k_n \delta\left(\sum_{j=1,n} \vec{k}_j - \vec{p}_T\right) \frac{d\sigma_{iN}}{d^2k_1} T_A(b) \times \cdots \times \frac{d\sigma_{iN}}{d^2k_n} T_A(b)$$

where the crossed-circle symbols denote appropriate integrations and summations over parton flavours i and j , $\phi_{i|h}$ are the PDFs in the projectile hadron, $d\sigma_{iN}$ is the cross section for a parton i scattering on a nucleon and $T_A(b)$ the A nucleus thickness function at impact parameter b (see Ref. [49] for details). At moderate p_T , the accumulation of transverse momentum due to multiple scatterings leads to an enhancement of transverse momentum spectra, and to a suppression of the low- p_T region due to energy-momentum conservation. At high p_T the binary scaled $p + p$ spectrum is recovered: no high- p_T suppression is predicted in this approach, except as a consequence of the nuclear modifications of PDFs. In early applications, the GE series (44) has been directly evaluated only up to the $n = 3$ parton scatterings, under severe approximations, and only for $\sqrt{s} \leq 40$ GeV [114, 234, 235]. Instead of evaluating the full GE series, other approximated GE models modify the pQCD rates through the inclusion of a phenomenological nuclear broadening of the intrinsic parton momentum k_T [139, 238-240], ignoring however the unitarity constraints built into the GE multi-scatterings. The GE series is directly computed via a numerical convolution of elementary parton-nucleon processes, assuming a decoupling of the transverse and longitudinal kinematics in Refs. [49, 162, 241], and with exact energy-momentum conservation up to 3 scatterings in Ref. [242].

The formulation preserves unitarity and is directly constrained to reproduce the absolute normalised spectra in $p + p$ collisions, and quantitatively incorporates kinematic phase-space limitations at large p_T . Thus, the p_T -broadening is computed without adjustable parameters, rather than assumed as an input. Midrapidity pion production data at $\sqrt{s_{NN}} = 20 - 200$ GeV can be well described (Fig. 39 left), but the large hadron suppression reported at forward rapidity at RHIC [243, 244] (Fig. 39 right) can be reproduced only within gluon saturation approaches [245, 246] or using extreme nuclear shadowing parametrisations [247].

- The colour dipole model

In Ref. [117, 249], the GE series is formulated in terms of the multiple scattering of a colour dipole on the nuclear target. The colour dipole cross section is determined phenomenologically by fits to lepton-proton and proton-proton scattering data [250, 251], and hadron production is determined from the overlap of the nuclear broadened dipole wave function with the hadron light-cone wave function. The computation of nuclear effects is carried out with no tunable parameters, and leads to a good description of midrapidity pion data (Fig. 27 left). This model allows for the inclusion of coherent multiple scattering [117], relevant at RHIC to LHC energies, and is equivalent to the GE model in the incoherent scattering limit. It can also describe in a unified formalism the p_T -broadening of DY lepton pairs [103, 252] and that of hadrons produced nDIS [29] (see Section 7.3). This approach also allows for a description of the forward rapidity hadron suppression at RHIC due to energy conservation and Sudakov suppression at the edge of the phase space, alternative to gluon saturation [253, 254]. Hadron suppression is predicted at forward rapidity also for lower energy collisions, $\sqrt{s_{NN}} = 63$ or 130 GeV, where gluon saturation

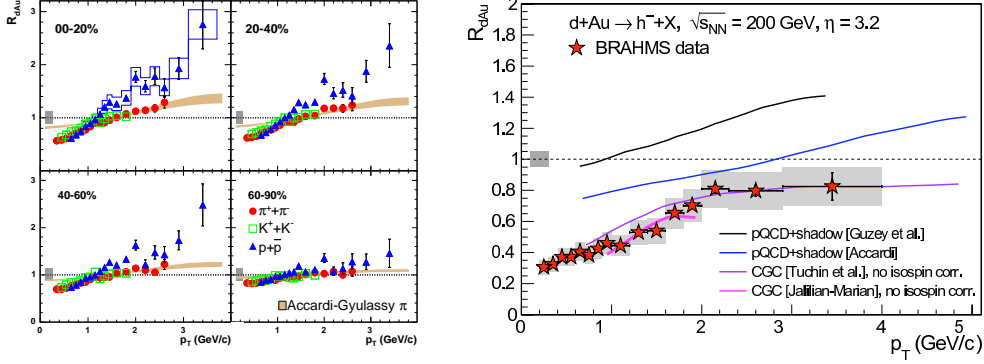


Fig. 39. – *Left*: GE multi-scattering computation [124] of neutral pion $R_{dAu}(p_T)$ at midrapidity in different centrality bins compared to PHENIX data at $\sqrt{s_{NN}} = 200$ [122]. Plot taken from Ref. [122]. *Right*: BRAHMS data on negatively charged hadron $R_{dAu}(p_T)$ at $\eta = 3.2$ compared to several models. From top to bottom: pQCD computation supplemented by nuclear shadowing effects by Guzey *et al.* [50]; GE model computation by Accardi *et al.* [124]; CGC model computations by Tuchin *et al.* [245] and by Jalilian-Marian [246]. Plot from Ref. [248].

effects are not expected to play a major role because of the rather large x_2 probed at these energies.

- Colour Glass Condensate

The Colour Glass Condensate (CGC) is an effective theory for the gluon field in hadron and nuclei at small x , see Ref. [255] for a recent review. At low- x the gluon occupation number is so large that the gluon field can be treated semi-classically and computed as a solution of the Yang-Mills equation of motion in the presence of random colour sources. Gluons with momenta lower than a scale Q_s are in the “saturation” regime with a density high enough that $2 \rightarrow 1$ gluon-gluon fusion processes limit a further growth; on the contrary at larger momenta the gluon field is in the DGLAP “dilute” regime. An intermediate “geometric scaling window” extends at momenta $Q_s < p_T < Q_s^2/Q_0$, where quantum effects from the saturation region further modify the evolution from the perturbative to the saturation region. Observables are computed as an average over the colour sources density ρ with a weight $W_y[\rho]$, depending on the gluon rapidity $y = \log(1/x)$. The quantum evolution of the gluon field with y is captured by the non-linear JIMWLK evolution equation [256-260]. Using a Gaussian approximation for the weight W , known as McLerran-Venugopalan model, gluon production in $p + A$ collision can be interpreted as multiple $2 \rightarrow 1$ partonic scatterings [261]. A comparison to the $2 \rightarrow 2$ multiple scatterings included in the GE models is discussed in Ref. [51].

When the correlations in the nuclear gluon field are local (i.e. in the incoherent scattering approximation), the gluon p_T -spectrum shows a peak structure which increases in magnitude and moves to higher p_T with increasing rapidity [262]. This agrees with RHIC data at midrapidity, but is at variance with forward rapidity measurements. In the deep saturation regime, the solution of the JIMWLK equation describes high density partons with non-local correlations, and suppresses gluon production over the whole p_T range, irrespective of the rapidity (see Fig. 40). The resulting picture [263, 264] is that at the values of x probed at RHIC at midrapidity, the nucleus wavefunction has not yet reached

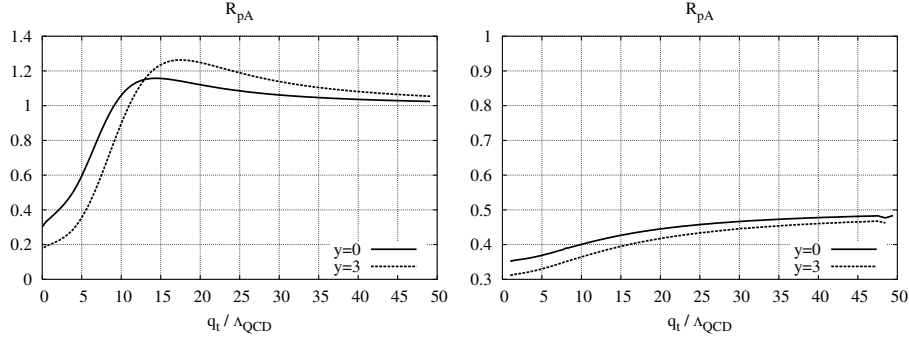


Fig. 40. – Cronin effect in the CGC formalism with naive quantum evolution (*left*) and with full evolution in the “deep saturation” limit (*right*). Figure taken from Ref. [262].

the saturation regimes – Q_s^2 is small, at most 2 GeV^2 – hence a description in terms of pQCD multi-scatterings is valid (and perhaps numerically more accurate [51]). At larger rapidities, the saturation scale increases and the nucleus wave function undergoes a longer quantum evolution, resulting in hadron suppression on a large p_T interval. Hence, gluon saturation may have indeed been revealed in the observed forward rapidity hadron suppression at RHIC.

To make quantitative contact with phenomenology, one approximates the proton as a dilute colour source, so that gluon production in $p + A$ collisions can be explicitly written in a k_T -factorised form [262]. The nucleus wavefunction is computed in terms of a colour dipole forward scattering amplitude, which is modeled in order to capture the analytic key features of the CGC, and to incorporate the transition to the semi-classical regime at lower rapidity [127, 245, 246, 265]. Examples from the computations of Refs. [245, 246] are shown in Fig. 39 (right).

An important limitation of parton multi-scattering models is their inability to explain the strong flavour dependence of the Cronin effect and the corresponding “baryon anomaly” ($\pi^\pm < K^\pm \ll p, \bar{p}$ at intermediate p_T) observed at RHIC. Indeed, if the p_T -broadening has a partonic origin, the only flavour dependence of the Cronin effect can be due to the different contribution of gluons and quarks to the final-state hadron, which cannot explain the large difference between protons and pions [49].

6.1.2. Final state parton recombination. – A description of hadronisation as parton recombination, as opposed to the parton fragmenting into the observed hadron, was proposed long ago to explain hadron production at large Feynman x_F in $h + A$ collisions [266]. The idea that two or three partons can recombine, or coalesce, into a meson or baryon has been revived [125, 126, 183-185, 267-269] because of recent experimental findings at RHIC, chiefly, the strong baryon enhancement (already observed in $h + A$ collisions at Fermilab, see Section 4), and the scaling of the elliptic flow of intermediate p_T hadrons with the number of their constituent quarks [270, 271]. The main idea is that whenever there is a large reservoir of partons in the final state, there is a lesser need to produce additional ones through parton splitting as assumed in parton fragmentation. Recent reviews of recombination models can be found in [233, 272].

In heavy-ion collisions at RHIC, a hot and dense medium made of deconfined soft quarks and gluons is created in the first instants after the collision. The parton reservoir is made of these thermal partons, which are distributed in momentum according to an exponential spectrum,

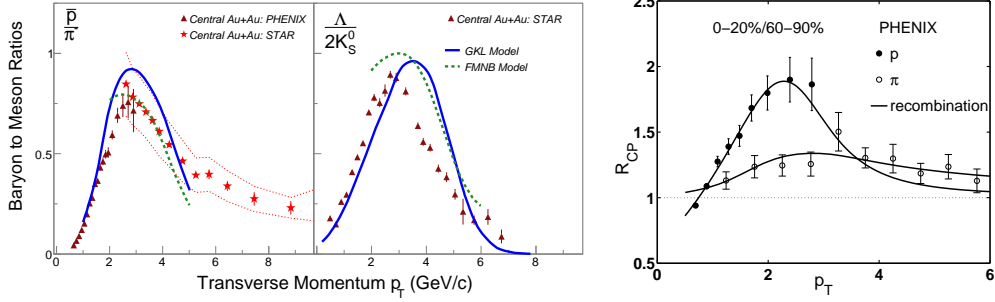


Fig. 41. – *Left*: Ratio of baryon yields to meson yields for central $Au + Au$ collisions at RHIC $\sqrt{s_{NN}} = 200$ GeV. The recombination model computations by Greco, Ko, Levai [185, 267] and by Fries, Müller, Nonaka, Bass [184, 268] for \bar{p}/π^- (left) and $\Lambda/2K_s^0$ (right) are compared to PHENIX and STAR data. Plot taken from Ref. [233]. *Right*: Hwa-Yang recombination model computation [125] of the Cronin effect for midrapidity pion and proton in $d + Au$ collisions at RHIC $\sqrt{s_{NN}} = 200$ GeV, compared to PHENIX data [119, 122]. Plot taken from Ref. [273].

$\sim e^{-p/T}$ with $T \approx 0.2$ GeV. At large momenta partons come dominantly from hard interactions and are distributed according to a power law, $\sim 1/p_T^n$, with $n \approx 7 - 8$. Parton fragmentation requires the production of a hard parton with large momentum $p_T > p_T^h$ to fragment into the hadron. On the contrary, parton recombination is kinematically favoured since 2 or 3 partons of *smaller* momenta $p_T < p_h$ can coalesce into the observed hadron. At large p_T , the fragmentation dynamics is supposed to dominate over recombination since thermal partons are suppressed, while recombination is expected to be important at low p_T . In an intermediate p_T range, the recombination of one hard parton together with one or two thermal partons becomes the dominant channel to produce a meson or a baryon. Recombination readily explains the Cronin effect of mesons and baryons at intermediate p_T : the larger the number of soft thermal partons involved in the recombination process, the larger the momentum broadening, leading to a stronger Cronin effect for baryons than for mesons. As can be seen in Fig. 41 left, these models turn out to reproduce well the data.

In $p + A$ collisions, the parton reservoir is made of the soft partons created in sequential nucleon-nucleon scatterings [125]; in particular, they can recombine among themselves into the observed low- p_T hadrons. Fitting the exponential soft parton spectrum to the observed yield of low- p_T hadrons in $p + p$ collisions, this recombination model can explain well the large difference in the baryon and meson Cronin effect in $d + Au$ collisions at RHIC (Fig. 29). Additionally, it can describe the observed suppression of intermediate p_T hadrons in forward rapidity bins, and also the negative/positive rapidity asymmetry of the Cronin effect at moderate η because its magnitude tracks the (soft) hadron rapidity distribution, which decreases in rapidity at $\eta \gtrsim -2$ [274]. The model is quite successful at RHIC energy in the range $-0.75 < \eta < 3.2$. An interesting check would be to measure hadron p_T spectra at $\eta \lesssim -2$, where the soft hadron yield starts decreasing with decreasing η . Therefore, the magnitude of the Cronin effect should peak at $\eta \approx -2$, and slowly decrease as η is reduced.

6.1.3. Origin of the Cronin effect. – In the parton recombination model, the Cronin effect is a final-state (FS) effect at the hadronisation stage rather than due to initial state (IS) or final-state parton rescatterings in the target nucleus. However, contributions to the Cronin effect from IS parton rescatterings cannot be entirely discarded. In fact, in $e + A$ collisions the multiplicity of

soft hadrons in the final state is much lower than in $p + A$ collisions, making the recombination mechanism much less effective, even though a large Cronin effect is observed in the HERMES and EMC data, see Section 3.2. (Another potential difficulty of the recombination models in nDIS would be to account for the anti-proton Cronin effect which is similar to that of the mesons, unlike in $h + A$ collisions where $p \approx \bar{p}$.) The same processes which cause the Cronin effect in $e + A$ collisions are also likely to be at work in $h + A$ collisions in addition to possible FS recombination effects. Indeed the hard partons are traversing two media, the cold nuclear target and the soft partons cloud created in the collisions, and both can contribute to the Cronin effect. Since these two media are well separated in space-time because of the formation time $\propto 1/\Lambda_{QCD}$ for the soft partons, multiple parton scatterings may add to the p_T -broadening from FS recombination.

The effect of a short quark life time, as indicated by HERMES data in nDIS, has not been included so far in recombination model computations. At RHIC energy the large DIS-equivalent $\nu = \mathcal{O}(1000 \text{ GeV})$ (see Section 2.2) ensures that parton fragmentation starts outside the cold nuclei. However, at small enough p_T , fragmentation may still start inside the soft parton cloud, thus reducing the quark path-length in the soft cloud, therefore reducing the probability of soft parton pick-up and the effectiveness of the recombination mechanism. At fixed-target energies $\nu = 10 - 100 \text{ GeV}$ hadronisation may in fact start inside the cold nucleus target, before the parton has any time to travel through the soft parton cloud, thus preventing altogether the recombination mechanism.

We finally remark that a precise understanding of the mechanisms underlying the Cronin effect in $h + A$ collisions is crucial for measurements of hadron quenching in $A + A$ collisions at the low SPS energy, $\sqrt{s_{NN}} = 17.3 \text{ GeV}$ [161]. In $A + A$ collisions, two competing effects modify hadron p_T spectra: (i) the p_T broadening caused by both targets, hence larger than in $h + A$ collisions, and (ii) the hadron suppression due to parton energy loss in the produced medium. The Cronin effect is observed in $h + A$ collisions to grow with decreasing $\sqrt{s_{NN}} = 200 - 27 \text{ GeV}$: the steeper transverse momentum spectra at lower energies translate into a larger relative enhancement of the yields for the same k_T “kick”. Hence, at SPS energy one can expect an even larger enhancement than observed at Fermilab. Therefore the $Pb + Pb/p + Pb \approx 0.5$ nuclear modification ratio observed by the WA98 collaboration [161] might be caused by a large parton energy loss in $Pb + Pb$ that outweighs a large Cronin effect [159, 161]. A numerical evaluation of jet quenching at fixed-target energies requires a precise theoretical and experimental control of the underlying Cronin effect (including baseline $p + p$ p_T spectra at SPS energies).

6.2. Energy loss in hot QCD matter . –

6.2.1. Formalisms. – The idea of parton energy loss in hot QCD matter was first discussed by Bjorken in the early eighties [131]. This process was then revived a decade later when for the first time Thoma and Gyulassy [132] and Gyulassy, Plümer, and Wang [275, 276] computed perturbatively the radiative energy loss of high-energy quarks in a QGP. Since then many approaches have been developed to determine the gluon radiation spectrum, $dI/d\omega$, of a hard parton undergoing multiple scattering. For a short discussion and comparison of the different energy loss formalisms, see Ref. [165]. Let us briefly recall the main assumptions made in each of the four main frameworks detailed there:

- Opacity expansions (BDMPS and GLV)

BDMPS developed the first perturbative framework to describe the medium-induced gluon emission process from the soft multiple scattering of hard partons in both cold [277] and hot [278] QCD matter. The calculation assumes that the number of collisions, or opacity, is large: $n = L/\lambda \gg 1$, where L is the medium length and λ the parton mean free path. The

typical momentum exchange in each scattering is given by the Debye mass of the medium, μ , and the hard scale of the calculation is $n \times \mu^2 = \hat{q}L \gg \Lambda_{\text{QCD}}^2$, where the transport coefficient $\hat{q} \equiv \mu^2/\lambda$ represents the scattering power of the QCD medium. The Landau-Pomeranchuk-Migdal (LPM) effect – basically the destructive interference of the gluon radiated on several scattering centres – takes place whenever the gluon lifetime $t = \omega/k_T^2$ exceeds its mean free path, that is for gluon energies larger than $\sim \mu^2\lambda$. Soft gluon emission is assumed, $\omega \sim \hat{q}L^2 \ll E$, although corrections $\mathcal{O}(\omega/E)$ were proposed in [108]. On the contrary, the formalism by Gyulassy, Lévai and Vitev (GLV) first took into account one hard scattering in the medium [279] (i.e. first order in n) and from this a recursive approach has been used to determine the gluon spectrum at any opacity [60, 138]. Such an expansion has also been rederived by Wiedemann in Ref. [280] from the light-cone path-integral (LCPI) approach to energy loss developed by Zakharov [143, 230] (and equivalent to the BDMPS framework described above, see [141]). All these approaches model the medium-modified fragmentation functions as a convolution of (vacuum) fragmentation functions, $D_k^h(z, Q^2)$, and an energy-loss probability distribution, $\mathcal{P}(\epsilon)$ [281]:

$$(45) \quad \tilde{D}_f^h(z, Q^2) = \int_0^{(1-z)E_f} d\epsilon \mathcal{P}(\epsilon) z^\star D_f^h(z^\star, Q^2),$$

where

$$z^\star = z/(1 - \epsilon/E_f)$$

is the rescaled momentum fraction carried away by the hadron h in presence of the QCD medium, and E_f is the energy of the parent parton in the medium rest frame. In heavy-ion collisions, for instance, $E_f = k_T$ for partons produced at mid-rapidity, while in semi-inclusive DIS to LO in the strong coupling constant the quark energy is given by the photon energy, $E_f = \nu$. The energy loss probability distributions $\mathcal{P}(\epsilon)$, also called *quenching weights*, will be discussed in Section 6.2.2.

- Higher-twist formalism (HT)

In the HT approach [92, 282, 283], power corrections proportional to $1/Q^2$ (where Q is the typical radiated gluon virtuality) and enhanced by the medium length L are included to the leading-twist total cross section in DIS, assuming that Q is much larger than the energy-scale exchanged μ between the hard parton (with energy E) and the medium: $E \gg Q \gg \mu$. This approach was first proposed in the context of DIS (see Section 6.3.2) where the strength of the higher-twist terms is monitored by a single parameter, C , which can be adjusted to fit the data just like \hat{q} in BDMPS or the initial gluon density dN^g/dy in GLV. For hot QCD media, a phenomenology based on a z -shift prescription for the FF, $z \rightarrow z/(1 - \epsilon/E_f)$ similarly to Eq. (45), was developed afterwards [282]. The energy loss ϵ can be related to C and is adjusted to fit the data.

- Thermal field theory (AMY)

The formalism of Arnold, Moore, and Yaffe (AMY) addresses the production of thermal photons in a finite-temperature QCD medium [284, 285] and was then extended to describe gluon emission from the scattering of “hard particles”, with energy $\mathcal{O}(T)$, on softer modes, $\mathcal{O}(gT)$. The photon/gluon emissions that are collinearly divergent were resummed to all orders in α_s , leading to a suppression as compared to the leading-order result because

of the LPM effect already discussed. This calculation should be accurate for asymptotically large temperatures, for which all the relevant (hard, soft, ultra-soft) scales are well separated: $T \gg gT \gg g^2T$.

An alternative Q^2 -shift prescription for medium modified fragmentation functions – which is quite different from the z -rescaling prescription (45) used in most applications – has been discussed in [29, 70]. Assuming that hadronisation occurs outside the medium, as in the above-mentioned energy loss models, an upper bound on hadron quenching can be obtained by considering

$$(46) \quad \tilde{D}_q^h(z, Q^2) = D_q^h(z, Q^2 + \Delta p_T^2),$$

with Δp_T^2 the parton in-medium p_T -broadening related to \hat{q} [140]. Numerical estimates show that such an effect is much smaller than observed in experimental data, which is interpreted as showing that mechanisms other than energy loss are at play in quenching hadron spectra. A detailed vacuum hadronisation model which tries to avoid this ambiguity [29] is briefly discussed at the end of Section 2.4, and its consequences for hadron quenching in cold nuclear matter will be reviewed in Section 7.3.

6.2.2. Quenching weights. – The quenching weights appearing in Eq. (45) have been computed numerically within the BDMPS approach by Salgado and Wiedemann (SW) for light partons [286, 287], and later on extended by Armesto, Salgado and Wiedemann (ASW) to include heavy quarks [288, 289]. They have also been studied in the GLV formalism in Ref. [290].

The ASW quenching weights are determined using the Poisson approximation of independent gluon emission [291],

$$(47) \quad \mathcal{P}(\epsilon) = \sum_{n=0}^{\infty} \frac{1}{n!} \left[\prod_{i=1}^n \int d\omega_i \frac{dI(\omega_i)}{d\omega} \right] \delta\left(\epsilon - \sum_{i=1}^n \omega_i\right) \exp\left[-\int d\omega \frac{dI}{d\omega}\right].$$

It depends on the characteristic radiated gluon energy $\omega_c = \hat{q}L/2$ and on the medium size parameter $R = \omega_c L$, where L is the parton in-medium path-length. The approximation of an asymptotically large medium, considered by BDMPS (supplemented in [59] with finite energy corrections of order $\mathcal{O}(\omega/E_f)$) would correspond to $R \rightarrow \infty$. At finite R , the parton has a probability p_0 of not interacting with the medium and therefore not to suffer any energy loss. Correspondingly, the quenching weight can be split in a discrete and continuum parts,

$$(48) \quad \mathcal{P}(\epsilon) = p_0 \delta(\epsilon) + P(\epsilon).$$

The quenching weight is computed for a static and uniform medium. In heavy-ion collision, the longitudinal expansion of the medium is taken into account by rescaling the transport coefficient according to an approximate scaling law discussed in [292]:

$$(49) \quad \hat{q}(L) = \frac{2}{L^2} \int_{\tau_0}^L d\tau (\tau - \tau_0) \hat{q}(\tau)$$

where α characterises the power-law time-dependence of the medium number-density, $\rho(\tau) \propto \tau^{-\alpha}$, and $\hat{q}(\tau) = \hat{q}(\tau_0) (\tau_0/\tau)^\alpha$. The purely longitudinal (or Bjorken) expansion corresponds to $\alpha = 1$, and is often assumed in phenomenological applications. When $t_0 \ll L$, Eq. (49) reduces to $\langle \hat{q} \rangle \simeq 2\hat{q}(t_0) t_0/L$ [293]. In nDIS, the medium is static but non-uniform, and an analogous scaling

law is proposed in Ref. [43]. Recently, a simple prescription has been given by Arnold in order to determine $dI/d\omega$ in a finite and expanding medium [294]. Therefore, applying this recipe using e.g. hydrodynamical space-time evolution will allow eventually for the computation of more realistic quenching weights. Also, Peshier has proposed a useful way to compute iteratively the quenching weights in Ref. [295] avoiding the need to compute inverse Laplace transforms (as done e.g. in [59, 286]).

6'2.3. Phenomenology. – Many phenomenological applications of the above formalisms have been carried out in order to describe or predict the production of large- p_T hadrons or jets in heavy-ion collisions (see Section 5 and Ref. [137] for a recent review). All models coincide in characterising the system with very large initial gluon densities ($dN^g/dy \approx 1400$), transport coefficients $\langle \hat{q} \rangle \approx 13 \text{ GeV}^2/\text{fm}$ and/or high temperatures $T \approx 400 \text{ MeV}$, in order to reproduce the existing high- p_T suppression. Yet, when trying to compare all model predictions through a common \hat{q} coefficient, differences of a factor of 3 – 4 appear [164]. Recently, progress has been made towards a more realistic implementation of energy-loss scenarios including a full hydrodynamical expansion of the produced medium – constrained by soft/global observables; first in [296-298] and more recently in [299-301]. These approaches aim at a consistent description of soft and hard probes and at a realistic extraction of the medium-parameter from fitting the large- p_T suppression data (see e.g. Fig. 31). A recent quantitative comparison of energy loss schemes under identical conditions (i.e. same medium evolution, same choice of parton distribution functions and scales, etc.) is presented in [302].

6'2.4. Modified DGLAP evolution. – As an alternative to the discussed energy loss formalisms based on an energy-rescaling of vacuum fragmentation-functions, attempts to reformulate parton energy loss in pQCD as a medium modification of the Dokshitzer-Gribov-Altarelli-Parisi (DGLAP) evolution of fragmentation functions have been recently suggested [303-305].

In the perturbative description of fragmentation processes, the produced parton of time-like virtuality Q radiates gluons in order to reduce its virtuality down to a soft scale $Q_0 = \mathcal{O}(1 \text{ GeV})$ where hadronisation takes place. The Q^2 -evolution is governed by the DGLAP equations [1-3], which control the probability that a quark, say, branches into a quark and a gluon in going from $Q^2 + dQ^2$ to Q^2 . Gluons also can split into a gg or a $q\bar{q}$ pair. The offspring partons can in turn split, iteratively. After each branching the scattered parton gains some p_T , which can be controlled by using p_T -dependent evolution equations [306]. Physically, the probabilistic picture of DGLAP evolution leads to a parton shower which can be simulated in a Monte Carlo generator.

In the presence of a QCD medium, the parton shower may be modified in basically two ways: (i) the splitting probability is enhanced, mocking radiative energy loss, and (ii) the partons can rescatter, leading to a stronger showering process and a p_T -broadening of both the leading particle and the shower. Various models for the medium-modified splitting enhancement have been proposed. In [304], under the assumption that splittings are independent, the in-medium splitting functions are

$$(50) \quad P(z) = P^{\text{vac}}(z) + \Delta P(z) ,$$

where z is the fractional momentum carried away by one of the split partons, and P^{vac} is the vacuum splitting probability. The additional term ΔP can be calculated from the medium induced gluon radiation spectrum, $dI/d\omega$, previously discussed. Medium-modified fragmentation functions at a scale Q are computed by evolving input fragmentation functions at a scale Q_0 according to the DGLAP equations with medium-modified splitting functions, see Fig. 42 left. A virtue of this approach is that at large virtualities, $Q \gg \Lambda_{\text{QCD}}$, the usual medium-modified fragmentation

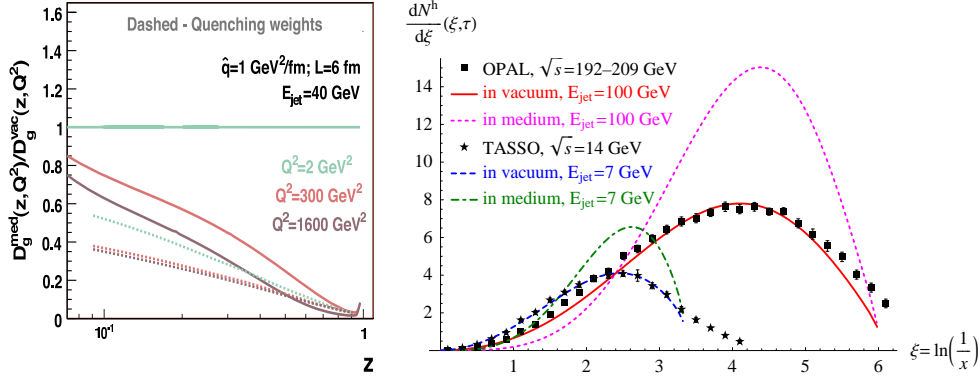


Fig. 42. – *Left*: Medium over vacuum ratio of the gluon fragmentation functions plotted for a medium with $\hat{q} = 10 \text{ GeV}^2/\text{fm}$ (green) and $\hat{q} = 50 \text{ GeV}^2/\text{fm}$ (red), and for two different medium lengths: $L = 2 \text{ fm}$ (solid) and 6 fm (dashed). Figure taken from Ref. [304]. *Right*: Single inclusive hadron distribution as a function of $\xi = \log(E_{\text{jet}}/p)$. e^+e^- data from TASSO [307] and OPAL [308] compared to vacuum-FFs (solid curves) and to medium-FFs (dashed/dotted curves, obtained with $f_{\text{med}} = 0.8$ in the LO splitting functions). Figure taken from Ref. [303].

functions defined by the quenching weights, Eq. (45) is formally recovered. In the approach of Borghini and Wiedemann [303], the medium effect is argued to modify the splitting functions by enhancing its singular part; for example, the quark splitting function is

$$(51) \quad P_{qq}(z) = C_F \left(\frac{2(1 + f_{\text{med}})}{(1 - z)_+} - (1 + z) \right),$$

where $f_{\text{med}} = 0$ gives back the vacuum P^{vac} . An interesting application is the medium modification of the single-inclusive energy distribution of hadrons inside a jet, $dN/d\xi$, where $\xi = \log(E_{\text{jet}}/E_h)$. This leads to a distortion of the usual hump-back plateau, predicted within the Modified Leading Logarithmic Approximation (MLLA) of QCD and observed experimentally in e^+e^- , DIS and hadronic collisions (for a review see e.g. [309]). As can be seen in Fig. 42 (right), the number of highly-energetic particles (small ξ) is suppressed while the soft gluon yield is enhanced at large ξ due to energy-momentum conservation. The inclusion of $2 \rightarrow 2$ elastic rescatterings, which accounts for elastic energy loss, can be accomplished by supplementing the DGLAP evolution equations with a gain and loss term, which describes partons scattered into and away from a given kinematic variable bin, and is also suitable for a Monte Carlo interpretation [305].

Several parton showers in the medium have been recently developed [310–314]. As compared to analytic calculations, parton showers have many advantages such as conserving energy-momentum throughout the evolution. They allow one to directly compare their multiple-differential hadronic distributions to experimental data, and thus give a better access to the microscopic dynamics. They also allow to study the particle and energy flow inside a jet. As an example, first results from the JEWEL parton shower [310], indicate that the distribution of 1, 2 and 3 jets events (reconstructed using a given granularity parameter, y_{cut}) is sensitive to the elastic or inelastic nature of parton rescatterings.

Applications of modified DGLAP equations have been studied only in the context of $A + A$ collisions (see, e.g., [215, 315]) testable at RHIC and LHC. It would be very interesting to also study jet modifications in $e + A$ collisions, which would be accessible at the Electron-Ion

Collider (Section 8.7.4), and the hadron p_T -broadening already under study at HERMES and CLAS (Section 8.1.3), although the lower virtualities of the latter limit the amount of QCD evolution (parton radiation) accessible.

6.3. Energy loss in cold QCD matter . –

Although the density of scattering centres in cold QCD matter is much smaller than in a deconfined state of matter such as a quark-gluon plasma, it is not a priori excluded to observe effects of parton energy loss in large nuclei [277]. As a matter of fact, several of the above-discussed parton energy loss formalisms should prove more appropriate to describe the rescattering of a hard parton off static nucleons rather than off quarks and gluons carrying thermal momenta, $p = \mathcal{O}(T)$. Moreover, the nuclear density is well known and the medium does not expand while the hard parton traverses it, unlike for the QGP whose energy density drops rapidly with proper time. For these reasons, cold QCD matter is an ideal testing ground to compare different energy loss formalisms and test the approximations made in their phenomenological applications.

One pragmatical approach, consists in comparing the nuclear DIS and $h + A$ hadroproduction data to NLO pQCD calculations (with nuclear PDFs) and simply encode any observed modifications of the final yields for various species in properly fitted medium-modified parton-to-hadron FFs [316]. More commonly, however, one tries to get a more physical insight on the mechanisms affecting hadron production in cold nuclear matter by describing parton multiple scatterings in nuclei within the BDMPS framework [277], as done for hot and dense QCD matter. In such an approach [278] one derives a simple relationship between the energy lost by the hard parton (per unit-length) and its transverse momentum broadening, [141]

$$(52) \quad -\frac{dE}{dz} = \frac{\alpha_s N_c}{4} \langle p_T^2 \rangle,$$

independent of the parton species. The transport coefficient of cold nuclear matter, $\hat{q} = \mu^2/\lambda$, governing the amount of energy loss or momentum broadening can be estimated perturbatively. It is related to the nuclear matter density, $\rho \simeq 0.17 \text{ fm}^{-3}$, and the gluon density, G , in a nucleon [277]:

$$(53) \quad \hat{q}^{\text{cold}} = \frac{4\pi^2 \alpha_s C_R}{N_c^2 - 1} \rho x G(x, Q^2)$$

where C_R is the colour charge of the parton, $(N_c^2 - 1)/2N_c$ and N_c for quarks and gluons respectively. The value x at which G should be evaluated is parametrically $(m_N \ell)^{-1}$, where the scale ℓ is larger than the mean free path of the hard parton, λ , and smaller than the medium length, L . The virtual scale Q^2 which enters G is of $\mathcal{O}(\hat{q}L)$. Using $\alpha_s \simeq 1/2$ at such low scales, and $xG(x, Q^2) \simeq 1$, the gluon ($C_R = C_A = N_c$) transport coefficient is roughly given by

$$(54) \quad \hat{q}^{\text{cold}} \simeq 0.05 \text{ GeV}^2/\text{fm}.$$

This value is much smaller than the *leading-order* BDMPS estimate for a hot plasma at RHIC temperatures, $\hat{q}^{\text{hot}} \simeq 2.2 \text{ GeV}^2/\text{fm}$, given in [144].

When discussing energy loss in cold nuclear matter, however, one should make an important distinction between initial-state and final-state energy loss [141, 317], because the medium-induced gluon radiation can interfere with the radiation originating at the hard scattering (see

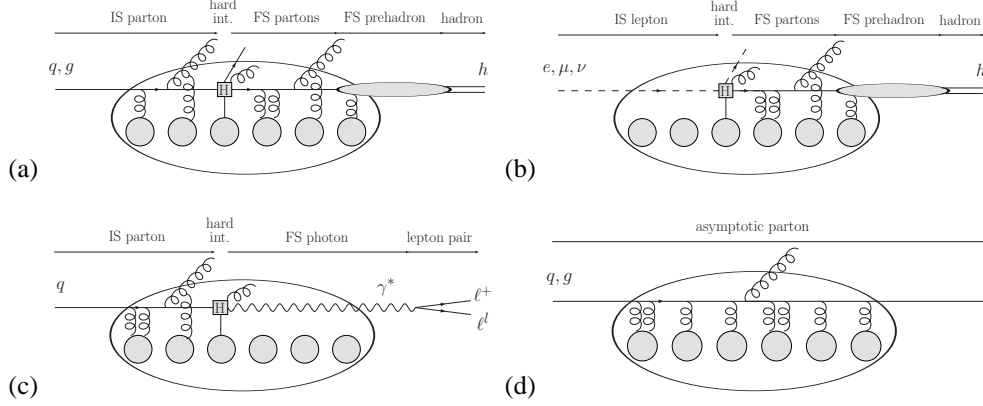


Fig. 43. – Sketch of parton propagation in cold nuclear matter in the nucleus rest frame. (a) Initial- and final- state interactions in $h + A$ collisions in the nucleus rest frame. (b) Absence of initial state interactions in $l + A$ collisions. (c) Absence of final-state interactions in DY events. (d) The theoretical case of an asymptotic parton penetrating the nucleus with no hard interactions. The nucleus is drawn as an oblong oval for illustrative purposes. The possibility that hadronisation starts inside the target nucleus is considered in this cartoon, see Section 7.

Fig. 43). In $h + A$ and $A + A$ collisions, both initial- and final-state interactions occur. If the rapidity of the parton which fragments in the observed hadron is far enough from projectile rapidity, initial-state and final-state radiation should not interfere, and may be treated independently. In semi-inclusive DIS, only final-state interaction may take place because the projectile lepton does not interact strongly with the nucleus. Similarly, in Drell-Yan lepton pair production only initial-state interactions occur; an advantage of the Drell-Yan processes is that conversion rate to a lepton pair is perturbatively calculable, unlike the non-perturbative fragmentation function converting a parton into an observed hadron. The theoretical important case of an asymptotic parton penetrating the nucleus with no hard interactions is also considered in the figure 43 (d). Because of the interference with the hard radiation, each of these energy-loss problems should be considered and solved separately, in order to probe the properties of cold nuclear matter such as its transport coefficient \hat{q} via measurements of the parton energy loss $-dE/dz$.

Baier *et al.* give in Ref. [141] the expression for the energy loss of an asymptotic quark:

$$(55) \quad -\frac{dE}{dz} = \frac{\alpha_s N_c}{4} \hat{q} L,$$

which is a factor 3 smaller than for a quark produced *inside* the medium [277]. Indeed, a quark coming from $-\infty$ has had the time to construct its gluon field and therefore will only start to radiate (medium-induced) gluons only after it has experienced a first single scattering in the medium, after a time $t = \mathcal{O}(\lambda)$. On the contrary, a quark produced in the medium immediately radiates soft gluons to get rid of its virtuality; this gluon emission interferes constructively with gluon emission stimulated by the medium.

In Ref. [317], initial- and final-state energy loss in cold QCD matter has been evaluated in the GLV formalism. The resulting fractional energy loss is shown in Fig. 44 as a function of the parton energy E_{jet} , for two sets of average momentum transfer squared μ^2 and parton mean free path λ corresponding to a fixed value of $\hat{q} = \mu^2/\lambda = 0.12 \text{ GeV}^2/\text{fm}$, and compared to the asymptotic parton case. There are large differences in initial- and final-state energy losses,

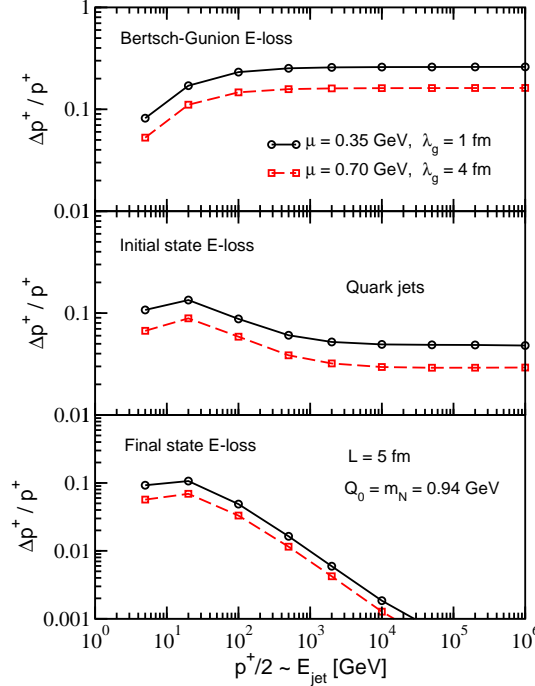


Fig. 44. – Fractional energy loss $\Delta p^+/p^+$ for massless quark partons versus the parton energy E_{jet} , in cold nuclear matter of length $L = 5$ fm. Two different sets of typical momentum transfer per scattering and gluon mean free path have been used for comparison. Plot taken from Ref. [317].

which are process-dependent and need to be correctly accounted for to experimentally access the properties of the nuclear medium. Furthermore, a single parameter such as the transport coefficient $\hat{q} = \mu^2/\lambda$ may not adequately describe the stopping power of cold nuclear matter, as shown by the different energy loss of the solid and dashed lines.

Keeping this in mind, we review in the following the existing phenomenological applications of energy loss computations in cold nuclear matter for semi-inclusive nuclear DIS and DY measurements. Table IX and Fig. 49 summarise various estimates of $-dE/dz$ from the existing data (see also the short reviews in Refs. [318, 319]).

6.3.1. Nuclear DIS in the BDMPS formalism . – In the BDMPS approach of Ref. [59, 320], extended in [43, 321] to include a realistic treatment of the nuclear geometry, the reduced quark energy at the time of hadronisation is translated into a shift of z_h in the vacuum fragmentation function $D \rightarrow \tilde{D}$ [281] via quenching weights. At leading order (LO) in perturbative QCD, the hadron multiplicity is then computed as follows:

$$(56) \quad \frac{1}{N_A^{\text{DIS}}} \frac{dN_A^h(z_h)}{dz_h} = \frac{1}{\sigma_{\ell A}} \int dQ^2 dv \sum_f e_f^2 q_{f/A}(x, Q^2) \frac{d\sigma_{lq}}{dQ^2 dv} \tilde{D}_{f/A}^h(z_h, Q^2),$$

where \tilde{D} is the medium-modified fragmentation function, Eq. (45), computed with $E_f = v$.

The LO computation is known to underestimate the experimentally measured average $\langle v \rangle_z$ and $\langle Q^2 \rangle_z$ in each z_h bin [64]. The problem, is likely to be solved at NLO. An effective way of

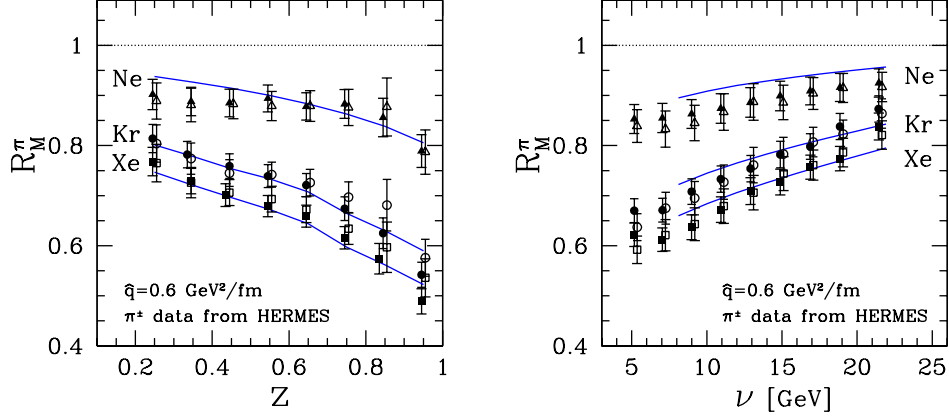


Fig. 45. – HERMES π^+ (full symbols) and π^- (open symbols) data [23] compared to BDMPS energy loss calculations using quenching weights following [43, 321].

circumventing it at LO is to approximate Eq. (56) by

$$(57) \quad \frac{1}{N_A^{DIS}} \frac{dN_A^h(z_h, Q^2)}{dz_h} \approx \frac{1}{\sigma_{tA}} \sum_f e_f^2 q_f \left(\langle x \rangle_z, \langle Q^2 \rangle_z \right) \frac{d\sigma_{lq}}{d\langle Q^2 \rangle d\langle v \rangle} \tilde{D}_{f/A}^h(z_h, \langle Q^2 \rangle_z) .$$

The value of the average variables $\langle x \rangle_z$ and $\langle Q^2 \rangle_z$ in each z_h -bin is taken from the measured values. This procedure is used in all computations based on LO cross-sections [29, 58, 61, 320, 321]. The only parameter of the computation, namely the transport coefficient at the centre of the nucleus, is found to be

$$(58) \quad \hat{q} = 0.6 \text{ GeV}^2/\text{fm}$$

in order to reproduce the latest pion quenching data on the Kr target from HERMES [23], see Fig. 45. When comparing the theoretical ν -distribution with data, mind that $\langle z_h \rangle_\nu \approx 0.3$, where the model tends to slightly overestimate the data. Note that the extracted cold matter \hat{q} value is a factor 10 larger than the perturbative estimate $\hat{q} \approx 0.05 \text{ GeV}^2/\text{fm}$ from Baier *et al.* [277].

An appropriate treatment of the medium geometry is important to extract the quenching parameter from the data [43, 321]. In Fig. 46, we compare experimental data for pion production on Kr to realistic and approximate geometries, using SW quenching weights. The crudest approximation is to use an average quark path-length $L \approx (3/4)R_A$, asymptotic quenching weights ($R \rightarrow \infty$) and a constant nuclear density, corresponding to a constant transport coefficient \hat{q} . This approximation is commonly considered, but cannot reproduce the z -dependence of the data (dotted line) even if $\hat{q} \approx 0.15 - 0.20 \text{ GeV}^2/\text{fm}$ is adjusted for the curve to touch the data.

We can improve these approximations in several steps: using asymptotic quenching weights with a variable medium length (dashed line), non-asymptotic quenching weights using a finite $R = \omega_c L$, either with fixed average L (dot-dashed line), or with variable L depending on the position of the γ^* -quark interaction point (solid line). The largest effect is given by the use of non-asymptotic quenching weights, mainly because of a non-zero probability of no energy loss, see Section 6.2.2. Modelling the full geometry instead of assuming a mean length gives a smaller but still important effect. In particular, when geometry is properly taken into account

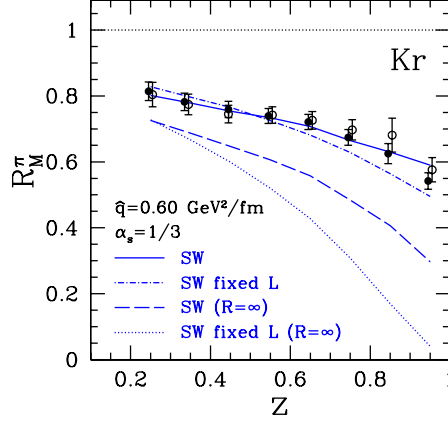


Fig. 46. – Realistic and approximate treatments of the nuclear geometry with quenching weights in the model of Ref. [43,321]. The upper two lines are computed with $R = \omega_c L$, the lower two lines with $R \rightarrow \infty$. Solid and dashed lines: variable quark path-length. Dotted and dot-dashed lines: fixed $L = (4/3)R_A$. Experimental data are for quenching of π^+ (full circles) and π^- (open circles) on Kr from HERMES [23].

there seems to be no need to invoke a finite quark lifetime to explain the large- z data, as proposed in Ref. [320].

Energy conservation, namely the constraint $\epsilon \leq E_q$, is not always fulfilled in the quenching weights because of the approximations involved in their determination. It can be imposed from the outside by cutting the quenching weight at $\epsilon = E_q$ and reweighting it to conserve probability [164]. Alternatively, one can cut the single gluon radiation spectrum at $\omega = E$, and consider $\mathcal{O}(\omega_c/E_q)$ corrections [59]. These corrections tend to reduce the quenching. Their effect increases with \hat{q} and A , and decreases with z_h . Their magnitude is about 5-10% for Kr targets, and typically comparable to the experimental error bars in the figure. Thus they are subleading compared to the effect of correctly implementing the nuclear geometry.

The flavour dependence of hadron quenching in the BDMPS formalism has been discussed in [320,322,323]. We can approximate the vacuum FF at large z_h by $D_q^h(z_h) \propto (1 - z_h)^{\beta_q^h}$, and read the value of the exponents from the global fits of Refs. [324] (Table 2 there). Taking into account that π^\pm production is dominated by u, d quarks, and K^\pm production is dominated by u, s quarks, at $Q^2 = 2 \text{ GeV}^2$ we have

$$(59) \quad D_{u,d}^{\pi^\pm}(z_h) \propto (1 - z_h)^1$$

$$(60) \quad D_{u,s}^{K^\pm}(z_h) \propto (1 - z_h)^{0.9}.$$

So at HERMES ($Q^2 \approx 2.5 \text{ GeV}^2$) we may expect a slightly stronger suppression for large- z_h pions than for kaons (this is opposite to what is asserted in Ref. [29], which assumes $\beta^\pi \approx 0.5$ and $\beta^K \approx 0.8$ on the basis of Regge phenomenology). Using the flavour separated global fit of Kretzer [325] one has $\beta^{K^+} < \beta^{K^-}$, which translates into a stronger quenching for K^- than for K^+ , compatible with data. The described flavor dependence of hadron attenuation in the BDMPS formalism is in agreement with HERMES data.

6.3.2. Nuclear DIS in the higher-twist formalism. – In Refs. [58,282,283] the medium modifications of the fragmentation functions are computed from leading twist and twist-4 contributions

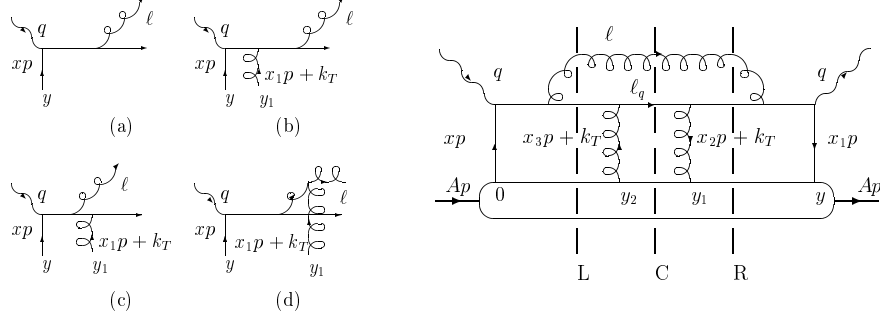


Fig. 47. – *Left*: Gluon radiation from a single scattering (a) and from double scattering (b-d). *Right*: a sample diagram for quark-gluon rescattering processes with 3 possible cuts. Figures taken from [282].

to the leading order DIS cross-section, including diagrams with one elastic quark-nucleus scattering and one radiated gluon, see Fig. 47. Both the struck quark and the radiated gluon are allowed to fragment according to vacuum FF. The obtained modified FF, \tilde{D} , can be modeled to a good accuracy by shifting z_h in the leading-twist fragmentation function

$$(61) \quad \tilde{D}(z_h) \longrightarrow \frac{1}{1 - \Delta z_h} D\left(\frac{z_h}{1 - \Delta z_h}\right)$$

where $\Delta z_h = \Delta E_q / \nu$ is the quark's fractional energy loss, and $\Delta E_q \approx 0.6 \langle z_g \rangle \nu$ with the average fractional energy $\langle z_g \rangle$ carried away by the radiated gluon computed diagrammatically [58, 282, 283]

$$(62) \quad \langle z_g \rangle \approx \alpha_s^2(Q^2) \tilde{C}(Q^2) m_N R_A^2 \frac{1}{\nu} f_g(1 - z_h),$$

where m_N is the nucleon mass and R_A the nuclear radius, and f_g is a function of $(1 - z_h)$ because of energy conservation [326]. The average gluon energy depends on one parameter, $\tilde{C}(Q^2)$, which represents the strength of parton-parton correlations in the nucleus. We can note the dependence on the square of the medium size, typical of the LPM effect in QCD. Inclusion of quark-quark double scatterings beside quark-gluon double scatterings leads, except for pions, to a different quenching of positively and negatively charged hadrons [327]:

$$R_M^{\pi^+} \simeq R_M^{\pi^-} \simeq R_M^{\pi^0} \\ R_M^{K^-} < R_M^{K^+}; \quad R_M^{\bar{p}} < R_M^p; \quad R_M^{h^-} < R_M^{h^+}$$

These features agree qualitatively with HERMES data [22, 23, 44], and with the BDMPS model previously discussed. A generalisation of the higher-twist formalism to include heavy-quark energy loss has been discussed in [328, 329].

To apply the model to HERMES data, the parameter \tilde{C} is fitted to the overall suppression of unidentified charged hadron on a nitrogen target: $\tilde{C}(Q^2) = 0.0060 \text{ GeV}^2$, with $\alpha_s(Q^2) = 0.33$ at $Q^2 = 3 \text{ GeV}^2$, which corresponds to an energy loss $dE/dz = -0.5 \text{ GeV/fm}$ for a Au nucleus [58], or equivalently to a transport coefficient $\hat{q} = 0.12 \text{ GeV}^2/\text{fm}$ [319]. The multiplicity ratio for other targets and parton species can then be computed without further adjusting the parameter, see Fig. 48. See also Ref. [93]. One observes an overall agreement with data, but with a tendency

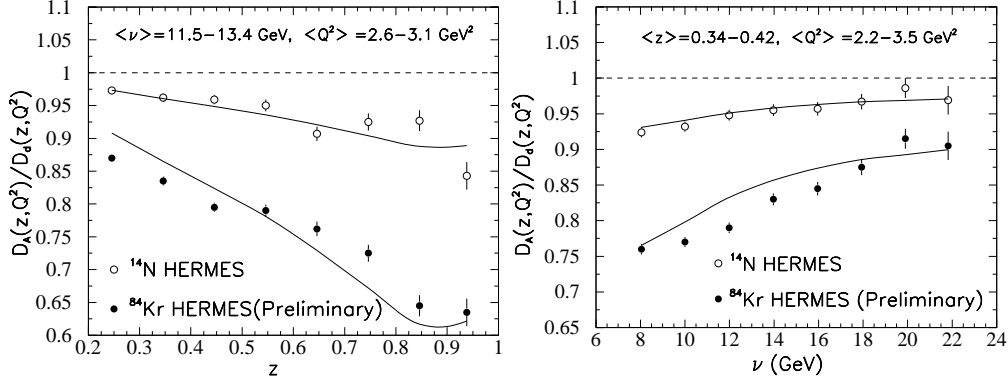


Fig. 48. – Multiplicity ratio computed in the high-twist formalism for parton radiative energy loss in nDIS. Figures taken from [58].

to overestimate the slope of $R_M(z_h)$ for heavy nuclei. As discussed above in connection with the BDMPS approach, this can be caused by a too schematic treatment of the medium geometry. Another important remark, is that the computations of Refs. [58, 93] include only twist-4 diagrams, i.e., up to one parton rescattering in the medium. This might not be sufficient for large targets such as Kr . A computation up to twist-6 (two scatterings) has been carried out in [330], however without comparison to experimental data. (An all-twist resummation for radiative processes is unfortunately very hard to achieve, but the first preliminary steps have been taken in Refs [331, 332].) Higher-twist effects on the DGLAP evolution of the fragmentation functions have been studied in Ref. [333], and reduce the slope of R_M at large z_h . We should finally note that coherent multiple parton scatterings may lead to an additional suppression of quark production [334], which would also reduce the slope of R_M .

6.3.3. Drell-Yan processes . – Since the lepton pair does not interact strongly with the nucleus, the Drell-Yan process offers a clean probe of the initial multiple scattering of the projectile parton (a quark to leading order in α_s) in the target nucleus before the hard process, $q\bar{q} \rightarrow \ell^+ \ell^-$, takes place. The effects of energy loss on the Drell-Yan cross section can be estimated from its production cross section at leading order,

$$(63) \quad \frac{d\sigma_{p+A}^{DY}}{dx_1 dx_2} = \frac{4\pi\alpha_{em}^2}{9s} \frac{x_1 x_2}{x_1 + x_2} \sum_i e_i^2 \left[q_{i/p}(x_1) \bar{q}_{i/A}(x_2) + \bar{q}_{i/p}(x_1) q_{i/A}(x_2) \right],$$

where the fractional momenta $x_{1,2}$ are related to the observable Feynman x_F and dilepton mass M as in Eq. (18) (see Section 2.1). At large $x_1 > 0.5$ and for $x_2 = 0.1 - 0.3$, where $\bar{q}_{i/D} \approx \bar{q}_{i/p}$, the ratio of the DY cross section on a nucleus A and on deuterium D can be approximated by

$$(64) \quad \frac{d\sigma_{p+A}^{DY}}{dx_1 dx_2} \bigg/ \frac{d\sigma_{p+D}^{DY}}{dx_1 dx_2} \sim \frac{q^{u/p}(x_1^A)}{q_{u/p}(x_1)} \sim \frac{(1-x_1^A)^\eta}{(1-x_1)^\eta},$$

where the large- x exponent is $\eta \simeq 3$ from quark counting rules [318]. Assuming that the projectile quark experiences an initial-state energy loss per unit length, $\alpha = -dE/dz$, we can set $x_1^A = x_1 + \alpha\langle L \rangle_A/E$, where E is the quark's energy, for the sake of a qualitative discussion. Hence, one

Reference	$-dE/dz$ (GeV/fm)	Observable
[283]	~ 1.2	Nuclear modification of $e + A$ fragmentation functions
[58]	~ 0.5	Nuclear modification of $e + A$ fragmentation functions
[277]	~ 0.4	p_T broadening of $p + A$ D-Y yield
[335]	0.20 ± 0.15	Nuclear dependence of 150 GeV $\pi + A$ D-Y cross sections
[100]	< 0.44	Nuclear dependence of 800 GeV $p + A$ D-Y cross sections
[336]	$1.12 \pm 0.15 \pm 0.21$	Nuclear dependence of 800 GeV $p + A$ D-Y cross sections
[337]	$0.95 \pm 0.21 \pm 0.21$	Nuclear dependence of 800 GeV $p + A$ D-Y cross sections
[338]	~ 2.8	p_T broadening of $p + A$ jets

TABLE IX. – List of published parton energy loss values in cold nuclear matter extracted from various $e + A$ and $h + A$ observables (adapted from Ref. [318]).

obtains

$$(65) \quad \frac{d\sigma_{p+A}^{DY}}{dx_1 dx_2} \bigg/ \frac{d\sigma_{p+D}^{DY}}{dx_1 dx_2} \sim 1 - \frac{3\alpha\langle L \rangle_A}{E_p(1 - x_1^p)},$$

where E_p is the incident proton's energy in the nucleus rest frame. This equation shows that the energy loss increasingly suppresses the DY cross-section the larger the nucleus, and the larger x_1 , or equivalently the larger $x_F = x_1 - x_2$ when $x_2 \ll 1$. A related observable is the dilepton p_T broadening, which is related to the p_T -broadening of the incoming quark caused by the parton initial state multiple scatterings (see Eq. (52)).

The wealth of experimental data, reviewed in Section 4.1, makes likely a precise estimate of the cold nuclear matter transport coefficient \hat{q}^{cold} , or more generally the amount of energy lost by fast quarks in heavy nuclei via expressions like Eq. (65). Note, however, that the nuclear modifications of the parton distribution functions (shadowing, anti-shadowing and the EMC effect depending on the typical values of x) [20, 109-111] play a role in the nuclear dependence of DY production, and would need to be better constrained.

In Ref. [339], the E772 and E866/NuSea data have been analyzed as a function of the momentum fraction x_1 as well as a function of the mass of the Drell-Yan pair, $M_{\ell^+\ell^-}$. The DY process is calculated using a dipole approach in the rest frame of the target nuclei, which is seen as the bremsstrahlung of a massive photon from the fast going incident quark, $q \rightarrow q\gamma^*$. This models allows the authors to compute equally the nuclear modifications of parton density in nuclei when the momentum fraction of the target parton, x_2 , is small, $x_2 \ll 1$ (shadowing). Performing a global fit of the E772 and E866/NuSea measurements, a huge energy loss has been extracted:

$$(66) \quad -\frac{dE}{dz} = 2.7 \pm 0.4 \pm 0.5 \text{ GeV/fm},$$

that is much larger than the above BDMPS-based expectation $-dE/dz \ll 1$ GeV/fm, but in fact this value includes “vacuum energy loss” [339] which should be removed to obtain the medium-induced energy loss. It was later shown, however, that the large uncertainty of the sea quark nPDF in the E772 and E866/NuSea data makes it difficult a model-independent extraction of energy loss in cold nuclear matter from those measurements [335]. Rather, it was proposed to use the lower energy pion-beam data from the NA3 collaboration which is sensitive to *valence quark* densities (while anti-quarks from the *sea* are probed in $p+A$ collisions) for which nuclear

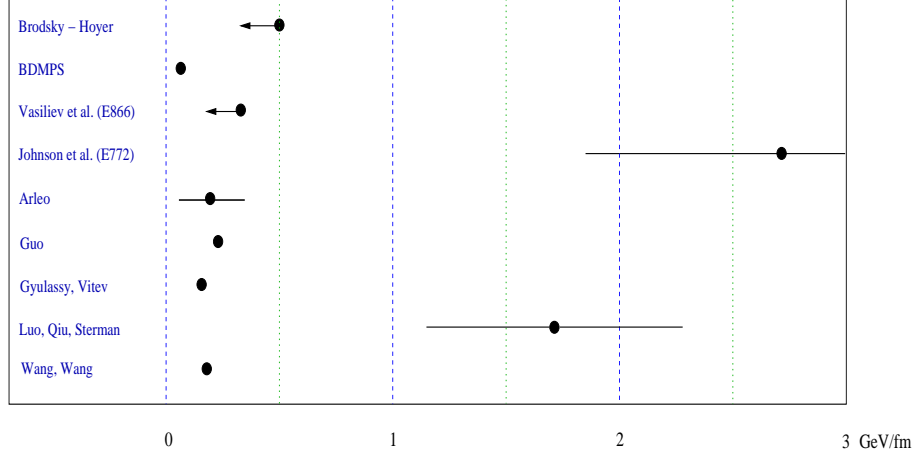


Fig. 49. – Compilation of the different estimates for the magnitude of an incoming quark mean energy loss per unit length, $(-dE/dz)_{\text{in}}$, in a $L = 5$ fm nucleus. Taken from Ref. [319].

modifications are known to be small. From the statistical analysis of these data, a much smaller quark energy loss in nuclei was obtained [335]

$$(67) \quad -\frac{dE}{dz} = 0.20 \pm 0.15 \text{ GeV/fm},$$

equivalent to $\hat{q} = 2(dE/dz)/L \approx 0.14 \pm 0.11 \text{ GeV}^2/\text{fm}$ [319], and in good agreement with the BDMPS estimate.

Various estimates on cold nuclear energy loss extracted phenomenologically from a variety of observables, are summarised in Fig. 49 and Table IX. Most of them point out to a rather small energy loss, $dE/dz \lesssim 0.5 \text{ GeV/fm}$. In order to clarify this issue, Garvey and Peng proposed [318] to measure the nuclear dependence of DY production in fixed-target $p + A$ collisions at low beam energies, $E_{\text{lab}} = 50, 120 \text{ GeV}$ (respectively $\sqrt{s_{NN}} = 9.8, 15 \text{ GeV}$), where the effects of energy loss prove the strongest.

6.3.4. Hadron-nucleus and nucleus-nucleus collisions .

The discussion of jet quenching in $A + A$ is typically focused on parton radiation in the hot medium created in the collision, and neglects energy losses in the nuclear target. Similarly, in $h + A$ collisions, where no hot and spatially extended medium is created, energy loss effects are totally disregarded. However, as discussed in Section 6.3, the cold QCD matter in the target nucleus can induce sizeable IS or FS parton energy loss in DY processes and $e + A$ collisions. Here we discuss cold matter energy loss effects on hadron production in $h + A$ and $A + A$, and review the phenomenological studies performed in Refs. [43, 340].

The initial state parton suffers multiple scatterings and medium-induced gluon radiation. In a simple phenomenological model [340], the resulting energy loss may be accounted for by a shift of the incoming parton fractional momentum, $x_1 \rightarrow x_1(1 - \epsilon)$, with $\epsilon = \kappa A^{1/3}$ the fractional IS energy loss. The effect of such energy loss is felt in a kinematic region where the flux of incoming partons varies rapidly with x_1 , typically at large rapidity. In [340], the suppression factor $R_{dAu}(p_T)$ for charged hadrons was computed including coherent parton multiple scatterings (higher twist shadowing) and energy loss. A value $\epsilon = 0.0175$ was fitted to STAR data on R_{dAu}

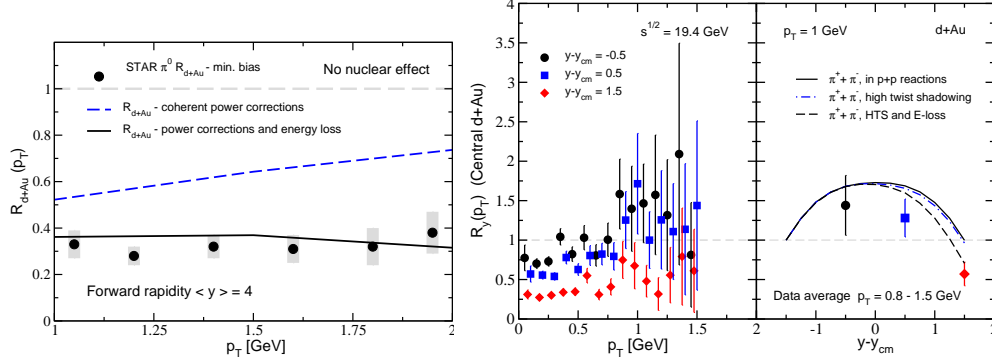


Fig. 50. – Effects of IS energy loss and shadowing (in the “high-twist” formalism) for hadron production in $d + Au$ collisions: $R_{dAu}(p_T)$ for forward pions measured in STAR at $\sqrt{s_{NN}} = 200$ GeV (*left*) and pion NA35 data at various rapidities at $\sqrt{s_{NN}} = 19.4$ GeV (*right*). Plots taken from Ref. [340].

for charged hadrons at $\eta = 4.1$ and $\sqrt{s_{NN}} = 200$ GeV, see Fig. 50. Applying the same formalism to CERN NA35 data at $\sqrt{s_{NN}} = 19.4$ GeV, one obtains a reasonable description of the rapidity dependence of R_{dAu} , and sees that IS state energy loss becomes relevant only at forward rapidity $y - y_{cm} \gtrsim 0$. According to the rapidity shifts listed in Table IV, we may expect a similar conclusion to hold for $y - y_{cm} \gtrsim 2(5)$ at RHIC (LHC).

As discussed in Ref. [43] and Section 2'2, a parton scattered at negative rapidity, $y - y_{cm} < 0$, in a $h + A$ collision travels in the same direction as the target nucleus: seen in the nucleus rest frame, it appears to move slowly and corresponds to a low value of ν in the language of $\ell + A$ collisions. Therefore, based on the observed suppression of hadron production in lepton-nucleus DIS [21, 22, 22, 45, 71] at low ν (see the kinematic analogy between DIS and $h + h$ collisions at LO in Section 2'2), we can expect non-negligible hadron suppression due to FS interactions in cold nuclear matter also in $h + A$ and $A + A$ collisions. Using Eq. (21), it is possible to plot the experimental nDIS data on R_M^h from HERMES and EMC in terms of the $h + h$ kinematic variables p_T , y_1 and z , which provides a rough estimate of final-state hadron attenuation in $h + A$ collisions [43]. The obtained quenching is not small, and increases with decreasing rapidity y_1 as expected from the kinematic analysis of Section 2'2. However, the p_T range covered by HERMES and EMC is quite limited compared to the p_T for which hadron production in $h + A$ and $A + A$ can be measured. Moreover the value of $z \approx z_h$ is not experimentally accessible in hadronic collisions and not easily correlated to the measured variables [43]. Furthermore, the A -dependence of hadron quenching in nDIS is non trivial, and very different from a naive A^α power law as often assumed, see Section 8'1.1. For these reasons, a theoretical estimate is needed for $h + A$ and $A + A$ collisions. This can be obtained in the energy loss model described in Section 6'3.1 [43], and is displayed in Fig. 51, which quantifies final-state “cold” hadron quenching by the ratio

$$(68) \quad R_{fs}^h(p_T, \bar{y}) = \frac{1}{A} \cdot \frac{d\sigma_{pA \rightarrow hX}}{dp_T^2 dy_1 dy_2} \left[\frac{1}{B} \cdot \frac{d\sigma_{pB \rightarrow hX}}{dp_T^2 dy_1 dy_2} \right]^{-1}.$$

The plots show a substantial final-state hadron quenching already for midrapidity hadrons at SPS and FNAL energy. At RHIC it is sizeable for $y_h \lesssim -2$, where it may play a role in understanding the evolution of the Cronin effect at backward rapidity, is still present at $y_h = 0$, where it is of

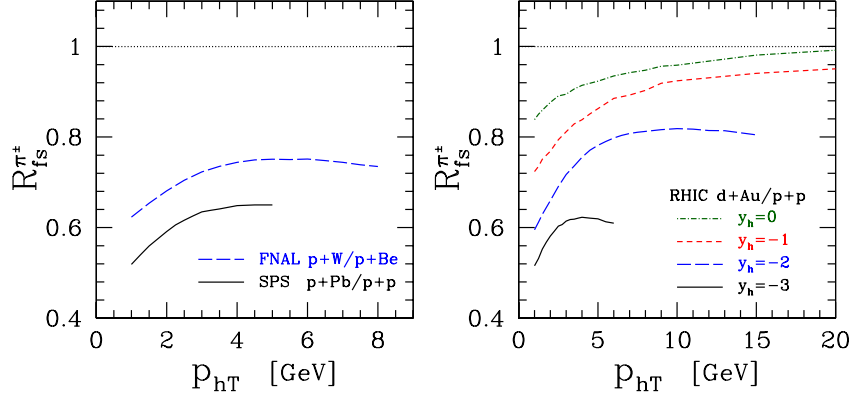


Fig. 51. – Energy loss model estimates of final-state hadron quenching in cold nuclear matter for midrapidity pions produced in $p + A$ collisions at SPS and FNAL fixed-target energies, and several negative rapidities at RHIC.

order 5% at $p_T \gtrsim 10$ GeV/c consistent with nuclear PDF modifications, and quickly disappears at forward rapidity. In $p + Pb$ at the LHC, we may expect negligible final-state effects at $y_h \gtrsim -3$ because of the rapidity shift Δy in Table IV. The rapidity regions in rapidity (measured in the centre-of-mass frame) where we can expect IS and FS hadron quenching in $h + A$ collisions are summarised in Table X.

In $A + A$ collisions the scattered partons can traverse two distinct QCD media: first the two colliding nuclei, then the hot medium formed after the collision. The two media are well separated in time since the time-scale for QGP formation, $\mathcal{O}(1 \text{ fm})$ is (much) larger than the crossing time of the colliding nuclei: $\tau_{cross} = 2R_A/\gamma \approx 1.5, 0.15, 5 \cdot 10^{-3} \text{ fm}$ at SPS, RHIC and LHC respectively. The degree to which the parton interacts with the 2 cold nuclei depends on rapidity: at mid-rapidity to the same degree; at large rapidity more strongly with the comoving nucleus and more weakly with the opposite moving nucleus. A rough estimate of the energy loss in the cold nuclei can be obtained by multiplying the R_{fs}^h values in Fig. 51 at η and $-\eta$. At RHIC midrapidity, cold quenching is less than 10% at $|y| \lesssim 1$, much smaller than the observed factor 4–5 hadron quenching observed in central $Au + Au$ collisions. At LHC, due to the even larger longitudinal boost, cold nuclear matter effects will be smaller than 10% in the $|y| \lesssim 4$ rapidity range. At SPS energy, cold quenching at midrapidity is of order 50% and may in fact be comparable to hot quenching: they both need to be taken into account in any QCD tomographic analysis to characterise the properties of the produced matter.

6.4. Jet quenching from AdS/CFT duality . –

The energy loss computations discussed so far are based on specific models of the medium rooted in perturbative QCD. On the other hand, indications come from RHIC data that the medium produced in heavy-ion collisions is strongly coupled, so that non-perturbative effects can become important [341]. However, non perturbative methods like lattice QCD have an intrinsic difficulty in computing dynamical properties, which are connected to the Minkowski geometry of space-time, and not easily simulated in Euclidean space-time as required by most lattice QCD methods.

A recent theoretical development, the Anti-de Sitter / Conformal Field Theory (AdS/CFT)

	SPS/FNAL	RHIC	RHIC	LHC
$\sqrt{s_{NN}}$ [GeV]	17-38	63	200	5500
IS	$\eta \gtrsim 0$	$\eta \gtrsim 1$	$\eta \gtrsim 2$	$\eta \gtrsim 5$
FS	$\eta \lesssim 2$	$\eta \lesssim 1$	$\eta \lesssim 0$	$\eta \lesssim -3$

TABLE X. – *Regions of rapidity where IS and FS effects in cold nuclear matter may play a role in quenching hadrons in $p + A$ collisions at various energies. In $A + A$ collisions the effects should be symmetrised in rapidity.*

duality [342-345], has given access to analytical calculations of the dynamical properties of a plasma in $\mathcal{N} = 4$ supersymmetric $SU(N_c)$ Yang-Mills (SYM) theory – rather than QCD – in the limit of strong coupling and large number of colours N_c , by relating them to a weakly-coupled string theory living in a 10 dimensional space. The AdS/CFT duality has been later extended to a large class of supersymmetric theories, and is also known under the name of gauge/string duality. Even though QCD and supersymmetric Yang-Mills theories are quite different in terms of running coupling and matter contents, recent experimental and theoretical considerations suggest that the many-body physics of the QGP near the phase transition, where experimental findings at RHIC suggest that the coupling is strong, is similar in the two theories [346].

More in detail, the computation of an observable in the quantum gauge theory at strong coupling can be rephrased as a classical computation of a related observable in a higher-dimensional gravity theory at weak coupling, where it is perturbatively calculable:

$$\mathcal{N} = 4 \text{ SYM} \leftrightarrow \text{type IIB string on } \text{AdS}_5 \times S^5$$

Here, $\mathcal{N} = 4$ means that the theory contains 4 supercharges, AdS_5 is a 5-dimensional space with constant and negative curvature, S^5 is a 5-dimensional sphere. For finite temperature gauge theories, relevant to the description of a QGP, the gravitational equivalent contains a special kind of black hole:

$$\mathcal{N} = 4 \text{ SYM at finite } T \leftrightarrow \text{type IIB string on (Schwarzschild-AdS}_5 \text{ black hole)} \times S^5$$

The details of the computation of dynamical quantities such as the drag force coefficient of a moving heavy-quark in the plasma, the quenching parameter \hat{q} , and the jet transverse momentum broadening in the AdS/CFT duality framework are reviewed and summarised in [346-348]. Although still highly speculative, the connection of these theoretically computable strong-coupling quantities with the physics of real-life QGP is opening new ways of understanding the deconfined phase of QCD near the critical temperature at a fundamental level.

7. – Hadron formation, propagation and interaction

In hadron absorption models, hadronisation is typically assumed to happen in two stages as shown in Fig. 52. One effectively identifies the prehadron production time and the colour neutralisation time: (i) the struck quark neutralises its colour and forms a so-called “prehadron”, which then (ii) collapses into the asymptotic hadron h (see Fig. 7 and Section 2.4). When the (pre)hadron is formed inside the nucleus, it can reinteract with the surrounding nucleons. The space-time evolution of the hadronising system can be computed using the non-perturbative Lund string model or in a pQCD-based approach. The various realisations of the two-stage model differ

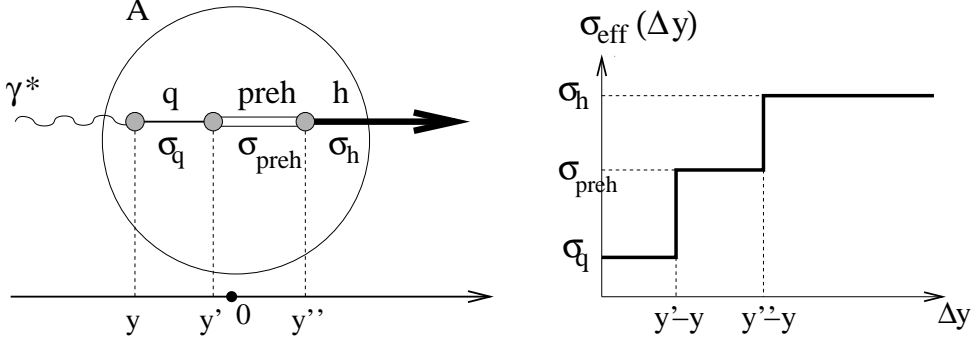


Fig. 52. – *Left*: Sketch of the time evolution of the hadronising system in the two-step hadronisation model: a quark q is struck at point y which evolves into a prehadron and hadron at point y' and y'' respectively (in the Lund string model, $y'' = y' + z_h v/\kappa$). *Right*: Sketch of the effective cross section (70).

by the assumptions concerning the prehadron production time t_{preh} , the hadron formation time t_h , the (pre)hadron interaction with QCD matter, and by the treatment or neglect of the subleading effects due to the quark propagation stage. Most models address absorption in cold nuclear matter, especially in $\ell + A$ collisions. We will mostly specialise the discussion to this case, and briefly comment about applications to $h + A$ and $A + A$ collisions.

7.1. Early string-based absorption models. –

The first nuclear absorption models [349-351] assumed a one-step hadronisation process, in which the struck quark propagates in the nucleus and interacts with the surrounding nucleons with cross section σ_q . After a time $\langle t_h \rangle \propto E_h \propto v$ the hadron is formed and interacts with cross section σ_h . However, the EMC collaboration showed in [45] that for any choice of the parameters σ_q and $\langle t_h \rangle$ only a poor description of charged hadron data in $\mu + A$ collisions could be achieved.

The idea of an intermediate “prehadronic” stage stage between the quark and the hadron was proposed in Ref. [63] in the context of the Lund string model. Hadronisation was imagined to proceed first through the breaking of the colour string stretched between the struck quark and the nucleus, then through the evolution of the string pieces, whose end-point quarks take some time to come together and finally recombine to form the final hadron (Fig. 53), see Section 2.4 for more details. Typically, it is assumed that the string breaking process does not depend on the nature of the target. The nuclear dependence comes from the interaction of the hadronising system with the surrounding nuclear medium. In principle, the hadronising system is allowed to interact at all stages with cross-sections σ_q , σ_{preh} , σ_h (Fig. 52, left). In the case of $\ell + A$ collisions, the hadron survival probability S_A , i.e., the probability that the produced (pre)hadron does not interact with the nucleus, can be approximated as [63]

$$\begin{aligned}
 (69) \quad S_A(z_h) &= \int db^2 \int_{-\infty}^{\infty} dy \rho_A(\vec{b}, y) \\
 &\times \int_y^{\infty} dy' D(z_h; y' - y) \left[1 - \int_y^{\infty} d\tilde{y} \sigma_{eff}(\tilde{y}, y') \rho_A(\vec{b}, \tilde{y}) \right]^{A-1},
 \end{aligned}$$

where ρ_A is the nuclear density normalised to 1, and $D(z_h; y' - y)$ is the probability for a string breaking (i.e. prehadron formation) at a distance $l_c \equiv y' - y$, called “constituent length”, from the

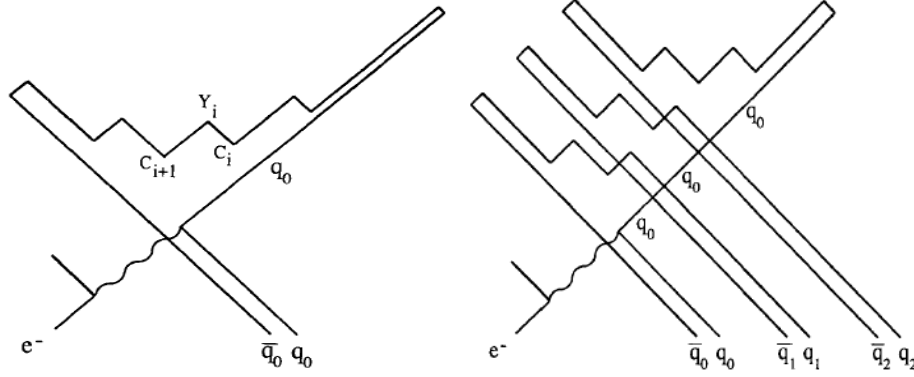


Fig. 53. – *Left*: Sketch of the independent Lund fragmentation model. C_i and Y_i are the constituent (pre-hadron) formation point and “yo-yo” (hadron) formation point, respectively. *Right*: Sketch of the string-flip model in cold QCD matter. The \bar{q}_i are diquark configurations initially connected to the quark q_i in one of the nucleons. Colour exchange interactions rearrange the string end-points in several short stringlets and a leading one with reduced energy. Figures taken from [352].

photon-quark interaction point. In the Lund string model, the hadron is then formed at a distance $l_y \equiv y' + z_h v / \kappa - y$, also called “yo-yo” length. The two-step dynamics is contained in the effective cross section

$$(70) \quad \sigma_{eff}(\tilde{y}, y') = \sigma_q \theta(y' - \tilde{y}) + \sigma_{preh} \theta(\tilde{y} - y') \theta\left(y' + \frac{z_h v}{\kappa} - \tilde{y}\right) + \sigma_h \theta\left(\tilde{y} - y' - \frac{z_h v}{\kappa}\right),$$

depicted in Fig. 52 right. Note that the *ansatz* (69)-(70) neglects elastic scatterings of the system, which induce an energy loss and feed down to lower z_h , so that its validity is confined to $z_h \gtrsim 0.4$. This limitation can be overcome in Monte Carlo implementations, see Ref. [352] and Section 7.4.

The early applications of the independent string fragmentation picture, [63, 353, 354] focused on the relevance of the constituent vs. yo-yo lengths (quark-to-prehadron vs. prehadron-to-hadron formation times) in describing hadron production data in $p + A$ and $\ell + A$ collisions assuming $\sigma_{preh} = \sigma_h$ or $\sigma_q = \sigma_{preh}$. The key point is that at large z_h , $l_y = l_h \propto z_h v$, while $l_c \propto (1 - z_h) v$. EMC data on lepton production of hadrons confirmed that it is in fact the constituent length l_c which controls hadron attenuation on nuclear targets, with a negligible contribution from the struck quark interactions: data could be well fitted with $\sigma_q \lesssim 0.75$ mb and $\sigma_{preh} = \sigma_h \approx 20$ mb [45], see Figure 54. In other words, the hadronising system starts interacting inelastically with QCD matter already at the prehadronic stage, well before the final hadron is formed.

The effect of the nuclear medium on the string breaking process has been considered in Refs. [352, 355]. The struck quark q_0 (see Fig. 53 right) can interact with other nucleons with a cross-section of the order of the hadronic one because of the non-zero transverse size of the string attached to it [355]. When it does so, there is a probability of colour exchange with the nucleon, so that the q_0 reconnects with the diquark \bar{q}_1 , and the quark q_1 with the diquark \bar{q}_0 originally attached to q_0 , and so on. This process was called a “string-flip” [352], and leads to the creation of a number of different string configurations:

$$\gamma^* A \rightarrow (\bar{q}_0 q_1) + (\bar{q}_1 q_2) + \dots + (\bar{q}_{n-1} q_n) + (\bar{q}_n q_0) + (A - n - 1)$$

Assuming a color-exchange cross-section σ_{ce} , the mean free path is $\lambda_{ce} = (\sigma_{ce} \rho_A)^{-1}$, with $\rho_A \approx$

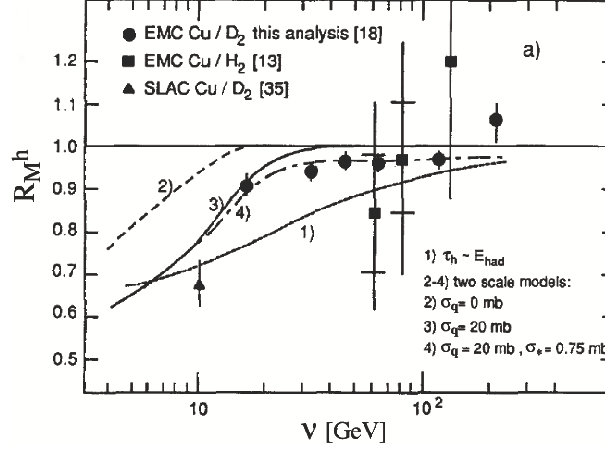


Fig. 54. – Comparison of EMC R_M^h data to the one- and two-step models with varying quark-nucleus and prehadron-nucleus cross sections. Adapted from Ref. [45].

0.17 fm^{-3} . The independent string fragmentation model is obtained in the limit $\lambda_{ce} \gg R_A$. In the opposite limit, $\lambda_{ce} \ll R_A$, the struck quark q_0 exits the medium reconnected to \bar{q}_n (leading string) close to the nucleus surface. Therefore all the hadron components are produced outside the nucleus and do not suffer nuclear absorption. The intermediate stringlets have typically a low mass $M \approx \sqrt{2km_N\lambda_{ce}} \approx 2 \text{ GeV}/c^2$, decay in a few low-energy hadrons, and do not contribute at large z_h . Suppression of large- z_h hadron production is then due to the energy lost by the leading string because of colour reconnections, and is independent of the details of the hadron or prehadron formation time. Defining the probability for a leading hadron of energy $E_h = z_h\nu$ to fragment out of a string with average energy-loss $\epsilon = \lambda_{ce}K$, and assuming it to be independent of the energy of the string, one obtains a medium modified fragmentation function

$$(71) \quad \tilde{D}_A(z_h) = D(z'_h) = D\left(\frac{z_h}{1 - \epsilon/\nu}\right).$$

For fragmentation functions decreasing with z_h , this leads to hadron attenuation: $\tilde{D}_A < D$. Eq. (71) is a close analogue of the z_h -shifted medium modified fragmentation function, see e.g. Eq. (45), used in the gluon bremsstrahlung energy-loss models considered in Section 6. The hadron attenuation caused by colour exchange can be naively interpreted as quark absorption in the nucleus

$$(72) \quad \tilde{D}_A(z_h) = D(z_h) \exp\left(-\sigma_q \int_y^{t_{preh}} dy' \rho_A(\vec{b}, y')\right).$$

However, the effective quark cross section σ_q is process-dependent. For lepto-production of light flavours it is rather small, in agreement with the phenomenological EMC fit [355].

Applications of the string-flip model to EMC data have been considered in Monte Carlo [352] and analytic [356] implementations in [352], a rather large cross-section $\sigma_{ce} = 30 \text{ mb}$ was considered, assuming a string to have a typical hadronic transverse size, so that $\lambda_{ce} \gg R_A$. Therefore, the leading string is produced at the surface of the nucleus, and hadron attenuation is purely due to the energy loss induced by colour exchanges, irrespective of the prehadron

production time. EMC hadron attenuation could be well reproduced both as a function of ν and of z_h . It leads to a slightly larger hadron suppression at $\nu \lesssim 20$ GeV and $z_h \gtrsim 0.5$ compared to the independent fragmentation model using the constituent length, otherwise giving comparable results. In Ref. [356], the colour exchange cross section was identified with the constituent-quark cross section in the additive quark model: $\sigma_{ce} \approx \sigma_q = 0.5\sigma_{\pi N} \approx 10$ mb. The smaller σ_{ce} leads to an intermediate model between the independent string fragmentation and pure string-flip model. However, computations turn out to underestimate the suppression in the EMC kinematics.

Finally, we should mention that extensions of string models to address double hadron attenuation have also been discussed [78, 357].

7.2. Modern string-based absorption models. –

Modern string-based absorption models build upon the early models discussed in the previous Section, exploring different possibilities for the effective cross section σ_{eff} and/or for the hadron survival probability (69). Their computations have also been compared to the more recent HERMES data on $e^- + A$ collisions at $E_e = 12 - 27$ GeV [21-23, 44].

The AGMP model [61, 64] is based on the Lund string model estimate of the formation times discussed in Section 2.4, and neglects the interactions of the struck quark ($\sigma_q = 0$ mb) in agreement with fits to EMC data [45]. In the HERMES kinematics one typically finds a production time $\langle t_{preh} \rangle \approx 4$ fm $< R_A$ and a hadron formation time $\langle t_h \rangle \approx 6 - 10$ fm $\gtrsim R_A$: the hadron is typically formed at the periphery or outside the nucleus so that its interaction with the medium is negligible. On the contrary, after its formation, the prehadron is allowed to interact with the surrounding nucleons with a cross section $\sigma_{preh}(\nu) = 0.80 \sigma_h(\nu)$ proportional to the experimental hadron-nucleon cross section σ_h (taking e.g. π^+ production data on a Kr target [23]). The probability $S_{f,h}^A(z, \nu)$ that the (pre)hadron – produced from the fragmentation of a quark scattered at point (b, y) – does not interact, can be computed using transport differential equations [61]:

$$(73) \quad S_{f,h}^A(z, \nu) = \int db^2 dy \rho_A(b, y) \times \int_y^\infty dx' \int_y^{x'} dx \frac{e^{-\frac{x-y}{\langle l_{preh} \rangle}}}{\langle l_{preh} \rangle} e^{-\sigma_{preh} \int_x^{x'} ds A \rho_A(b, s)} e^{-\frac{x'-x}{\langle \Delta l \rangle}} e^{-\sigma_h \int_{x'}^\infty ds A \rho_A(b, s)}$$

where $\Delta l = l_h - l_{preh}$, and ρ_A is the nuclear density. The hadron multiplicity is computed, at leading order in pQCD, as

$$(74) \quad \frac{1}{N_A^{DIS}} \frac{dN_A^h(z)}{dz} = \frac{1}{\sigma_{\ell A}} \int dx dv \sum_f e_f^2 q_f(x, Q^2) \frac{d\sigma_{\ell f}}{dx dv} S_{f,h}^A(z, \nu) D_f^h(z, Q^2).$$

Here $\sigma_{\ell f}$ and $\sigma_{\ell A}$ are the lepton-quark and lepton-nucleus cross sections, q_f is the f -quark distribution function, and D_f^h its fragmentation function. The model is applicable for $0.4 \lesssim z \lesssim 0.9$, where it describes EMC [64] and HERMES [61, 64] experimental data on a wide range of hadron flavours and targets, see Fig. 55. As it stands, the pure-absorption AGMP model does not predict a dependence of the attenuation ratio R_M on Q^2 , because neither the prehadron production time t_{preh} derived in the Lund model, nor its assumed cross section σ_{preh} depend on it. This assumption does not contradict the slightly rising $R_M(Q^2)$ measured at HERMES [23], see Section 3.2.

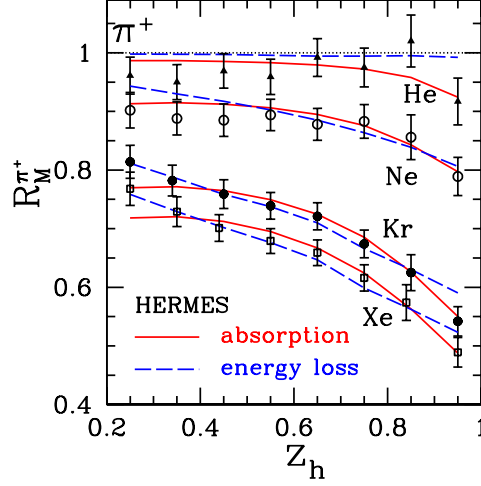


Fig. 55. – Lund string model based absorption model [64, 321] (solid) and energy-loss model [43, 321] (dashed) compared to HERMES data on π^+ production [23]. The prehadron cross section is $\sigma_{preh} = 0.8\sigma_h$ and the transport coefficient is $\hat{q} = 0.6 \text{ GeV}^2/\text{fm}$. Experimental statistical and systematic errors have been added in quadrature.

A different variation of the two-scale model has been proposed in Refs. [358, 359]. The authors argue that in 3+1 dimensions, the yo-yo time is ill-defined because the end quarks of a string snippet never really meet together, and propose instead that the hadron is formed after a proper time for quark recombination, τ_r , following string breaking at a time t_{str} taken from the PYTHIA generator. Then, the hadron formation time is simply set to $t_h = (t_{preh} + \tau_r)v_{str}\gamma_{str}$, and boosted according to the string velocity v_{str} and Lorentz factor γ_{str} . The system does not interact in the nucleus until hadron formation, at which time it starts interacting with the full hadron-nucleus cross section analogously to the AGMP approach. The model does a fair job in describing pion and kaon attenuation on N and Kr [21, 22] at $z_h \gtrsim 0.4$, with a flavour-dependent recombination proper time $\tau_r(\pi) = 0.8 \text{ fm}$ and $\tau_r(K^-) = 0.4 \text{ fm}$. It is interesting to note that the fitted values are such that $\tau_r(h) \approx 1/m_h$. However, this model overestimates the recently measured suppression on Xe targets [23], and no comparison to EMC data is provided.

Extensions of the two-scale model based on Eqs. (69)-(70) have been considered in Refs. [78, 357], and more recently compared to double hadron attenuation at HERMES [24] in Refs. [94, 95, 360].

7.3. The colour dipole model. –

In Ref. [29] the formation of a leading hadron ($z_h \gtrsim 0.5$) is described in a pQCD-inspired approach based on Refs. [66-68], see also Section 2.4: a hard gluon radiated at the interaction point splits into a $q\bar{q}$ pair, and the \bar{q} recombines with the struck q to form the leading prehadron, which evolves into the observed hadron. The time development of hadronisation is included in this picture by observing that the radiated gluon can be physically distinguished from the struck quark only after a coherence time $t_c = 2E\alpha(1-\alpha)/k_T^2$, where k_T and $\alpha = E_g/v$ are the transverse momentum and fractional energy of the emitted gluon. If the leading hadron is produced at large z_h and contains the struck quark, none of the radiated gluons can be emitted with $\alpha > 1 - z_h$ by energy conservation. The time-dependence of the energy radiated into the emitted gluons is

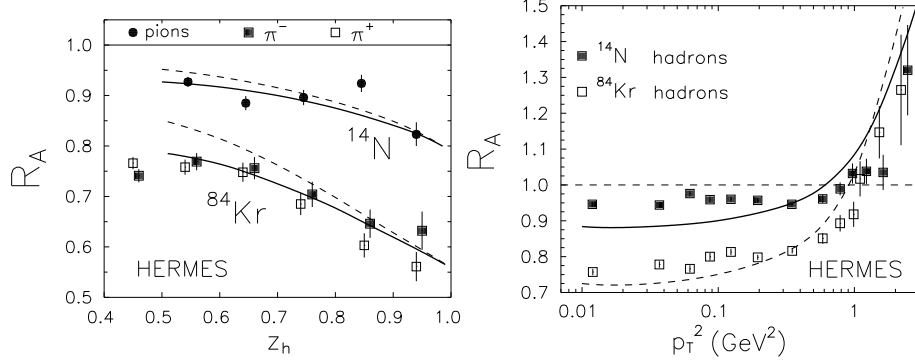


Fig. 56. – Colour dipole model [29] (dashed: absorption only, solid: absorption and induced energy loss) compared to HERMES hadron multiplicity ratios on N and Kr targets [22]. *Left:* z_h distribution. *Right:* p_T distributions.

computed as

$$(75) \quad \Delta E(t, z_h, Q^2) = \int_{\Lambda_{QCD}^2}^{Q^2} dk_T^2 \int_{1-z_h}^1 dz \alpha v \frac{dN_g}{dk_T^2 dz} \Theta(t - t_c) ,$$

where $dN_g/dk_T^2 dz = \alpha_s(k_T^2)/(3\pi) 1/(zk_T^2)$ is the Gunion-Bertsch spectrum of radiated gluons [69]. The upper limit is imposed by the fact that gluons with $k_T > Q$ should be considered part of the struck quark [11]. Next, the gluon (with momentum k_T) splits into a $q\bar{q}$ pair. In the large- N_c approximation, the antiquark and the struck quark form a colourless dipole, which is identified as a prehadron. The prehadron production time is identified with the coherence time of the gluon (rather than with the $q\bar{q}$ splitting time) and hadron formation is computed by the overlap of the $q\bar{q}$ dipole with the hadron light-cone wave function Ψ_h . Assuming that the q and the \bar{q} in the pair share the same amount of gluon energy and transverse momentum, one can compute the probability distribution $W(t, z_h, Q^2, \nu)$ that the prehadron is formed at a time t after the γ^*q interaction:

$$(76) \quad W(t, z_h, Q^2, \nu) = N \int_0^1 \frac{d\alpha}{\alpha} \int_{\Lambda_{QCD}^2}^{Q^2} \frac{dk_T^2}{k_T^2} \delta \left[z_h - \left(1 - \frac{\alpha}{2} \right) \frac{E_q(t)}{\nu} \right] \frac{\exp(-t/t_c)}{t_c} \\ \times \left| \Psi_h \left(\frac{\alpha}{2-\alpha}, \frac{3}{4} k_T \right) \right|^2 \exp(-\tilde{N}_g(z_h, t, Q^2, \nu)) ,$$

where, $E_q(t) = \nu - \Delta E(t)$, Ψ_h is the hadron light-cone hadron wave function, \tilde{N}_g is the number of gluons radiated within a time t , and N is a normalisation factor. Numerical results are presented in Fig. 11. Integrating W over t one obtains the vacuum fragmentation function for the leading hadron which compares favourably with global fit FF from Refs. [324, 325] in the range $z_h = 0.5 - 0.9$ and $Q^2 = 2 - 10 \text{ GeV}^2$.

The $q\bar{q}$ dipole, which is assumed to be formed with a Gaussian transverse size around an average $\langle R_l^2 \rangle \propto 1/Q^2$, propagates through the nucleus and fluctuates in size. According to colour transparency, see Sect. 7.5, it interacts with the nucleus with a cross section $\sigma_{q\bar{q}} = C(E_h)r^2$. All effects of fluctuations and nuclear interactions are computed in a path-integral formalism for

dipole propagation in QCD matter [361, 362]. Finally, the effective in-medium fragmentation function reads

$$(77) \quad D_A^h(z_h, Q^2, \nu) = \int db^2 \int_{-\infty}^{\infty} dy \rho_A(\vec{b}, y) \int_0^{\infty} dt W(t, z_h, Q^2, \nu) Tr(b, y + t)$$

where $Tr(b, y + t, \infty)$, called nuclear transparency in [29], is the probability for a prehadron not to be absorbed in the nucleus. The hadron attenuation ratio can then be approximated as $R_M^h \approx D_A^h/D_D^h$.

Finally, medium-induced energy loss is included in the model as an increase in the parton energy loss proportional to the quark transverse momentum broadening Δp_T^2 , according to the relation $\Delta E_{\text{ind}} = \frac{3}{8} \alpha_s \Delta p_T^2 L$, derived in Baier *et al.* (BDMPS) [140]. (Note that this formula is valid for an asymptotically large medium, which is not the case in $e + A$ collisions; the authors of [29] argue that finite medium size corrections are small at HERMES energy, but their effect might in fact be non-negligible, see Fig. 46.) The induced energy loss modifies the production time distribution via

$$(78) \quad \begin{aligned} \Delta E &\rightarrow \Delta E + \Delta E_{\text{ind}} \\ Q^2 &\rightarrow Q^2 + \Delta p_T^2, \end{aligned}$$

with Δp_T^2 computed in the colour dipole formalism [141, 142]: $\Delta p_T^2 = 2C(E_q)\rho_A L$. This leads to an additional, but subleading, hadron suppression compared to the effect of prehadron absorption, as shown by the two curves in Fig. 56 left.

The parameters of the model are fitted to other processes than hadron production in $l + A$ collisions and, in this sense, the approach can be considered parameter-free. The comparison to HERMES experimental data for π^\pm production is shown in Fig. 56. The model can also describe the smaller K^+ suppression compared to π^\pm (not shown here), as well as the EMC data at $z_h > 0.5$. Use of the colour dipole formalism allows also the computation of the Cronin effect, shown against data in Fig. 56 right. The Q^2 dependence of R_M is discussed in Sect. 7.5 (see Fig. 61). An interesting consequence of this formalism is that the prehadron production time is inversely proportional to Q^2 :

$$(79) \quad \langle t_{\text{preh}} \rangle \propto (1 - z_h) \frac{z_h \nu}{Q^2}.$$

where $\nu \approx E_q$. Technically, this arises from the upper limit of integration in Eq. (76). Physically, it is interpreted saying that a quark which is struck by a photon of large virtuality radiates more intensely than for a lower virtuality: as a consequence, it will be able to travel only a shorter distance before hadronising at a given z_h . In $p + A$ and $A + A$ collisions, $Q^2 \propto p_{Th}^2$ and for midrapidity hadrons $E_q \approx p_{Th}$, hence $\langle t_{\text{preh}} \rangle \propto 1/p_T$. So, the prehadron production time actually shrinks with increasing p_T , instead of increasing because of the large Lorentz boost. This would imply that prehadrons are formed well inside the hot medium produced in $A + A$ collisions at any p_T . Experimental confirmation of Eq. (79) is thus very important. It can be accomplished in a direct way by measuring the hadron p_T -broadening, or indirectly with a scaling analysis of R_M , see Sect. 8.1.

7.4. The GiBUU transport Monte Carlo. –

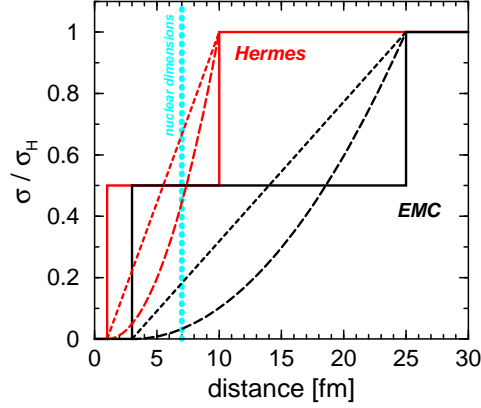


Fig. 57. – Sketch of the time evolution of the (pre)hadronic cross section for arbitrarily chosen formation times. Solid lines are for constant σ_{preh} , dotted and dashed lines are Eq. (84) for $n = 1, 2$. A typical nuclear distance of 7 fm is indicated as a vertical dashed line. Figure taken from Ref. [363].

In Refs. [363,364] a Monte Carlo event generator has been used to explore hadron attenuation in $\ell + A$ collisions in the framework of a transport model based on the Boltzmann-Uehling-Uhlenbeck (BUU) equation. In this approach, the lepton-nucleus interaction is split into two parts:

1. The exchanged virtual photon produces a final state X which is determined using the Monte Carlo generators PYTHIA and FRITIOF based on the Lund string model. Nuclear effects like binding energies, Fermi motion, Pauli blocking and coherence length effects that lead to nuclear shadowing are also implemented.
2. The state X is propagated through the nuclear target using a BUU transport model [364, 365] which – through a probabilistic coupled-channel computation – accounts for particle creation, annihilation and elastic scattering in the final-state interactions.

The latest implementation of the code is known as GiBUU [363]. The space-time evolution of hadronisation has been explored using two concepts of prehadron differing mainly in the treatment of the production time t_{preh} : set to zero in transport models [366-368], and depending on the energy and momentum of the string fragments in the Lund model, see Sections 2'4 and 7'1.

In Ref. [364], the “transport model” view is adopted. The string decay into colour neutral prehadrons is assumed to happen instantaneously, hence $t_{preh} = 0$ fm. Hadrons are assumed to form after a fixed proper formation time $\tau_f = 0.5$ fm in the hadron rest frame, which is then boosted to the laboratory frame,

$$(80) \quad t_h = \frac{z_h \gamma}{m_h} \tau_f .$$

Between the prehadron and hadron formation times, only beam and target remnants, i.e., hadrons containing the valence quark of the struck nucleon or of the resolved photon, are allowed to interact with the rest of the nucleus. Specifically, the prehadron cross section is assigned according to the constituent quark model:

$$(81) \quad \sigma_{preh}^{\text{baryon}} = \frac{n_{\text{org}}}{3} \sigma_h^{\text{baryon}} \quad \sigma_{preh}^{\text{meson}} = \frac{n_{\text{org}}}{2} \sigma_h^{\text{meson}}$$

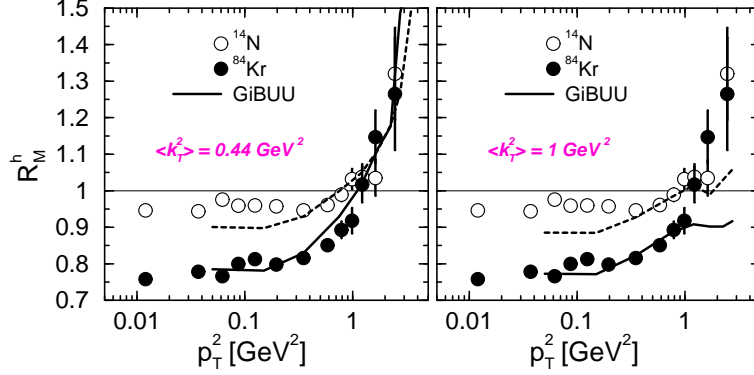


Fig. 58. – Multiplicity ratio in the GiBUU model as a function of p_T . Computations are done with parton intrinsic momentum $\langle k_T^2 \rangle = 0.44 \text{ GeV}^2$ (left) and $\langle k_T^2 \rangle = 1 \text{ GeV}^2$ (right). HERMES data are from [22]. Plot taken from [363].

where n_{org} denotes the number of quarks or antiquarks in the hadron coming from the beam or target nucleon. This model can describe fairly well HERMES data for π^\pm , π^0 and K^\pm at large $z_h \gtrsim 0.4$. For smaller z_h some discrepancy for K^+ production on light nuclei emerges, related in part to the assignment of the pre-kaon cross section (81), in part to feed-down due to the decay of diffractively produced ρ mesons into K^+K^- , or due to πN interactions. The results for baryons are less good, especially for p production, which cannot explain the strong rise of experimental R_M^p at $z_h \lesssim 0.5$. However, the biggest challenge for this space-time scenario is in connection to EMC data, whose suppression is vastly overestimated due to the unlikely assumption of an instantaneous conversion of string fragments into colour neutral prehadrons and of an instantaneous jump from the prehadron to the hadron cross-sections at time t_h .

The solution proposed in Ref. [364] and fully worked out in Ref. [363] is to use the concept of prehadron coming from the Lund model, and time-dependent prehadron cross sections. The PYTHIA generator is used as main source of information on the string fragmentation process. In the Lund string model, we can actually associate three time scales to each hadron: the times t_{p1} and t_{p2} at which the constituents of the hadron are created, and the time t_h at which the constituents meet and form the hadron. The prehadron production time is then defined as

$$(82) \quad t_{\text{preh}} = \min(t_{p1}, t_{p2}) .$$

This definition is different from what is commonly used, see Sections 7.1 and 7.2. Most notably, the rank-1 hadron contains the struck quark, which preexists the γ^*N interaction: hence, $t_{\text{preh}}^{\text{rank-1}} = 0$. The determination of the prehadron and hadron formation time is carried out on an event-by-event basis by extracting the corresponding information from the PYTHIA generator as described in detail in [65]. An interesting result is that the prehadron and hadron formation times are quite insensitive to the hadron mass, contrary to the common assumption that they scale with a Lorentz boost factor $\propto 1/m_h$. The prehadron cross section includes the main features of colour transparency, and is allowed to vary in time according to linear and quadratic evolution, or to a quantum diffusion picture, see Eqs. (84)-(85). The requirement of reproducing both HERMES and EMC data rules out the quadratic evolution, and slightly favours the quantum diffusion picture with $\sigma_{\text{preh}} \propto 1/Q^2$ at $t = t_{\text{preh}}$, instead of $\sigma_{\text{preh}} = 0$, see Figs. 59 and 60 left. The model performs well in describing the flavour dependence of R_M at HERMES, with the exception of a

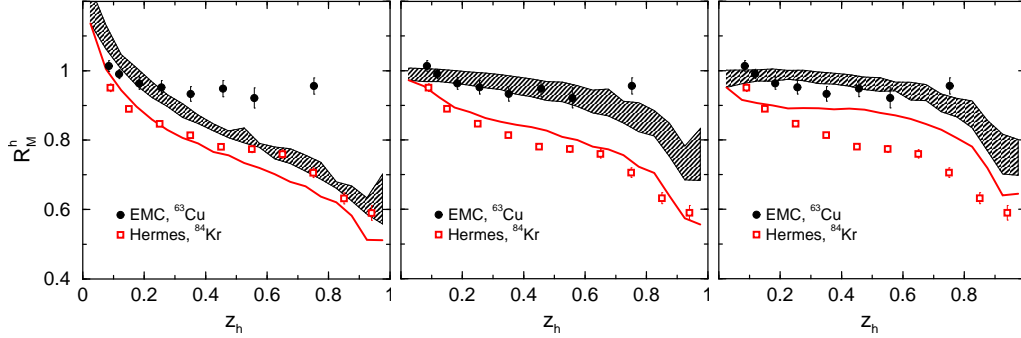


Fig. 59. – Multiplicity ratio in the GiBUU model, compared to HERMES at $E_e = 27$ GeV [22] and EMC at $E_e = 100 - 280$ GeV [45] data. The upper and lower bounds of the shaded band corresponds to higher and lower EMC beam energy, respectively. The prehadron cross section evolution is constant (83), linear and quadratic in time (84), from left to right. Plot taken from [363].

slight underestimate of K^- attenuation over the whole z_h range, and the lack of a strong rise in the proton sector at $z_h \lesssim 0.4$. It can also describe well the Cronin effect on hadron p_T distributions, without need for a broadening of the intrinsic parton transverse momentum $\langle k_T \rangle$ as commonly assumed, see Fig. 58.

An important lesson coming from these simulations is that the geometrical acceptance of the experiment does not fully cancel out in the double ratio which defines the hadron attenuation ratio R_M^h Eq. (28), especially at low $z_h \lesssim 0.4$. This is shown in Fig. 60 right, where unidentified charged hadron attenuation on Kr at HERMES [22] is computed with a 4π detector (dashed line) and the HERMES detector geometric acceptance (solid line), which is important at $z_h \lesssim 0.4$ [364]. In both computations the full kinematic cuts have been included; the dotted line shows the effect of neglecting the $E_h \geq 1.4$ GeV cut.

7.5. Q^2 evolution and time-dependence of the prehadron cross section. –

In the context of string models, hadron attenuation is typically constant in Q^2 . However, a dependence of the prehadron cross section on Q^2 is to be expected on general grounds due to colour transparency (see e.g. [369]), which is a direct consequence of the composite nature of hadrons being made of quarks so that hadrons fluctuate between quark configurations of different sizes. In [370-373] it was found that in scattering of colour neutral objects, configurations with small transverse size b have cross section $\propto b^2$. The size of a colour neutral prehadron is likely to be determined by the hard scale Q^2 of the process, so that we may expect, at least for the leading prehadron, $\sigma_{preh} \propto 1/Q^2$.

After its production, the prehadron must evolve in size until hadron formation; correspondingly, its cross section will evolve in time from σ_{preh} to σ_h . Let us picture the prehadron as a $\bar{q}q$ colour dipole for simplicity. In Ref. [11], it was shown that in a classical picture the size of a pair of colour charges with average $\sqrt{\langle k_T^2 \rangle}$ evolves linearly in time. Therefore, due to colour transparency, its cross section evolves quadratically: $\sigma_{preh} \propto t^2$. If one includes the uncertainty principle in these considerations, the assumption of fixed transverse momentum is not valid, since as $r \rightarrow 0$ we have $k_T \rightarrow \infty$. As a consequence, the rise of the cross section is softened and becomes linear in time: $\sigma_{preh} \propto t$. On the other hand, the struck quark is not a bare particle, but is still accompanied by those parts of the original nucleon field with Fourier components

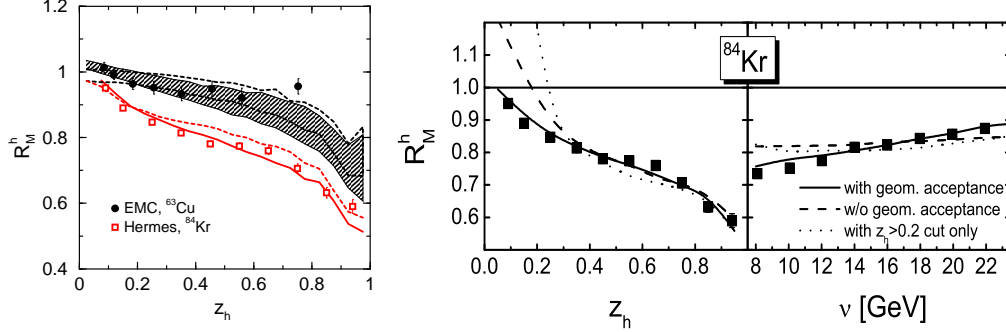


Fig. 60. – *Left*: As in Fig. 59, but for the quantum diffusion scenario (85) compared to the linear time-dependence scenario (dashed line). Plot taken from [363]. *Right*: Effect of the HERMES detector geometric acceptance on measurements of charged hadron attenuation. Solid line: full geometric and kinematic cuts. Dashed line: 4π detector with full kinematic cuts. Dotted line: 4π detector with $E_h \geq 1.4$ GeV cut neglected. Figure taken from Ref. [364].

satisfying $k_T^2 > Q^2$. Hence, the time dependence of σ_{preh} may be expected to lie between linear and quadratic.

In the context of semi-inclusive hadron production in $\ell + A$ collisions, this idea has been phenomenologically explored in Refs. [363, 364] using the GiBUU Monte Carlo generator (see Section 7.4 for more details) and in [360] in the context of the two-scale string model, see Section 7.2. The time evolution of the prehadron cross section is also implemented by means of the colour dipole model in the perturbative fragmentation model of [29], which also includes a Q^2 -dependent production time $t_{preh} \propto (1 - z_h)\nu/Q^2$, see Section 7.3.

In Ref. [363], four scenarios have been explored. In the first, the prehadron cross section is kept fixed,

$$(83) \quad \sigma_{preh} = \frac{1}{2}\sigma_h ,$$

where the proportionality factor has been chosen to reproduce HERMES data. (Note that different proportionality factors arise in different models due to different assumptions on the underlying space-time development of hadronisation, e.g., $\sigma_{preh} = 0.67\sigma_h$ in [61], where prehadron interactions are treated differently.) In the next two scenarios,

$$(84) \quad \sigma_{preh}(t) = \left(\frac{t - t_{preh}}{t_h - t_{preh}} \right)^n \sigma_h \quad n = 1, 2$$

corresponding to the quantum mechanical linear time dependence and the classical quadratic time dependence discussed in [11]. Note that at $t = t_{preh}$, the prehadron is created with zero cross section, and that no dependence on Q^2 is included. The last scenario implements the quantum diffusion picture of Ref. [374], which combines the linear rise in time with a non-zero and Q^2 -dependent value for the initial prehadron cross section:

$$(85) \quad \sigma_{preh}(t) = \sigma_0 + (1 - \sigma_0) \left(\frac{t - t_{preh}}{t_h - t_{preh}} \right) \sigma_h \quad \sigma_0 = r_{lead} \frac{1\text{GeV}^2}{Q^2} ,$$

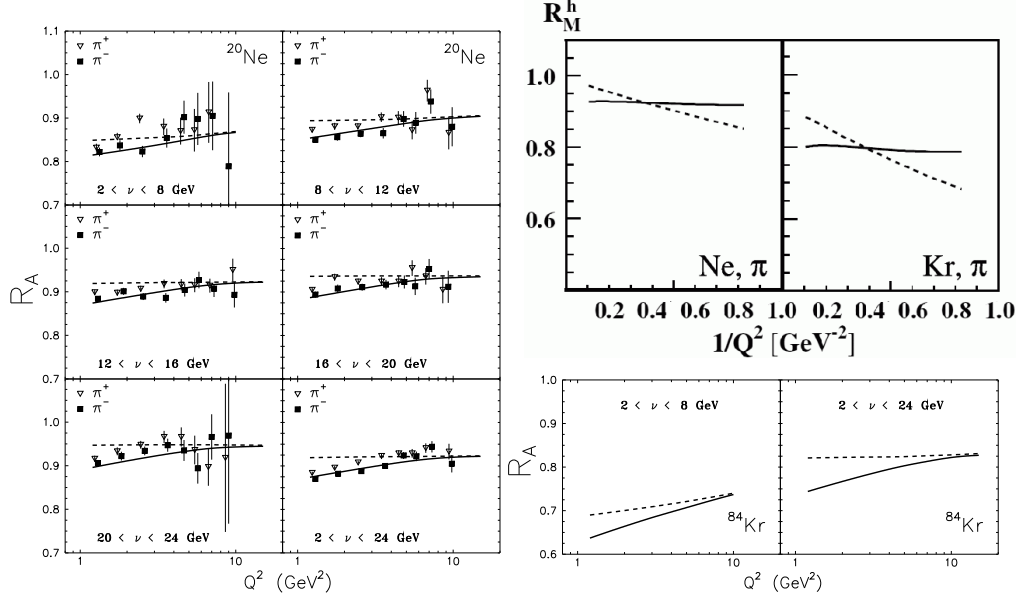


Fig. 61. – *Left and bottom right:* Q^2 dependence of hadron attenuation in the colour dipole model of Ref. [29] for Ne and Kr, respectively. Solid lines include medium-induced gluon bremsstrahlung, dashed lines do not. Points are preliminary HERMES data [23]. *The two plots are taken from [29]. Top right:* Q^2 dependence of hadron attenuation in the absorption model of Ref. [360]. Solid lines computed in the improved two-scale model, with time evolution of the prehadron cross section. Dashed lines computed in the two-scale model without time evolution of the prehadron cross section. Plot adapted from [360].

where r_{lead} is the number of the struck nucleon valence quarks contained in the produced hadron divided by its number of valence quarks. E.g, a leading pion has $r_{lead} = 1/2$ and a subleading one has $r_{lead} = 0$, see Section 7.4. In all scenarios, the prehadronic cross section is 0 before $t = t_{preh}$ and reaches the hadronic σ_h at $t = t_h$, and includes the basic features of colour transparency. These cross sections are sketched in Figure 57. While HERMES data alone do not give enough leverage to distinguish between these time evolution scenarios [360, 364], the combined analysis of EMC and HERMES data singles out the linear evolution scenario [363], see Fig. 59. However, it cannot distinguish between an initial $\sigma_{preh} = 0$ or $\sigma_{preh} \propto 1/Q^2$, despite a large difference in the average $\langle Q^2 \rangle$ in the two cases, even though the latter is slightly preferred, see Fig. 60 left. This result is in line with the slow variation of the attenuation ratio R_M with Q^2 observed at HERMES [23].

An analysis of the Q^2 dependence of R_M^h has been performed in [29, 360]. Based on colour transparency, one expects $R_M = a + b/Q^2 + \mathcal{O}(1/Q^4)$ with negative b . However, if time evolution of the prehadron cross section to reach the full hadronic one is sufficiently fast, its Q^2 dependence can become negligible. This is shown in Fig. 61, top right, as difference between the solid and dashed line, computed with a linear time dependence (Eq. (85)) and no time dependence respectively [360]. In [29], where colour transparency and the time evolution of the prehadron cross section are naturally implemented in the light-cone dipole formalism, two further elements contribute to the Q^2 dependence of R_M^h . The first is the Q^2 dependence of the production time $t_{preh} \propto 1/Q^2$, which increases the in-medium prehadron path length and consequently its attenuation with increasing Q^2 , working in the opposite direction as colour transparency. The net

effect is an almost Q^2 -independent attenuation ratio for light nuclei, which gains a small slope on heavy targets or for low ν cuts, see Fig. 61. The second is medium-induced gluon bremsstrahlung, which induces an additional attenuation at small Q^2 , but whose effect disappears at large Q^2 , see Fig. 61. A comparison of model computation with HERMES data on Q^2 distributions in light and medium-heavy nuclei (Ne , Kr , Xe) from Ref. [23], which show a pretty slow variation of R_M with Q^2 , and the forthcoming JLab multi-differential measurements of z and Q^2 distributions will shed light on this problem.

In Ref. [61, 64], a different kind of Q^2 dependence has been explored, namely, the possibility of a modification of fragmentation functions induced by a partial deconfinement in the nuclear wave function [375-377]. It results in a Q^2 rescaling of the FF:

$$(86) \quad D(z_h, Q^2) \rightarrow D(z_h, \xi_A(Q^2)Q^2) \quad \xi_A(Q^2) = \left(\frac{\lambda_A}{\lambda_0}\right)^{2\alpha_{s0}/\alpha_s(Q^2)}$$

where α_{s0} is the strong coupling constant computed at the scale at which DGLAP evolution starts, λ_0 is the nucleon radius in the vacuum and λ_A is the radius in the medium. The rescaling factor ξ_A depends on the amount of nucleon overlap in the nuclear wave functions, and depends on Q^2 because of DGLAP evolution [376, 377].

The phenomenological consequence is a multiplicity ratio which slightly decreases with Q^2 contrary to what is experimentally observed: partial deconfinement does not seem to affect fragmentation functions (even though it might modify the parton distribution functions, and lead to a possible explanation of the EMC effect [109]). This might have to do with the fact that hadrons are typically formed outside the medium in the HERMES kinematics, so that deconfinement is not affecting them. At JLab, or for smaller values of ν at HERMES, hadrons will be in part formed inside the medium and partial deconfinement may affect their fragmentation.

In summary, the Q^2 dependence of hadron attenuation is very sensitive to the underlying dynamics of the hadronisation process. However, since different physics inputs in theory models can have similar effects on the computation of R_M^h , this observable must be used in conjunction with others like the hadron transverse momentum broadening, and with the requirement to describe attenuation in both low-energy experiments (CLAS, HERMES) and high-energy experiments (EMC), to sort out the physics underlying hadron attenuation.

7.6. Prehadron absorption in hot QCD matter. –

In Ref. [378, 379], prehadron absorption in hot nuclear matter as a mechanism for jet quenching in $A + A$ collisions, has been considered in the context of a transport model similar to the GiBUU model described in Sect. 7.4. The medium formation and evolution is described in the Hadron-String Dynamics (HSD) approach [367, 380, 381]. The prehadron formation and evolution is the same as in the GiBUU model, with the additional assumption that hadrons are not allowed to be formed if the medium energy density at their point in space and time is above the critical energy density for a QGP formation, $\epsilon_c = 1 \text{ GeV/fm}^3$. This requirement mimics the effect of a QGP on high-energy hadrons, even though the produced medium in the HSD simulations is always a hadron gas. Note, however, that the energy-density cut is not assumed to affect the prehadronic states. In addition, the model phenomenologically includes the Cronin enhancement at intermediate p_{Th} by a nuclear enhancement of the intrinsic parton transverse momentum.

Two different scenarios for the space-time evolution of prehadrons have been used in the simulations. In the first scenario, the leading prehadron cross section is constant and the hadron formation proper time is kept fixed at $\tau = 0.5 - 0.8 \text{ fm}$. The resulting hadron suppression is mostly due to the interaction of the leading prehadron with the medium, and is sufficient to

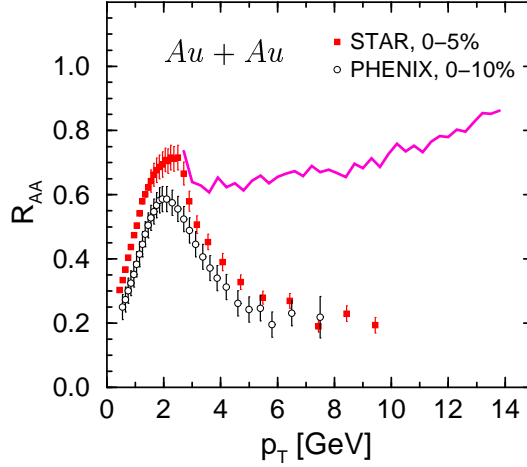


Fig. 62. – Suppression factor R_{AA} as a function of $p_T \equiv p_{Th}$, for midrapidity charged hadrons in 0-5% central $Au + Au$ collisions at RHIC top energy, $\sqrt{s_{NN}} = 200$ GeV. The solid curve is the hadron quenching computed when the leading prehadron cross section rises linearly in time according to Eq. (84) with $t_{preh} = 0$ and $n = 1$. Experimental data are from Refs. [149, 156]. The figure is taken from Ref. [378].

explain most of the hadron quenching at RHIC. This is interpreted by the authors as evidence that prehadronic final-state interactions can result in the observed jet quenching results. However, when the leading prehadron cross section grows linearly with time, as requested by a consistent description of HERMES and EMC data for nuclear DIS [363], the resulting hadron quenching is clearly insufficient to explain data for RHIC central $Au + Au$ collisions, see Fig. 62. Therefore, prehadronic final state interactions seem ruled out as main mechanism for hadron quenching at RHIC, while they may in fact be responsible for hadron quenching in $e + A$ collisions.

The reason may be that, contrary to the assumptions in the HSD model, prehadrons cannot be formed in the QGP phase ($\epsilon > \epsilon_c$) because of the screening of the colour force needed to bind them. If this is the case, the struck quark remains bare and interacts with the medium until it escapes from it or until the medium enters the hadron gas phase. Only at this point the hadronisation process can start but at this stage the medium is too dilute and the prehadronic interactions are too weak to substantially contribute. On the other hand, in the QGP phase, partonic energy loss can be important because of the large colour charge density. If this explanation is correct, it would be interesting to confront the HSD prehadron absorption model with $R_{p_b p_b}(p_T)$ data at SPS energies (note, however, that we currently lack high- p_T $p + p$ spectra at around $\sqrt{s_{NN}} = 17$ GeV [159]) where the QGP is formed in a more restricted range of centralities, if at all, and is shorter lived than at RHIC. A good description of peripheral collisions data may validate the model, so that a substantial overestimate of central collision data might be interpreted as evidence for the formation of a QGP.

8. – Challenges and outlook

In this last Section, we discuss observables that can help to better understand parton propagation and fragmentation in QCD matter and, in particular, the relative role of perturbative parton energy loss (Section 6) and prehadron absorption (Section 7) mechanisms. We conclude with a review of proposed future facilities and experiments.

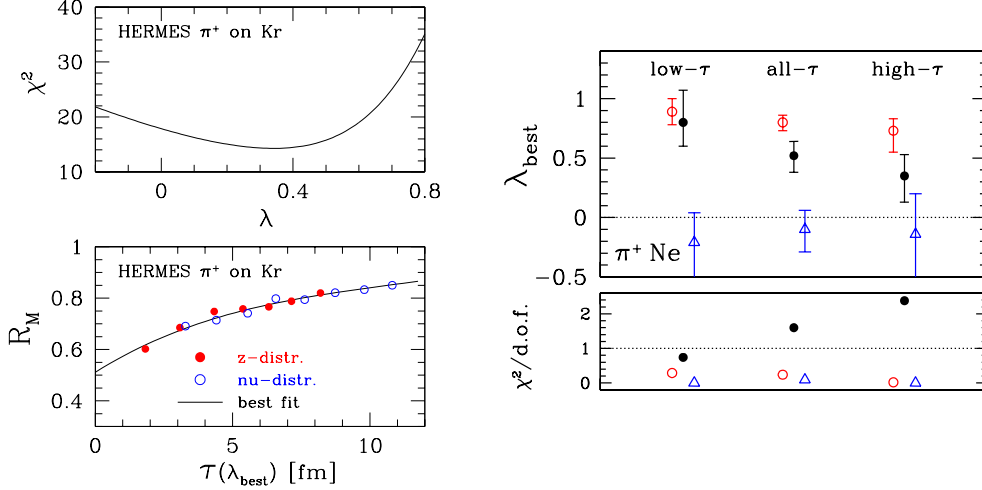


Fig. 63. – Results of the production-time τ scaling analysis of HERMES data on π^+ production on Kr targets [22]. *Left*: z - and ν - distributions as a function of τ with corresponding χ^2 as a function of the exponent λ . *Right*: Scaling exponent and χ^2 per degree of freedom for “low- τ ” and “high- τ ” data sets compared to the full data set for pion production on Ne targets corresponding to “medium- τ ”. Black disks: π^+ from preliminary HERMES data [383]. Red circles: π^+ from the AGMP absorption model [61, 326]. Blue triangles: π^\pm from the energy loss model of Refs. [320, 326].

8.1. Partonic versus (pre)hadronic energy loss in nuclear DIS. –

Despite very different assumptions on the parton lifetime, the models presented in Section 6 (resp. 7) based on partonic (resp. prehadronic) degrees of freedom, usually reproduce quite well the experimental results on the multiplicity ratio R_M^h in $e + A$ collisions. It is therefore necessary to study observables which are more directly sensitive to the space-time evolution of the hadronisation process and can discriminate between partonic and pre-hadronic contributions. Candidates suggested in the literature include the atomic mass A dependence of the nuclear attenuation, its production time scaling, and the hadron transverse momentum broadening.

8.1.1. Mass number dependence. – The mass number dependence of the nuclear attenuation ratio $1 - R_M^h$ had been suggested as an observable sensitive to the different mechanisms involved in the hadronisation process. To leading order in $A^{1/3}$, one expects $1 - R_M^h \propto A^{2/3}$ in energy loss models because the average energy loss $\Delta E_q \propto \langle L_q^2 \rangle \propto A^{2/3}$ for partons with asymptotic energies, due to the LPM interference in QCD [140]. On the other hand, in absorption models the survival probability is proportional to the amount of traversed matter, so that $1 - R_M^h \propto \langle L_A \rangle \propto A^{1/3}$ [349–351]. However, it has been recently shown [61, 321, 363, 382] that this simplistic argument does not really hold for absorption models, where additional powers of $A^{1/3}$ need to be introduced to account for non-zero values of $\langle t_{preh} \rangle$, thus predicting $R_M^h \propto A^{2/3} + \mathcal{O}(A)$ as in energy loss models. Moreover, hadron attenuation is not likely to be describable by a simple A^α power-law for nuclei with $A \gtrsim 80$ [326].

8.1.2. Production time scaling in $nDIS$. – In Ref. [384] it is conjectured that R_M should depend on a scaling variable τ defined as

$$(87) \quad \tau = C z_h^\lambda (1 - z_h) \mu \nu ,$$

rather than on z_h and ν separately, i.e.

$$(88) \quad R_M = R_M[\tau(z_h, \nu)].$$

The scaling exponents λ and μ can be obtained by a best fit analysis of data or theoretical computations, whereas the proportionality constant C cannot be determined from the fit. Both absorption and energy loss models can be distinguished by the value of the scaling exponent: a positive λ value is characteristic of absorption models, which assume a short $\langle t_{preh} \rangle$ with a functional form similar to Eq. (87); while a zero or negative $\lambda \lesssim 0$ is predicted within energy loss models due to energy conservation (a parton cannot radiate more energy than $(1 - z_h)\nu$).

The fits performed in Ref. [384] and similarly in Ref. [23] (with $\mu = 1$ taken from analytical Lund model computations [63, 64]) show that τ is indeed a good scaling variable to analyze the HERMES data, see Fig. 63 (left), and furthermore it lives up to the promise of separating energy loss and absorption models. The charged pion data exhibit globally a clear $\lambda = 0.5 \pm 0.15$, which, being positive and different from zero, indicates that pre-hadronic effects significantly contribute to R_M^π and allows to interpret $\tau \approx \langle t_{preh} \rangle$. Moreover, it has been shown by applying different cuts on z_h and ν that the λ exponent derived from experimental data decreases with increasing τ , thus suggesting an increasing contribution of partonic energy loss, see Fig. 63 (right). Finally, the slight pion-charge and nuclear-mass number dependence of the λ exponent observed in Ref. [384] may indicate additional dynamics beside production time and prehadron absorption. Fits to other hadron flavors, such as kaons, protons and antiprotons, are less conclusive due to the limited statistics.

In conclusion, the τ -scaling analysis of R_M seems a promising tool for studying energy-loss and formation-time contributions to hadron attenuation. However, new higher precision data sets in a wider range of ν , mass number and hadron flavors are necessary to determine a possible scaling with $\mu \neq 1$ and to fully exploit this observation.

8'1.3. p_T -broadening and prehadron formation time. – The scaling analysis for R_M just described gives only indirect evidence of the pre-hadron formation time effects, but does not allow to measure the absolute scale of $\langle t_{preh} \rangle$. A more sensitive observable to the pre-hadron formation time is the hadron transverse momentum broadening $\Delta\langle p_T^2 \rangle$ in nDIS compared to a proton or deuteron target [29, 70]. The p_T -broadening is commonly believed to arise essentially during parton propagation because the prehadron is the quark momentum broadening Δp_T^2 is proportional to the quark path-length in the nucleus [140], and the prehadron is supposed to have a negligible elastic cross section [29]. Under these assumptions, and remembering that hadron and parton transverse momenta are related by $p_T = zk_T$ [385] with $z \approx z_h$ at LO, we obtain

$$(89) \quad \langle \Delta\langle p_T^2 \rangle \rangle \approx z_h^2 \hat{q} \langle t_{preh} \rangle$$

with \hat{q} the partonic transport coefficient, and the prehadron formation time obtained from the discussed scaling analysis:

$$(90) \quad \langle t_{preh} \rangle = C z_h^{0.5 \pm 0.15} (1 - z_h) \nu,$$

with C setting the overall scale of the production time to be determined from broadening data.

The seemingly linear in $A^{1/3}$ dependence at HERMES (Figure 21) leads to the conclusion that the prehadron is formed close to the surface or outside the heaviest nucleus, at least at the average kinematics $\langle z_h \rangle = 0.41$ and $\langle \nu \rangle = 14.0$ GeV. Using an average in-medium path length

	$\langle Q^2 \rangle$ [GeV ²]	$\langle \nu \rangle$ [GeV]	$\langle z \rangle$	$\frac{\langle Q^2 \rangle}{2m_N \langle \nu \rangle}$	$\langle t_p \rangle$ [fm]
$\langle \Delta p_{Th}^2 \rangle$ vs A					
Ne (2.3 fm)	2.4	13.7	0.42	0.09	4.2
Kr (3.7 fm)	2.4	13.9	0.41	0.09	4.2
Xe (4.3 fm)	2.4	14.0	0.41	0.09	4.3
$\langle \Delta p_{Th}^2 \rangle$ vs z					
	2.4	14.6	0.30	0.09	4.5
	2.4	13.3	0.53	0.10	3.7
	2.3	12.6	0.74	0.10	2.3
	2.2	10.8	0.92	0.11	0.7
$\langle \Delta p_{Th}^2 \rangle$ vs ν					
	2.1	8.1	0.48	0.14	2.4
	2.5	12.0	0.42	0.11	3.7
	2.6	15.0	0.40	0.10	4.6
	2.4	18.6	0.36	0.07	5.8
$\langle \Delta p_{Th}^2 \rangle$ vs Q^2					
	1.4	14.0	0.41	0.06	4.2
	2.4	14.1	0.41	0.10	4.2
	4.5	14.5	0.39	0.16	4.3

TABLE XI. – Average HERMES kinematics for the p_T -broadening results [386, 387]. In parentheses (next to the target nucleus symbol) is the average in-medium path length of the hadronising system $\langle L_A \rangle \approx (3/4)R_A$, with $R_A = (1.12 \text{ fm})A^{1/3}$. The production time is computed according to Eqs. (89)-(90) with $C = 0.8 \text{ fm/GeV}$. The average $\langle x_B \rangle$ is very well approximated by $\langle Q^2 \rangle / (m_N \langle \nu \rangle)$.

$\langle L_{Xe} \rangle \approx (3/4)R_{Xe} = 4.3 \text{ fm}$ in Eq. (90) one finds

$$(91) \quad C \gtrsim 0.8 \text{ fm/GeV} .$$

The resulting prehadron production time is plotted in Fig. 64 left, and computed for each experimental bin in Table XI. However, the size of the p_T -broadening requires $\hat{q} \approx 0.03 \text{ GeV}^2/\text{fm}$, which is much smaller than the $\hat{q} = 0.60 \text{ GeV}^2/\text{fm}$ obtained by fitting HERMES data on R_M with a pure energy loss model. Part of this discrepancy is due to the fact that the energy loss model used in the fit of R_M is known to systematically overestimate the transport coefficient compared to other implementations [166]. However, this can hardly explain the factor ~ 20 discrepancy found here. One possible explanation is that $\langle t_{preh} \rangle$ is in fact smaller than just estimated.

Turning to the z_h dependence (Figure 20), the observed decrease as $z_h \rightarrow 1$ is qualitatively compatible with the production times just derived (because $\langle t_{pre} \rangle \rightarrow 0$ as $z_h \rightarrow 1$), but also with long formation times and a pure energy loss scenario (because energy conservation requires $\Delta E_q \leq (1 - z_h)\nu$). However, in either case it is very hard to reproduce the detailed shape in z_h . Indeed, due to the z_h^2 factor in Eq. (89) in both cases $\langle \Delta p_T^2 \rangle$ would have a peak at $z_h \gtrsim 0.7$, shifting to larger z_h values as A decreases. (Note that this behaviour of the peak with A is rather independent of the detailed shape of $\langle t_{preh} \rangle$.) This is at variance with HERMES data, which show a fixed peak around $z_h \approx 0.5$, whose size increases with A . One scenario not considered so far in literature involves short formation times with large transport coefficients, to explain the shape in z_h , and a non-negligible prehadron elastic cross section to explain the A dependence

On the other hand, the basically flat in ν dependence of the broadening would be compatible with the production time estimate of Eq. (91). However, one should keep in mind that $\langle x \rangle$ de-

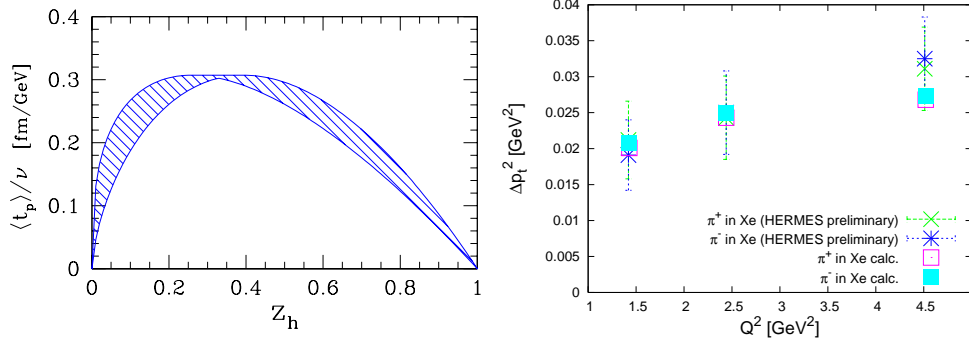


Fig. 64. – *Left*: Pre-pion formation time per unit ν estimated in Ref. [384]. *Right*: hadron p_T -broadening at HERMES as a function of Q^2 compared to the computations of Ref. [390].

creases with ν so that NLO contributions increase; since they tend to decrease the average energy of the fragmenting quarks they might in fact contribute to tilt down the slope.

Finally, the linear increase of $\Delta\langle p_T^2 \rangle$ with Q^2 observed at HERMES (see e.g. Fig. 64) remains a challenge to current theoretical models. This dependence is in sharp contrast with the inverse power dependence from the colour dipole model of Ref. [29], thus ruling out the predicted $t_{preh} \propto E_{preh}/Q^2$ behaviour due to the stronger gluon radiation. A flat Q^2 predicted within most string-based models is also at variance with these data. Since a growing in Q^2 prehadron formation time seems unlikely, dynamical effects at the parton level are needed in addition to prehadron absorption to explain the Q^2 -behaviour. Three mechanisms have been suggested in Ref. [388]:

1. *Medium-enhanced DGLAP evolution.* The longer medium-enhanced DGLAP evolution [303-305, 389] at larger Q^2 would imply a stronger gluon radiation, hence a larger p_T -broadening than at low Q^2 .
2. *Next-to-leading order processes.* At NLO, gluon fusion process, $\gamma^* + g \rightarrow q + \bar{q}$, imply $E_q < \nu$, hence a smaller production time and p_T -broadening than at LO. The increasing importance of LO vs. NLO processes as $x_B = Q^2/(2m_N\nu)$ increases could lead to the observed p_T -broadening dependence on Q^2 .
3. *Prehadrons with very short production time,* and inelastic cross section $\sigma_{preh}(t_p) \propto 1/Q^2$ slowly evolving in time. Under these conditions, they will be the less absorbed the larger Q^2 , suffer a smaller surface bias and contribute more to $\Delta\langle p_T^2 \rangle$.

Reference [388] also argues that studying the p_T -broadening simultaneously binned in x and Q^2 allows one to factor out the trivial $\nu = Q^2/(2m_N x_B)$ kinematic correlations and to distinguish the proposed scenarios.

The effect of medium modification of the DGLAP evolution has been explored quantitatively in Ref. [390], which proposes

$$(92) \quad \Delta\langle p_T^2 \rangle(Q^2) = \Delta\langle p_T^2 \rangle(\bar{Q}^2) + z_h^2 \nu \hat{q} \left(\frac{1}{\bar{Q}^2} - \frac{1}{Q^2} \right).$$

The first term is the p_T -broadening from quark multiple scatterings, computed at $\bar{Q}^2 = 2.5 \text{ GeV}^2$ using $\langle t_p \rangle = 1.19 z_h^{0.61} (1 - z_h)^{1.09} \nu / \kappa$ from [61, 64] and a transport coefficient $\hat{q} = 0.032 \text{ GeV}^2/\text{fm}$

calculated in the dipole model for quark-nucleon scattering. The second term models the effects of the medium modified DGLAP evolution from Ref. [305]. Numerical results are presented in Fig. 64 right. Note that Eq. (92) predicts a plateau in $\Delta\langle p_T^2 \rangle$ at $Q^2 \gtrsim 4 \text{ GeV}^2$, which should be experimentally verified.

8'1.4. A path forward. – As we have seen, HERMES data suggest relatively short production times, such that the prehadron is formed in average close to the nucleus surface, or even much more inside as the z_h dependence of the p_T -broadening seems to require. The details of the ν dependence of the p_T -broadening and its linear increase with Q^2 demand for parton-level dynamics typically not included in theoretical models.

To clarify this complex interplay between parton dynamics and hadronisation, one needs detailed theoretical computations, combining energy loss and prehadron absorption up to NLO, and accounting for surface bias effects mostly neglected in these simplified considerations. A production time scaling analysis of high precision R_M data coupled to a detailed study of the p_T broadening dependence on all kinematic variables is likely to reveal the size of the production time and yield information on parton versus (pre)hadron dynamics. Experimentally, progress will be achieved by multi-dimensional binning, improved statistics for different hadron flavours, and using an extended set of targets up to Pb .

The CLAS experiment is ideally suited for such a programme, but has a reduced range in $\nu \lesssim 5 \text{ GeV}$, which enhances the role of prehadron absorption over parton energy loss, and in $x_B \gtrsim 0.1$. Its preliminary data follow the same qualitative behaviour of HERMES data, but the measured p_T -broadening is larger than what would be naively extrapolated from HERMES results based on the different average $\langle \nu \rangle$. This might be due to a significant prehadron elastic cross section, $\sigma_{preh}^{el} \propto \sigma_h^{el}$, additionally contributing to the hadron p_T -broadening at CLAS, but negligible at HERMES [390]. The origin of the CLAS/HERMES discrepancy needs clarification.

Finally, the Electron-Ion Collider (EIC) [46, 47], able to span from very small to large x_B , may clarify the role of LO and NLO processes. Furthermore, it will provide a large range in ν , which will allow for the study of purely partonic in-medium propagation and the calibration of energy-loss models.

8'2. π^0 vs. η attenuation. –

The measurement of π^0 and η suppression, which have a similar valence quark content but different masses and different hadronic cross sections, can provide an interesting cross-check of the hadronisation picture and time-scales for (pre)hadron formation. In $Au + Au$ collisions at RHIC, the PHENIX experiment [147] has shown a similar suppression $R_{AA}(p_T)$ ratio for the two species up to $p_T \approx 10 \text{ GeV}/c$, with the π^0/η ratio independent of the collision system or centrality of the $Au + Au$ collisions within uncertainties, see Fig. 30 (right). Such a result is naturally explained if the suppression takes place at the *partonic* level before the quenched parton fragments into final hadrons [146, 147], i.e., hadronisation occurs on timescales larger than the typical medium size. Yet, hadronisation in a deconfined QGP could be delayed compared to cold QCD matter at least until the medium temperature falls below the critical one. In fact results from $e + A$ collisions at HERMES, where the quark energy $\nu \approx p_{T|RHIC}$ but the virtuality $Q^2 = 2.5 \text{ GeV}^2 \ll p_T^2 = \mathcal{O}(100 \text{ GeV}^2)$, seem to favour much shorter hadronisation timescales for hard partons (Sect. 8'1).

It would be thus important to measure and compare π and η attenuation in nDIS experiments, where clean measurements are possible and no QGP is formed. These measurements are planned for the CLAS experiment and will also be very important in a hadronisation physics programme at the proposed EIC.

8'3. *Baryon formation* . –

Protons, and in general 3-quark baryon species, seem to follow a different nuclear modification pattern than mesons in both cold and hot nuclear matter. In nDIS, the difference observed in proton vs. mesons multiplicity ratios resembles the anomalous baryon enhancement reported at intermediate $p_T \approx 1.5 - 8$ GeV/c in proton-nucleus and heavy-ion collisions. However, antiprotons follow the mesons attenuation pattern, unlikely what happens in $p + A$ collisions where both baryons and antibaryons are anomalously enhanced. Contrasting the baryon nuclear modifications in nDIS and $p + A$ collisions will clearly lead to a more profound understanding of the hadronisation mechanism.

8'4. *High- p_T hadrons at fixed-target energies* . –

The detailed interpretation of the nucleus-nucleus and proton-nucleus data and the relative roles of high- p_T hadron suppression and Cronin enhancement at around $\sqrt{s_{NN}} = 20$ GeV is obscured by the current absence of a direct measurement of the corresponding $p + p$ reference spectra at these energies. Use of various $p + p$ interpolations [159, 391] compared with the $A + A$ data measured at top SPS [160, 161] or low RHIC [176] energies, seems to indicate the onset of parton energy loss in this energy range. Precise tests of the mechanisms of p_T broadening in $p + A$ and of parton and/or (pre)hadron energy loss in $A + A$ require the measurement of the baseline vacuum production of various hadron species in a perturbative regime ($p_T \gtrsim 2$ GeV/c) in $p + p$ collisions at $\sqrt{s_{NN}} = 20$ GeV. Such large statistics measurements can hopefully be made in coming low energy scans at RHIC (and at higher luminosity in the planned RHIC-II upgrade).

8'5. *The heavy flavour puzzle* . –

The solution of the intriguing heavy-flavour results at RHIC, namely the larger than expected suppression of heavy flavour production in central $A + A$ collisions, is likely to provide important insights in our theoretical understanding of parton propagation and hadronisation, and on the nature of the Quark-Gluon Plasma.

On the theory side it has already prompted a revision of established ideas and stimulated many new ones, see Section 5'2. However, no consensus has been reached yet on the physical mechanism behind the large heavy-flavour suppression. Interestingly, heavy quark energy loss and in-medium propagation are processes that can be addressed in AdS/CFT-based descriptions of the QGP, and they are very promising to investigate the relevance of string-theory methods for discussing QCD near the deconfinement phase transition [392].

On the experimental side, new clues will be offered in the near future by experimental upgrades at RHIC, aimed at directly identifying D and B mesons and at measuring their individual suppression factors [194]. At the LHC, heavy-flavour production will be more abundant, and its nuclear modification one of the main areas of experimental interest because of their potential role in identifying and studying the QGP properties [393, 394, 418]. At the Electron-Ion Collider, a clean measurement of D and B suppression will also be able to discriminate the proposed mechanisms, and remove the uncertainties in the interpretation of the data due to the modelling of the medium created in $A + A$ collisions, and to possible in-medium regeneration processes.

8'6. *Dihadron and photon-hadron correlations* . –

High- p_T two- and three-hadron correlations have proven a rich field to characterise medium modifications of parton fragmentation in $A + A$ collisions, see Section 5'3. One can more directly

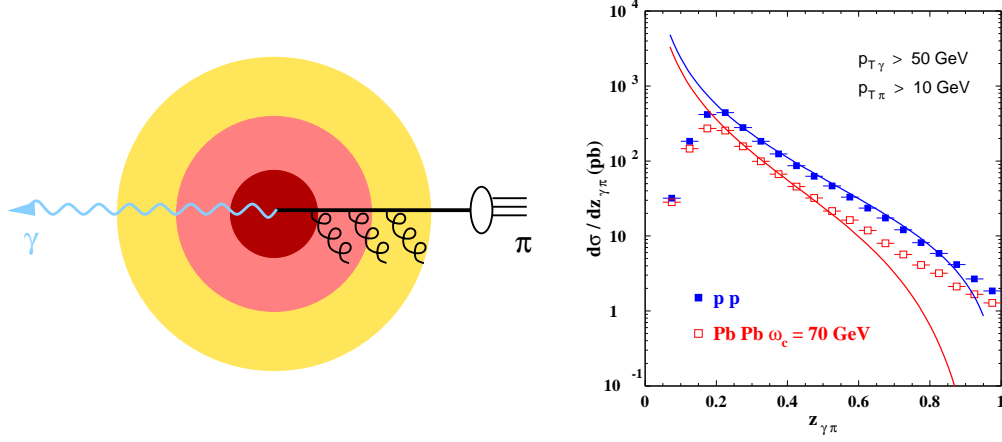


Fig. 65. – *Left*: A leading-order channel for $\gamma\pi^0$ production. *Right*: $\gamma\pi^0$ imbalance distributions using $p_{T\pi}^{\text{cut}} = 10$ GeV/c and $p_{T\gamma}^{\text{cut}} = 50$ GeV. The solid lines show the (rescaled) quark fragmentation functions used in the calculation.

access medium-modified FF in heavy-ion collisions by tagging large- p_T particle production with prompt photons, as suggested in [281] and later investigated in detail at RHIC and LHC energy [228, 395]. As shown in Fig. 65 left, at large p_T and leading order in α_s , a photon is produced directly in the hard subprocess, back-to-back to e.g. a quark which loses energy in the medium before fragmenting into a pion. Because of momentum conservation, the experimental $\gamma\pi^0$ momentum imbalance variable, $z_{\gamma\pi} \equiv -\mathbf{p}_{T\pi} \cdot \mathbf{p}_{T\gamma} / |\mathbf{p}_{T\gamma}|^2$, reduces at LO to the theoretical hadron fractional momentum z which can therefore be experimentally estimated. In Fig. 65 right, the $\gamma\pi^0$ distributions is computed in QCD at LO in $p + p$ and $Pb + Pb$ collisions at the LHC. The observable tracks the quark FF into pions until the onset of the photon-fragmentation channel at large $z_{\gamma\pi}$ in a wide range of $z_{\gamma\pi}$. This simple connection between $z_{\gamma\pi}$ and z , is however complicated by the effects of higher-order corrections or initial- and final-state soft gluon radiation. The most important background channel, to be reduced with appropriate kinematics and isolation cuts, is photon production by the collinear fragmentation of a hard parton.

In contrast to heavy-ions, only dihadron correlations in z_h have been measured in $e + A$ collisions, see Section 3.5. They are the analog of the “same-side” (intrajet) dihadron correlation in $A + A$ integrated over the azimuthal angle, but are not affected by the complication of hot QCD matter effects. In the HERMES kinematics, $\langle x \rangle \approx 0.1$ where the gluon density is comparable to the quark density. Hence the processes $\gamma + q \rightarrow q + g$ and $\gamma + g \rightarrow q + \bar{q}$ may compete with the LO $\gamma + q \rightarrow q$ scattering. For NLO processes, the smaller parton energy implies a larger nuclear suppression for either hadron, which in turn biases the hard scattering towards the nuclear surface. Moreover, the subleading hadron may be produced with larger z than the leading hadron, which complicates a naive interpretation of the observable. For these reasons, the relative importance of NLO compared to LO hadron production may be amplified in dihadron correlation compared to single-inclusive observables. An observable which is directly sensitive to $\mathcal{O}(\alpha_s)$ partonic cross sections, and could cross-check the dihadron z_h correlations, is the dihadron azimuthal correlation relative to the virtual photon direction.

Photon-hadron correlations will be one of the key measurements at CLAS, and very interesting for a hadronisation programme at the EIC. Moreover, the photon-hadron transverse momentum imbalance with respect to the virtual photon axis will allow one to study the analog of the

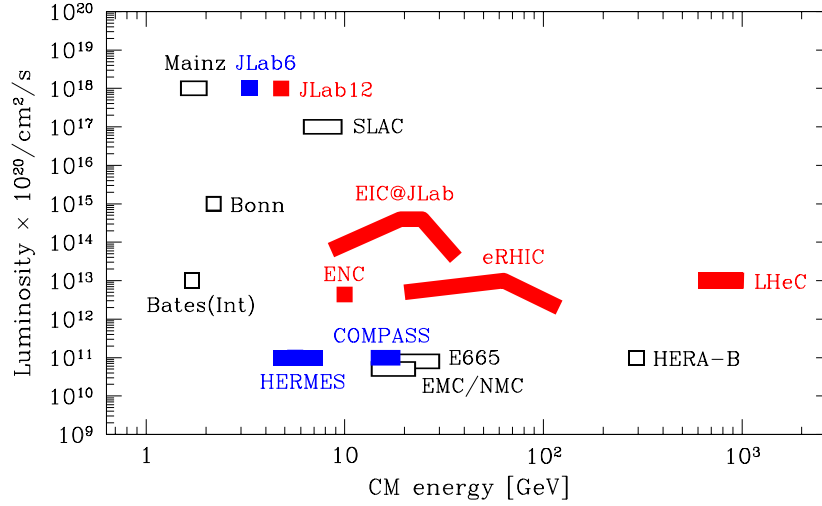


Fig. 66. – Centre-of-mass energy vs. luminosity of past, present, approved and proposed lepton-nucleus facilities and experiments.

same-side (inrajete) hadron correlations with the added advantage of measuring the transverse momentum of the jet.

8.7. Future perspectives . –

The challenges just discussed can be addressed and likely solved at future facilities planned (or proposed) to become operational within the next decade and beyond. The LHC heavy-ion programme, the RHIC-II upgrade, the 12-GeV upgrade at Jefferson Lab, and the Electron Ion Collider are examples of planned new facilities with capabilities that will significantly increase the existing experimental reach in terms of energy and luminosity, see Fig. 66.

8.7.1. The 12-GeV Jefferson lab upgrade. – The 12-GeV accelerator upgrade of JLab will significantly extend existing experimental capabilities by doubling the accelerator electron-beam energy and by increasing the luminosity by at least an order of magnitude for large-acceptance fixed-target measurements. The CLAS12 spectrometer will operate with a continuous luminosity of $1\text{--}2 \times 10^{35} \text{ cm}^{-2} \text{ s}^{-1}$ for nuclear target experiments with an 11-GeV electron beam. The planned particle identification scheme, which will directly identify pions, low-energy charged kaons, neutral kaons, protons, and electrons, can be upgraded to include direct detection of higher-energy charged kaons as well. With the increased luminosity comes access to rarer hadrons whose attenuation in the nuclear medium has never before been explored.

Table XII lists hadrons accessible with CLAS12 that are stable over nuclear distance scales. Nuclear attenuation measurements can be performed for all of these hadrons, and transverse momentum broadening will be directly accessible for a number of the listed hadrons. Estimations for the CLAS12 geometric acceptances for these particles are plotted in Fig. 67. As can be seen, a systematic study of the mass dependence for two-quark systems is feasible for eight meson species with a range of masses spanning nearly $1 \text{ GeV}/c^2$. Further, new insights into the poorly-understood hadronisation mechanisms for baryons can be gained by studying the series of eight

hadron	$c\tau$	mass (GeV/c ²)	flavour content	detection channel	Production rate per 1k DIS events
π^0	25 nm	0.13	$u\bar{u}d\bar{d}$	$\gamma\gamma$	1100
π^+	7.8 m	0.14	$u\bar{d}$	direct	1000
π^-	7.8 m	0.14	$d\bar{u}$	direct	1000
η	0.17 nm	0.55	$u\bar{u}d\bar{d}s\bar{s}$	$\gamma\gamma$	120
ω	23 fm	0.78	$u\bar{u}d\bar{d}s\bar{s}$	$\pi^+\pi^-\pi^0$	170
η'	0.98 pm	0.96	$u\bar{u}d\bar{d}s\bar{s}$	$\pi^+\pi^-\eta$	27
ϕ	44 fm	1.0	$u\bar{u}d\bar{d}s\bar{s}$	K^+K^-	0.8
f_1	8 fm	1.3	$u\bar{u}d\bar{d}s\bar{s}$	$\pi\pi\pi\pi$	-
K^+	3.7 m	0.49	$u\bar{s}$	direct	75
K^-	3.7 m	0.49	$\bar{u}s$	direct	25
K^0	27 mm	0.50	$d\bar{s}$	$\pi^+\pi^-$	42
p	stable	0.94	ud	direct	530
\bar{p}	stable	0.94	$\bar{u}\bar{d}$	direct	3
Λ	79 mm	1.1	uds	$p\pi^-$	72
$\Lambda(1520)$	13 fm	1.5	uds	$p\pi^-$	-
Σ^+	24 mm	1.2	us	$p\pi^0$	6
Σ^0	22 pm	1.2	uds	$\Lambda\gamma$	11
Ξ^0	87 mm	1.3	us	$\Lambda\pi^0$	0.6
Ξ^-	49 mm	1.3	ds	$\Lambda\pi^-$	0.9

TABLE XII. – *Final-state hadrons potentially accessible for formation length and transverse momentum broadening studies in CLAS12. The rate estimates were obtained from the LEPTO event generator for an 11-GeV incident electron beam. (The criteria for selection of these particles was that $c\tau$ should be larger than the nuclear dimensions, and their decay channels should be measurable by CLAS12.)*

baryon species indicated in this table. While experimentally challenging, the baryon measurements have the potential to open up a completely new realm of studies of hadron formation for three-quark systems.

8.7.2. Other fixed target experiments: DIS and DY. – The ongoing fixed-target COMPASS experiment [396] with its up to 190 GeV muon beam, can cover a much larger ν and Q^2 range than HERMES or JLab. In particular, due to the higher reach in ν , one can select partons hadronising outside the medium, and cleanly test parton energy loss models by studying the hadron p_T -broadening. Therefore, a $\mu + A$ experimental programme at COMPASS would be very desirable to improve our knowledge of the space-time evolution of hadronisation and anticipate some of the results expected at the future electron-ion colliders discussed in Sect. 8.7.4. At the same time the availability of a high-energy proton or pion beam would allow measuring nuclear modifications of DY processes and studying the interplay of initial state and final state parton energy loss within the same detector.

Dedicated high-statistics medium energy DY experiments have been proposed in [318] to precisely measure initial-state parton energy loss in nuclear targets. The authors considered using the proton beams from the 120 GeV Fermilab Main Ring Injector and the future 50 GeV Japan Hadron Facility (JPARC). The kinematic acceptance of a dimuon spectrometer proposed for the Fermilab Experiment E906 [397] and a similar spectrometer considered [398, 399] at JPARC. The nuclear partons are probed in the $0.1 < x < 0.5$ region where the anti-shadowing and the

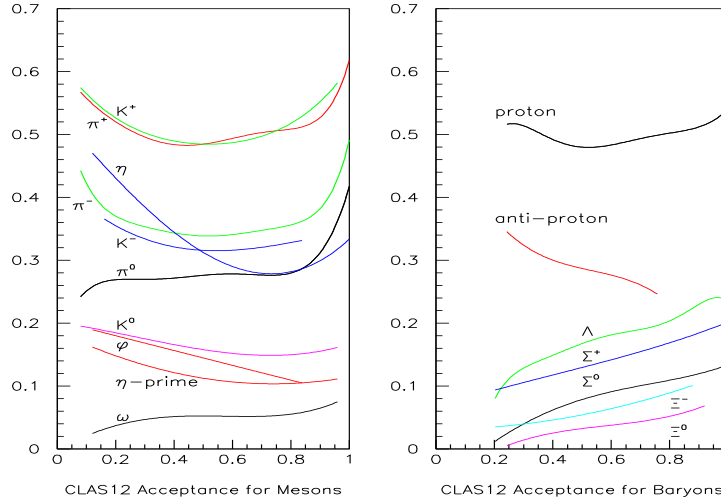


Fig. 67. – Acceptances for mesons and baryons in the CLAS12 experiment at the proposed 12-GeV JLab facility.

EMC effect on nuclear PDFs interferes with energy loss suppression of DY events. However, in this x -region nuclear PDFs are well determined in global fits [400-402].

The interplay of hadron attenuation and p_T -broadening in nDIS and DY nuclear modifications in $p + A$ collisions will be vital to constrain energy-loss models and characterise the stopping power of cold nuclear matter.

8'7.3. Other fixed target experiments: high- p_T hadron spectra. – The study of high- p_T hadron spectra in $p + p$ to $A + A$ collisions in the SPS energy range is fundamental for precisely detect and study QGP formation in heavy-ion collisions. Such a programme is one of the aims of the NA61 experiments at CERN [403], which upgrades the NA49 spectrometer, and also by the NA60 [404] and SELEX [405] experiments, originally focused on quarkonium and charmed hadron production and nuclear modifications.

The peculiarity of NA60 and SELEX is that they mount multiple nuclear targets on the same beam: from Beryllium to Uranium in NA60; Copper and Carbon in SELEX. As emphasised in [162] this target setup allows a high-precision measurement of the ratio of *differential cross-sections* for inclusive hadron production on two different nuclei, $R_{pA/pB}^\sigma = \frac{1}{A} \frac{d\sigma^{pA}}{dp_T^2 dy} / \frac{1}{B} \frac{d\sigma^{pB}}{dp_T^2 dy}$ where B is the lightest available nucleus. Indeed, the beam luminosity as well as part of the systematic errors cancel in the ratio. The A dependence of the ratio is analogous to the centrality dependence, but eliminates the large experimental uncertainties due to the determination of the centrality and to the normalisation of the Cronin ratio. Moreover, without need of centrality cuts the statistics may be sufficient to probe the high- p_T region and test the mechanism underlying the Cronin effect.

8'7.4. Electron-ion colliders. – An electron-ion collider would significantly complement and add new dimensions to the experimental studies at fixed target facilities, by extending the range of accessible lepton, E_e , and ion, E_A , energies. Proposed designs for an electron-ion collider currently have a fairly wide range of luminosities and centre-of-mass energies, see Table XIII. The Electron-Ion Collider (EIC) is a proposed US-based facility, which would provide

	ENC	EIC@JLab			eRHIC			LHeC
		low	med	high	med	high	full	
E_e [GeV]	3.3	3	3-5	11	3	10	30	70
E_A [GeV/A]	7.5	6	30	30	50	100	125	2750
\sqrt{s} [GeV]	10	9	19-25	36	24	98	122	880
\mathcal{L} [$10^{33} \text{ cm}^{-2} \text{ s}^{-1}$]	0.44	6	40	4	0.5	1	0.2	1

TABLE XIII. – Beam energies E , center of mass energies \sqrt{s} , and luminosity \mathcal{L} , for $e + A$ collisions at the ENC (at FAIR), the EIC (BNL and JLab designs), and the LHeC (ring-ring mode) proposed facilities.

$E_e = 3 - 20$ GeV and $E_A = 15 - 100$ AGeV [46, 47]. There are currently two complementary conceptual proposals [47, 406]: (i) eRHIC would add an electron beam to the existing RHIC ion accelerator at BNL – the option of staging it, and first realise a lower energy version with $E_e = 2 - 4$ GeV, based on an energy recovery linear accelerator for the electron beam is being actively discussed [407, 408]; (ii) EIC@JLab would add an ion accelerator to the CEBAF upgraded 12-GeV electron ring at Jefferson Lab [409, 410]. The eRHIC concept emphasises the energy range; the EIC@JLab concept will reach up to 100 times more luminosity, but with lower maximum energy. In both cases polarised proton and light-ion beams will be available. The Large Hadron-electron Collider (LHeC) is a proposed upgrade of the LHC at CERN [411, 412], and will reach much higher energies than the EIC still with a good luminosity, but only with unpolarised hadron beams. Finally, the idea of building a low-energy electron-nucleon (ENC) collider at FAIR has recently been advanced [413]: the goal is to have a centre-of-mass energy between HERMES and COMPASS, but up to a factor 100 higher luminosity and polarised hadron beams. Here, we will focus on the EIC capabilities, but most of the discussed measurements will be in principle possible also at the LHeC and, with the exception of jet measurements, at the ENC.

The EIC will provide virtual photons with energies in the $\nu = 10 - 1600$ GeV range, large Q^2 up to 1000 GeV^2 , and low $x \gtrsim 10^{-5}$. Its high luminosity will allow access to rare signals, multi-differential measurements, and dihadron and γ -hadron correlations. It will be able to cross-check HERMES and CLAS measurements, while offering many more channels and an extended kinematic range to study hadronisation inside the nucleus at low ν , as well as testing basic QCD processes such as non-Abelian parton energy loss and the space-time evolution of the DGLAP shower at high ν . EIC will be unique, compared to HERA (HERMES) and JLab (CLAS), in the following areas:

- At the large ν accessible at the EIC, hadrons will clearly be formed outside the nuclear medium, so that effects due to the propagation of the struck quark can be experimentally isolated. One will have new access to p_T -broadening studies, which can cleanly probe the parton radiative energy loss as predicted by pQCD at asymptotic energy. It will also be possible to study in detail the interplay of radiative and collisional parton energy loss, medium modifications of the DGLAP evolution, and test factorisation for the fragmentation functions.
- Heavier mesons like η and ϕ will be more abundantly produced than at HERMES/JLab. At both medium-low and large ν , comparing their quenching to that of their lighter π and K counterparts will provide important clues about parton propagation and hadronisation, see Sect. 8'2.
- The EIC excellent low- x coverage provides increased production of heavy flavour and quarkonia. In particular, it will be possible to study the heavy quarks energy loss through

the B and D meson suppression. Theoretical mechanisms proposed to explain charmonium suppression in $p + A$ and $A + A$ collisions can be put to the test in a clean experimental environment by studying J/ψ , ψ' and χ spectra.

- The large Q^2 coverage will access a truly perturbative QCD regime, whose prediction can be more confidently tested against the data, in particular colour transparency effects and the Q^2 -dependence of the observables discussed in this review, like the hadron p_T -broadening.
- Baryon production through parton fragmentation will also be accessible, because of the collider mode and the accessible final-state invariant masses. This will allow studying baryon transport in cold QCD matter and the baryon anomalies observed in fixed target $e + A$ collisions at HERMES and in heavy-ion collisions at RHIC. The ability to identify a good variety of baryons, including the strange and charmed sector, will be a key to this programme.
- For the first time, jet physics in DIS with a nuclear target will be experimentally accessible. In particular, medium modifications of the jet shape, and the comparison of light-quark to heavy-quark and gluon initiated jets will shed light on the mechanisms underlying parton energy loss. These studies can also be extended to dijet or γ -jet correlations.

In summary, the collider kinematics and associated detectors with excellent calorimetry, particle identification, vertex detection, and rapidity coverage will allow for a comprehensive programme to better understand how parton energy loss and fragmentation occur in cold QCD matter.

By contrast, the ENC will cover a smaller the $\nu = 10 - 50$ GeV range, which might or might not be sufficient to ensure hadronisation outside the nuclear medium. The high luminosity and rather symmetric kinematics would however ensure the possibility of a rich hadronisation programme complementing and extending the HERMES results.

8.7.5. RHIC II . – In order to undertake extensive high-statistics studies of processes with low cross sections in $A + A$ collisions, an upgrade of the RHIC luminosity will be necessary as well as a comprehensive new detectors [414]. Key measurements will include two-particle correlations up to a p_T range where fragmentation can be safely tested and extended to include heavy identified hadrons. In addition, a comprehensive set of measurements of photon-jet correlations, and heavy-quark tagged jets can provide valuable information on parton energy loss and hadronisation mechanisms. The capabilities of the proposed new detector include: (i) excellent charged particle momentum resolution up to $p_T = 40$ GeV/c in the central rapidity region, (ii) complete hadronic and electromagnetic calorimetry over a large phase space, (iii) particle identification up to large p_T (20 – 30 GeV/c) including hadron and lepton separation in the central and forward regions, and (iv) high rate detectors, data acquisition, and trigger capabilities.

8.7.6. LHC . – The possibility of colliding heavy nuclei with high luminosity at the Large Hadron Collider (LHC) offers a unique opportunity to investigate in detail the behaviour of strongly interacting matter under extreme conditions of density and temperature. The factor 30 increase in $\sqrt{s_{NN}}$ relative to RHIC corresponds to a huge increase in kinematic and statistical reach for hard probes, and new channels will become available [172] such as detailed jet studies (jet shapes, medium-modified fragmentation functions) [137].

ALICE: – The ALICE experiment was designed specifically to tackle as many measurements as possible in the high multiplicity environment of heavy-ion collisions. ALICE aims firstly at accumulating sufficient integrated luminosity in $Pb + Pb$ collisions at $\sqrt{s_{NN}} = 5.5$ TeV, as well as to carry out studies of $p + p$ and $p + A$ collisions in order to establish the benchmark processes

under the same experimental conditions. ALICE can measure heavy-flavour production down to very low p_T because its unique low transverse-momentum cutoff for particle detection. This can be achieved by using inclusive large impact-parameter lepton detection, and by reconstructing exclusive charm-meson decays at relatively low p_T . As a result, the measurement of the total heavy flavour cross section will require a smaller extrapolation and will thus show improved precision. As discussed in §6 a very attractive methods to study hadron jets is to tag high energy hadrons or jets with prompt photons emitted opposite to the hadrons or jet directions. The combined use of the PHOTon Spectrometer (PHOS) – with excellent energy resolution although in a limited acceptance – and the ElectroMagnetic Calorimeter (EMCal) – about seven times larger in acceptance but with slightly worse resolution and coarser granularity – and the central tracking system for charged particles, will allow one to recover a large fraction of the jet energy, thus reducing sensitivity to the specific pattern of fragmentation, and to perform γ -hadron and γ -jet correlations measurements.

ATLAS: – ATLAS is the largest particle detector ever constructed, and its design, like CMS, is aimed at addressing a broad variety of physics processes [415]. The detector design has many features that make it ideal for studies of heavy-ion collisions [416]. A central solenoid magnet and large outer toroidal field magnets provide momentum analysis for the tracking systems. The large acceptance electromagnetic and hadronic calorimeters have longitudinal segmentation and fine transverse segmentation, covering the range in pseudorapidity $|\eta| < 3.2$ (electromagnetic) and $|\eta| < 4.9$ (hadronic), providing excellent photon and jet physics coverage. The high precision silicon tracking system covers the range $|\eta| < 2.5$ and the external muon spectrometers cover $|\eta| < 2.7$, for large-acceptance dimuon studies of heavy quark systems. A fast, three-level trigger system and a high-rate data acquisition system are designed for triggering on rare, high- p_T particles and jets.

This instrumentation provides excellent tools for study of several observables relevant to heavy-ion collisions. Study of hard interactions and jet quenching will be a strong focus, and are closely connected to the topics in this review. The acoplanarity of di-jet pairs should provide sensitivity to the angular diffusion of high- p_T partons in the medium. Jet properties that will be measured include transverse momentum spectra, hadron fragmentation functions, and jet shapes; di-jet angle and energy correlations may be able to separately quantify collisional and radiative energy loss of hard-scattered partons. In addition, measurements of quarkonia in bottom and charm systems, as well as of D and B mesons, will open up detailed studies of heavy quark jet quenching at high E_T .

CMS: – CMS is a general purpose experiment at the LHC designed to explore the physics at the TeV energy scale [417] including comprehensive measurements in $Pb + Pb$ collisions [418]. The CMS detector features a 4 T solenoid surrounding central silicon pixel and microstrip tracking detectors and electromagnetic (ECAL, $|\eta| < 3$) and hadronic (HCAL $|\eta| < 5$) calorimeters, and muon detectors ($|\eta| < 2.4$) embedded in the flux return iron yoke of the magnet. CMS is the largest acceptance detector at the LHC with unique forward detection capabilities with the HF and CASTOR calorimeters ($5.1 < |\eta| < 6.6$). CMS is, by design, very well adapted to detect and reconstruct high- p_T and high-mass particles. The experiment can significantly extend the p_T reach with respect to RHIC, thanks to the large hard cross sections at 5.5 TeV, the large acceptance of its tracking system ($|\eta| < 2.5$), and its high- p_T triggering capabilities. The silicon trackers have excellent reconstruction performances starting above $p_T > 0.3$ GeV/c with a low fake track rates in central $Pb + Pb$. Within $|\eta| < 1$, the p_T resolution is better than 2% up to the highest p_T values reachable. The leading hadron suppression can thus be measured with low uncertainties all the way up to 300 GeV/c, allowing us to clearly discriminate between various

model predictions (Fig. 32, left).

Full jet reconstruction in $Pb + Pb$ collisions can be performed in CMS using the ECAL and HCAL calorimeters. Jets start to be distinguishable above the background at $E_T \sim 30$ GeV and can be fully reconstructed above 75 GeV (efficiency and purity close to 100%) with a good energy resolution (better than 15%). The expected jet E_T spectrum after one month of $Pb + Pb$ running (0.5 nb^{-1}) – taking into account High Level Trigger bandwidths and quenching effects as implemented in HYDJET [314] – reaches up to $E_T \approx 0.5$ TeV in central $Pb + Pb$, and will give access to detailed differential studies of jet quenching phenomena (jet shapes, energy-particle flows within the jet, ...). The possibility of CMS not only to fully reconstruct jets, but to tag them with prompt γ and/or Z bosons [419] and to carry out detailed studies in the c , b quark sector will be very valuable to clarify the response of strongly interacting matter to fast heavy-quarks, and will provide accurate information on the transport properties of QCD matter.

9. – Conclusions

The physics of parton propagation, interaction and fragmentation in both cold and hot strongly interacting matter has been reviewed. The most recent theoretical and experimental results on hadron production in deep inelastic lepton-nucleus scattering (nDIS), high-energy hadron-nucleus ($h + A$) and heavy-ion ($A + A$) collisions as well as Drell-Yan processes in hadron-nucleus interactions have been discussed. The main motivation of such studies is to provide new insights on the mechanisms of parton fragmentation and on the space-time evolution of quark and gluon hadronisation. Those are complex dynamical processes characterised at some stage by energy scales for which the QCD coupling becomes large and thus cannot be completely addressed with standard perturbative QCD tools.

The operational approach consists in comparing the modifications in hadron production observed in a “cold QCD matter” environment (as found in nDIS or $p + A$ collisions) as well as in “hot QCD matter” (created in $A + A$ collisions) with respect to the measurements in the “QCD vacuum” (in DIS off protons or in proton-proton collisions). The quantitative comparisons are carried out using various phenomenological ratios (hadron multiplicity ratio R_M^h in nuclear DIS, or nuclear modification factor $R_{pA,AA}$ in nuclear collisions) as a function of the relevant variables: hadron momentum, fraction of the photon energy, virtuality, hadron flavour, size of the medium, etc. In the case of cold nuclear matter, the detailed study of the observed deviations with respect to vacuum production allows one to constrain various models describing the space-time evolution of parton fragmentation and, in the case of nucleus-nucleus collisions, also to characterise the (thermo)dynamical properties of the hot and dense QCD matter produced in the reaction.

A detailed comparison of the kinematics and phase-spaces in nDIS experiments at CERN, HERA and JLab and in proton-nucleus (FNAL, SPS, RHIC) and heavy-ions (SPS, RHIC) collisions, indicates that the range of relevant hadron energies measured is comparable, $E_h \approx 2\text{--}20$ GeV, as well as typical values of fractional momentum of the parent parton energy carried away by the leading hadron, $z \approx 0.4\text{--}0.9$. The same is not true, however, for the parton virtualities Q involved which are at least a factor of five larger for the hadrons produced at RHIC top energies ($Q \lesssim 20$ GeV) than those typical at HERMES/JLab ($Q \lesssim 3$ GeV). Therefore a direct comparison of hadron suppression data from nDIS to $h + A$ and $A + A$ collisions is not possible, and theoretical models are needed to connect both colliding systems.

The main theoretical approaches to account for parton propagation and fragmentation in QCD matter can be roughly divided in two groups: (i) models rooted in perturbative-QCD studies of non-Abelian parton energy loss via gluon Bremsstrahlung or in-medium modifications of the DGLAP equations for gluon radiation, followed by hadronisation of the final state hadrons in

the vacuum, and (ii) approaches mostly based on modifications of the non-perturbative Lund string fragmentation model that account for the interaction in the nuclear medium of a colorless pre-hadronic stage.

The range of application of these two classes of models depends on the value of the parton lifetime, i.e., by the time t_{preh} needed to produce a prehadron. Simple perturbative estimates indicate that the typical parton lifetime at HERMES or RHIC strongly depends on the hadron mass. For pions, one obtains lifetimes $t_{preh} \approx 20 - 30$ fm, larger than the nuclear radius, although modified versions of the Lund and dipole fragmentation models indicate smaller lifetimes, $t_{preh} \lesssim 6$ fm. For heavier particles such as K, η, p , one finds $t_{preh} \approx 6 - 9$ fm, and even smaller values for heavy-flavor mesons, $t_{preh}(B, D) \lesssim 1$ fm. Therefore it is in general necessary to incorporate prehadron-medium interactions in the theoretical models, and to look for experimental observables able to distinguish them from purely partonic interactions and measure t_{preh} .

A simple way to test the different models and their underlying assumptions is to study hadron production in nDIS and Drell-Yan processes in $h + A$ collisions, where the traversed medium is static, if not uniform, and its properties are well known. This cold nuclear matter information serves then as baseline for $A + A$ collisions, where a number of new mechanisms modifying high- p_T hadron production can be used to “tomographically” study the thermodynamical and transport properties of the hot and dense matter created.

Lepton-nucleus DIS

The recent HERMES and older EMC data on hadron attenuation in nDIS, encoded in the $R_M^h(z, \nu; A)$ ratio, support a picture where the space-time evolution of the fragmentation process is modified by the surrounding matter, with a sizeable inelastic cross section between the colorless pre-hadronic state and the nuclear medium. However, when the detailed geometry and finite size of the target nucleus are taken into account, nDIS data can also be described in terms of parton energy loss alone.

Additional observables sensitive to the underlying dynamics of the hadronisation process have been investigated. In particular, the observed slow variation of R_M with Q^2 disfavors mechanisms like partial deconfinement and puts additional constraints on other theoretical models. The rising and seemingly linear behavior of the hadron p_T -broadening $\langle \Delta p_T \rangle$ vs. A at HERMES supports the conclusion that the prehadron is formed close to or just outside the nucleus surface (at $\langle \nu \rangle \approx 14$ GeV and $Q^2 \approx 2.5$ GeV²) and allows to estimate the prehadron production time. The details of the ν dependence of the p_T -broadening, and especially its linear increase with Q^2 are better interpreted in terms of medium-modified DGLAP evolution, and demand for NLO computations so far neglected. However, the shape of $\langle \Delta p_T \rangle$ vs. z_h cannot be qualitatively understood by current prehadron absorption or energy loss computations, and is challenging theory models.

Hadron-nucleus collisions

The observation of a Cronin enhancement ($R_{pA} > 1$) of the hadron yields in the range $p_T = 2 - 8$ GeV/c is a characteristic feature of high-energy proton-nucleus collisions at fixed target energies (FNAL, SPS, HERA-B). At RHIC top energies, intermediate- p_T proton, but barely meson, production is enhanced in $d + Au$ collisions and the typical R_{dA} maximum around 2 GeV/c is progressively suppressed as the rapidity increases. The usual interpretation of the Cronin effect is based on multiple scatterings of the parton prior to its fragmentation. Both initial- and final-state interactions must play a role in order to explain the various experimental observations. On the one hand, the disappearance of the enhancement at forward rapidities is easily explained

by non-linear QCD evolution of the initial-state parton distributions (though may also be due to effects occurring at the edge of phase space). On the other hand, DY data suggest that parton rescatterings contribute only a small amount to the hadron enhancement and, in addition, final-state coalescence of the scattered parton with other soft partons in the nuclear environment naturally explains the larger enhancement observed for baryons compared to mesons. The Cronin effect helps thus to study the hadronisation mechanism in hadronic interactions at intermediate p_T , which may be dominated by parton recombination rather than by independent parton fragmentation. Detailed control of the role of all these mechanisms is important to help identify the onset of high- p_T hadron suppression in $A + A$ collisions in the $\sqrt{s} = 10 - 100$ GeV range.

Nucleus-nucleus collisions

The two most notable experimental results in $Au + Au$ collisions at RHIC are (i) the observed factor of ~ 5 suppression of high- p_T hadrons, and (ii) the strongly distorted azimuthal distributions of secondary hadrons emitted in the away-side hemisphere of a high- p_T trigger hadron. Their properties such as magnitude and light flavour “universality”, and their dependence on p_T , centrality, path-length, and $\sqrt{s_{NN}}$ are in quantitative agreement with the predictions of models based on non-Abelian gluon radiation off hard scattered partons traversing the dense QCD medium. The confrontation of these models to the data permits to derive the initial gluon density $dN^g/dy \approx 1400$ and transport coefficient $\hat{q} = \mathcal{O}(10 \text{ GeV}^2/\text{fm})$ of the produced medium at RHIC. Yet, other observations such as the same suppression factor for light- and heavy-quark mesons, and the less suppressed baryon compared to meson production indicate that the standard factorisation assumption of vacuum hadronisation after in-medium radiation, implicit in all parton energy loss formalisms, may well not hold. At lower collision energy, with shorter propagation times and a less dense final state medium, hadron suppression in the cold nuclear targets may compete with that originating from the hot medium.

Outlook

We have reviewed a set of observables and new or improved measurements that can answer several of the open questions mentioned here and discussed in detail in this review. They include multi-dimensional p_T -broadening measurements, hadron-hadron and hadron-photon correlations, heavy flavor and jet shape modifications in nDIS, improved DY measurements and large- p_T hadron spectra in $h + A$ collisions, heavy quark tagging in $A + A$ collisions. These observables can be addressed at new facilities planned for the near or medium-term future, such as RHIC-II, JLab12, and the Electron-Ion Collider (which in particular will open the study of purely partonic in-medium processes in DIS). They can also be addressed by new experiments at existing facilities, such as NA61 at SPS, or by a creative use of data taken at closed experiments such as NA60 or SELEX, among others. The combination of new results, theoretical developments, and an open mind to combine information from traditionally different fields such as DIS and hadronic collisions will doubtlessly lead to a more profound knowledge of parton propagation and fragmentation, quark and gluon hadronisation, and the properties of strongly interacting QCD matter.

* * *

A.A. wishes to thank J. Morfín for helpful discussions and encouragement, and acknowledges support by DOE contract No. DE-AC02-06CH11357, DOE contract No. DE-AC05-06OR23177 (under which Jefferson Science Associates, LLC operates Jefferson Lab), and NSF award No. 0653508. F.A. would like to thank the hospitality of CERN TH division, where part of this

work was carried out. D.d'E. acknowledges support by 6th EU Framework Programme under contract MEIF-CT-2005-025073. W.B. acknowledges support from DOE contract No. DE-AC05-06OR23177 (under which Jefferson Science Associates, LLC operates Jefferson Lab) and Conicyt/Fondecyt Grant 1080564.

REFERENCES

- [1] V. N. Gribov and L. N. Lipatov, Sov. J. Nucl. Phys. **15** (1972) 438–450.
- [2] G. Altarelli and G. Parisi, Nucl. Phys. **B126** (1977) 298.
- [3] Y. L. Dokshitzer, Sov. Phys. JETP **46** (1977) 641–653.
- [4] B. Andersson, Camb. Monogr. Part. Phys. Nucl. Phys. Cosmol. **7** (1997) 1–471.
- [5] G. Marchesini and B. R. Webber, Nucl. Phys. **B310** (1988) 461.
- [6] J. D. Bjorken, Lect. Notes Phys. **56** (1976) 93.
- [7] S. J. Brodsky Topics in nuclear Chromodynamics: Color transparency and hadronization in the nucleus'. 3rd Lake Louise Winter Inst. on QCD: Theory and Experiment, Lake Louise, Canada, Mar 6-12, 1988.
- [8] J. W. Cronin *et al.*, Phys. Rev. **D11** (1975) 3105.
- [9] D. Antreasyan *et al.*, Phys. Rev. **D19** (1979) 764.
- [10] J. C. Collins, D. E. Soper and G. Sterman, Adv. Ser. Direct. High Energy Phys. **5** (1988) 1–91.
- [11] Y. L. Dokshitzer, V. A. Khoze, A. H. Mueller and S. I. Troian Basics of perturbative QCD. Gif-sur-Yvette, France: Ed. Frontières (1991) 274 p.
- [12] P. M. Nadolsky *et al.*, arXiv:0802.0007.
- [13] A. D. Martin, R. G. Roberts, W. J. Stirling and R. S. Thorne, Phys. Lett. **B604** (2004) 61–68.
- [14] G. Watt, A. D. Martin, W. J. Stirling and R. S. Thorne, arXiv:0806.4890.
- [15] M. Hirai, S. Kumano, T. H. Nagai and K. Sudoh, Phys. Rev. **D75** (2007) 094009.
- [16] D. de Florian, R. Sassot and M. Stratmann, Phys. Rev. **D75** (2007) 114010.
- [17] S. Albino, B. A. Kniehl and G. Kramer, arXiv:0803.2768.
- [18] S. Albino *et al.*, arXiv:0804.2021.
- [19] S. Albino *et al.*, arXiv:0804.2021.
- [20] N. Armesto, J. Phys. **G32** (2006) R367–R394.
- [21] HERMES Collaboration, A. Airapetian *et al.*, Eur. Phys. J. **C20** (2001) 479–486.
- [22] HERMES Collaboration, A. Airapetian *et al.*, Phys. Lett. **B577** (2003) 37–46.
- [23] HERMES Collaboration, A. Airapetian *et al.*, Nucl. Phys. **B780** (2007) 1–27.
- [24] HERMES Collaboration, A. Airapetian *et al.*, Phys. Rev. Lett. **96** (2006) 162301.
- [25] BRAHMS Collaboration, I. Arsene *et al.*, Nucl. Phys. **A757** (2005) 1–27.
- [26] B. B. Back *et al.*, Nucl. Phys. **A757** (2005) 28–101.
- [27] STAR Collaboration, J. Adams *et al.*, Nucl. Phys. **A757** (2005) 102–183.
- [28] PHENIX Collaboration, K. Adcox *et al.*, Nucl. Phys. **A757** (2005) 184–283.
- [29] B. Z. Kopeliovich, J. Nemchik, E. Predazzi and A. Hayashigaki, Nucl. Phys. **A740** (2004) 211–245.
- [30] A. Adil and I. Vitev, Phys. Lett. **B649** (2007) 139–146.
- [31] J. Carlson, J. B. Kogut and V. R. Pandharipande, Phys. Rev. **D28** (1983) 2807.
- [32] T. Hatsuda and T. Kunihiro, Phys. Rept. **247** (1994) 221–367.
- [33] MiniBooNE Collaboration, A. A. Aguilar-Arevalo *et al.*, Phys. Rev. Lett. **100** (2008) 032301.
- [34] OPERA Collaboration, M. Guler *et al.*, . CERN-SPSC-2000-028.
- [35] MINOS Collaboration, P. Adamson *et al.*, arXiv:0806.2237.
- [36] S. Dytman, H. Gallagher and M. Kordosky, arXiv:0806.2119.
- [37] O. Buss, T. Leitner, U. Mosel and L. Alvarez-Ruso, Phys. Rev. **C76** (2007) 035502.
- [38] T. Leitner, L. Alvarez-Ruso and U. Mosel, Phys. Rev. **C74** (2006) 065502.
- [39] T. Leitner, L. Alvarez-Ruso and U. Mosel, Phys. Rev. **C73** (2006) 065502.
- [40] T. Leitner, U. Mosel and L. Alvarez-Ruso, Int. J. Mod. Phys. **A22** (2007) 416–423.
- [41] R. D. Field, . Redwood City, USA: Addison-Wesley (1989) 366 p. (Frontiers in physics, 77).
- [42] J. C. Collins and D. E. Soper, Nucl. Phys. **B193** (1981) 381.

- [43] A. Accardi, Phys. Rev. **C76** (2007) 034902.
- [44] **HERMES** Collaboration, P. B. van der Nat, Acta Phys. Polon. **B35** (2004) 139–143.
- [45] **European Muon** Collaboration, J. Ashman *et al.*, Z. Phys. **C52** (1991) 1–12.
- [46] A. Deshpande, R. Milner, R. Venugopalan and W. Vogelsang, Ann. Rev. Nucl. Part. Sci. **55** (2005) 165–228.
- [47] **EIC** Collaboration, C. A. Aidala, [arXiv:0806.4933](#).
- [48] K. J. Eskola and H. Honkanen, Nucl. Phys. **A713** (2003) 167–187.
- [49] A. Accardi and M. Gyulassy, Phys. Lett. **B586** (2004) 244–253.
- [50] V. Guzey, M. Strikman and W. Vogelsang, Phys. Lett. **B603** (2004) 173–183.
- [51] A. Accardi, Acta Phys. Hung. **A22** (2005) 289–299.
- [52] M. L. Miller, K. Reygers, S. J. Sanders and P. Steinberg, Ann. Rev. Nucl. Part. Sci. **57** (2007) 205–243.
- [53] B. Z. Kopeliovich *et al.*, [arXiv:0809.4613](#).
- [54] S. R. Amendolia *et al.*, Phys. Lett. **B146** (1984) 116.
- [55] S. R. Amendolia *et al.*, Phys. Lett. **B178** (1986) 435.
- [56] I. Sick, Phys. Lett. **B576** (2003) 62–67.
- [57] Y. A. Simonov, Phys. Atom. Nucl. **71** (2008) 1048–1076.
- [58] E. Wang and X.-N. Wang, Phys. Rev. Lett. **89** (2002) 162301.
- [59] F. Arleo, JHEP **11** (2002) 044.
- [60] M. Gyulassy, P. Lévai and I. Vitev, Nucl. Phys. **B594** (2001) 371–419.
- [61] A. Accardi, D. Grunewald, V. Muccifora and H. J. Pirner, Nucl. Phys. **A761** (2005) 67–91.
- [62] B. Andersson, G. Gustafson, G. Ingelman and T. Sjostrand, Phys. Rept. **97** (1983) 31–145.
- [63] A. Bialas and M. Gyulassy, Nucl. Phys. **B291** (1987) 793.
- [64] A. Accardi, V. Muccifora and H.-J. Pirner, Nucl. Phys. **A720** (2003) 131–156.
- [65] K. Gallmeister and T. Falter, Phys. Lett. **B630** (2005) 40–48.
- [66] E. L. Berger, Z. Phys. **C4** (1980) 289.
- [67] E. L. Berger, Phys. Lett. **B89** (1980) 241.
- [68] B. Z. Kopeliovich, H. J. Pirner, I. K. Potashnikova and I. Schmidt, Phys. Lett. **B662** (2008) 117–122.
- [69] J. F. Gunion and G. Bertsch, Phys. Rev. **D25** (1982) 746.
- [70] B. Z. Kopeliovich, J. Nemchik and I. Schmidt, Nucl. Phys. **A782** (2007) 224–233.
- [71] L. S. Osborne *et al.*, Phys. Rev. Lett. **40** (1978) 1624.
- [72] **European Muon** Collaboration, A. Arvidson *et al.*, Nucl. Phys. **B246** (1984) 381.
- [73] **E665** Collaboration, M. R. Adams *et al.*, Phys. Rev. **D50** (1994) 1836–1873.
- [74] W. K. Brooks and H. Hakobyan, AIP Conf. Proc. **1056** (2008) 215–222.
- [75] **BEBC WA21/WA59** Collaboration, W. Burkot *et al.*, Z. Phys. **C70** (1996) 47–53.
- [76] J. P. Berge *et al.*, Phys. Rev. **D18** (1978) 1367.
- [77] **Aachen-Bonn-CERN-Democritos-London-Oxford-Saclay** Collaboration, H. Deden *et al.*, Nucl. Phys. **B198** (1982) 365.
- [78] J. Czyzewski, Phys. Rev. **C43** (1991) 2426–2431.
- [79] **NOMAD** Collaboration, P. Astier *et al.*, Nucl. Phys. **B609** (2001) 255–279.
- [80] **NOMAD** Collaboration, M. Veltri, Nucl. Phys. Proc. Suppl. **112** (2002) 124–131.
- [81] N. M. Agababyan *et al.*, Phys. Atom. Nucl. **66** (2003) 1310–1318.
- [82] N. A. Pavel, Nucl. Phys. **A532** (1991) 465c–488c.
- [83] L. Hand *et al.*, Z. Phys. **C1** (1979) 139–142.
- [84] **E665** Collaboration, M. R. Adams *et al.*, Z. Phys. **C65** (1995) 225–244.
- [85] N. Akopov *et al.*, Nucl. Instrum. Meth. **A479** (2002) 511–530.
- [86] **PHENIX** Collaboration, S. S. Adler *et al.*, Phys. Rev. Lett. **91** (2003) 172301.
- [87] **STAR** Collaboration, B. I. Abelev *et al.*, Phys. Rev. Lett. **97** (2006) 152301.
- [88] **HERMES** Collaboration, A. Airapetian *et al.*, [arXiv:0906.2478](#).
- [89] X. Guo and J.-w. Qiu, Phys. Rev. **D61** (2000) 096003.
- [90] H. Hakobyan, PhD Thesis, Yerevan State University, June 2008.
- [91] K. Gallmeister, W. Cassing, T. Falter and U. Mosel, Int. J. Mod. Phys. **A20** (2005) 615–617.
- [92] A. Majumder, E. Wang and X.-N. Wang, Phys. Rev. Lett. **99** (2007) 152301.
- [93] A. Majumder and X.-N. Wang, [arXiv:0806.2653](#).

- [194] N. Akopov, L. Grigoryan and Z. Akopov, Eur. Phys. J. **C49** (2007) 1015–1021.
- [195] N. Akopov, L. Grigoryan and Z. Akopov, Eur. Phys. J. **C52** (2007) 893–898.
- [196] P. L. McGaughey, J. M. Moss and J. C. Peng, Ann. Rev. Nucl. Part. Sci. **49** (1999) 217–253.
- [197] G. T. Garvey and J.-C. Peng, Prog. Part. Nucl. Phys. **47** (2001) 203–243.
- [198] J. C. Peng, arXiv:0807.3538.
- [199] S. Gavin *et al.*, Int. J. Mod. Phys. **A10** (1995) 2961–2998.
- [100] **FNAL E866** Collaboration, M. A. Vasilev *et al.*, Phys. Rev. Lett. **83** (1999) 2304–2307.
- [101] K. J. Eskola, V. J. Kolhinen and C. A. Salgado, Eur. Phys. J. **C9** (1999) 61–68.
- [102] D. M. Alde *et al.*, Phys. Rev. Lett. **64** (1990) 2479–2482.
- [103] M. B. Johnson, B. Z. Kopeliovich and I. Schmidt, Phys. Rev. **C75** (2007) 064905.
- [104] **NA3** Collaboration, J. Badier *et al.*, Phys. Lett. **B104** (1981) 335.
- [105] **NA10** Collaboration, P. Bordalo *et al.*, Phys. Lett. **B193** (1987) 373.
- [106] **NA38** Collaboration, C. Baglin *et al.*, Phys. Lett. **B268** (1991) 453–456.
- [107] D. M. Alde *et al.*, Phys. Rev. Lett. **66** (1991) 2285–2288.
- [108] A. S. Ito *et al.*, Phys. Rev. **D23** (1981) 604.
- [109] P. R. Norton, Rept. Prog. Phys. **66** (2003) 1253–1297.
- [110] G. Piller and W. Weise, Phys. Rept. **330** (2000) 1–94.
- [111] D. F. Geesaman, K. Saito and A. W. Thomas, Ann. Rev. Nucl. Sci. **45** (1995) 337–390.
- [112] R. P. Bickerstaff, M. C. Birse and G. A. Miller, Phys. Rev. Lett. **53** (1984) 2532–2535.
- [113] R. P. Bickerstaff, M. C. Birse and G. A. Miller, Phys. Rev. **D33** (1986) 3228–3245.
- [114] P. B. Straub *et al.*, Phys. Rev. Lett. **68** (1992) 452–455.
- [115] **WA80** Collaboration, R. Albrecht *et al.*, Eur. Phys. J. **C5** (1998) 255–267.
- [116] H.-B. Collaboration, arXiv:0812.0471.
- [117] B. Z. Kopeliovich, J. Nemchik, A. Schafer and A. V. Tarasov, Phys. Rev. Lett. **88** (2002) 232303.
- [118] **PHENIX** Collaboration, S. S. Adler *et al.*, Phys. Rev. Lett. **94** (2005) 082302.
- [119] **PHENIX** Collaboration, S. S. Adler *et al.*, Phys. Rev. Lett. **98** (2007) 172302.
- [120] **PHENIX** Collaboration, A. Adare *et al.*, Phys. Rev. Lett. **101** (2008) 232301.
- [121] **STAR** Collaboration, B. I. Abelev *et al.*, arXiv:0801.0450.
- [122] **PHENIX** Collaboration, S. S. Adler *et al.*, Phys. Rev. **C74** (2006) 024904.
- [123] **PHENIX** Collaboration, S. S. Adler *et al.*, Phys. Rev. **C77** (2008) 014905.
- [124] A. Accardi, arXiv:hep-ph/0212148.
- [125] R. C. Hwa and C. B. Yang, Phys. Rev. Lett. **93** (2004) 082302.
- [126] R. C. Hwa and C. B. Yang, Phys. Rev. **C70** (2004) 037901.
- [127] D. Kharzeev, Y. V. Kovchegov and K. Tuchin, Phys. Rev. **D68** (2003) 094013.
- [128] J. Jalilian-Marian, Y. Nara and R. Venugopalan, Phys. Lett. **B577** (2003) 54–60.
- [129] R. Baier, A. Kovner and U. A. Wiedemann, Phys. Rev. **D68** (2003) 054009.
- [130] J. L. Albacete, N. Armesto, A. Kovner, C. A. Salgado and U. A. Wiedemann, Phys. Rev. Lett. **92** (2004) 082001.
- [131] J. D. Bjorken, . FERMILAB-PUB-82-059-THY.
- [132] M. Gyulassy, M. Plumer, M. Thoma and X. N. Wang, Nucl. Phys. **A538** (1992) 37c–50c.
- [133] D. A. Appel, Phys. Rev. **D33** (1986) 717.
- [134] J. P. Blaizot and L. D. McLerran, Phys. Rev. **D34** (1986) 2739.
- [135] C. A. Salgado and U. A. Wiedemann, Phys. Rev. Lett. **93** (2004) 042301.
- [136] I. Vitev, S. Wicks and B.-W. Zhang, JHEP **11** (2008) 093.
- [137] D. d’Enterria, arXiv:0902.2011.
- [138] M. Gyulassy, P. Lévai and I. Vitev, Phys. Rev. Lett. **85** (2000) 5535–5538.
- [139] I. Vitev and M. Gyulassy, Phys. Rev. Lett. **89** (2002) 252301.
- [140] R. Baier, Y. L. Dokshitzer, A. H. Mueller, S. Peigne and D. Schiff, Nucl. Phys. **B484** (1997) 265–282.
- [141] R. Baier, Y. L. Dokshitzer, A. H. Mueller and D. Schiff, Nucl. Phys. **B531** (1998) 403–425.
- [142] U. A. Wiedemann, Nucl. Phys. **A690** (2001) 731–751.
- [143] B. G. Zakharov, JETP Lett. **65** (1997) 615–620.
- [144] R. Baier and D. Schiff, JHEP **0609** (2006) 059.
- [145] **PHENIX** Collaboration, S. S. Adler *et al.*, Phys. Rev. **C76** (2007) 034904.
- [146] **PHENIX** Collaboration, S. S. Adler *et al.*, Phys. Rev. Lett. **96** (2006) 202301.

- [147] **PHENIX** Collaboration, S. S. Adler *et al.*, Phys. Rev. **C75** (2007) 024909.
- [148] **PHENIX** Collaboration, A. Adare *et al.*, arXiv:0804.4168.
- [149] **STAR** Collaboration, J. Adams *et al.*, Phys. Rev. Lett. **91** (2003) 172302.
- [150] I. Vitev, J. Phys. **G30** (2004) S791–S800.
- [151] T. Sjostrand *et al.*, Comput. Phys. Commun. **135** (2001) 238–259.
- [152] **PHENIX** Collaboration, K. Adcox *et al.*, Phys. Rev. Lett. **88** (2002) 022301.
- [153] **PHENIX** Collaboration, S. S. Adler *et al.*, Phys. Rev. Lett. **91** (2003) 072301.
- [154] **STAR** Collaboration, C. Adler *et al.*, Phys. Rev. Lett. **89** (2002) 202301.
- [155] **PHENIX** Collaboration, K. Adcox *et al.*, Phys. Lett. **B561** (2003) 82–92.
- [156] **PHENIX** Collaboration, S. S. Adler *et al.*, Phys. Rev. **C69** (2004) 034910.
- [157] **PHENIX** Collaboration, S. S. Adler *et al.*, Phys. Rev. Lett. **94** (2005) 232301.
- [158] **PHENIX** Collaboration, A. Adare *et al.*, arXiv:0804.4168.
- [159] D. d’Enterria, Phys. Lett. **B596** (2004) 32–43.
- [160] **WA98** Collaboration, M. M. Aggarwal *et al.*, Eur. Phys. J. **C23** (2002) 225–236.
- [161] **WA98** Collaboration, M. M. Aggarwal *et al.*, Phys. Rev. Lett. **100** (2008) 242301.
- [162] A. Accardi, Eur. Phys. J. **C43** (2005) 121–125.
- [163] S. Turbide, C. Gale, S. Jeon and G. D. Moore, Phys. Rev. **C72** (2005) 014906.
- [164] A. Dainese, C. Loizides and G. Paic, Eur. Phys. J. **C38** (2005) 461–474.
- [165] A. Majumder, J. Phys. **G34** (2007) S377–388.
- [166] S. A. Bass *et al.*, arXiv:0808.0908.
- [167] K. J. Eskola, H. Honkanen, C. A. Salgado and U. A. Wiedemann, Nucl. Phys. **A747** (2005) 511–529.
- [168] M. Gyulassy and L. McLerran, Nucl. Phys. **A750** (2005) 30–63.
- [169] I. Vitev, Phys. Lett. **B606** (2005) 303–312.
- [170] H. Buesching, Eur. Phys. J. **C49** (2006) 41.
- [171] **PHENIX** Collaboration, S. S. Adler *et al.*, Phys. Rev. **C71** (2005) 034908.
- [172] N. Armesto (ed.) *et al.*, J. Phys. **G35** (2008) 054001.
- [173] D. d’Enterria, Eur. Phys. J. **C43** (2005) 295–302.
- [174] S. Jeon and G. D. Moore, Phys. Rev. **C71** (2005) 034901.
- [175] **PHENIX** Collaboration, K. Reygers, arXiv:0804.4562.
- [176] **PHENIX** Collaboration, A. Adare *et al.*, Phys. Rev. Lett. **101** (2008) 162301.
- [177] I. Vitev, Phys. Lett. **B639** (2006) 38–45.
- [178] **PHENIX** Collaboration, . A. Adare, arXiv:0903.4886.
- [179] V. S. Pantuev, JETP Lett. **85** (2007) 104–108.
- [180] Q. Wang and X.-n. Wang, Phys. Rev. **C71** (2005) 014903.
- [181] **STAR** Collaboration, B. Mohanty, arXiv:0804.4760.
- [182] **STAR** Collaboration, J. Adams *et al.*, Phys. Lett. **B637** (2006) 161–169.
- [183] R. C. Hwa and C. B. Yang, Phys. Rev. **C67** (2003) 034902.
- [184] R. J. Fries, B. Muller, C. Nonaka and S. A. Bass, Phys. Rev. **C68** (2003) 044902.
- [185] V. Greco, C. M. Ko and P. Levai, Phys. Rev. Lett. **90** (2003) 202302.
- [186] S. J. Brodsky and A. Sickles, Phys. Lett. **B668** (2008) 111–115.
- [187] Y. L. Dokshitzer and D. E. Kharzeev, Phys. Lett. **B519** (2001) 199–206.
- [188] X. M. Zhang, D. C. Zhou and W. C. Xiang, Int. J. Mod. Phys. **E16** (2007) 2123–2129.
- [189] S. Peigne and A. V. Smilga, arXiv:0810.5702.
- [190] **PHENIX** Collaboration, S. S. Adler *et al.*, Phys. Rev. Lett. **96** (2006) 032301.
- [191] **STAR** Collaboration, B. I. Abelev *et al.*, Phys. Rev. Lett. **98** (2007) 192301.
- [192] **PHENIX** Collaboration, A. Adare *et al.*, Phys. Rev. Lett. **98** (2007) 172301.
- [193] M. Djordjevic, M. Gyulassy, R. Vogt and S. Wicks, Phys. Lett. **B632** (2006) 81–86.
- [194] A. D. Frawley, T. Ullrich and R. Vogt, Phys. Rept. **462** (2008) 125–175.
- [195] I. Vitev, J. Phys. **G35** (2008) 104011.
- [196] M. Cacciari, PoS **HEP2005** (2006) 137.
- [197] N. Armesto, M. Cacciari, A. Dainese, C. A. Salgado and U. A. Wiedemann, Phys. Lett. **B637** (2006) 362–366.
- [198] **PHENIX** Collaboration, . A. Adare, arXiv:0903.4851.
- [199] **STAR** Collaboration, A. Mischke, arXiv:0804.4601.

- [200] M. Cacciari, P. Nason and R. Vogt, Phys. Rev. Lett. **95** (2005) 122001.
- [201] M. G. Mustafa and M. H. Thoma, Acta Phys. Hung. **A22** (2005) 93–102.
- [202] S. Wicks, W. Horowitz, M. Djordjevic and M. Gyulassy, Nucl. Phys. **A784** (2007) 426–442.
- [203] A. Peshier, Phys. Rev. Lett. **97** (2006) 212301.
- [204] A. Peshier, Eur. Phys. J. **C49** (2007) 9–12.
- [205] S. Peigne and A. Peshier, arXiv:0802.4364.
- [206] P. B. Gossiaux, J. Aichelin and A. Peshier, Phys. Rev. **C78** (2008) 014904.
- [207] P. R. Sorensen and X. Dong, Phys. Rev. **C74** (2006) 024902.
- [208] G. Martinez-Garcia, S. Gadrat and P. Crochet, Phys. Lett. **B663** (2008) 55–60.
- [209] J.-w. Qiu and I. Vitev, Phys. Lett. **B570** (2003) 161–170.
- [210] STAR Collaboration, C. Adler *et al.*, Phys. Rev. Lett. **90** (2003) 082302.
- [211] PHENIX Collaboration, A. Adare *et al.*, Phys. Rev. **C78** (2008) 014901.
- [212] PHENIX Collaboration, A. Adare *et al.*, Phys. Rev. **C77** (2008) 011901.
- [213] H. Zhang, J. F. Owens, E. Wang and X.-N. Wang, Phys. Rev. Lett. **98** (2007) 212301.
- [214] STAR Collaboration, J. Adams *et al.*, Phys. Rev. Lett. **97** (2006) 162301.
- [215] A. D. Polosa and C. A. Salgado, Phys. Rev. **C75** (2007) 041901.
- [216] J. Ruppert and B. Muller, Phys. Lett. **B618** (2005) 123–130.
- [217] L. M. Satarov, H. Stoecker and I. N. Mishustin, Phys. Lett. **B627** (2005) 64–70.
- [218] J. Casalderrey-Solana, E. V. Shuryak and D. Teaney, J. Phys. Conf. Ser. **27** (2005) 22–31.
- [219] I. M. Dremin, Nucl. Phys. **A767** (2006) 233–247.
- [220] V. Koch, A. Majumder and X.-N. Wang, Phys. Rev. Lett. **96** (2006) 172302.
- [221] B. Betz, M. Gyulassy, D. H. Rischke, H. Stocker and G. Torrieri, arXiv:0804.4408.
- [222] F. Arleo, JHEP **07** (2007) 032.
- [223] S. Turbide, C. Gale, E. Frodermann and U. Heinz, Phys. Rev. **C77** (2008) 024909.
- [224] B. G. Zakharov, JETP Lett. **80** (2004) 617–622.
- [225] PHENIX Collaboration, T. Isobe, J. Phys. **G34** (2007) S1015–1018.
- [226] I. Vitev and B.-W. Zhang, Phys. Lett. **B669** (2008) 337–344.
- [227] S. Jeon, J. Jalilian-Marian and I. Sarcevic, Phys. Lett. **B562** (2003) 45–50.
- [228] F. Arleo, JHEP **09** (2006) 015.
- [229] P. Arnold, G. D. Moore and L. G. Yaffe, JHEP **11** (2001) 057.
- [230] B. G. Zakharov, JETP Lett. **63** (1996) 952–957.
- [231] B. G. Zakharov, JETP Lett. **80** (2004) 1–6.
- [232] R. J. Fries, B. Müller and D. K. Srivastava, Phys. Rev. Lett. **90** (2003) 132301.
- [233] R. J. Fries, V. Greco and P. Sorensen, arXiv:0807.4939.
- [234] A. Krzywicki, J. Engels, B. Petersson and U. Sukhatme, Phys. Lett. **B85** (1979) 407.
- [235] M. Lev and B. Petersson, Z. Phys. **C21** (1983) 155.
- [236] A. Accardi and D. Treleani, Phys. Rev. **D64** (2001) 116004.
- [237] M. Gyulassy, P. Levai and I. Vitev, Phys. Rev. **D66** (2002) 014005.
- [238] X.-N. Wang, Phys. Rev. **C61** (2000) 064910.
- [239] E. Wang and X.-N. Wang, Phys. Rev. **C64** (2001) 034901.
- [240] Y. Zhang, G. I. Fai, G. Papp, G. G. Barnafoldi and P. Levai, Phys. Rev. **C65** (2002) 034903.
- [241] A. Accardi and M. Gyulassy, J. Phys. **G30** (2004) S969–S974.
- [242] E. Cattaruzza and D. Treleani, Phys. Rev. **D69** (2004) 094006.
- [243] BRAHMS Collaboration, I. Arsene *et al.*, Phys. Rev. Lett. **98** (2007) 252001.
- [244] STAR Collaboration, J. Adams *et al.*, Phys. Rev. Lett. **97** (2006) 152302.
- [245] D. Kharzeev, Y. V. Kovchegov and K. Tuchin, Phys. Lett. **B599** (2004) 23–31.
- [246] J. Jalilian-Marian, Nucl. Phys. **A748** (2005) 664–671.
- [247] G. G. Barnafoldi, A. Adeluyi, G. Fai, P. Levai and G. Papp, arXiv:0807.3384.
- [248] D. d’Enterria, J. Phys. **G34** (2007) S53–S82.
- [249] M. B. Johnson, B. Z. Kopeliovich and A. V. Tarasov, Phys. Rev. **C63** (2001) 035203.
- [250] K. J. Golec-Biernat and M. Wusthoff, Phys. Rev. **D59** (1999) 014017.
- [251] K. J. Golec-Biernat and M. Wusthoff, Phys. Rev. **D60** (1999) 114023.
- [252] M. B. Johnson *et al.*, Phys. Rev. **C75** (2007) 035206.
- [253] B. Z. Kopeliovich, J. Nemchik, I. K. Potashnikova, M. B. Johnson and I. Schmidt, Phys. Rev. **C72** (2005) 054606.

- [254] J. Nemchik, V. Petracek, I. K. Potashnikova and M. Sumera, Phys. Rev. **C78** (2008) 025213.
- [255] F. Gelis, T. Lappi and R. Venugopalan, Int. J. Mod. Phys. **E16** (2007) 2595–2637.
- [256] J. Jalilian-Marian, A. Kovner, L. D. McLerran and H. Weigert, Phys. Rev. **D55** (1997) 5414–5428.
- [257] J. Jalilian-Marian, A. Kovner, A. Leonidov and H. Weigert, Nucl. Phys. **B504** (1997) 415–431.
- [258] J. Jalilian-Marian, A. Kovner, A. Leonidov and H. Weigert, Phys. Rev. **D59** (1999) 014014.
- [259] E. Iancu, A. Leonidov and L. D. McLerran, Nucl. Phys. **A692** (2001) 583–645.
- [260] E. Iancu, A. Leonidov and L. D. McLerran, Phys. Lett. **B510** (2001) 133–144.
- [261] E. Iancu, K. Itakura and L. McLerran, Nucl. Phys. **A724** (2003) 181–222.
- [262] J. P. Blaizot, F. Gelis and R. Venugopalan, Nucl. Phys. **A743** (2004) 13–56.
- [263] E. Iancu, K. Itakura and D. N. Triantafyllopoulos, Nucl. Phys. **A742** (2004) 182–252.
- [264] R. Baier, Y. Mehtar-Tani and D. Schiff, Nucl. Phys. **A764** (2006) 515–527.
- [265] A. Dumitru, A. Hayashigaki and J. Jalilian-Marian, Nucl. Phys. **A765** (2006) 464–482.
- [266] K. P. Das and R. C. Hwa, Phys. Lett. **B68** (1977) 459.
- [267] V. Greco, C. M. Ko and P. Levai, Phys. Rev. **C68** (2003) 034904.
- [268] R. J. Fries, B. Muller, C. Nonaka and S. A. Bass, Phys. Rev. Lett. **90** (2003) 202303.
- [269] D. Molnar and S. A. Voloshin, Phys. Rev. Lett. **91** (2003) 092301.
- [270] **STAR** Collaboration, J. Adams *et al.*, Phys. Rev. Lett. **92** (2004) 052302.
- [271] **PHENIX** Collaboration, A. Adare *et al.*, Phys. Rev. Lett. **98** (2007) 162301.
- [272] R. C. Hwa, J. Phys. **G35** (2008) 104017.
- [273] R. C. Hwa, Eur. Phys. J. **C43** (2005) 233–237.
- [274] R. C. Hwa, C. B. Yang and R. J. Fries, Phys. Rev. **C71** (2005) 024902.
- [275] X.-N. Wang, M. Gyulassy and M. Plumer, Phys. Rev. **D51** (1995) 3436–3446.
- [276] M. Gyulassy and X.-n. Wang, Nucl. Phys. **B420** (1994) 583–614.
- [277] R. Baier, Y. L. Dokshitzer, A. H. Mueller, S. Peigné and D. Schiff, Nucl. Phys. **B484** (1997) 265–282.
- [278] R. Baier, Y. L. Dokshitzer, A. H. Mueller, S. Peigné and D. Schiff, Nucl. Phys. **B483** (1997) 291–320.
- [279] M. Gyulassy, P. Levai and I. Vitev, Nucl. Phys. **B571** (2000) 197–233.
- [280] U. A. Wiedemann, Nucl. Phys. **B588** (2000) 303–344.
- [281] X.-N. Wang, Z. Huang and I. Sarcevic, Phys. Rev. Lett. **77** (1996) 231–234.
- [282] X.-N. Wang and X. Guo, Nucl. Phys. **A696** (2001) 788–832.
- [283] X.-f. Guo and X.-N. Wang, Phys. Rev. Lett. **85** (2000) 3591–3594.
- [284] P. Arnold, G. D. Moore and L. G. Yaffe, JHEP **06** (2002) 030.
- [285] P. Arnold, G. D. Moore and L. G. Yaffe, JHEP **12** (2001) 009.
- [286] C. A. Salgado and U. A. Wiedemann, Phys. Rev. **D68** (2003) 014008.
- [287] <http://csalgado.web.cern.ch/csalgado/swqw.html>.
- [288] N. Armesto, C. A. Salgado and U. A. Wiedemann, Phys. Rev. **D69** (2004) 114003.
- [289] N. Armesto, A. Dainese, C. A. Salgado and U. A. Wiedemann, Phys. Rev. **D71** (2005) 054027.
- [290] M. Gyulassy, P. Lévai and I. Vitev, Phys. Lett. **B538** (2002) 282–288.
- [291] R. Baier, Y. L. Dokshitzer, A. H. Mueller and D. Schiff, JHEP **09** (2001) 033.
- [292] C. A. Salgado and U. A. Wiedemann, Phys. Rev. Lett. **89** (2002) 092303.
- [293] R. Baier, Nucl. Phys. **A715** (2003) 209–218.
- [294] P. Arnold, arXiv:0808.2767.
- [295] A. Peshier, arXiv:0801.0595.
- [296] T. Hirano and Y. Nara, Phys. Rev. **C66** (2002) 041901.
- [297] T. Hirano and Y. Nara, Prog. Theor. Phys. Suppl. **151** (2003) 133–137.
- [298] T. Hirano and Y. Nara, Phys. Rev. Lett. **91** (2003) 082301.
- [299] T. Renk, J. Ruppert, C. Nonaka and S. A. Bass, Phys. Rev. **C75** (2007) 031902.
- [300] A. Majumder, C. Nonaka and S. A. Bass, Phys. Rev. **C76** (2007) 041902.
- [301] G.-Y. Qin *et al.*, Phys. Rev. **C76** (2007) 064907.
- [302] S. A. Bass *et al.*, J. Phys. **G35** (2008) 104064.
- [303] N. Borghini and U. A. Wiedemann, arXiv:hep-ph/0506218.
- [304] N. Armesto, L. Cunqueiro, C. A. Salgado and W.-C. Xiang, JHEP **02** (2008) 048.
- [305] S. Domdey *et al.*, arXiv:0802.3282.
- [306] F. A. Ceccopieri and L. Trentadue, Phys. Lett. **B636** (2006) 310–316.

- [307] **TASSO** Collaboration, W. Braunschweig *et al.*, *Z. Phys.* **C47** (1990) 187–198.
- [308] **OPAL** Collaboration, G. Abbiendi *et al.*, *Eur. Phys. J.* **C27** (2003) 467–481.
- [309] V. A. Khoze and W. Ochs, *Int. J. Mod. Phys.* **A12** (1997) 2949–3120.
- [310] K. Zapp, G. Ingelman, J. Rathsmann, J. Stachel and U. A. Wiedemann, [arXiv:0804.3568](#).
- [311] T. Renk, *Phys. Rev.* **C78** (2008) 034908.
- [312] N. Armesto, L. Cunqueiro and C. A. Salgado, [arXiv:0809.4433](#).
- [313] I. P. Lokhtin *et al.*, [arXiv:0810.2082](#).
- [314] I. P. Lokhtin and A. M. Snigirev, *Eur. Phys. J.* **C45** (2006) 211–217.
- [315] S. Sapeta and U. A. Wiedemann, *Eur. Phys. J.* **C55** (2008) 293–302.
- [316] R. Sassot, M. Stratmann and P. Zurita, [arXiv:0906.5521](#).
- [317] I. Vitev, *Phys. Rev.* **C75** (2007) 064906.
- [318] G. T. Garvey and J. C. Peng, *Phys. Rev. Lett.* **90** (2003) 092302.
- [319] F. Arleo *et al.*, [arXiv:hep-ph/0310274](#).
- [320] F. Arleo, *Eur. Phys. J.* **C30** (2003) 213–221.
- [321] A. Accardi, *Acta Phys. Hung.* **A27** (2006) 189–192.
- [322] F. Arleo, *Nucl. Phys.* **A755** (2005) 515–518.
- [323] F. Arleo, [arXiv:hep-ph/0309108](#).
- [324] B. A. Kniehl, G. Kramer and B. Potter, *Nucl. Phys.* **B582** (2000) 514–536.
- [325] S. Kretzer, *Phys. Rev.* **D62** (2000) 054001.
- [326] A. Accardi, *Eur. Phys. J.* **C49** (2007) 347–353.
- [327] B.-W. Zhang, X.-N. Wang and A. Schaefer, *Nucl. Phys.* **A783** (2007) 551–554.
- [328] B.-W. Zhang, E. Wang and X.-N. Wang, *Phys. Rev. Lett.* **93** (2004) 072301.
- [329] B.-W. Zhang, E.-k. Wang and X.-N. Wang, *Nucl. Phys.* **A757** (2005) 493–524.
- [330] Y. Guo, B.-W. Zhang and E. Wang, *Phys. Lett.* **B641** (2006) 38–44.
- [331] A. Majumder and B. Muller, *Phys. Rev.* **C77** (2008) 054903.
- [332] A. Majumder, R. J. Fries and B. Muller, *Phys. Rev.* **C77** (2008) 065209.
- [333] A. Majumder, [arXiv:0901.4516](#).
- [334] X. Guo and J. Li, [arXiv:0705.4211](#).
- [335] F. Arleo, *Phys. Lett.* **B532** (2002) 231–239.
- [336] **FNAL E772** Collaboration, M. B. Johnson *et al.*, *Phys. Rev. Lett.* **86** (2001) 4483–4487.
- [337] M. B. Johnson *et al.*, *Phys. Rev.* **C65** (2002) 025203.
- [338] R. Baier, Y. L. Dokshitzer, A. H. Mueller and D. Schiff, *Phys. Rev.* **C58** (1998) 1706–1713.
- [339] M. Johnson, V. Litvinenko and G. Swift, . Presented at IEEE Particle Accelerator Conference (PAC2001), Chicago, Illinois, 18–22 Jun 2001.
- [340] I. Vitev, J. T. Goldman, M. B. Johnson and J. W. Qiu, *Phys. Rev.* **D74** (2006) 054010.
- [341] E. Shuryak, *Prog. Theor. Phys. Suppl.* **168** (2007) 320–329.
- [342] J. M. Maldacena, *Adv. Theor. Math. Phys.* **2** (1998) 231–252.
- [343] E. Witten, *Adv. Theor. Math. Phys.* **2** (1998) 253–291.
- [344] E. Witten, *Adv. Theor. Math. Phys.* **2** (1998) 505–532.
- [345] S. S. Gubser, I. R. Klebanov and A. M. Polyakov, *Phys. Lett.* **B428** (1998) 105–114.
- [346] M. Natsuume, [arXiv:hep-ph/0701201](#).
- [347] J. Casalderrey-Solana and C. A. Salgado, *Acta Phys. Polon.* **B38** (2007) 3731–3794.
- [348] J. D. Edelstein and C. A. Salgado, *AIP Conf. Proc.* **1031** (2008) 207–220.
- [349] N. N. Nikolaev, *Z. Phys.* **C5** (1980) 291.
- [350] A. Bialas, *Acta Phys. Polon.* **B11** (1980) 475.
- [351] A. Bialas and T. Chmaj, *Phys. Lett.* **B133** (1983) 241.
- [352] M. Gyulassy and M. Plumer, *Nucl. Phys.* **B346** (1990) 1–16.
- [353] A. Bialas and J. Czyzewski, *Phys. Lett.* **B222** (1989) 132.
- [354] J. Czyzewski, *Acta Phys. Polon.* **B21** (1990) 41–45.
- [355] B. Z. Kopeliovich, *Phys. Lett.* **B243** (1990) 141–143.
- [356] J. Czyzewski and P. Sawicki, *Z. Phys.* **C56** (1992) 493–498.
- [357] A. Bialas and J. Czyzewski, *Z. Phys.* **C47** (1990) 133–136.
- [358] K. Fialkowski and R. Wit, *Eur. Phys. J.* **A32** (2007) 213–218.
- [359] K. Fialkowski and R. Wit, [arXiv:0705.4354](#).
- [360] N. Akopov, L. Grigoryan and Z. Akopov, *Eur. Phys. J.* **C44** (2005) 219–226.

- [361] B. Z. Kopeliovich, A. V. Tarasov and A. Schafer, Phys. Rev. **C59** (1999) 1609–1619.
- [362] B. Z. Kopeliovich, A. Schafer and A. V. Tarasov, Phys. Rev. **D62** (2000) 054022.
- [363] K. Gallmeister and U. Mosel, Nucl. Phys. **A801** (2008) 68–79.
- [364] T. Falter, W. Cassing, K. Gallmeister and U. Mosel, Phys. Rev. **C70** (2004) 054609.
- [365] M. Effenberger, E. L. Bratkovskaya and U. Mosel, Phys. Rev. **C60** (1999) 044614.
- [366] M. Effenberger and U. Mosel, Phys. Rev. **C62** (2000) 014605.
- [367] W. Cassing and E. L. Bratkovskaya, Phys. Rept. **308** (1999) 65–233.
- [368] S. A. Bass *et al.*, Prog. Part. Nucl. Phys. **41** (1998) 255–369.
- [369] P. Jain, B. Pire and J. P. Ralston, Phys. Rept. **271** (1996) 67–179.
- [370] F. E. Low, Phys. Rev. **D12** (1975) 163–173.
- [371] S. Nussinov, Phys. Rev. Lett. **34** (1975) 1286–1289.
- [372] W. R. Greenberg and G. A. Miller, Phys. Rev. **D47** (1993) 1865–1878.
- [373] W. R. Greenberg and G. A. Miller, Phys. Rev. **C49** (1994) 2747–2762.
- [374] G. R. Farrar, H. Liu, L. L. Frankfurt and M. I. Strikman, Phys. Rev. Lett. **61** (1988) 686–689.
- [375] J. Dias de Deus, Phys. Lett. **B166** (1986) 98.
- [376] F. E. Close, R. L. Jaffe, R. G. Roberts and G. G. Ross, Phys. Rev. **D31** (1985) 1004.
- [377] R. L. Jaffe, F. E. Close, R. G. Roberts and G. G. Ross, Phys. Lett. **B134** (1984) 449.
- [378] W. Cassing, K. Gallmeister and C. Greiner, Nucl. Phys. **A735** (2004) 277–299.
- [379] K. Gallmeister and W. Cassing, Nucl. Phys. **A748** (2005) 241–259.
- [380] W. Ehehalt and W. Cassing, Nucl. Phys. **A602** (1996) 449–486.
- [381] J. Geiss, W. Cassing and C. Greiner, Nucl. Phys. **A644** (1998) 107–138.
- [382] H. P. Blok and L. Lapikas, Phys. Rev. **C73** (2006) 038201.
- [383] HERMES Collaboration, G. Elbakian in *Proceedings of “DIS 2003”, St.Petersburg, April 23-27, 2003*; V.T. Kim and L.N. Lipatov eds., p. 597, 2003.
- [384] A. Accardi, Phys. Lett. **B649** (2007) 384–389.
- [385] J. C. Collins and D. E. Soper, Nucl. Phys. **B194** (1982) 445.
- [386] Y. van Haarlem, “The HERMES recoil photon-detector and nuclear p_T -broadening at HERMES”. (DESY-THESIS-2007-033).
- [387]
- [388] A. Accardi, arXiv:0808.0656.
- [389] F. A. Ceccopieri and L. Trentadue, Phys. Lett. **B660** (2008) 43–48.
- [390] S. Domdey, D. Grunewald, B. Z. Kopeliovich and H. J. Pirner, arXiv:0812.2838.
- [391] F. Arleo and D. d’Enterria, Phys. Rev. **D78** (2008) 094004.
- [392] W. A. Horowitz and M. Gyulassy, Phys. Lett. **B666** (2008) 320–323.
- [393] ALICE Collaboration, F. Carminati *et al.*, J. Phys. **G30** (2004) 1517–1763.
- [394] ALICE Collaboration, B. Alessandro *et al.*, J. Phys. **G32** (2006) 1295–2040.
- [395] F. Arleo, P. Aurenche, Z. Belghobsi and J.-P. Guillet, JHEP **11** (2004) 009.
- [396] COMPASS Collaboration, P. Abbon *et al.*, Nucl. Instrum. Meth. **A577** (2007) 455–518.
- [397] D. F. Geesaman, P. E. Reimer *et al.*, . Fermilab proposal Projects-doc-395, <http://projects-docdb.fnal.gov/cgi-bin/ShowDocument?docid=395>.
- [398] M. Asakawa *et al.*, . KEK-REPORT-2000-11.
- [399] J. C. Peng, G. T. Garvey, J. M. Moss, S. Sawada and J. Chiba, arXiv:hep-ph/0007341.
- [400] D. de Florian and R. Sassot, Phys. Rev. **D69** (2004) 074028.
- [401] M. Hirai, S. Kumano and T. H. Nagai, Phys. Rev. **C76** (2007) 065207.
- [402] K. J. Eskola, H. Paukkunen and C. A. Salgado, JHEP **04** (2009) 065.
- [403] NA61 Collaboration, M. Posiadala, arXiv:0901.3332.
- [404] A. Baldit *et al.*, . CERN-SPSC-2000-010.
- [405] J. Engelfried *et al.*, Nucl. Instrum. Meth. **A502** (2003) 285–288.
- [406] Common ENC/EIC workshop, GSI, Darmstadt, Germany, 28-30 May 2009, <https://indico.gsi.de/conferenceTimeTable.py?confId=436>.
- [407] A. Deshpande, “Physics and status of the Electron-Ion Collider (EIC)”, talk at PANIC08, <http://www.weizmann.ac.il/MaKaC/conferenceDisplay.py?confId=0>.
- [408] V. Litvinenko. talk at [406].
- [409] Y. Zhang. talk at [406].
- [410] R. Ent. talk at [406].

- [411] J. B. Dainton, M. Klein, P. Newman, E. Perez and F. Willeke, *JINST* **1** (2006) P10001.
- [412] 1st ECFA-CERN LHeC Workshop, Divonne-les-Bains, France, 1-3 September 2008, <http://indico.cern.ch/conferenceDisplay.py?confId=31463>.
- [413] A. Jankowiak. talk at [406].
- [414] A. Frawley *et al.*, "Future Science at the Relativistic Heavy Ion Collider", BNL-77334-2006-IR (2006).
- [415] **ATLAS** Collaboration, G. Aad *et al.*, [arXiv:0901.0512](https://arxiv.org/abs/0901.0512).
- [416] **ATLAS** Collaboration, B. Wosiek, *Acta Phys. Polon.* **B38** (2007) 1047–1055.
- [417] **CMS** Collaboration, G. L. Bayatian *et al.*, *J. Phys.* **G34** (2007) 995–1579.
- [418] **CMS** Collaboration, D. d’Enterria (ed.) *et al.*, *J. Phys.* **G34** (2007) 2307–2455.
- [419] **CMS** Collaboration, C. Loizides, *J. Phys.* **G35** (2008) 104166.